PROGRESS IN RESEARCH

April 1, 2016 - March 31, 2017

CYCLOTRON INSTITUTE

Texas A&M University

College Station, Texas

PROGRESS IN RESEARCH

APRIL 1, 2016 - MARCH 31, 2017

Prepared By

The Cyclotron Institute Staff

Texas A&M University

College Station, TX 77843-3366

Phone: (979) 845-1411
Fax: (979) 845-1899

Web: http://cyclotron.tamu.edu

July 2017

TABLE OF CONTENTS

SECTION I: NUCLEAR STRUCTURE, FUNDAMENTAL INTERACTIONS AND ASTROPHYSICS

SECTION II: HEAVY ION REACTIONS

SECTION III: NUCLEAR THEORY

SECTION IV: SUPERCONDUCTING CYCLOTRON, INSTRUMENTATION AND RIB UPGRADE

SECTION V: PUBLICATIONS

SECTION VI: APPENDIX

Introduction
April 1, 2016 – March 31, 2017

Progress in research and operations at the Texas A&M Cyclotron Institute is summarized in this report for the period April, 1, 2016 through March 31, 2017. The format follows that of previous years. Sections I through III contain reports from individual research projects. Operation and technical developments are given in Section IV. Section V lists the publications with Cyclotron Institute authors and outside users and the Appendix gives additional information including talks presented by members of the Institute during the past year. Once again, the full volume of this year's Progress in Research is available only on our web site (http://cyclotron.tamu.edu). *Since most of the contributions presented here are truly reports on progress in research, results and conclusions should not be quoted from the report without the consent of the authors.*

We are pleased to announce that Dr. Che-Ming Ko was named a Distinguished Professor, Dr. Saskia Miodeusewski was promoted to full Professor and Dr. Jeremy Holt was awarded an NSF CAREER Award. Dr. Joseph Natowitz and Dr. Dave Youngblood both retired after 50 years on the faculty.

The K500 provided an impressive 6,200 hours of beam for both science and radiation effects testing. The K150 cyclotron provided again, a record 3,800 hours of beam on target and is now being used by external users for radiation effects testing with its proton beams. The list of beams from the K150 included protons (strip extracted), deuterons (strip extracted), ^{4}He, ^{10}B, ^{19}F, ^{22}Ne, ^{23}Na, ^{25}Mg and ^{28}Si. Proton beams from the K150 (strip extracted) are now available from 3 MeV to 50 MeV. Also, the K150 ^{4}He beam is of note because 5 particle-microamps of beam at 7.2 MeV/u were provided on target for the production of ^{211}At from ^{4}He+^{209}Bi. Progress was made with the light-ion guide (LIG) project in that ^{64}Ga 12+ ions were produced, charge-bred and extracted from the charge-breeding ECR source (CB-ECR). Also, this year, the K150 and K500 cyclotrons were used together for the first time to attempt to produce and re-accelerate the ^{64}Ga 12+ radioactive ions.

As in previous reports, I include here some highlights of work carried out over the past year.

- We have settled a longstanding controversy over the calculation of Internal Conversion Coefficients (ICCs): Should the effects of the vacancy in the atomic shell left behind by the departing conversion electron be accounted for or not? By making precise measurements of ICCs for E3 and M4 transitions in eight nuclei spanning the range $47 < Z < 79$, we have been able to distinguish between results from the two methods used to calculate ICCs, and have unequivocally demonstrated that the vacancy effects must be included. This result has already impacted the way in which ICCs are being calculated by the National Nuclear Data Center.

- We have commissioned the TIARA detector array, coupling it to the MDM and four HPGe clovers.

- We have completed a four-experiment science campaign with TIARA, constraining important reactions in nova nucleosynthesis and the S-process.

- A new method for indirect radiative capture reactions that allows one to measure (p,γ), (α,γ) and (n,γ) astrophysical radiative capture reactions on stable and unstable isotopes has been suggested. A special attention is given to the "holy grail" reaction $^{12}C(\alpha,\gamma)^{16}O$.

- RHIC gluon polarization measurements were identified as the BNL research highlight in the 2016 Annual Report on the State of the DOE National Laboratories.

- A new method has been developed to resum the interaction contribution to the equation of state of strongly coupled systems in the Luttinger-Ward-Baym formalism. When applied to the quark-gluon plasma using interactions constrained by lattice QCD, large collisional widths dissolve the quark and gluon quasi-particles while broad hadronic bound states emerge as the dominant degrees of freedom near the critical temperature.

- A previously developed rate equation approach for quarkonium kinetics in hot QCD matter has been deployed to bottomonium production in heavy-ion collisions, including in-medium binding energies and dissociation rates.

- The strong suppression of the Y(2S) observed at the LHC provides a clean signal of deconfinement, while the suppression of Y(1S) states yields a measure of color screening of the short-distance QCD force.

- Recent experiments on In and Tl extraction into either betainium-based fluorinated ionic liquids or carboxylic acid-based deep eutectic mixtures from hydrochloric acid media have shown promising results for an effective transfer of these elements into an organic phase, which is beneficial for a future chemical study of their heavy homolog nihonium (Z = 113).

- The heavy elements group has studied the reactions of ^{40}Ar with lanthanide targets, and cross sections were measured for the complete fusion, neutron evaporation channels. Preliminary results indicate that the data are consistent with previous results, and further strengthen the argument that the production of new superheavy elements will be very difficult.

- The NZ equilibration curve for the dynamical component is consistent with the overall NZ equilibration curve in deformed projectile-like fragments.

- Using the Gibbs-Tolman-Widom concept of sharp equimolar surface we have derived the pressure and equation of state for finite nuclei within the extended Thomas Fermi approximation for the energy density functional.

- We have developed a method for unitarity restoration in the nuclear spectral function by modifying the optical model green function and applied it in the study of the isoscalar giant monopole resonance.

- With the nuclear polarization of laser-cooled atoms at TRINAT determined to be 99.13(9)%, we have made a 0.3% measurement of the beta asymmetry parameter, A_β. This is the most precise relative measurement of a polarized angular distribution parameter in any nuclear system, including the neutron.

- A prototype cylindrical Penning trap, 80 mm in diameter, has been installed and commissioned. We have demonstrated trapping of stable K and Na and the ability to excite the ion motions. Resonance scans have been made demonstrating mass-resolving powers at the ppm level.

- A study based on an extended relativistic Vlasov–Uehling–Uhlenbeck transport model, which includes both the pion in-medium effects and the in-medium threshold effects on Delta resonance production and decay, has shown that to reproduce the available experimental data on charged pion ratio in high-energy heavy ion collisions requires a nuclear symmetry energy that has a density slope of about 59 MeV at normal nuclear matter density, consistent with current constraints from other observables.

- A new method for automated particle identification of charged particle in ΔE-E telescopes has been developed.

Institute scientists remain active in a number of collaborative research efforts around the world. Major programs include: mass measurements using the Penning Trap at the University of Jyväskylä; continued work with the STAR collaboration at RHIC; measurements of beta decays with the TRINAT collaboration at TRIUMF; ANASEN at MSU; and participation in the SAMURAI collaboration at RIBF in Tokyo, Japan.

I am indebted to Dr. Y.-W. Lui for assembling this report.

S.J. Yennello
July 14, 2017

SECTION I

NUCLEAR STRUCTURE, FUNDAMENTAL INTERACTIONS AND ASTROPHYSICS

Superallowed beta decay

J.C. Hardy, I.S. Towner, V.E. Iacob, H.I. Park, N. Nica, M. Bencomo, T. Eronen,
V. Horvat, and L. Chen

Superallowed $0^+ \rightarrow 0^+$ beta decay between T=1 analogue states has been a subject of continuous and often intense study for five decades. The *ft* values of such transitions are nearly independent of nuclear-structure ambiguities and depend uniquely on the vector part of the weak interaction. Their measurement gives us access to clean tests of some of the fundamental precepts of weak-interaction theory, and, over the years, this strong motivation has led to very high precision being achieved both in the experiments and in the theory used to interpret them. We have a major program at the Cyclotron Institute to study superallowed beta decay.

To obtain the *ft* value for any transition, three quantities must be measured: the half-life $t_{1/2}$ of the parent, the Q_{EC} value for the transition of interest, and the branching ratio R for that transition. Our most recent complete survey of world data on these superallowed decays, published in 2015 [1], provides a critical evaluation of all the experimental data and final *ft* values obtained from the averaged results, to which radiative and isospin-symmetry-breaking corrections have been applied in order to derive a final set of “corrected ft values”, denoted $\mathcal{F}t$ for 14 transitions known to ~0.1% precision. Last year, we made an interim update of this survey [2], the results from which are shown in Fig. 1. Excellent consistency among the average $\mathcal{F}t$ values for all 14 transitions – an expected consequence of the conservation of vector current (CVC) – confirms the validity of the correction terms; and our recent measurement of ^{38}Ca decay [3,4], which closely compares a pair of mirror superallowed transitions with A = 38, further supports that validity.

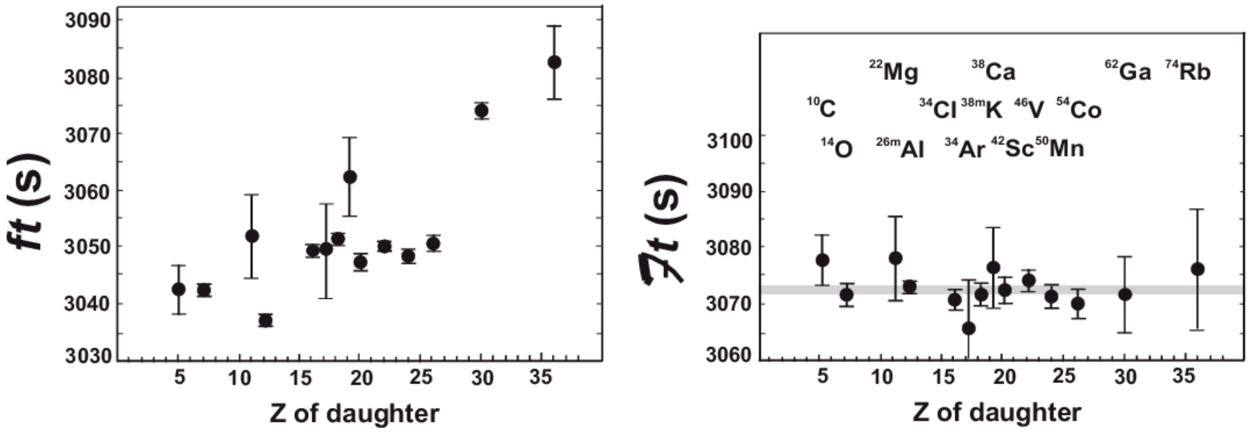

FIG. 1. Results from the 2015 survey [1] updated to 2016 [2]: The uncorrected *ft* values for the 14 best known superallowed decays appear on the left; the same results but incorporating the radiative and isospin-symmetry-breaking correction terms are on the right. The grey band in the right panel is the average $\mathcal{F}t$ value and its uncertainty.

The resultant average $\mathcal{F}t$ value, when combined with the muon lifetime, yields the up-down quark-mixing element of the Cabibbo-Kobayashi-Maskawa (CKM) matrix, V_{ud} = 0.97420(21), a result that is consistent with, but more precise than, values we have obtained in previous analyses of superallowed β decay. The unitarity test on the top row of the matrix becomes $|V_{ud}|^2 + |V_{us}|^2 + |V_{ub}|^2 = 0.99963$ (49) if the Particle Data Group recommended value for V_{us} is used. However, recent lattice QCD calculations have introduced some inconsistency into kaon-decay measurements of V_{us} and V_{us}/V_{ud} . In ref. [1], we have examined the impact of these new results on the unitarity test and conclude that there is no evidence of any statistically significant violation of unitarity. Finally, from the $\mathcal{F}t$ -value data we also set limits on the possible existence of scalar interactions.

This result is not only a significant verification of the standard model but the uncertainty quoted on the sum provides a tight limit on any possible new physics beyond the standard model, such as right-hand currents, extra *Z* bosons or supersymmetric models. In short, superallowed $0^+ \rightarrow 0^+$ beta decay provides a high-profile application of nuclear-physics measurements to the study of fundamental symmetries, a subject of vital interest to both nuclear and particle physicists. Although much has already been achieved in this field by nuclear physicists, improvements are still possible. Reducing the uncertainty on the unitarity sum – and, with it, the scope for new physics – remains the primary goal of our research program.

Our approach follows from the observation [1] that the second largest contributor to the uncertainty in V_{ud} is the theoretical uncertainty in the nuclear-structure-dependent corrections, δ_{NS} and δ_C, used in the derivation of the $\mathcal{F}t$ values. Though these corrections are only of order 1%, their effect is very significant: The bottom two panels of Fig. 1 show the result of applying the nuclear-structure-dependent corrections, δ_{NS} and δ_C (together with δ'_R, which is nearly independent of *Z*). Obviously they act very well to remove the considerable "scatter" in *ft* values apparent in the panel on the left, replacing it with the consistent set of corrected $\mathcal{F}t$ values appearing on the right. Since these corrections were determined [5] completely independently of the superallowed decay data, this consistency in $\mathcal{F}t$ values is already a powerful validation of the calculations, but obviously the remaining uncertainty still influences the final result for V_{ud}.

Even though the 2015 survey [1] included more than 222 individual measurements (and the 2016 update includes a dozen more) relating to 14 precisely known *ft* values, it is still possible for well selected experiments to make real improvements in the validation tests of the nuclear-structure-dependent correction terms. At TAMU we are currently focusing on adding to the *ft*-value list new superallowed transitions, selected from amongst those with *large* calculated corrections. If the *ft* values measured for cases with large calculated corrections also turn into corrected $\mathcal{F}t$ values that are consistent with the others, then this must verify the calculations' reliability for the existing cases, which have smaller corrections. We are studying decays from $T_z = -1$ parent nuclei, which consistently have higher predicted structure-dependent correction terms than the well-known $T_z = 0$ cases.

Of particular importance are the four $T_z = -1$ parent nuclei – ^{26}Si, ^{34}Ar, ^{38}Ca and ^{42}Ti – whose decays are mirrors to well-known superallowed decays from $T_z = 0$ parents. Specifically, the mirror-decay pairs are $^{26}\text{Si} \rightarrow {}^{26m}\text{Al} \rightarrow {}^{26}\text{Mg}$, $^{34}\text{Ar} \rightarrow {}^{34}\text{Cl} \rightarrow {}^{34}\text{S}$, $^{38}\text{Ca} \rightarrow {}^{38m}\text{K} \rightarrow {}^{38}\text{Ar}$ and $^{42}\text{Ti} \rightarrow {}^{42}\text{Sc} \rightarrow {}^{42}\text{Ca}$. Their importance stems from our observation that the ratio of mirror *ft* values for such cases is very sensitive to the model used to calculate the small isospin-symmetry-breaking corrections δ_{NS} and δ_C. The details have been described in our report on the first measurement of a mirror pair, with $A = 38$ [3]. Until very recently, none of the T_z = -1 parent decays was known precisely enough to provide a statistically significant constraint on the correction terms via the ratio of mirror *ft* values, but we are now well on our way to rectifying this situation.

After a long period of incremental upgrades to our experimental techniques, we succeeded in pushing our precision in branching ratio measurements close to ±0.1%, our ultimate goal. This is crucial for the characterization of T_z = -1 parent decays, which – unlike T_Z = 0 decays – exhibit a number of strong Gamow-Teller branches that compete with the superallowed Fermi branch. A demonstration of our success in this endeavor is our measurement of the superallowed branching ratio for the decay of ^{38}Ca ($t_{1/2}$ = 444 ms) to a precision of ±0.2%, where that precision was actually limited by counting statistics, not systematics [3,4]. To our knowledge, this is the most precise direct branching-ratio measurement ever made for short-lived beta emitter. It also provides the first mirror pair of $0^+ \rightarrow 0^+$ superallowed emitters (^{38}Ca and ^{38}K^m) that is precise enough to distinguish meaningfully between the Saxon-Woods-based radial-overlap correction, δ_{C2}, and the one based on Hartree-Fock radial wave functions. It favors the former over the latter, but we must await results from the other mirror pairs before we can be confident of the verdict.

We are now well embarked on the measurement of the remaining three accessible pairs. We have already completed measurements of the half-life and branching ratio for the superallowed decay of ^{34}Ar [6]. However, the branching-ratio result depends critically on the gamma-branching of the 666-keV level populated by beta decay in the daughter, ^{34}Cl: A possible weak branch from this level has 519 keV, which would be masked in our spectrum by the tail of the strong 511-keV annihilation peak. We are planning a (p, γ) measurement at Notre Dame to determine the relative intensity of this branch before we publish our results. In addition, we have made a successful measurement of the ^{26}Si beta-decay branching ratios, which is under analysis as the thesis project of M. Bencomo [7]. Finally we have made initial measurements of the half-life of ^{42}Ti, which have been analyzed [8]. A final measurement is scheduled for us to achieve the precision we seek.

We continue the endeavor to improve our data acquisition techniques for half-life measurements, making use of a TDC-based approach and a digital-pulse-analysis system, in addition to our longstanding analog technique. We are just concluding our analysis of a measurement of the half-life of another T_Z = -1 superallowed emitter, ^{30}S, in which we used all three different methods for taking data [9]. In the same context, we continue to explore potential improvements in the statistical handling of our data [10].

With a somewhat different focus, in late 2015 we began a new measurement of the branching ratio for the superallowed decay of ^{10}C. Currently the uncertainty on the branching ratio dominates the uncertainty in the ^{10}C $\mathcal{F}t$ value. However, more interesting than just the precision of the $\mathcal{F}t$ value itself is its relationship to the world average of $\mathcal{F}t$ values for transitions in heavier nuclei, since the ^{10}C transition is the most sensitive to the possible presence of a scalar current. Currently the $\mathcal{F}t$ value for ^{10}C is slightly higher than the world average $\mathcal{F}t$ value, with an error bar that just about touches the world average value's error bar. If a more precise $\mathcal{F}t$ value of ^{10}C were found to deviate with greater statistical significance, it would be a signal for the existence of a scalar current. This work is still in progress [11].

Finally, each superallowed *ft*-value determination depends critically on the precision of the corresponding Q_{EC}-value measurement, which enters to the fifth power in the determination of *f*. In past years we have made many such measurements with the JYFLTRAP Penning-trap mass spectrometer at the University of Jyvaskyla cyclotron facility in Finland, where we collaborate with the team there. This facility is ideally suited to the measurement of Q_{EC}-values, which, with technical developments, have now reached sub-100-eV precision. So far we have measured the Q_{EC}-values for 10 superallowed emitters there: ^{10}C, ^{26}Al^{m}, ^{34}Cl, ^{34}Ar, ^{38}K^{m}, ^{38}Ca, ^{42}Sc, ^{46}V, ^{50}Mn, and ^{54}Co. It is now possible to improve some of the earliest measurements we made there. We have recently done so for the case of ^{42}Sc [12], reducing the uncertainty from ±210 eV to ±53 eV.

[1] J.C. Hardy and I.S. Towner, Phys. Rev. C **91**, 025501 (2015).

[2] J.C. Hardy and I.S. Towner, Proceedings of CKM2016, the 9th International Workshop on the CKM Unitarity Triangle (to be published in Proceedings of Science).

[3] H.I. Park, J.C. Hardy, V.E. Iacob, M. Bencomo, L. Chan, V. Horvat, N. Nica, B.T. Roeder, E. Simmons, R.E. Tribble, and I.S. Towner, Phys. Rev. Lett. **112**, 102502 (2014).

[4] H.I. Park, J.C. Hardy, V.E. Iacob, M. Bencomo, L. Chen, V. Horvat, N. Nica, B.T. Roeder, E. McCleskey, R.E. Tribble and I.S. Towner, Phys. Rev. C **92**, 015502 (2015).

[5] I.S. Towner and J.C. Hardy, Phys. Rev. C **77**, 025501 (2008).

[6] V.E. Iacob *et al.*, *Progress in Research,* Cyclotron Institute, Texas A&M University (2016-2017), p. I-12.

[7] M. Bencomo *et al.*, *Progress in Research,* Cyclotron Institute, Texas A&M University (2016-2017), p. I-7.

[8] H.I. Park *et al.*, *Progress in Research,* Cyclotron Institute, Texas A&M University (2016-2017), p. I-15.

[9] J.C. Hardy *et al.*, *Progress in Research,* Cyclotron Institute, Texas A&M University (2016-2017), p. I-10.

[10] V. Horvat and J.C. Hardy, *Progress in Research,* Cyclotron Institute, Texas A&M University (2017-2017), p. IV-33.

[11] T. Eronen *et al.*, *Progress in Research,* Cyclotron Institute, Texas A&M University (2016-2017), p. I-5.

[12] T. Eronen *et al.*, *Progress in Research,* Cyclotron Institute, Texas A&M University (2016-2017), p. I-16.

Superallowed beta branching-ratio measurement of ^{10}C

T. Eronen, J.C. Hardy, V. Iacob, H.I. Park, M. Bencomo, L. Chen, V. Horvat, N. Nica,
B.T. Roeder, and A. Saastamoinen

^{10}C is the lightest superallowed $0^+ \rightarrow 0^+$ β emitter. Its superallowed branch is one of the 14 most precisely measured transitions that are used to derive the upper left element, V_{ud}, of the Cabibbo-Kobayashi-Maskawa (CKM) quark mixing matrix [1,2]. This element is an essential ingredient of the most demanding test available of the unitarity of the CKM matrix, a fundamental principle of the Standard Model of Particle Physics.

For each contributing superallowed transition, its comparative half-life, or $\mathcal{F}t$ value, has been determined to a precision of ~0.1%. This means that the three experimental quantities required (half-life, superallowed β-branching ratio and the decay Q_{EC}-value) and several (small) theoretical corrections must each be known to even higher precision.

What makes ^{10}C an especially interesting case is its sensitivity to the possibility of a scalar weak current, the presence of which would be a signal for physics beyond the Standard Model. Currently, the $\mathcal{F}t$ value of ^{10}C is slightly off from the world-average, hinting at interesting possibilities. To confirm whether the ^{10}C $\mathcal{F}t$ value really points towards physics beyond the Standard Model, more precise input data are needed to determine its $\mathcal{F}t$ value with greater precision. The half-life, Q_{EC} value and the theoretical corrections are all known to contribute less than 0.04 % to the $\mathcal{F}t$ value's relative uncertainty. What sticks out is the branching ratio, which is "only" known to ±0.13 %. Our goal is to equal or improve this uncertainty.

There are two major reasons that the branching-ratio measurement is such a challenge. The first is that the superallowed 0^+ state in the daughter nucleus depopulates by the emission of a 1022-keV gamma ray. This is exactly twice the energy of the 511-keV photons released by positron annihilation, which means that *piled-up* detector signals contribute unwanted counts to the 1022-keV γ-ray peak. The second reason is that the branching ratio itself is very small (1.4646(19)%). These two factors lead to opposite demands: The first calls for low count rates, while the second requires a vast amount of data to achieve statistical precision.

We have now made two one-week-long measurements to determine the branching ratio. The first measurement was carried out in November 2015 and the second in July 2016. In the first run, we used our well-established beta-gamma coincidence setup, composed of a finely calibrated HPGe detector [3] and a plastic scintillator detector [4]. The second measurement was more "experimental". Instead of using the scintillator, which has ~45% solid-angle coverage, we opted to use our 4π proportional gas counter which has nearly 100% coverage. Unfortunately, the insulation vacuum of the HPGe detector failed during the second measurement so we had to resort to our less-well-calibrated back-up HPGe detector.

In principle, the determination of the ^{10}C superallowed branching ratio is simple since the beta decay proceeds either through the T=1, 0^+ state or a lower-energy T=0, 1^+ state in the daughter ^{10}B; the branch to the ground state is second forbidden. The 0^+ state depopulates by emitting 1022-keV and 718-keV gamma rays, while the 1+ state depopulates by just emitting a 718 keV gamma ray. The superallowed branching ratio is then just the ratio of 1022-keV to 718-keV gamma rays. In practice this is not at all simple because of various systematic effects, including pile-up of annihilation radiation. The data analysis is progressing.

To arrive at the absolute number of 718-keV and 1022-keV gamma rays measured in β-γ coincidence, the efficiency of both the HPGe detector (for gammas) and the beta detector (either the scintillator or the gas detector) are needed. Both efficiencies are obtained from Monte Carlo simulations, the former being anchored by meticulous experimental calibration [3]. As a further check of the HPGe efficiencies we produced a calibration source that had vary similar γ-ray energies to the ^{10}C decay; this also allowed us to use the data from our backup detector.

The 511+511 pileup was characterized with sources and allowed us to determine the pileup "time constant" to within a few percent precision. This is enough to allow us to reach our goal of 0.1% precision, since we tuned the decay rate during the measurements so that the 1022-keV peak never contained more than a 5% contribution from pileup events.

We aim to finish the analysis during 2017.

[1] J.C. Hardy *et al., Progress in Research,* Cyclotron Institute, Texas A&M University (2016-2017), p. I-1.

[2] J.C. Hardy and I.S. Towner, Phys. Rev. C **91**, 025501 (2015).

[3] R.G. Helmer *et al*., Nucl. Instrum. Methods Phys. Res. **A511**, 360 (2003).

[4] H.I. Park *et al*., Phys. Rev. C **92**, 015502 (2015).

Superallowed β-decay branching ratio measurement of ^{26}Si

M. Bencomo, J.C. Hardy, V.E. Iacob, H.I. Park, L. Chen, V. Horvat, N. Nica, B.T. Roeder,
A. Saastamoinen, and I.S. Towner

We have measured the branching ratios for the superallowed $0^+ \rightarrow 0^+$ β^+ emitter ^{26}Si (Fig. 1). Since the Q_{EC} [1] value and half-life [2] have already been measured, the branching ratio for the superallowed transition allows us to determine the *ft* value. This completes the second pair of mirror superallowed transitions between T=1 states: $^{26}\mathrm{Si} \rightarrow {}^{26m}\mathrm{Al}$ and $^{26m}\mathrm{Al} \rightarrow {}^{26}\mathrm{Mg}$. Previous measurements of the *A*=38 mirror transitions, $^{38}\mathrm{Ca} \rightarrow {}^{38m}\mathrm{K}$ and $^{38m}\mathrm{K} \rightarrow {}^{38}\mathrm{Ar}$, showed that the ratio of mirror *ft* values is very sensitive to the model used to calculate the small isospin-symmetry-breaking corrections required to extract V_{ud}. In calculating this correction both Woods-Saxon (WS) and Hartree-Fock (HF) radial wave functions have been used, with the experimental results from the first pair favoring the Woods-Saxon option [3]. In an effort to determine if this conclusion is generally applicable we undertook the measurement of ^{26}Si decay.

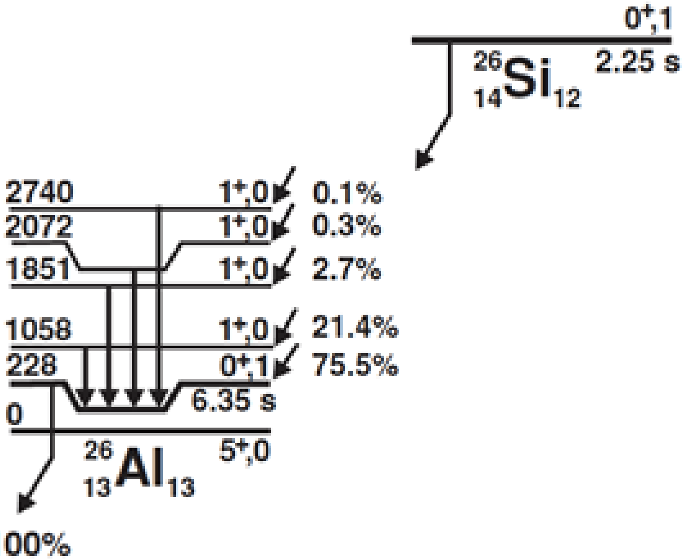

FIG. 1. Decay scheme of ^{26}Si showing only those features of relevance to the superallowed β decay. All energies in keV. Data taken from Ref. [4].

In our last report, we focused on explaining some of the largest corrections that need to be taken into account in our analysis in order to obtain a branching ratio. We explained in some detail the corrections for random coincidences, parent-daughter fraction, coincidence summing and impurities. Other smaller corrections, such as dead time, bremsstrahlung, and preemption of real coincidences were only mentioned. We have now determined these smaller corrections and obtained branching ratios for the 1^+ states populated by Gamow-Teller β decay, and from that we have determined the superallowed branching ratio to the 0^+ state by subtraction. Here we present the results for the corrections not previously reported:

Dead time - This refers to the time during which the electronics are busy processing a signal from the detector. The dead time for β detection is small, ~450 ns. The γ detection on the other hand is much slower and the dead time depends on the rate of coincident and singles γ rays. The rate of coincident γ rays averaged 116 counts/s and the γ singles averaged 457 counts/s. The correction factor was determined to be 1.0235.

Preemption of real coincidences - There is a small probability that coincidences are lost due to random coincidences preempting a real one. This occurs when the master trigger for our system is activated by a real β-γ coincidence opening a coincidence window, but a random β event closes it before the real one does. The correction factor was determined to be 1.0038.

Bremsstrahlung - Bremsstrahlung radiation is emitted when positrons from ^{26}Si stop in or near the β detector. This is another source of coincident summing. Bremsstrahlung produces a continuous energy spectrum instead of a clear peak in the γ-ray spectrum. To determine this contribution we need the areas of all γ-ray peaks multiplied by their total-to-peak ratio we then sum the results and subtract from the total spectrum area. The difference is then the contribution from bremsstrahlung. The contribution was determined to be 162 counts.

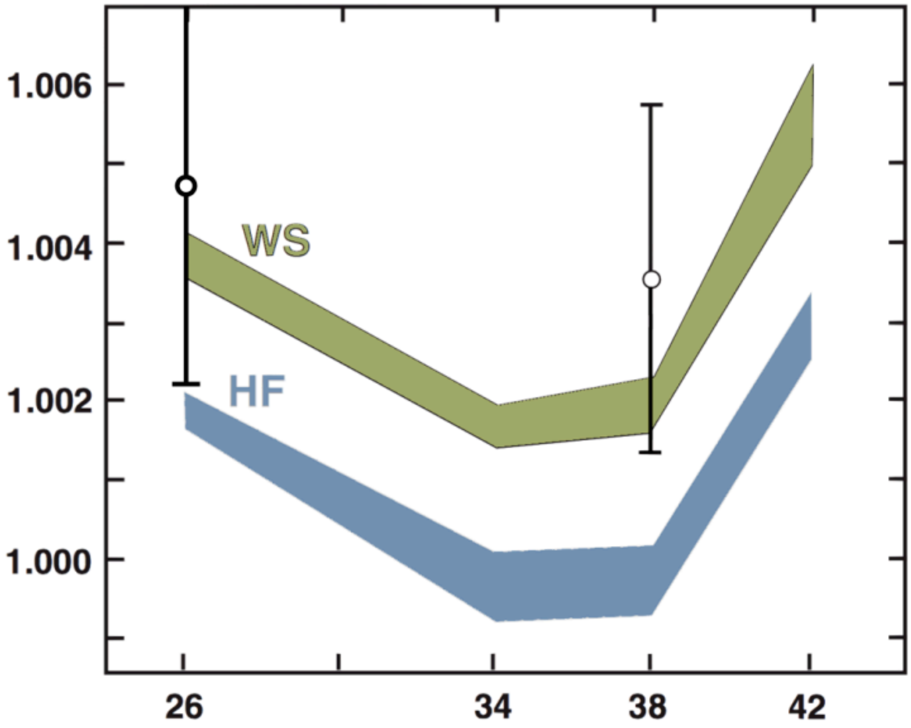

FIG. 2. Preliminary result for the ratio of *ft* values of the *A* = 26 pair as well as the previous result for *A* = 38.

With all these corrections completed, we can determine the branching ratio to the 1^+ state in ^{26}Si at 1058 keV, the most intense branch. Obtaining the relative intensities of the other γ-ray peaks with respect to the 829-keV peak, we determine the total of the Gamow-Teller branches to be 24.31%. If we then subtract from 100% we obtain the superallowed branching ratio to be 75.69%. (The final uncertainty is yet to be determined.) These numbers should be considered preliminary since one more correction – to account for the small probability that γ rays are recorded by the β detector – still needs to be done. However if this preliminary number is combined with the known half-life and Q_{EC} value for ^{26}Si decay, the ratio of *ft* values for the mirror *A*=26 pair supports the A=38 result (see Fig. 2) in favoring the calculation with Woods-Saxon radial wavefunctions.

[1] T. Eronen *et al.*, Phys. Rev. C **79**, 032802(R) (2009).
[2] V.E. Iacob, J.C. Hardy, A. Banu, L. Chen, V.V. Golovko, J. Goodwin, V. Horvat, N. Nica, H.I. Park, L. Trache, and R.E. Tribble. Phys. Rev. C **82**, 035502 (2010).
[3] H.I. Park *et al.*, Phys. Rev. Lett. **112**, 102502 (2014).
[4] J.C. Hardy and I.S. Towner, Phys. Rev. C **79**. 055502 (2009).

Half-life of the superallowed beta emitter, ^{30}S

J.C. Hardy, I.S. Towner, V.E. Iacob, H.I. Park, N. Nica, M. Bencomo, V. Horvat, and L. Chen

The superallowed $0^+ \rightarrow 0^+$ β-decay branch from ^{30}S is not one of the fourteen $0^+ \rightarrow 0^+$ transitions that have been measured to ±0.1% precision or better. The most recent survey of world data [1] gives ft = 3005(41) s and $\mathcal{F}t$ = 3016(41) s for the ^{30}S transition, a precision of ±1.35%, which is more than a factor of 10 too large for it to contribute to fundamental tests of the weak interaction or of isospin symmetry breaking [2]. The predominant contribution (±1.34%) to the large uncertainty is from the branching ratio, which is based on a single 1963 measurement. Though the half-life is known much more precisely, it is still not adequate since its world-average value [1] is quoted to ±0.14% and that is based on two measurements, only one of which has 0.14% precision. Alone among the three required experimental quantities, the Q_{EC} value can be considered to be measured with sufficient precision: Its contribution to the ft-value uncertainty is merely ±0.03%.

The ^{30}S case is an interesting one because its calculated nuclear-structure-dependent correction term is unusually large: *viz.* $\delta_C - \delta_{NS} = 1.040(32)\%$. We argue that such a case offers a good test of the correction terms themselves: If the measured ft value for such a transition yields a corrected $\mathcal{F}t$ value that is consistent with the other well-known cases, then this serves to verify the calculations' reliability for the existing cases, which have smaller corrections [2].

We have chosen to begin with a measurement of the half-life of ^{30}S. Quite apart from its ultimate benefit in contributing to a usefully precise ft value, the measurement also offers an excellent opportunity to compare results from the various techniques we now have available to measure half-lives. Unlike most T_Z = -1 superallowed β emitters, ^{30}S does not feed a second $0^+ \rightarrow 0^+$ β transition from its daughter. The 0^+, T=1 state populated in ^{30}P decays electromagnetically to the ground state, which proceeds by ordinary allowed β decay to ^{30}Si with a half-life of 2.498(4) min. Thus there is a very clean separation between the ^{30}S half-life of 1.18 s and that of its daughter, which is more than a factor of 100 longer. Because we detect the positrons from both decays simultaneously in the same detector, this separation between parent and daughter half-lives makes it possible in principle to achieve much higher precision on the parent half-life than is possible when both activities have very similar half-lives. This makes possible a very demanding comparison of the results based on different experimental techniques.

We produced a ^{30}S radioactive beam via the p(^{31}P,2n)^{30}S reaction, with a 30 A-MeV ^{31}P primary beam impinging on a H_2 cryogenic gas-target kept at a pressure of 2 atm and at liquid-nitrogen temperature. A high purity ^{30}S beam was then selected with the Momentum Achromat Recoil Separator (MARS), extracted into air, where it passed through a thin plastic scintillator, a series of Al degraders, and eventually implanted in the 76-μm-thick Mylar tape of our fast tape-transport system. The thickness of the Al degraders was experimentally tuned to optimize the implantation and purity of the ^{30}S beam.

Data were collected in cycles: After ^{30}S nuclei had been implanted for a pre-selected time interval (of the same order as the ^{30}S half-life), the beam was turned off and the tape-transport system moved the sample in ~175 ms to a well-shielded location 90 cm away, stopping it in the center of a 4π proportional gas counter. The decay positrons were then detected for twenty half-lives (24 s). These collect-move-detect cycles were computer controlled and their timing was continuously monitored on-line. They were repeated, with a separate decay spectrum recorded for each, until the desired overall statistics had been achieved. In its shielded location, the gas counter had a background rate of about 0.5 counts/s, which was 3-4 orders of magnitude lower than the initial count rate for each collected sample.

The total measurement took 6 days, with the first half dedicated to our digital system. In that case, the signal from the gas proportional counter was amplified by two cascaded fast amplifiers with total gain of 1000, before being sent to a high-speed digitizer (NI-5154) for digitizing and pulse capture. The second half of the measurement we replaced the digital system with our standard analogue electronics (see, for example, [3]) and, in parallel, our TDC-based system [4]. Thus we have two sets of independent data, one processed via digital pulse analysis, and the other via either multiscaler spectra or event-by-event time stamps. The analysis is nearly complete.

[1] J.C. Hardy and I.S. Towner, Phys. Rev. C **91**, 025501 (2015).
[2] J.C. Hardy *et al.*, *Progress in Research,* Cyclotron Institute, Texas A&M University (2016-2017), p. I-1.
[3] H.I. Park *et al.*, Phys. Rev. C **85**, 035501 (2012).
[4] V. Horvat and J.C. Hardy, *Progress in Research,* Cyclotron Institute, Texas A&M University (2010-2011), p. V-51.

Impact of weak gammas in the superallowed β decay of ^{34}Ar

V.E. Iacob and J.C. Hardy

We have reported previously on our precise measurements of the half-life and branching ratios for the decay of ^{34}Ar [1-3]. In order to achieve the desired accuracy (better than 0.1%) for the superallowed branching ratio, a thorough inspection is required of the γ-ray spectrum in coincidence with ^{34}Ar betas to identify weak peaks that could have been missed or are at the statistical limit of observation.

All γ-ray transitions in ^{34}Cl ($E^* < 5040$ keV) that could possibly be fed in the beta-decay of ^{34}Ar have been considered and upper intensity-limits were assessed. Each limit was derived from statistical considerations for a 2×FWHM-wide region centered on the potential candidate; this region covers 98% of the events included in a Gaussian shaped peak. Each value was further reinforced by a visual inspection of the original spectrum, on which a virtual peak (with the correct FWHM and upper-limit area) was superimposed.

While the majority of the potential γ rays lie in regions where the background is easy to handle, some required special attention. This is the case with our most important finding in this analysis: the 519-keV γ ray, which is located in the vicinity of the annihilation-radiation peak. (See Fig. 1.) The intensity of the latter makes the analysis quite demanding: Only a finely tuned fit of the dominant 511-keV peak can give us access to a realistic area for the 519-keV peak. To get a reliable description of the 511-keV peak, a quite elaborate fit function was used. It is described as: 1) a Gaussian; plus 2) a short-range

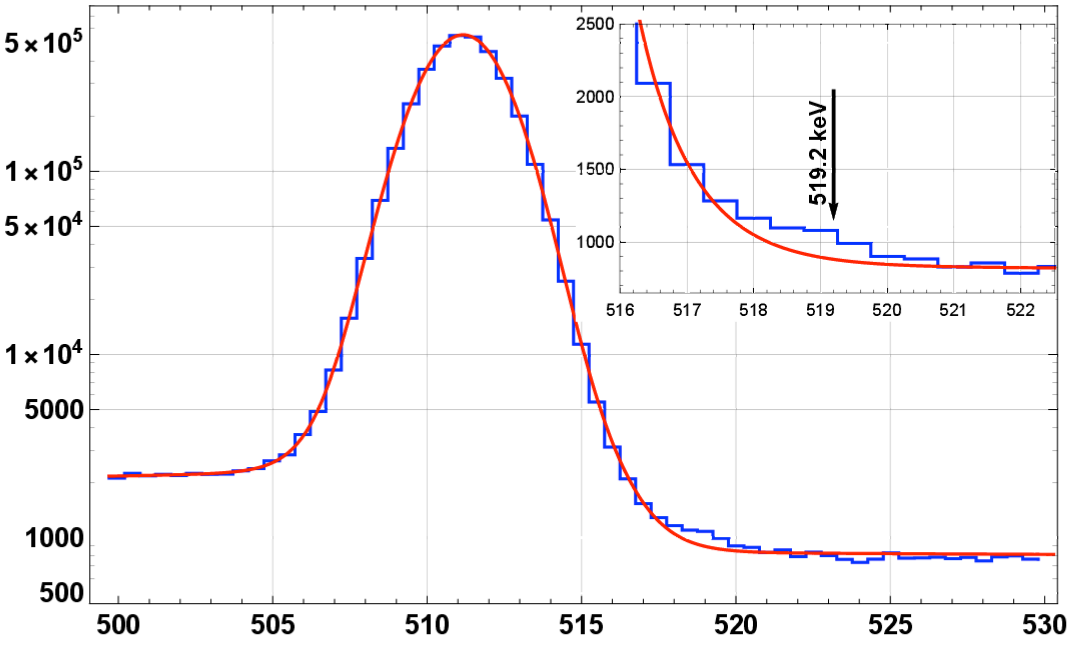

FIG. 1. Finely tuned fit of the annihilation peak observed in beta-gamma coincidences. The fit function contains 12 parameters. The inset zooms in on the right wing of the peak and clearly shows an excess of counts around 519.2 keV; the associated FWHM is consistent with the value expected for this energy.

skewed Gaussian on the left side; plus 3) a long-range skewed Gaussian on the left side; and 4) a short-range skewed Gaussian on the right side. The background under both peaks is described as: 1) a linear polynomial; plus 2) a step function.

With all these terms, the fit curve (the red-line in Fig. 1) passes through the centers of all channels describing the annihilation peak. The inset zooms in on the region centered at 519 keV and shows clearly a bump containing 700(200) events. The area of this peak is consistent with an intensity of 3% relative to the 666-keV γ-ray, the most intense one observed in the decay of ^{34}Ar. As seen in Fig. 2, the overall impact of the 519-keV gamma is small (the beta branch populating the 666-keV level is 2.6%); nevertheless, it needs to be accounted for in any precise analysis of the superallowed branching ratio or the half-life.

The main consequence of the presence of any of these weak branches is to increase of the total branching ratio for $0^+ \rightarrow 1^+$, Gamow-Teller branches; this in turn reduces the branching ratio deduced for the superallowed branch.

The effect that weak γ-ray branches potentially have on the ^{34}Ar half-life is less obvious. In the case of the 519-keV γ-ray, its presence induces a small change in the fitted ^{34}Ar half-life. Here is why: When we measure the half-life, we use our 4π proportional counter, which records the positrons from the 844-ms decay of ^{34}Ar and from the 1.53-s ground-state decay of its daughter, ^{34}Cl. Because their half-lives are related by nearly a factor of 2, the combined decay cannot be fitted as two independent decays. The only way to obtain a precise result is to incorporate the parent-to-daughter link as a constraint in the fitting procedure. If all the decay branches from ^{34}Ar ultimately populate the ^{34}Cl ground state, this linkage is one-to-one. However, the excited state at 666 keV, which is populated in the beta-decay of

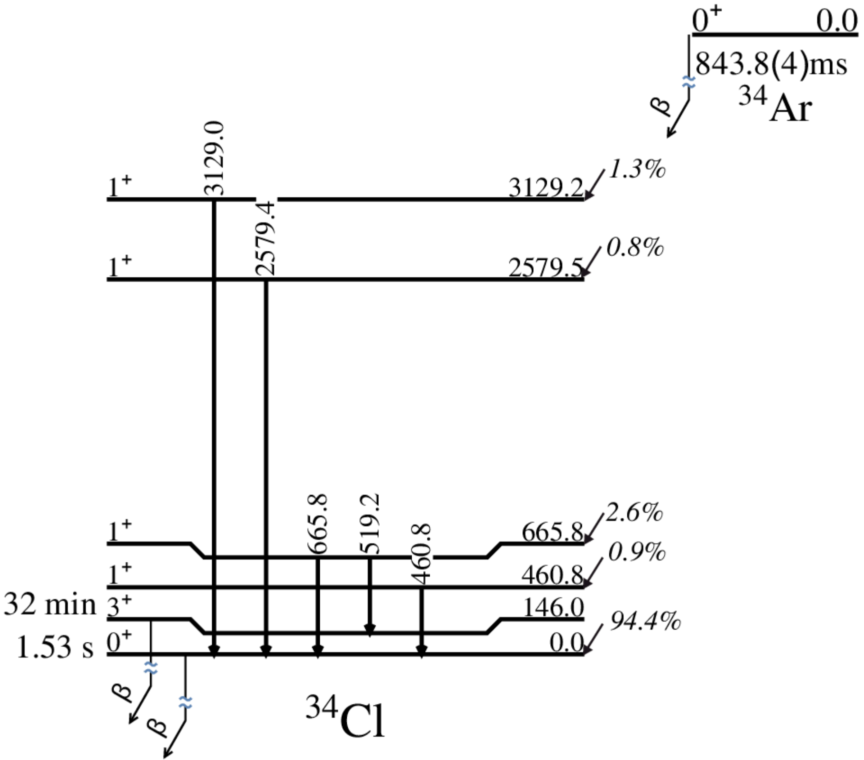

FIG. 2. Simplified decay scheme of ^{34}Ar as observed in beta-gamma coincidences**.**

^{34}Ar, can decay via a 669- or a 519-keV γ-ray. (See Fig. 2.) The latter populates the isomeric level at 146 keV, which has a half-life of 32min. Thus, this decay path for the 666-keV state does not lead to the subsequent emission of a beta from the decay of ^{34}Cl within our measurement time window. Thus, the parent-daughter linkage must be adjusted to account for the loss of betas from the daughter decay.

We plan a more definitive measurement of the γ-decay branching from the 666-keV level in ^{34}Cl by means of a collaborative (p, γ) experiment at Notre Dame University.

[1] V.E. Iacob, *et al.*, *Progress in Research*, Cyclotron Institute, Texas A&M University (2014-2015), p. I-46.

[2] V.E. Iacob, *et al.*, *Progress in Research*, Cyclotron Institute, Texas A&M University (2014-2015), p. I-48.

[3] V.E. Iacob, *et al.*, *Progress in Research*, Cyclotron Institute, Texas A&M University (2015-2016), p. I-14.

Precise half-life measurement of ^{42}Ti

H.I. Park, J.C. Hardy, V.E. Iacob, V. Horvat, M. Bencomo, L. Chen, N. Nica, B.T. Roeder,
and A. Saastamoinen

We have made a second attempt to measure the half-life of ^{42}Ti to high precision. The critical change from our first measurement [1] was that we removed the time delay between the beginning of each count period, as defined by the fast tape-transport system, and the actual start time when data are recorded with our standard analog electronics. This was a feature we had introduced for our branching ratio measurements and had inadvertently left connected for the first half-life measurement of ^{42}Ti.

Once again we produced ^{42}Ti using the ^{4}He (^{40}Ca, 2n) ^{42}Ti reaction in inverse kinematics, with a primary ^{40}Ca beam energy of 32 MeV/nucleon. With extraction slits on the MARS recoil spectrometer set tight, by depositing the ^{42}Ti samples near the back of the collection tape we could ensure that most of the produced impurities passed through the tape without stopping, leaving behind a rather pure ^{42}Ti sample. In addition to acquiring data from the proportional gas counter with our standard analogue electronics, we also ran a TDC-based system in parallel so that we could record the absolute time information event-by-event for the same data. The use of this second data-taking method offers a means to test for possible systematic effects in the measurement, as well as an opportunity to improve our data-acquisition techniques for all half-life measurements.

Unfortunately, our second measurement suffered from a failure of the fast tape-transport system to place the collected source consistently into the center of the detector. This newly encountered instability significantly decreased the overall statistics we could obtain during the seven days of beam time. Another issue arose from the operation of the gas counter. In all such measurements we intend to operate the detector in a flat "plateau" region. In this case, as usual, we determined the plateau region in advance by using a ^{90}Sr/^{90}Y beta source and measuring the count rate as a function of applied detector voltage at the three different thresholds (50, 100, and 150 mV) used in our half-life measurement. Since count rate is nearly independent of detector bias in the plateau region, this operating condition ensures that our detection efficiency, which is close to 100%, is essentially independent of count rate. We repeated the ^{90}Sr/^{90}Y source measurement at the end of the experiment to confirm that our operating range for the detector bias voltage had remained unchanged. To our surprise, the plateau region was somewhat narrower than that obtained before the experiment began, indicating that the settings used during the measurement might not all have been safely within the plateau region. Thus we are concerned that our ^{42}Ti half-life measurement might have been compromised by a rate-dependent detection efficiency. Our analysis is currently progressing but with great attention being paid to possible rate-dependent effects.

In the meantime, the tape-transport system has been repaired and the gas-counter repeatability has been (re)established. An additional measurement with all systems in prime operating condition is planned for late summer.

[1] H.I. Park *et al.*, *Progress in Research*, Cyclotron Institute, Texas A&M University (2015-2016), p. I-17.

Superallowed beta decay Q-value of ^{42}Sc

T. Eronen,[1,2] J.C. Hardy,[2] L. Canete,[1] A. Jokinen,[1] J. Hakala,[1] A. Kankainen,[1] V.S. Kolhinen,[1] J. Koponen,[1] I.D. Moore,[1] I.M. Murray,[1] H. Penttila,[1] I. Pohjalainen,[1] O. Poleshchuk,[1]
J. Reinikainen,[1] S. Rinta-Antila,[1] N. Soukout,[1] A. Voss,[1] and J. Aysto[1]
[1]*Department of Physics, University of Jyvaskyla, Finland*
[2]*Cyclotron Institute, Texas A&M University, Texas, USA*

The $0^+ \rightarrow 0^+$ β decay of ^{42}Sc belongs to the traditional set of well known superallowed beta emitters. Its corrected $\mathcal{F}t$ value is known to better than 0.1 % and has a significant impact on the world average $\mathcal{F}t$ value [1]. Out of the three experimental quantities (half-life, branching ratio and Q_{EC} value) required to determine the $\mathcal{F}t$ value, the uncertainty contribution of the Q_{EC} value is second largest and is due to discrepant measurements. A "scale factor" of 3.0 is needed to account for the discrepancy [2]: Although all four contributing measurements have uncertainties of approximately 200 eV, their average has an uncertainty of 300 eV! The new measurement reported here has an uncertainty of 53 eV, a substantial improvement over all previous measurements, including our own previous measurement from 2006 [3].

We carried out the Q_{EC}-value measurement in the accelerator laboratory of the University of Jyvaskyla, Finland, using the JYFLTRAP Penning trap setup [4], which consists of a radio frequency cooler-buncher and two Penning traps. The first trap is used to prepare clean samples of ^{42}Sc or its co-produced beta-decay daughter ^{42}Ca. The actual mass measurement depended on a determination of the free-space cyclotron frequency for both parent and daughter ions. The Q_{EC} value was then obtained from the frequency ratio of the two. Since the parent-daughter ions have the same A/q, systematic frequency shifts are nearly identical for both ion species and thus do not significantly contribute to the Q_{EC}-value uncertainty [5]. The main difference to our previous measurement in 2006 is that this time we used the Ramsey ion-excitation technique, which gives a significant boost to the precision. In addition, thanks to system improvements, we could use longer ion-excitation times, which also helped to boost the precision.

Finally, the Q_{EC} value was obtained with a ±53 eV uncertainty, which is about four times more precise than our previous result and the three results obtained by others. Before this measurement, the uncertainty contribution to the $\mathcal{F}t$ value from the Q_{EC} value and the half-life were about equal; now the Q_{EC}-value contribution is about a factor of four lower. If the half-life could be measured more precisely, say with a factor of four improvement as well, then ^{42}Sc would have one of the most precise experimental *ft*-value of all measured cases. The paper describing these results [6] was chosen by the editors of Physical Review C as an "editor's suggestion."

[1] J.C. Hardy *et al., Progress in Research,* Cyclotron Institute, Texas A&M University (2016-2017), p. I-1.
[1] J.C. Hardy and I.S. Towner, Phys. Rev. C **91**, 025501 (2015).
[2] T. Eronen *et al.*, Phys. Rev. Lett. **97**, 232501 (2006).
[3] T. Eronen *et al.*, Eur. Phys. J. A **48**, 46 (2012).

[4] R. Roux *et al.*, Eur. Phys. J. D **67**, 146 (2013).
[5] T. Eronen, J.C. Hardy *et al*., Phys. Rev. C **95**, 025501 (2017).

Tests of internal-conversion theory

J.C. Hardy, N. Nica, V.E. Iacob, and M.B. Trzhaskovskaya[1]
[1]*Petersburg Nuclear Physics Institute, Gatchina RU-188300, Russia*

Except for the very lightest nuclei, where internal conversion is weakest, most nuclear decay schemes depend upon calculated internal conversion coefficients (ICCs). Electromagnetic decay intensities are usually determined from gamma-ray measurements combined with calculated ICCs. Consequently, the reliability of the calculations is a matter of some importance, especially where precise decay-scheme data are required, for example in detector calibration. Until quite recently, although various tables of calculated ICCs were readily available, most ICC measurements were relatively imprecise, being aimed only at determining transition multi-polarities. Rarely were they precise enough to distinguish among different calculations or indeed to establish if any of the calculations reproduced reality. We are rectifying this deficiency.

When we began our program of precise measurements in 2004, the then-current survey of world data [1] included barely twenty ICC values measured to ±2% or better, and eighty more with up to 5% precision. They were divided 45-55 between *K*-shell ICCs (α_K) and total ICCs (α_T), respectively. Based on these data, the authors concluded that all previous tables of ICCs exhibited a 3% systematic bias, but that a table by Band *et al.* [2], which was new at the time, agreed well with the data (within ~1%). This new table was calculated in the framework of the Dirac-Fock method, with the exchange between bound electrons as well as between bound and free electrons treated exactly, an important improvement. Unfortunately, however, the best agreement with the available experimental data was achieved with a version of this calculation in which the final-state electron wave-function was computed in a field that did not include any provision for the atomic vacancy created by the conversion process. Yet the vacancy must be there, since atomic-shell-vacancy lifetimes are known generally to be much longer than the time for a conversion electron to leave the vicinity of the atom. This is an unsatisfactory paradox!

We found ourselves uniquely positioned to potentially resolve the paradox. For our program to measure branching ratios for superallowed β emitters, we had efficiency calibrated an HPGe detector to high precision over a wide range of energies. This would allow us to measure the *K* x rays and γ rays from a converted transition in the same well-calibrated detector, thus affording access to the transition's α_K value with a minimum of systematic uncertainty. For an isolated electromagnetic transition that converts in the atomic *K* shell, the observation of a *K* x ray is a signal that an electron conversion has taken place; whereas a γ ray indicates that no conversion has taken place. If both x rays and γ rays are recorded in a measurement, then the value of α_K is given by

$$\alpha_K \omega_K = \frac{N_K}{N_\gamma} \cdot \frac{\varepsilon_\gamma}{\varepsilon_K}, \tag{1}$$

where ω_K is the *K*-shell fluorescence yield; N_K and N_γ are the respective peak areas of the *K* x rays and the γ ray; and ε_K and ε_γ are the respective detector photopeak efficiencies.

Not many nuclei feature a single isolated transition, but a number of cases have small enough interference from other converted transitions that the corrections to Eq. (1) are manageable, allowing the α_K value still to be extracted with percent precision. Since we began this program, we have published α_K values for *E*3 transitions in two nuclei, ^{111}Cd [3] and ^{134}Cs [4,5], and *M*4 transitions in five nuclei, ^{119}Sn [6,7], ^{127}Te [8], ^{137}Ba [4,5], ^{193}Ir [9,10], and ^{197}Pt [11]. Described elsewhere in this report are final results on an *M*4 transition in ^{125}Te [12]; preliminary results on an *E*3 transition in ^{103}Rh [13] and well developed plans for measuring another *M*4 transition, in ^{93}Nb [14].

The results from our completed measurements appear in Fig. 1, where they are compared with two theoretical models, one that ignores the atomic vacancy and one that includes it. It is immediately evident that the data are completely inconsistent with the no-vacancy theory and in remarkable agreement with the vacancy-inclusive theory. This is consistent with the known vacancy lifetimes, and resolves the earlier paradox.

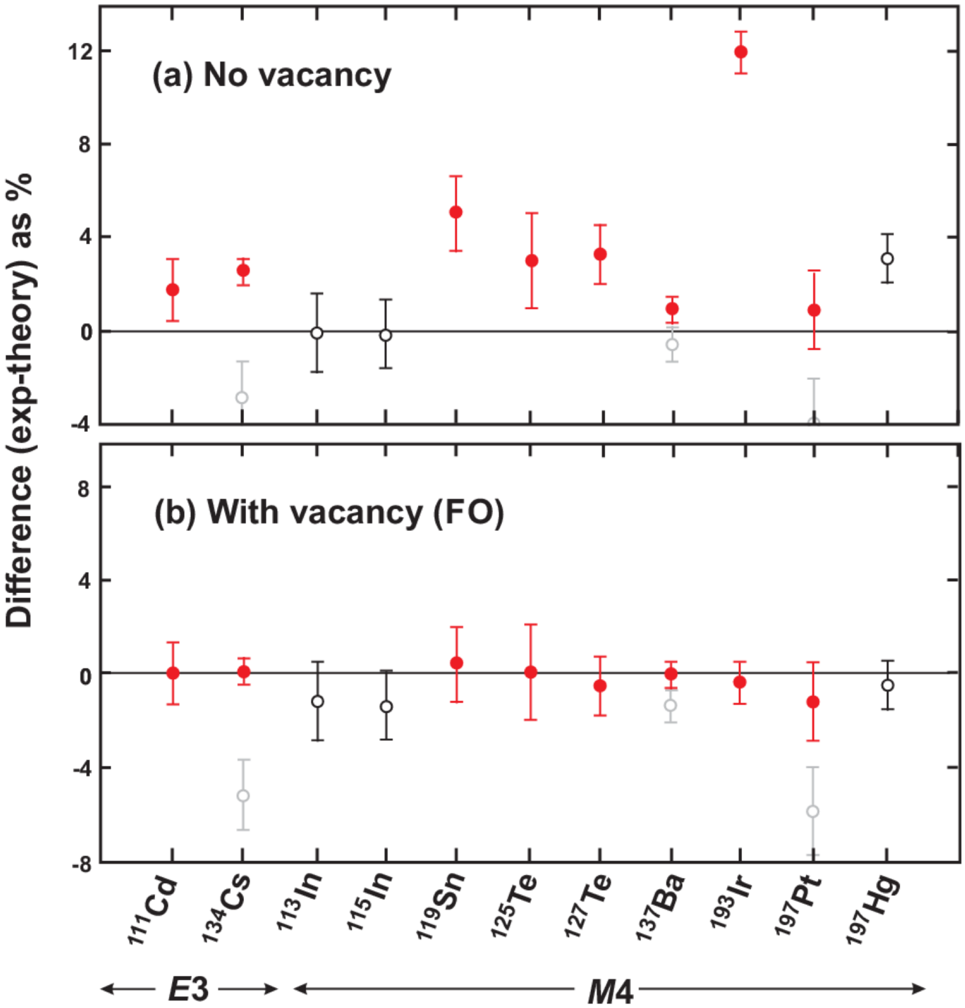

FIG. 1. Percentage differences between the measured and calculated α_K values for the Dirac-Fock calculations with and without provision for the atomic vacancy. Solid (red) circles are our measurements; open circles refer to pre-2002 results, the ones in gray having been replaced. The figure shows all α_K values for high-multiplicity transitions (E3 and above) that are known to ±2% or better.

A few of the cases we measured were chosen not because they were particularly sensitive to the vacancy/no-vacancy choice in the calculations, but because previous results disagreed with *both* types of calculation. These discrepancies have been removed as well. Note though that among the eleven precisely measured α_K values in Fig. 1, there are eight that statistically distinguish between the vacancy and no-vacancy calculations, and they all present a consistent picture that favors inclusion of the atomic vacancy in ICC calculations. All but one of these cases come from our work.

[1] S. Raman, C.W. Nestor Jr., A. Ichihara, and M.B. Trzhaskovskaya, Phys. Rev. C **66**, 044312 (2002).

[2] I.M. Band, M.B. Trzhaskovskaya, C.W. Nestor Jr., P. Tikkanen, and S. Raman, At. Data Nucl. Data Tables **81**, 1 (2002).

[3] N. Nica, J.C. Hardy, V.E. Iacob, T.A. Werke, C.M. Folden III, L. Pineda, and M.B. Trzhaskovskaya, Phys. Rev. C **93**, 034305 (2016).

[4] N. Nica, J.C. Hardy, V.E. Iacob, W.E. Rockwell, and M.B. Trzhaskovskaya, Phys. Rev. C **75**, 024308 (2007).

[5] N. Nica, J.C. Hardy, V.E. Iacob, C. Balonek, and M.B. Trzhaskovskaya, Phys. Rev. C **77**, 034306 (2008).

[6] N. Nica, J.C. Hardy, V.E. Iacob, M. Bencomo, V. Horvat, H.I. Park, M. Maguire, S. Miller, and M.B. Trzhaskovskaya, Phys. Rev. C **89**, 014303 (2014).

[7] J.C. Hardy, N. Nica, V.E. Iacob, S. Miller, M. Maguire, and M.B. Trzhaskovskaya, Appl. Rad and Isot. **87**, 87 (2014).

[8] N. Nica, J.C. Hardy, V.E. Iacob, H.I. Park, K. Brandenburg, and M.B. Trzhaskovskaya, Phys. Rev. C **95**, 034325 (2017); and *Progress in Research*, Cyclotron Institute Texas A&M University (2016-2017) p. I-28.

[9] N. Nica, J.C. Hardy, V.E. Iacob, S. Raman, C.W. Nestor Jr., and M.B. Trzhaskovskaya, Phys. Rev. C **70**, 054305 (2004).

[10] N. Nica, J.C. Hardy, V.E. Iacob, J.R. Montague, and M.B. Trzhaskovskaya, Phys. Rev. C **71**, 054320 (2005).

[11] N. Nica, J.C. Hardy, V.E. Iacob, J. Goodwin, C. Balonek, M. Hernberg, J. Nolan, and M.B. Trzhaskovskaya, Phys. Rev. C **80**, 064314 (2009).

[12] N. Nica, J.C. Hardy, V.E. Iacob, T.A. Werke, C.M. Folden III, K. Ofodile, and M.B. Trzhaskovskaya, *Progress in Research*, Cyclotron Institute Texas A&M University (2016-2017) p. I-25; Phys. Rev. C. (Submitted).

[13] N. Nica *et al., Progress in Research*, Cyclotron Institute Texas A&M University (2016-2017) p. I-23.

[14] N. *Nica et al., Progress in Research*, Cyclotron Institute Texas A&M University (2016-2017) p. I-21.

Test of internal-conversion theory with precise γ- and x-ray spectroscopy of ^{93m}Nb: source preparation

N. Nica, J.C. Hardy, E.E Tereshatov, and C.M. Folden III

One of the cases of interest in our series of precision ICC measurements is the 30.8-keV, *M*4 transition in ^{93m}Nb ($T_{1/2}$=16.12 y), through which we can extend the range of our measurements down to Z = 41. There have been previous measurements of this transition, with the most precise result – published more than 40 years ago – giving α_K = 25,800(1,500) [1]. This result can be compared with the theoretical values[1] α_K (FO) = 26,000 and α_K(NH) = 23,900, where "FO" designates a calculation that takes into account the atomic vacancy by the so called "frozen orbital" approximation, and "NH" is the result of a "no hole" calculation, with the atomic vacancy ignored. Since the 6% precision of the experimental result is insufficient to distinguish clearly between the two theoretical results, we intend to re-measure this transition. See Ref. [2] for details of our measurement techniques.

We have purchased 40 μCi of ^{93m}Nb in the form of niobium nitrate in solution (1M HNO_3 + 0.3M HF) from Eckert & Ziegler. The supplier stated that the solution also contains about ten times as much active ^{94}Nb, which fortunately has a much longer half-life ($T_{1/2}$=20,300 y) and consequently much lower specific activity. Our preliminary measurements have identified both the 702.6-keV and 871.1-keV transitions in ^{94}Nb decay (as well as their coincidence summing peak), together with the *K* x rays of Nb; a small peak was also visible at 31 keV, which is likely our transition of interest, although conclusive identification awaits a full impurity analysis.

To prepare the ^{93m}Nb source, the so-called molecular plating technique will be used. In principle the idea is to dissolve the analyte in an organic solution and apply a bias voltage to this solution to collect the material on the surface of one of electrodes. The procedure development includes several stages, such as experiments with stable niobium (standard ICP-MS solution), creation of LabVIEW-controlled software to monitor the electrodeposition process, and voltage/current variation to optimize the conditions and the source quality. Isopropanol was chosen as a well-known medium for electrodeposition, because it has a higher electrical window than that of any aqueous solutions.

In the tests performed with stable niobium, we used the high-voltage power-supply unit SRS PS300, which provides up to 1250 V and 20 mA, to create the electrical field. The unit was designed to provide only a constant voltage, while the current depends on the chemical condition and the metal concentration. In order to have some flexibility within the deposition and to record the voltage/current values, the power supply was connected to a PC controlled via LabVIEW software. The program we created allows us to set the desired current, while the voltage will be automatically adjusted to compensate for the material loss during the process. A series of experiments was performed to check if the molecular plating technique is applicable for Nb electrodeposition if the ^{93m}Nb solution contains trace amounts of hydrofluoric acid (HF). The presence of HF could lead to niobium forming a very stable oxyfluorocomplex $NbOF_3$. Nevertheless, EDS and XPS analyses of the deposited layer (performed at Material Characterization Facility, TAMU) indicated that niobium was electrodeposited on the aluminum

---

[1] Calculated with the interpolator code BrIcc (http://bricc.anu.edu.au)

electrode mostly in the form of niobium oxide Nb_2O_3. Optimization of niobium electrodeposition parameters will be finalized within the next round of experiments.

The work is in progress and will proceed with deposition and measurement of the radioactive ^{93m}Nb source.

[1] M. Jurcevic, A. Ljubicic, and D.Rendic, Fizika **8**, 81 (1976).

[2] J.C. Hardy *et al.*, *Progress in Research,* Cyclotron Institute, Texas A&M University (2016-2017) p. I-18

Tests of internal-conversion theory with precise γ- and x-ray spectroscopy: the case of ^{103m}Rh studied by the ^{103}Pd electron-capture decay

N. Nica, J.C. Hardy, V. Horvat, V.E. Iacob, H.I. Park, V. Sabla, and M.B. Trzhaskovskaya[1]
[1]*Petersburg Nuclear Physics Institute, Gatchina RU-188300, Russia*

As part of our program to test internal-conversion theory through precision measurements of *K*-conversion coefficients, α_K [1], we undertook a measurement of the *E*3 decay of the ^{103m}Rh isomer, which we populated via the electron-capture decay of ^{103}Pd. Because the electron-capture decay gives rise to x rays that are indistinguishable from the x rays associated with the *E*3 decay, to extract α_K we must use a modified version of Eq. (1) in Ref. [1]:

$$\alpha_K = \frac{1}{\omega_K} \cdot \frac{N_K}{N_\gamma} \cdot \frac{\varepsilon_\gamma}{\varepsilon_K} - P_{\varepsilon,K} \cdot (1 + \alpha_T) \quad (1)$$

,

where ω_K is the K-shell fluorescence yield, which we take from Ref. [2]; N_K and N_γ are the peak areas of the *K* x rays and γ ray, respectively; and ε_K and ε_γ are the corresponding detector efficiencies. In this particular case α_K depends on the total ICC, α_T, and on the probability for the K-shell electronic capture, $P_{\varepsilon,K}$, a quantity that can be precisely calculated.

The ^{103}Pd source was prepared by thermal neutron activation at the Triga reactor of the Texas A&M Nuclear Science Center. A foil of 99.95% chemically pure palladium from *Goodfellow,* 4 microns thick and 25 × 25 mm^2, was activated for 10 hours in a neutron flux of 7.5×10^{12} n/(cm^{2}s). The sample was then allowed to decay for about three weeks, after which we measured it intermittently for about 3.5 months, using both our well-calibrated HPGe detector, and a Si detector. A thorough impurity analysis was completed, which revealed the presence of the Rh K_α- K_β coincidence-summing peak at about 42.8 keV. The consequence of this observation is that the 39.7-keV γ-ray peak of interest must be contaminated by the Rh K_α- K_α coincidence-summing peak at about 40.2 keV, unresolved by our spectroscopic chain. Using the visible K_α K_β summing peak as a template we could correct for the invisible presence of the K_α- K_α summing peak.

There is a further complication however. Since Eq. (1) contains two unknowns, α_K and α_T, a second study of the same transition, but populated by the β^- decay of ^{103}Ru, is needed to determine both quantities independently. The ^{103}Ru-decay measurement is currently underway. In the meantime, we take α_K from calculations, and solve eq. (1) to get the total ICC, α_T. For the value of α_K we used 131.3(39), which is an average value of 135.2 if the atomic vacancy is included in the "frozen orbital" approximation and 127.4 if the vacancy is ignored, with an uncertainty covering both values. These theoretical values were obtained with the interpolator code BrIcc [1]. Our preliminary result for α_T thus becomes 1435(44).

When compared with calculations, this result shows better agreement with the "frozen orbital" calculation, which gives 1404, than it does with the calculation that ignores the atomic vacancy, which

---

[1] (http://bricc.anu.edu.au) of 135.2 (including vacancy, "frozen orbital" approach) and 127.4 (excluding vacancy).

gives 1389. However this result is only derived to demonstrate consistency. A really useful result awaits completion of our measurement on the β^- decay of ^{103}Ru, when the two modes of producing ^{103m}Rh can be used in conjunction to solve for both α_T and α_K.

[1] J.C. Hardy *et al*., *Progress in Research,* Cyclotron Institute, Texas A&M University (2016-2017) p. I-18.
[2] E. Schönfeld and H. Janssen, Nucl. Instrum. Methods Phys. Res. **A369,** 527 (1996).

Precise measurement of α_K and α_T for the 109.3-keV *M*4 transition in ^{125}Te: test of internal-conversion theory

N. Nica, J.C. Hardy, V.E. Iacob, T.A. Werke, C.M. Folden III, K. Ofodile, and M.B. Trzhaskovskaya[1]
[1]*Petersburg Nuclear Physics Institute, Gatchina RU-188300, Russia*

Last year, we reported [1] on a measurement of the internal conversion coefficients (ICC), α_K and α_T, for the 109.3-keV *M*4 transition in ^{125}Te. At that time, analysis was incomplete and only preliminary results were presented. In the meantime, the analysis has been completed and the results submitted for publication [2].

In simple cases with a single transition that can convert in the K shell, the value of α_K is given by

$$\alpha_K = (N_K/N_\gamma)(\varepsilon_\gamma/\varepsilon_K)(1/\omega_K)\ , \qquad (1)$$

where ω_K is the fluorescence yield, N_K and N_γ are the total number of observed K x rays and γ rays, respectively; and ε_γ and ε_K are the corresponding photopeak detection efficiencies.

The decay of the 57.4-day isomer in ^{125}Te decay is not that simple, as illustrated by its decay scheme in Fig. 1. The presence of a second transition, having 35.5 keV, in cascade with the *M*4 transition adds a

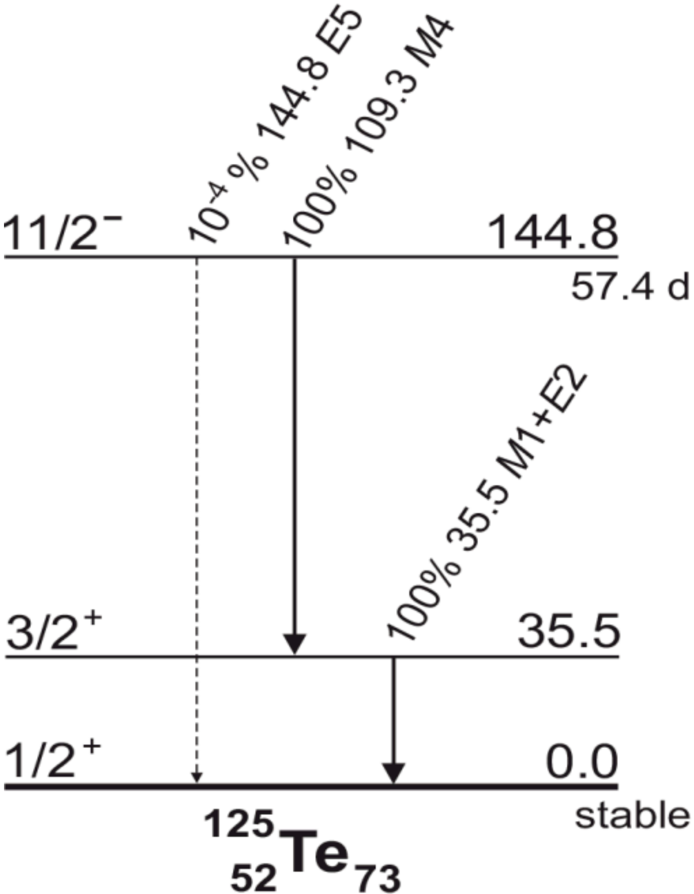

FIG. 1. Decay scheme for the 57.4-day isomer in ^{125}Te.

complication to our measurement. In this case, we must extract the α_K value for the 109.3-keV transition, with the help of a modified version of Eq. (1): *viz.*

$$\alpha_{K109} = (1/N_{\gamma109})(\varepsilon_{\gamma109}/\varepsilon_K)(1/\omega_K)\ \{N_K - \alpha_{K36}\, N_{\gamma36}\,(\varepsilon_K/\varepsilon_{\gamma36})\,\omega_K\}, \qquad (2)$$

where the subscripts 109 and 36 on a quantity denote the transition – either the 109.3-keV or 35.5-keV one – to which the quantity applies. Unfortunately, the 35.5-keV $M1+E2$ transition has a large value of α_{K36} = 11.64(4), so the K x rays from its conversion constitute about 60% of the total strength of the tellurium K x-ray peaks in the spectrum. This dilutes the precision with which we can determine the α_K value for the $M4$ transition. Nevertheless, it does offer an advantage: the opportunity to measure α_T as well as α_K for the 109.3-keV transition.

Although two transitions contribute to the K x ray peaks, there is no side feeding of the intermediate state so we can make use of the fact that the total transition intensities must be equal. Thus, we can determine α_{T109} via the equation

$$(1 + \alpha_{T109})\ (N_{\gamma109}/\varepsilon_{\gamma109}) = (1 + \alpha_{T36})\ (N_{\gamma36}/\varepsilon_{\gamma36})\ . \qquad (3)$$

To prepare our source, we first obtained tellurium metal powder enriched to 99.93(2)% in ^{124}Te from Isoflex USA. With it, we produced a thin neutron-activation target of ^{124}TeO on a pure aluminum backing by the molecular plating technique. The average thickness of ^{124}TeO was determined to be 308(9) μg/cm^2 as measured by mass. Then, this target was activated for a total of 24 hours in a neutron flux of ~7.5×10^{12}n/(cm^{2}s) at the TRIGA reactor in the Texas A&M Nuclear Science Center. Upon removal from the reactor, the active sample was stored for 3 weeks, after which time we acquired sequential gamma-ray spectra for 112 hours with our HPGe detector.

In analyzing our data, we took the N values from our spectra and the γ-ray efficiencies from our well-established HPGe detector calibration [3]. The K x-ray efficiency, ε_K, we took from a calibration we made more recently with a ^{109}Cd source [4]. All efficiencies took careful account of "self-attenuation" in the source material itself, an important effect both for the K x rays and for the 35.5-keV gamma rays. Our two ICC results appear in the top line of Table I, where each can be compared with three theoretical values, one that was calculated without accounting for the atomic vacancy and two that included the vacancy in different approximations, the "frozen orbital" (FO) or the "self-consistent field" (SCF).

Table I. Comparison of the measured α_K and α_T values for the 109.276(15)-keV $M4$ transition from ^{125m}Te with calculated values based on three different theoretical models. Shown also are the percentage deviations Δ from the experimental value, calculated as (experiment-theory)/theory.

Model	**α_K**	**Δ(%)**	**α_T**	**Δ(%)**
Experiment	185.0(40)		350.0(38)	
Theory				
No vacancy	179.5(1)	+3.0(22)	348.7(3)	+0.4(11)
Vacancy FO	185.2(1)	-0.1(22)	355.6(3)	-1.6(11)
Vacancy SCF	184.2(1)	+0.4(22)	354.2(3)	-1.2(11)

Clearly the result for α_K agrees well with the calculations that incorporate the vacancy. This is consistent with all our previous measurements of α_K.

The situation is more ambiguous for α_T: In that case our measured result agrees best with the no-vacancy calculation but it is consistent as well with the SCF version of the calculation, which includes the vacancy. Note also that the measured value of α_{T109} depends on a calculated value for α_{T36}, which in turn depends on the measured $E2/M1$ mixing ratio [5] for the 35.5-keV transition. If that mixing ratio were wrong, it could have an impact on our α_{T109} result.

[1] N. Nica *et al.*, *Progress in Research,* Cyclotron Institute, Texas A&M University (2015-2016), p I-22.

[2] N. Nica, J.C. Hardy, V.E. Iacob, T.A. Werke, C.M. Folden III, K. Ofodile, and M.B. Trzhaskovskaya, Phys. Rev. C (Submitted).

[3] J.C. Hardy *et al.*, Appl. Radiat. Isot. **56**, 65 (2002) ; R.G. Helmer *et al.*, Nucl. Instrum. Methods Phys. Res. **A511**, 360 (2003); R.G. Helmer *et al.*, Appl. Radiat. Isot. **60**, 173 (2004).

[4] N. Nica, J.C. Hardy, V.E. Iacob, M. Bencomo, V. Horvat, H.I. Park, M. Maguire, S. Miller, and M.B. Trzhaskovskaya, Phys. Rev. C **89**, 014303 (2014).

[5] J. Katakura, Nucl. Data Sheets **112**, 495 (2011).

Precise measurement of α_K for the 88.2-keV *M*4 transition in ^{127}Te: test of internal-conversion theory

N. Nica, J.C. Hardy, V.E. Iacob, H.I. Park, K. Brandenburg, and M.B. Trzhaskovskaya[1]
[1] *Petersburg Nuclear Physics Institute, Gatchina RU-188300, Russia*

Several years ago, we reported [1] on a measurement of the internal conversion coefficient (ICC), α_K, for the 88.2-keV *M*4 transition in ^{127}Te. At that time, analysis was incomplete and only preliminary results were presented. In the meantime, the analysis has been completed and the results have been recently published [2]. Since the experimental details were described in our earlier progress report [1], we focus here on the analysis.

In simple cases with a single transition that can convert in the K shell, the value of α_K is given by

$$\alpha_K = (N_K/N_\gamma)(\varepsilon_\gamma/\varepsilon_K)(1/\omega_K), \tag{1}$$

where ω_K is the fluorescence yield, N_K and N_γ are the total number of observed K x rays and γ rays, respectively; and ε_γ and ε_K are the corresponding photopeak detection efficiencies. The decay scheme of the 106-day isomer in ^{127}Te is shown in Fig. 1. With a single electromagnetic decay path, directly feeding

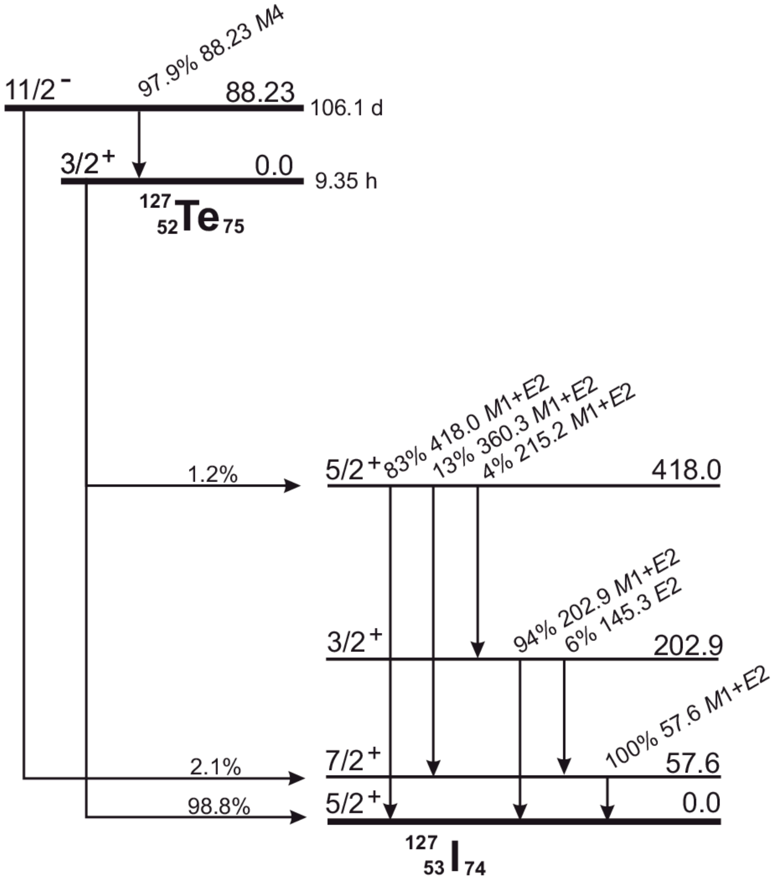

FIG. 1. Decay scheme for the 106-day isomer in ^{127}Te, illustrating the channels important to this measurement.

the ground state, it clearly satisfies the condition required for the validity of Eq. (1).

The only complication is that the isomer also has a 2.1% β-branch to an excited state in ^{127}I, which decays by a 57.6-keV transition with an α_K value of 3.16. This leads unavoidably to the presence of iodine *K* x rays. Though their intensity is only a few percent that of the predominant tellurium x rays, the two groups are unresolved from one another in our detector, so the iodine component must be carefully accounted for. The ^{127}Te ground state β decays as well, but only weakly populates an excited state, the decay of which produces considerably less conversion.

In analyzing our data, we took the *N* values from our spectra and the γ-ray efficiencies from our well-established HPGe detector calibration [3]. The *K* x-ray efficiency, ε_K, we took from a calibration we made more recently with a ^{109}Cd source [4]. The iodine *K* x rays, whose contribution must be subtracted from the measured (unresolved) x-ray peaks, predominantly arise from conversion of the 57.6-keV transition in ^{127}I, which is populated via the β decays of the isomeric and ground states of ^{127}Te. This transition has $M1+E2$ character with a measured mixing ratio and an α_{K58} value of 3.16(5). By inverting Eq. (1) we derived the iodine x-ray intensity from this α_{K58} value and the measured number of counts in the 57.6-keV γ-ray peak.

Our result for α_{K88}, the *K*-conversion coefficient of the 88.2-keV transition, appears in the top line of Table I, where it can be compared with three theoretical values, one that was calculated without accounting for the atomic vacancy and two that included the vacancy in different approximations, the "frozen orbital" (FO) or the "self-consistent field" (SCF). Clearly the result for α_K agrees well with the calculations that incorporate the vacancy. This is consistent with all our previous measurements of α_K.

Table I. Comparison of the measured α_K value for the 88.23(7)-keV *M*4 transition from ^{127m}Te with calculated values based on three different theoretical models. Shown also are the percentage deviations Δ from the experimental value, calculated as (expt-theory)/theory.

Model	α_K	Δ(%)
Experiment	484(6)	
Theory		
No vacancy	468.6(17)	+3.3(13)
Vacancy FO	486.4(17)	-0.1(13)
Vacancy SCF	483.1(17)	+0.4(13)

As a byproduct of this measurement, we could determine the β-branching ratio of the isomeric state in ^{127}Te. The 57.6-keV level in ^{127}I is populated by two β-decay branches, one from the isomeric state and the other from the ground state of ^{127}Te. Since the ground state has a half-life of 9.35 hours and our spectrum was acquired more than a month after activation, the two decays were certainly in secular equilibrium for our measurement. Under these conditions, we see from the decay scheme that the 57.6-keV state is fed ~13 times more strongly from the isomer than it is from the ground state. As a consequence, it is possible to use the ratio of intensities of the γ-ray peaks at 57.6 and 88.2 keV to extract a rather precise value for the strength of the stronger β branch even though the strength of the weaker branch remains relatively imprecise.

We determined the β branching ratio of the isomeric state to be 2.14(3)%. This compares favorably with, but is 7 times more precise than, the only previous measurement of this quantity, 2.4(2)%, which was published in 1970 [5].

[1] N. Nica *et al.*, *Progress in Research,* Cyclotron Institute, Texas A&M University (2013-2014), p I-26.

[2] N. Nica, J.C. Hardy, V.E. Iacob, T.A. Werke, C.M. Folden III, K. Ofodile, and M.B. Trzhaskovskaya, Phys. Rev. C **95**, 034325 (2017).

[3] J.C. Hardy *et al.*, Appl. Radiat. Isot. **56**, 65 (2002) ; R.G. Helmer *et al.*, Nucl. Instrum. Methods Phys. Res. **A511**, 360 (2003); R.G. Helmer *et al.*, Appl. Radiat. Isot. **60**, 173 (2004).

[4] N. Nica, J.C. Hardy, V.E. Iacob, M. Bencomo, V. Horvat, H.I. Park, M. Maguire, S. Miller, and M.B. Trzhaskovskaya, Phys. Rev. C **89**, 014303 (2014).

[5] K.E. Apt, W.B. Walters, and G.E. Gordon, Nucl. Phys. **A152**, 344 (1970).

Precision γ-ray branching-ratio measurements for long-lived fission products of importance to stockpile stewardship

K. Kolos,[1] A.M. Hennessy,[2] J.A. Clark,[3] J.C. Hardy,[4] V.E. Iacob,[4] G.E. Miller,[2] E. Norman,[5] G. Savard,[3]
N.D. Scielzo,[1] A.J. Shaka,[2] M.A. Stoyer,[1] and A.P. Tonchev[1]
[1]Lawrence Livermore National Laboratory, [2]University of California at Irvine, [3]Argonne National Laboratory, [4]Texas A&M University, [5]University of California at Berkeley

Introduction

One of the most straightforward and reliable ways to determine the number of fissions that occurred in a chain reaction is done via detection of the characteristic γ rays emitted during the β-decay of the fission product. These γ rays are emitted in only a fraction of the decays, and this fraction (the γ-ray branching ratio) must be known accurately to determine the total number of fissions. The fission products ^{95}Zr, ^{144}Ce, and ^{147}Nd (along with other long-lived isotopes) play a crucial role in science-based stockpile stewardship. The γ-ray branching ratio of ^{147}Nd is known to only 8% uncertainty [1], hence leading to an 8% contribution to the uncertainty in fission-chain yield. The ^{144}Ce γ-ray branching-ratio values [2] are dominated by the results of a single measurement [3] performed about 40 years ago and have yet to be confirmed at that precision. Precise values of these absolute γ-ray branching ratios are desired for national-security applications and to greatly improve the precision and reliability with which the number of fissions can be determined.

Although the level schemes of the isotopes of interest are well known, there are several challenges in precisely measuring these γ-ray branching ratios. These isotopes have Q values of less than 1.2 MeV and β-energy spectra that peak near zero energy. The efficiencies of the β detector and γ-ray detector have to be well characterized and impurities and self-attenuation of the low-energy β particle in the sample must be minimized. The approach that has been developed in the past year to determine the γ-ray branching ratios consists of producing radiopure sources using low-energy ion beams from the CARIBU facility at Argonne National Laboratory (ANL) and performing β counting using a custom-made 4π gas proportional counter in coincidence with γ spectroscopy using the precisely-calibrated HPGe detector [4,5] at Texas A&M University.

Previous Work

High-purity samples of ^{95}Zr (50 Bq), ^{144}Ce (360 Bq), and ^{147}Nd (1500 Bq) were collected on thin (40 μg/cm^2) carbon foil backings using low-energy mass-separated beam of A=95, 144, and 147 fission products from CARIBU over several 2-day collection periods. Within a few hours after implantation on the collection foil, all the shorter-lived species β decay to the long-lived species of interest as illustrated for the case of ^{147}Nd in Fig. 1. During collection, a HPGe detector was used to monitor the implantation rate and to provide additional information on the purity of the ion beam by detecting the characteristic γ-rays from the shorter-lived fission products that make up the beam. The produced sources, which each have half-lives of 11 days or longer, were then shipped to Texas A&M for the branching-ratio measurements. Subsequent γ-ray spectroscopy measurements at TAMU revealed small levels of ^{131}I and ^{103}Ru in the ^{147}Nd sample and ^{103}Ru in the ^{144}Ce sample, most likely from molecules containing isotopes from these lighter mass chains. These additional isotopes will necessitate corrections between 0.3-2.5% for the branching-ratio determination.

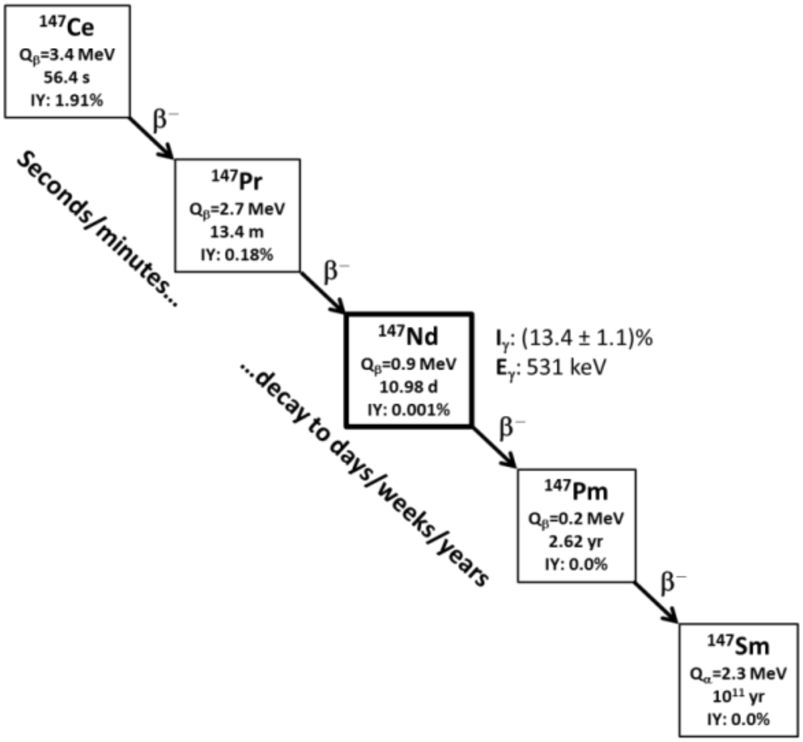

FIG. 1. CARIBU delivered intense, mass-separated beams consisting of isotopes from a single mass chain. For the mass-147 chain, the independent yield (IY) from fission initially generates mostly ^{147}Ce (and nuclei that decay to ^{147}Ce) and some ^{147}Pr nuclei. These nuclides both have half-lives of the order of minutes, and β^- decay within ~2 hours to create a pure sample of ^{147}Nd. Over time, the daughter nucleus ^{147}Pm grows in from the decay of ^{147}Nd. However, this is a small background that can be precisely tken into account.

At Texas A&M, the samples were placed in the center of a 4π gas proportional counter used for β detection. This newly-built detector has no internal windows, and therefore the β particles that emerge from the foil immediately enter the active volume of the detector. The performance of the counter was investigated using ^{95}Zr samples produced using a nuclear reactor and using CARIBU beams. The detector response agreed well with GEANT4 simulations and this work was summarized in the PhD thesis [6] of Brian Champine of the University of California at Berkeley.

The γ-ray measurements, performed both with and without coincident β-particle detection, were performed in the standard measurement geometry used by the Texas A&M group for many precise γ-ray branching-ratio measurements [7-9] and for detailed studies of internal conversion [10-12]. In this geometry, the efficiency of the detector is known to about 0.2% over the energy range of 50 keV to 2 MeV [4,5].

The decays of the ^{95}Zr, ^{144}Ce, and ^{147}Nd samples were studied over multiple weeks in 2017 and the analysis is currently underway. The γ-ray spectra for the β-γ coincidence results obtained are shown in Fig. 2. In each case, the daughter product is also radioactive and the contribution to the β emission rate from the sample must be taken into account. For the ^{144}Ce and ^{147}Nd samples, additional corrections to the β emission rate of 0.3% and ~2.5%, respectively, must be made to account for other long-lived fission products found in the sample.

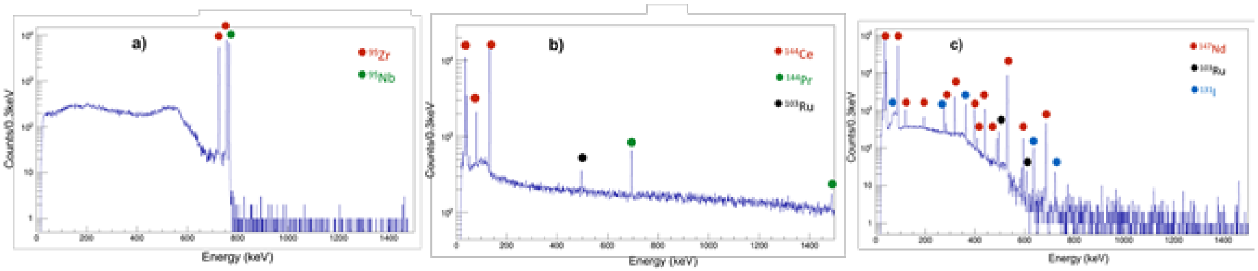

FIG. 2. The γ-ray energy spectra for β-γ coincidences for the a) ^{95}Zr, b) ^{144}Ce, and c) ^{147}Nd samples. In the ^{95}Zr sample, the only observed γ-ray lines are from the decays of ^{95}Zr and the daughter ^{95}Nb, which at the time of the measurement accounted for about 30% of the total activity of the sample. For the ^{144}Ce sample, several γ rays from the daughter ^{144}Pr ($t_{1/2}$=17.3 min), which is in equilibrium with ^{144}Ce, and a small (0.3%) contribution from the decay of ^{103}Ru can also been seen. For the ^{147}Nd sample, in addition to the many lines from the decay of ^{147}Nd, several lines from ^{131}I and ^{103}Ru indicate 2% and 0.3% contributions, respectively, to the total β-decay rate of the sample.

The γ-ray branching ratios are being determined from the ratio of the β-γ coincidence detection rates to the β particle detection rates, after correcting for detector efficiencies and the contribution to the β-decay rate from the daughter isotopes and any observed contaminants. The efficiency of the β counter largely divides out in the measurement and can be determined by comparing the number of γ-rays detected both with and without the coincidence detection of β particles. It is anticipated that with the data collected with these foils, the branching ratios can be determined to 1-2% precision. The γ-ray branching ratios in the decay of ^{95}Zr are already well established at 0.5% precision [13] and serve here as a confirmation of the accuracy of the measurement approach. These results will be a major part of the PhD thesis of Amber Hennessy, a graduate student at UC Irvine.

This work was supported in part by LLNL LDRD under project 15-ERD-015.

[1] N. Nica, Nucl. Data Sheets **110**, 749 (2009).
[2] J.K. Tuli, Nucl. Data Sheets **56**, 607 (1989).
[3] K. Debertin, U. Schotzig, K.F. Walz, and H.M. Weiss, Ann. Nucl. Energy **2**, 37 (1975).
[4] J.C. Hardy, V.E. Iacob, M. Sanchez-Vega, R.T. Effinger, P. Lipnik, V.E. Mayes, D.K. Willis, and R.G. Helmer, Applied Radiation and Isotopes **56**, 65 (2002).
[5] R.G. Helmer, J.C. Hardy, V.E. Iacob, M. Sanchez-Vega, R.G. Neilson, and J. Nelson, Nucl. Instrum. Methods Phys. Res. **A511**, 360 (2003).
[6] B. Champine, Ph.D. Thesis, University of California at Berkeley (2016).
[7] J.C. Hardy *et al.*, Phys. Rev. Lett. **91**, 082501 (2003).
[8] V.E. Iacob *et al.*, Phys. Rev. C **74**, 015501 (2006).
[9] D. Melconian *et al.*, Phys. Rev. C **85**, 025501 (2012).
[10] N. Nica *et al.*, Phys. Rev. C **71**, 054320 (2005).
[11] N. Nica *et al.*, Phys. Rev. C **77**, 034306 (2008).
[12] N. Nica *et al.*, Phys. Rev. C **80**, 064314 (2009).

[13] S.K. Basu, Nucl. Data Sheets **111**, 2555 (2010).

United States Nuclear Structure Data Program (USNDP) and Evaluated Nuclear Structure Data File (ENSDF) at Texas A&M University

N. Nica[1] and J.C. Hardy
[1]*Under contract with Brookhaven National Laboratory,*
Since 1/1/17 funded by Cyclotron Institute DOE Grant

Since 2005 we have been an important partner in the nationwide United States Nuclear Data Program (USNDP), which is part of the Nuclear Structure and Decay Data (NSDD) international nuclear data-evaluation network. USNDP is in fact the main part of the NSDD network, making the greatest effort in completion of the goals of the nuclear-structure data evaluation communities. Nuclear data evaluation is a national-interest activity financed by DOE, through which relevant nuclear-science results in virtually all world publications are retrieved and put together in a large Evaluated Nuclear Structure Data File (ENSDF) database according to general polices, a set of rules that makes possible a standard approach through which the data are uniformly evaluated.

This activity is carried out by a relatively small group of professionals located mostly in national laboratories but also hosted by a few universities. The nuclear data network is the nodal point for the wide dissemination of nuclear knowledge to many users, from those in basic science to those engaged in commercial applications in American and international businesses. The output is published in the Nuclear Data Sheets, an Elsevier publication, and also is disseminated by different on-line databases, which can be retrieved at the NNDC site (http://www.nndc.bnl.gov), IAEA Vienna's site (http://www-nds.iaea.org), and other locations.

Starting at the beginning of 2017 our status in the evaluation network has changed. Since 2005, evaluation work at the Cyclotron Institute has been funded by a contract with Brookhaven National Laboratory. From 2017 on, it will be funded directly as part of the DOE Grant for the Cyclotron Institute at 0.67% FTE, with one of us (NN) as principal investigator, and the other (JCH) as scientific adviser. While initially this is primarily an administrative change, it will qualify us to become in future a standalone evaluation center, the seventh in the US.

In the 12 years that the Cyclotron Institute of Texas A&M has been involved, we have completed and published the evaluation of mass chains covering a large part of the nuclear chart. We have published in Nuclear Data Sheets the superheavy A=252 mass chain [1]; the very data-rich mid-mass chains, A=140 [2], A=141 [3], A=147 [4] and A=148 [5]; the relatively lighter chains, A=97 [6] and A=84 [7], the latter in a large international collaboration; and in collaboration with B. Singh and a group of authors from McMaster University, Canada, we also published the A=77 [8], A=37 [9], A=36 [10], and A=34 [11] chains. At the beginning of 2016 another big mass chains, A=157 was published in Nuclear Data Sheets [12], followed by A=158 in the 2017 March-April issue of the same journal [13]. Another two massive mass chains, A=140 and A=155 are in the pipeline for publication.

During the spring of 2017 we started a new full evaluation for the mass chain A=160, updating it to include all the publications that have appeared since the last evaluation closed in June 2005. The chains consist of the following A=160 isobars: Nd, Pm, Sm, Eu, Gd, Tb, Dy, Ho, Er, Tm, Yb, Lu, Hf, Ta, W, and Re: in total 16 nuclei. Our bibliographical search found that, since June 2005, 383 papers were published concerning this mass chain, of which 337 were primary references (most important); 92% of all publications are experimental. The work is in progress.

[1] N. Nica, Nucl. Data Sheets **106**, 813 (2005).
[2] N. Nica, Nucl. Data Sheets **108**, 1287 (2007).
[3] N. Nica, Nucl.Data Sheets **122**, 1 (2014).
[4] N. Nica, Nucl. Data Sheets **110**, 749 (2009).
[5] N. Nica, Nucl. Data Sheets **117**, 1 (2014).
[6] N. Nica, Nucl. Data Sheets **111**, 525 (2010).
[7] D. Abriola *et al.*, Nucl. Data Sheets **110**, 2815 (2009).
[8] B. Singh and N. Nica, Nucl. Data Sheets **113**, 1115 (2012).
[9] J. Cameron, J. Chen, B. Singh, and N. Nica, Nucl. Data Sheets **113**, 365 (2012).
[10] N. Nica, J. Cameron, and B. Singh, Nucl. Data Sheets **113**, 1 (2012).
[11] N. Nica and B. Singh, Nucl. Data Sheets **113**, 1563 (2012).
[12] N. Nica, Nucl.Data Sheets **132**, 1 (2016).
[13] N. Nica, Nucl.Data Sheets **142**, 1 (2017).

Commissioning of the TIARA for Texas experimental station

G. Christian, E.A. Bennett, S. Dede, S. Ota, A. Saastamoinen
W.N. Catford,[1] S. Hallam,[1] G. Lotay,[1] M. Mouhkaddam,[1] and R. Wilkinson[1]
[1]*University of Surrey, Guildford GU2 5XH, United Kingdom*

Single- and multi nucleon transfer reactions such as (d, p) and (^{6}Li, d) are valuable tools for obtaining spectroscopic information on nuclei away from stability. Their sensitivity to excitation energies, orbital angular momenta, and single-particle (or pair/cluster) strengths make them ideal tools for studying the evolution of nuclear structure away from the valley of stability and for constraining the strengths of key, isolated resonances involved in stellar nucleosynthesis. Transfer reactions performed in forward kinematics using the MDM spectrometer have played a key role in the scientific program at the TAMU Cyclotron Institute for many years. A prime example is the long and successful program of constraining astrophysical reactions using the ANC technique. Looking towards the future, the anticipation of re-accelerated rare isotope beams (RIBs) from the light- and heavy-ion guide upgrades motivates the development of new experimental stations which are optimized for studying transfer reactions in inverse kinematics, with the short-lived RIBs impinging on light targets.

In order to study transfer reactions in inverse kinematics with re-accelerated RIBs, the TIARA (transfer and inelastic scattering all-angle reaction array) experimental setup [1] has been moved from its former home at GANIL in Caen, France and re-commissioned at the Cyclotron Institute, where it is commonly referred to as “TIARA for Texas” (T4T). TIARA consists of two silicon detector arrays which are optimized for detecting the target-like ejectiles emitted from transfer and elastic scattering reactions in inverse kinematics. The first detector array is 16-strip annular DSSD which can be placed either upstream or downstream of the target depending on the desired reaction kinematics. The second detector array is compact silicon “barrel” composed of position-sensitive resistive strip detectors which surrounds the reaction target covering laboratory angles from $30^{\circ} - 145^{\circ}$. Together these detector arrays provide good angular coverage and resolution for both the ejectiles emitted in the transfer reaction under study and elastically-scattered target nuclei which are used for the absolute cross section normalization. At the Cyclotron Institute, TIARA is installed at the target position of the MDM magnetic spectrometer and further coupled to four HPGe clovers borrowed from the HYPERION array. This setup allows beam-like recoils to be detected in the focal plane of the MDM, in coincidence with reaction events in the TIARA Si detectors. This coincidence technique virtually eliminates any background from fusion-evaporation reactions. Furthermore, the coupling with HPGe detectors allows measurement of the gamma-rays emitted in the de-excitation of states populated in transfer reactions, allowing states which are nearly degenerate in energy to be separated in the data analysis. The HPGe detectors are arranged in a compact geometry surrounding the target to maximize efficiency, which is around 10% for gamma rays with an energy of ~1 MeV.

Following its installation the T4T setup was commissioned in a series of stable beam experiments performed in the Fall of 2016, each targeted at constraining key resonance strengths involved in astrophysical nucleosynthesis. The first two experiments, ^{19}F(d,p)^{20}F and ^{23}Na(d,p)^{24}Na are aimed at studying the mirrors of important proton-capture resonances affecting nucleosynthesis in classical novae.

For more details on the latter reaction, see the report "Studying the ^{23}Na(d,p)^{24}Na reaction to constrain the astrophysical ^{23}Mg(p,γ)^{24}Al reaction rate". The other two experiments were aimed at constraining the properties of resonances in ^{26}Mg which affect the overall rate of the ^{22}Ne(α,n)^{25}Mg reaction in AGB stars. This reaction is one of only two sources of neutrons for the slow neutron capture process which is partially responsible for the formation of elements heavier than iron. Resonant states in ^{26}Mg were populated and studied using both the ^{25}Mg(d,p)^{26}Mg and ^{22}Ne(^{6}Li, d)^{26}Mg reactions. See the report "Study of the astrophysical α + ^{22}Ne reaction using ^{6}Li(^{22}Ne,^{26}Mg)d alpha transfer with TIARA and the MDM spectrometer".

The data from these four experiments are in the early stages of analysis; however, at present a number of key features demonstrating the performance of the system can already be identified. Figure 1 demonstrates the performance of the T4T system in making spectroscopic measurements of the ^{19}F(d,p)^{20}F reaction. As can be seen in panel a), the system displays good particle identification from measurements of E-ΔE in the MICROMEGA detector at the focal plane of the MDM, with the loci of ^{20}F recoils and ^{19}F beam clearly separated. Panel b) shows kinematic lines observed in the backward-angle Si detector, with the expected kinematic curves from ^{19}F(d,p)^{20}F superimposed and matching well with the data. Panel c) shows the ^{20}F excitation energy spectrum calculated from the measured proton energies and

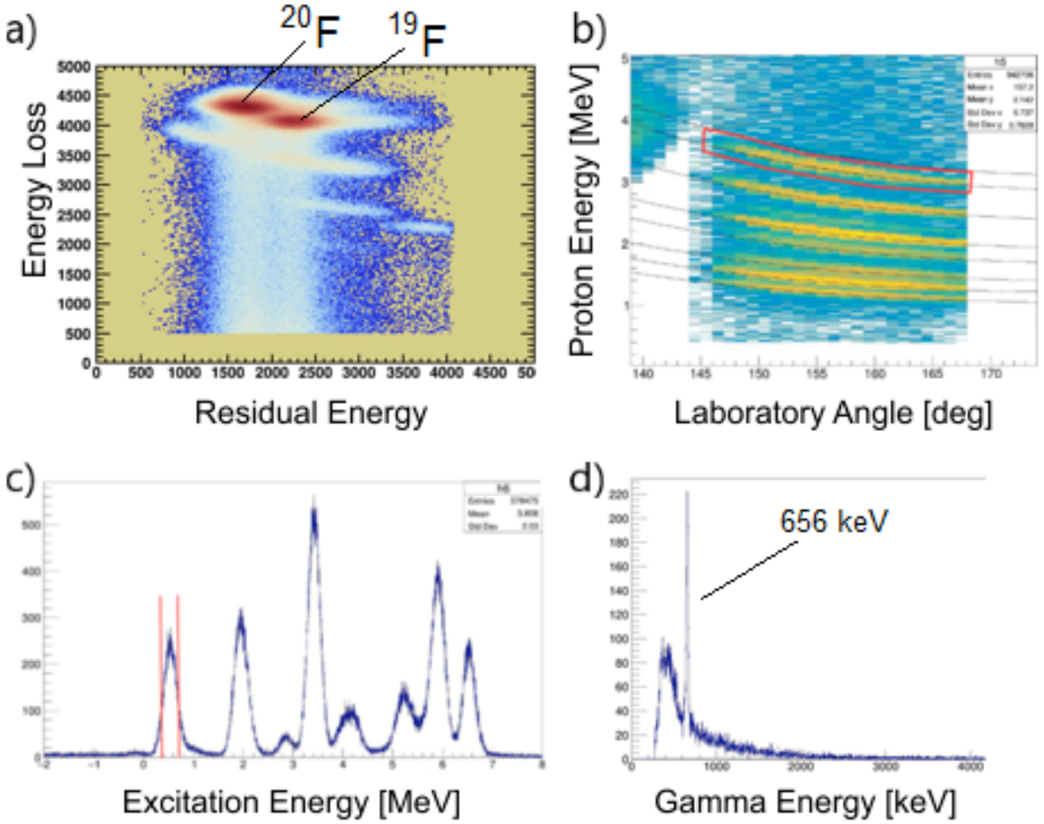

FIG. 1. Sample plots showing the performance of the T4T spectroscopic system. All plots are from data taken on the ^{19}F(d,p)^{20}F reaction. a) Sample E-ΔE particle ID plot in the Micromega detector at the MDM focal plane. b) Proton kinematic lines observed in the backward-angle annular Si detector. c) Excitation energy spectrum of ^{20}F observed in the backward-angle annular Si detector. d) Gamma-ray energy spectrum, gated on the first excited state in ^{20}F at 656 keV.

angles in the annular Si detector. Excited states in ^{20}F are clearly present, and the excitation energy resolution is approximately 200 keV FWHM (these data were taken with a 200 μg/cm^2 CD$_2$ target). Panel d) demonstrates the performance of the gamma-ray detection system, showing the Doppler-corrected HPGe spectrum gated on the 656 keV first excited in ^{20}F. The 656 keV peak from the direct decay of this state to the ground state is clearly evident. The resolution for the Doppler-corrected gamma-rays in this energy regime is approximately 10 keV FWHM.

Fig. 2 demonstrates the performance of the system for measuring the target-like products of elastic scattering, which is essential for determining the beam + target luminosity needed to extract absolute cross sections. Panel a) shows the Si barrel energy vs. angle plots observed by impinging ^{25}Mg at 10A MeV on a CD$_2$ target. A kinematic curve from d(^{25}Mg, ^{25}Mg)d elastic scattering is clearly evident on top of background from fusion-evaporation. Panel b) shows a projection onto the angle axis, for a narrow slice in energy. The peak from elastic scattering is clearly identifiable, and in the final analysis its area can be extracted from a simple Gaussian + polynomial background fit.

Analysis of the data from all of the TIARA stable-beam experiments is ongoing, and it is expected that absolute differential cross sections will be obtained for the states of astrophysical interest. Future experiments with TIARA will focus on astrophysically-motivated (d,p) reactions performed both with RIBs from the light-ion guide upgrade, as well as long-lived radioactive isotopes of nickel and iron placed directly into the K500 ion source.

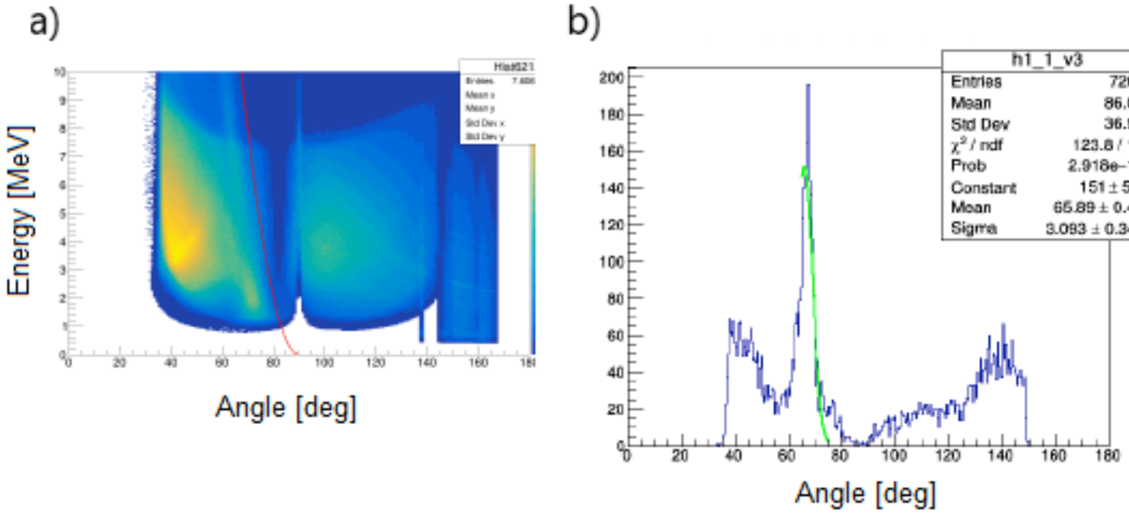

FIG. 2. Sample plots demonstrating the performance of the Si barrel detector for measuring d(^{25}Mg, ^{25}Mg)d elastic scattering. Panel a) shows the elastic scattering kinematic curve sitting on top of a background from fusion-evaporation. Panel b) shows a projection onto the angle axis of the plot in panel a), gated on a narrow slice in energy. The peak from elastically-scattered deuterons is clearly evident on top of fusion-evaporation background.

[1] M. Labiche *et al.*, Nucl Instrum. Methods Phys. Res. **A614**, 439 (2010).

Study of the astrophysical α + ^{22}Ne reaction using ^{6}Li(^{22}Ne,^{26}Mg)*d* alpha transfer with TIARA and the MDM spectrometer

S. Ota, E.A. Bennett, G. Christian, S. Dede, H. Jayatissa, J. Hooker, C. Hunt,
C. Magana, G. Rogachev, A. Saastamoinen, S. Upadhyayula,
W.N. Catford,[1] S. Hallam,[1] G. Lotay,[1] M. Mouhkaddam,[1] and R. Wilkinson[1]
[1]*University of Surrey, Guildford GU2 5XH, United Kingdom*

In the He-burning phase of massive stars, the ^{22}Ne(α,n)^{25}Mg reaction is considered to be a main neutron source driving the synthesis of nuclides in the A=60-90 mass range during the *s* process [1]. A variety of attempts to experimentally determine the rate for this reaction in the Gamow window corresponding to *s* process temperatures (T = 0.2-0.3 GK) have been made either through direct ^{22}Ne(α,n)^{25}Mg measurements [2] or indirect measurements such as ^{22}Ne(^{6}Li,*d*)^{26}Mg [3-5]. However, direct measurements have been hindered by the small cross section due to the Coulomb barrier and the resonances at E_α < 830 keV (E_α: energy of α particle in the laboratory system) have not been identified with this method. The indirect measurements have identified many low-energy resonances, but unambiguous determination of the resonance parameters such as spin-parity (J^π), partial wave widths of respective decay channels (Γ_γ, Γ_n and Γ_α) in ^{26}Mg produced by α + ^{22}Ne has remained a longstanding problem, especially for resonances near the Gamow peak (E_α = 400 – 1000 keV). Of these uncertainties, the ratio of Γ_n and Γ_γ to determine the branching ratio of *n* and γ emission channels plays an important role in obtaining the neutron yield for the *s* process. The ^{22}Ne(α,γ)^{26}Mg reaction (Q=10.615 MeV), which competes with the ^{22}Ne(α,n)^{25}Mg reaction (open above the excitation energy of ^{26}Mg, E_x=11.093 MeV), may be of considerable strength and could significantly suppress neutron production during He burning (E_x=10.9-11.5 MeV). To address this problem, we performed an experiment using the ^{6}Li(^{22}Ne,^{26}Mg)d α-transfer reaction in this work. Because both the α and ^{22}Ne have ground states with $J^\pi=0^+$, the α-transfer reaction preferentially populates natural parity states in ^{26}Mg. This helps to enable studies of the resonance parameters of astrophysically relevant natural parity states in ^{26}Mg. Furthermore, the inverse kinematics approach enables us to determine Γ_n / Γ_γ by direct measurements of the ratio of produced ^{25}Mg and ^{26}Mg ions.

We performed the experiment at Cave 3 using a 7 MeV/u ^{22}Ne beam from the K150 cyclotron. ^{6}Li-enriched (99%) lithium flouride (LiF) targets with a thickness of 30 μg/cm^2 on a graphite backing foil (10 μg/cm^2) were prepared so that the energy loss of the ^{22}Ne beam and deuterons in those materials will be negligibly small. The beam bombarded the target at an intensity of about 3 nA for about 10 days. Recoil Mg ions were transported to the Oxford ionization chamber at the back of the MDM spectrometer [6]. The Oxford chamber consists of four proportional wire counters to determine the trajectories of particles and two MicroMegas detectors to measure the deposited energies in the gas (see details in [7]). Since the Mg ions are stopped inside the chamber and the first and the second MicroMegas detectors provide ΔE and E_{res} (residual energy), respectively. The Mg ions are clearly identified from other elements using a conventional E-ΔE technique as shown in Fig. 1. Furthermore, it was found ^{26,25}Mg isotopes were clearly identified from each other based on the focal plane positions (Fig. 2). A large Si detector array, TIARA [8] surrounded by four HPGe clover detectors, was used for particle identification and measuring the angular distribution of light particles (deuterons). The energies of deuterons were measured to determine excitation energies of ^{26}Mg and the background events such as compound nucleus reaction were minimized to be negligibly small in the data by requiring the coincidence detection of Mg ions and deuterons.

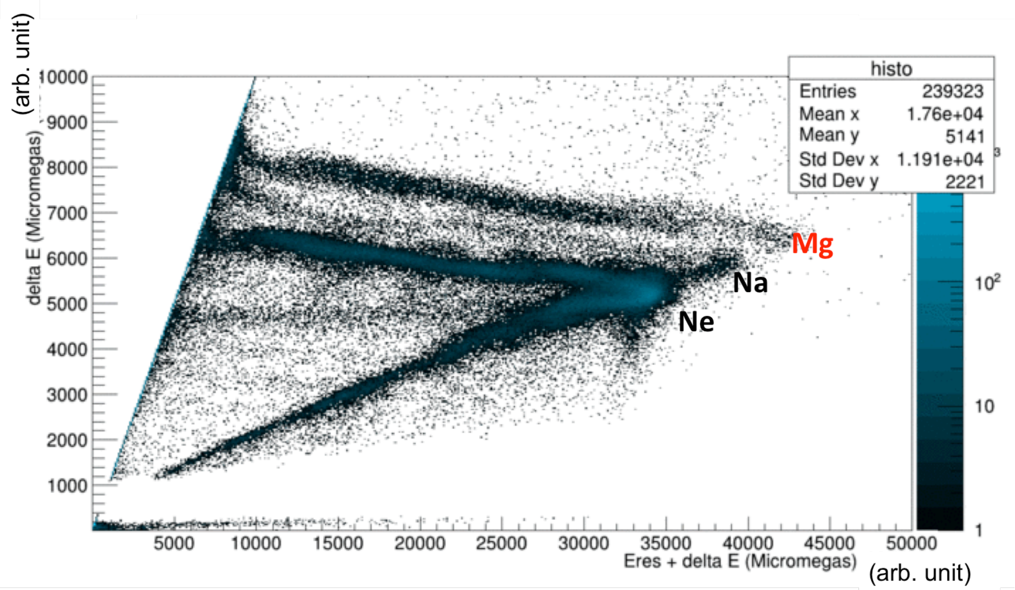

FIG. 1. Particle identification of Mg ions using a conventional E-ΔE method. Mg ions are stopped inside the Oxford chamber and ΔE and E_{res} signals are obtained from the deposited energies in two MicroMegas detectors, respectively.

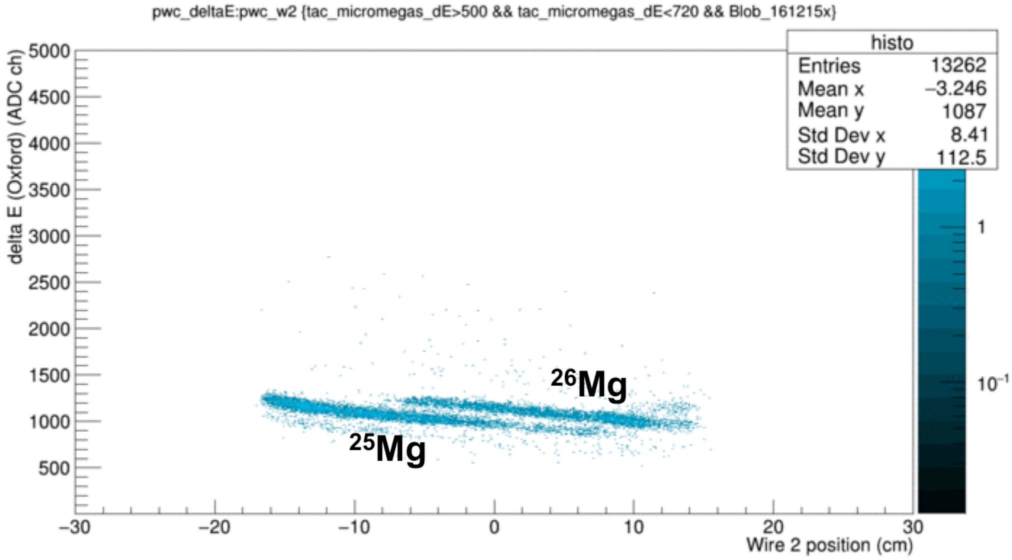

FIG. 2. Isotope separation of ^{25,26}Mg ions based on positions detected in the second proportional wire of Oxford chamber.

Currently, further data analysis combined with all the data from TIARA, Ge detectors, and Oxford chamber is ongoing. Fig.3 shows the preliminary ^{26}Mg excitation energy spectra gated on ^{26}Mg and ^{25}Mg (produced by neutron emission of ^{26}Mg above the neutron separation energy (S_n)), respectively. While some resonance peaks are clearly confirmed, the expected four resonance states in the Gamow window are not resolved yet. After some corrections for, e.g., beam position and energy losses in Si dead-layers and targets are made, however, further improvement of energy resolution will be achieved. We expect various resonance parameters of ^{26}Mg in the Gamow peak such as J^{π}, E_x, Γ_n, Γ_γ will be elaborated shortly to study the s-process neutron source.

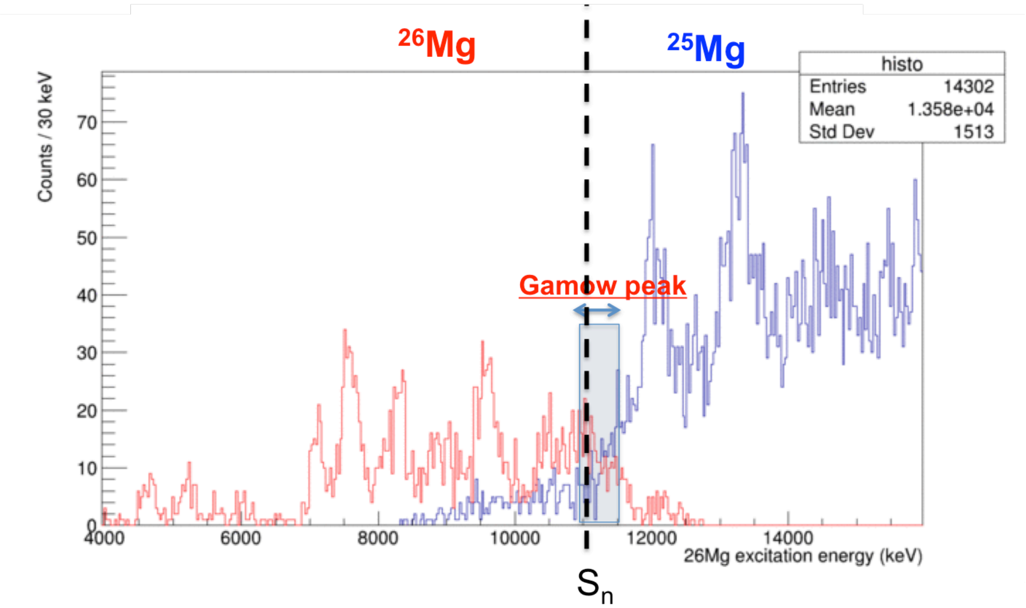

FIG. 3. ^{26}Mg excitation energy spectrum from the preliminary online data analysis. Four resonance peaks are expected in the Gamow peak window.

[1] F. Kappeler, Prog. Part. Nucl. Phys. **43**, 419 (1999).

[2] M. Jaeger *et al.*, Phys. Rev. Let. **87**, 20 (2001).

[3] U. Giesen *et al.*, Nucl. Phys. **A561**, 95 (1993).

[4] C. Ugalde *et al.*, Phys. Rev. C **76**, 025802 (2007).

[5] R. Talwar *et al.*, Phys. Rev. C **93**, 055803 (2016).

[6] D.M. Pringle *et al.*, Nucl. Instrum. Methods Phys. Res **A245**, 230 (1986).

[7] A. Spiridon *et al.*, Nucl. Instrum. Methods Phys. Res **B376**, 364 (2016).

[8] M. Labiche *et al.*, Nucl. Instrum. Methods Phys. **A614**, 439 (2010).

Studying the ^{23}Na(d,p)^{24}Na reaction to constrain the astrophysical ^{23}Mg(p,γ)^{24}Al reaction rate

E.A. Bennett, W.N. Catford,[1] G. Christian, S. Dede, S. Hallam,[1] G. Lotay,[1] S. Ota,
A. Saastamoinen, and R. Wilkinson[1]
[1]*University of Surrey, Surrey, United Kingdom*

In classical novae, the ^{23}Mg(p,γ)^{24}Al reaction provides an escape from the Ne-Na cycle and is therefore important in understanding nucleosynthesis in the A>20 mass range. Classical novae occur in binary star systems where one of the two main sequence stars has regressed to a white dwarf. When the white dwarf's companion star sheds its matter, the white dwarf begins to accrete hydrogen-rich materials on its surface. The burning of the materials raises the white dwarf's temperature and runaway nuclear reactions begin. It is at these increased temperatures that the proton capture reaction on ^{23}Mg outpaces the β decay reaction favored at lower temperatures [1,2]. The ^{24}Al generated by this proton capture reaction quickly decays into ^{24}Mg and allows entrance into the Mg-Al cycle [3].

Several resonances may be of astrophysical interest; however, at novae temperatures, the resonance at ~475 keV is thought to be the dominant contributor to the reaction rate [2]. Multiple experiments have investigated the excited states in ^{24}Al that correspond to the resonances of astrophysical interest. A fusion-evaporation experiment at Gammasphere found the energy of this resonance to be 473 ± 3 keV [4], by performing in-beam γ-ray spectroscopy on the ^{24}Al nucleus. While this is regarded as the most precise measurement to date, other particle spectroscopy experiments have placed the resonance energy between 456 ± 10 keV and 497 ± 5 keV [3]. A direct measurement of the ^{23}Mg(p,γ)^{24}Al reaction was performed at DRAGON, using a ^{23}Mg beam impinging on a windowless H_2 gas target. This experiment determined a resonance energy of 485.7 keV and a resonance strength of 38 meV [4]. However, the authors were only able to weakly exclude the possibility of a stronger resonance lying at the edge of their gas target, in the region where the gas pressure has not reached equilibrium. These uncertainties motivate additional experiments constraining the strength of the ~475 keV resonance.

We believe an indirect measurement of the resonance strength will either verify or throw into question the DRAGON measurement. Since ^{24}Na is the isobaric analogue of ^{24}Al, we can easily make an indirect measurement using the stable beams available to us at the Cyclotron Institute. Specifically, we use the ^{23}Na(d,p)^{24}Na reaction in inverse kinematics to extract the spectroscopic factor for the mirror of the ~475 keV resonance in ^{23}Mg + p. Given the spectroscopic factor for ^{24}Na and ^{24}Al is the same, we can then use this to calculate the proton width and, utilizing the known gamma width, can extract the resonance strength. The experiment conducted here at the Cyclotron Institute was performed using TIARA, a compact silicon detector array designed to study direct reactions in inverse kinematics [5]. We impinged a 10A MeV beam of ^{23}Na on a 500 μg/cm^2 CD_2 target mounted in the center of the TIARA chamber. In conjunction with the MDM and Oxford Detector, we are able to look at protons from the ^{23}Na(d,p)^{24}Na reaction in the backward angle silicon array with relatively high precision. HPGe detectors mounted around the target position also allow for gamma-ray spectroscopy.

Fig. 1 shows a sample online proton spectrum we observed during one of our runs. The spectrum clearly shows several excited states in the ^{24}Na nucleus, including the mirror of the astrophysical state of interest, which lies at 2514 keV. We are currently in the process of performing the offline analysis to extract the differential cross section for population of this state in ^{23}Na(d,p)^{24}Na. Analysis continues on the data set and we hope to use our final results to determine if another run at DRAGON is warranted to repeat the direct measurement of the ^{23}Mg(p,γ)^{24}Al reaction.

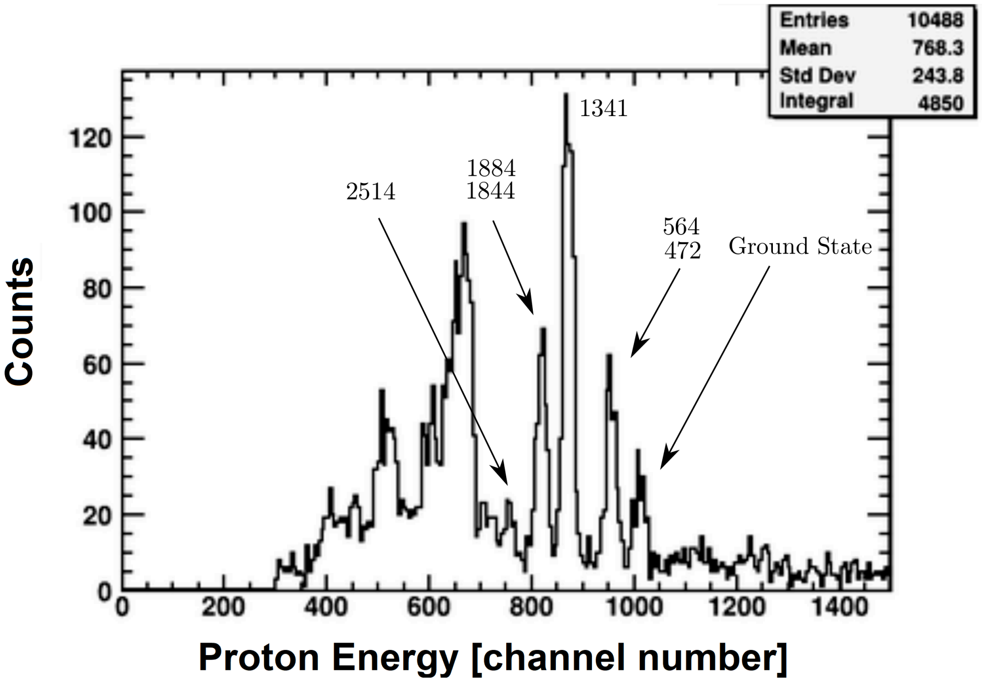

FIG. 1. A sample proton spectrum seen during our experiment. This spectrum includes labels for several suspected resonance energies in the ^{24}Na nucleus.

[1] H. Herndl *et al.*, Phys. Rev. C **58**, 1798 (1998).

[2] U. Chowdhury *et al.*, Phys. Rev. C **92** 045803 (2015).

[3] L. Erikson *et al.*, Phys. Rev. C **81** 045808 (2010).

[4] G. Lotay *et al.*, Phys. Rev. C **77** 042802(R) (2008).

Measurement of β-delayed protons from decay of ^{31}Cl covering the Gamow window of ^{30}P(p,γ)^{31}S at typical nova temperature

A. Saastamoinen, B.T. Roeder, A. Spiridon, R. Chycz, R.E. Tribble,
E. Pollacco,[1] L. Trache,[2] and I. Stefanescu[2]
[1]*IRFU, CEA Saclay, Gif-sur-Yvette, France*
[2]*National Institute of Physics and Nuclear Engineering, Bucharest-Magurele, Romania*

The thermonuclear runaway in classical novae proceeds through radiative proton capture reactions (p,γ) involving proton rich sd-shell nuclei close to the dripline. Many of the capture reactions at typical peak nova temperatures of 0.2-0.4 GK are dominated by resonant capture. Therefore, the key parameters in understanding the astrophysical reaction rates are the energies, decay widths and spins of these resonances. One of the bottleneck reactions in the ONe nova nucleosynthesis is the radiative proton capture ^{30}P(p,γ)^{31}S.

In absence of intense ^{30}P radioactive beams, the experimental efforts for finding and studying the resonances in ^{31}S have concentrated on using a variety of indirect methods. One indirect method with high selectivity is the allowed β-decay of the $3/2^+$ ground state of ^{31}Cl which populates excited states in ^{31}S, corresponding to $l = 0$ resonances ($J^\pi = 1/2^+, 3/2^+$) and $l = 2$ resonances ($J^\pi = 5/2^+$). An observation, or non-observation, of β -delayed protons or γ -rays from the levels with uncertain or contradicting spin assignments [1] will help constraining the possible astrophysically important states. The previous efforts on measuring β-delayed protons from the states of astrophysical interest in ^{31}S ($E_x \sim 100-500$ keV) have not been successful for the fact that these studies suffered from the intense β-background in the setups utilizing Silicon detectors [2,3]. Recently, a high statistics measurement of β-delayed γ-rays from decay of ^{31}Cl identified a new candidate for a resonance in the middle of the Gamow window [4]. Since the new level is seen populated in β-decay, it opens possibility for determining the proton branching ratio, which is one of the pieces of information needed for the experimental determination of the experimental value of the resonance strength.

We have done a measurement of β-delayed protons from ^{31}Cl with the newly built and commissioned AstroBox2 detector, based on Micro Pattern Gas Amplifier Detector (MPGAD) technology [5]. An intense and pure beam of ^{31}Cl was produced by bombarding a LN$_2$ cooled H$_2$ target at 2 atm with a 40-MeV/u ^{32}S beam from the K500 cyclotron at the Cyclotron Institute. The ^{31}Cl beam resulting from ^{1}H(^{32}S,^{31}Cl)^{2}n inverse kinematics reaction were separated with the MARS separator. The beam was implanted and stopped inside the gas volume of the AstroBox2 for the decay study. In this experiment we managed to suppress the β-background down to 100 keV, allowing a background free study of β-delayed proton emitting states in ^{31}S throughout the whole Gamow window of the ^{30}P(p,γ)^{31}S reaction. The experiment was calibrated by using known β-delayed protons from ^{25}Si [5,6]. Fig. 1 shows a multiplicity = 1 gated spectrum from one of the MPGAD pads, compared to a GEANT4 simulation. The data shows a good agreement with previously known higher energy protons. Moreover, a previously unobserved proton group is seen at the low energy part of the spectrum. The measured decay energy agrees with the new state which was observed in a recent βγ-study of decay of ^{31}Cl [4]. The data are under further analysis.

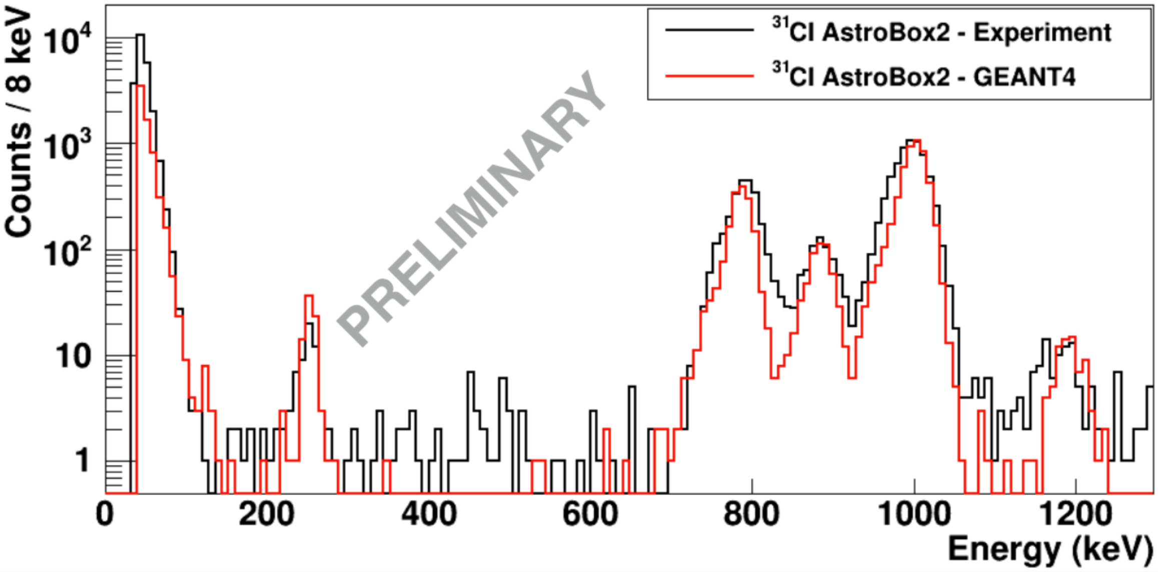

FIG. 1. The spectrum of β-delayed protons from ^{31}Cl compared to GEANT4 simulation. The intensities of the known proton groups agree with the experiments conducted with Si-detectors [2,3]. The low energy peak is in close agreement with the recently observed β-delayed γ-rays from a state in ^{31}S [6], suggesting the same origin.

[1] C. Ouellet and B. Singh, Nucl. Data Sheets **114**, 209 (2013).

[2] A. Kankainen *et al.*, Eur. Phys. J. A **27**, 67 (2006).

[3] A. Saastamoinen *et al.*, AIP Conf. Proc. **1409**, 71 (2011).

[4] M.B. Bennett *et a*l., Phys. Rev. Lett. **116**, 102502 (2016).

[5] A. Saastamoinen *et al.*, Nucl. Instrum. Methods Phys. Res. **B376**, 57 (2016).

[6] J.-C. Thomas *et al.*, Eur. Phys. J. A **21**, 419 (2004).

The study of ^{27}Si(p, γ)^{28}P reaction using its mirror ^{27}Al(n, γ)^{28}Al

A. Spiridon, R. Chyzh, M. Dag, B.T. Roeder, A. Saastamoinen, and R.E. Tribble

X-ray bursts are the most frequent thermonuclear explosion occurring in the universe and represent one type of phenomena responsible for heavier element nucleosynthesis. For this reason and others, a number of powerful X-ray observatories have been used to take large amounts of data on these bursts. The interpretation of these observations, however, is problematic due to the lack of a complete understanding of the nuclear physics at the base of these phenomena [1]. Among the various processes occurring in X-ray bursts, the most important is the rp-process. It is dominated by (p, γ), (α, p) reactions and β-decays. Critical nuclear data is needed related to these processes such as: nuclear masses, β-decay rates and reaction rates. There have been major strides made for the first two parameters. However, as most of the nuclei participating in the rp-process do not exist as stable nuclei, most of the reaction rates, so far, have only been estimated based on theory [2].

As with any nuclear reaction network, some reactions are more important than others. Several have been suggested for X-Ray bursts following different model calculations. One such reaction that we chose to research is the radiative proton-capture reaction ^{27}Si(p, γ)^{28}P. We studied this indirectly using the mirror reaction ^{27}Al(n, γ)^{28}Al with the purpose of using the properties of the mirror nuclei ^{27}Al and ^{28}Al in the estimation of the reaction rate.

A series of 4 experiments were done for this with the purpose of obtaining (1) the elastic cross-section distribution for optical model potential parameters and (2) the neutron transfer cross-section distribution for the DWBA analysis and the determination of the asymptotic normalization coefficients.

The first pair of experiments was done in direct kinematics with a beam of ^{13}C at 12 MeV/n on targets of ^{27}Al of different thicknesses (100 μg/cm^2, 270 μg/cm^2 and 800 μg/cm^2). The second pair was done in inverse kinematics with a beam of ^{27}Al at 12 MeV/n on a target of ^{13}C (100 μg/cm^2). All four studies were done at Texas A&M University using beams accelerated by the K150 cyclotron. The reaction products were separated using the Multipole-Dipole-Multipole (MDM) spectrometer and the nuclei of interest were observed with the Oxford focal plane detector.

Preliminary results can be seen in the Fig. 1. Pictures (top left) and (top right) show the angular distributions of the elastic and transfer cross-sections in C.M. for direct kinematics. Similarly, pictures (bottom left) and (bottom right) show the angular distributions of the elastic and transfer cross-sections in C.M. for inverse kinematics. Fig. 2 shows various attempts at optical potential fits with the Wood-Saxon model for the data in Fig. 1, (top left) and (bottom left). However, there are discrepancies in the data that we suspect are related to normalization factors (possibly related to the Faraday Cup measurements or the target thickness determination) or analysis errors and this has lead to the decision to reanalyze everything.

Currently, there is no preliminary estimation of the ^{27}Si(p, γ)^{28}P reaction rate yet as that is the final step in the analysis.

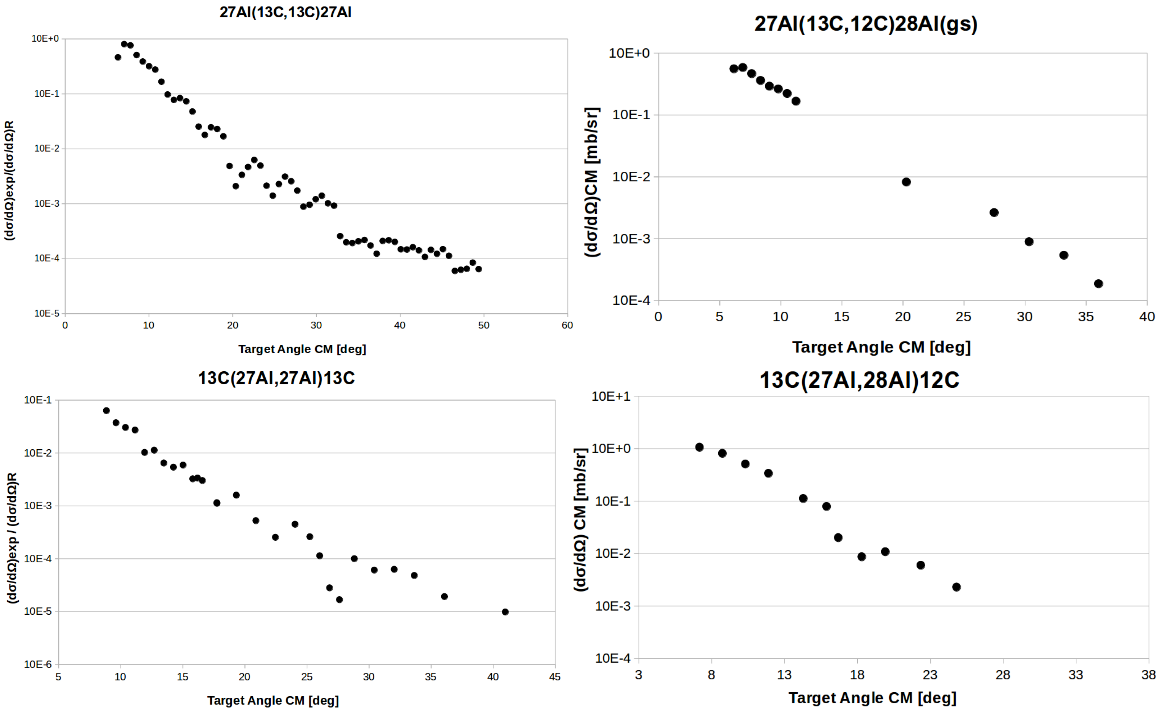

FIG. 1. Measured angular distributions of the cross sections for (top left) ^{27}Al(^{13}C,^{13}C)^{27}Al, (top right) ^{27}Al(^{13}C,^{12}C)^{28}Al, (bottom left) ^{13}C(^{27}Al,^{27}Al)^{13}C, and (bottom right) ^{13}C(^{27}Al,^{28}Al)^{12}C.

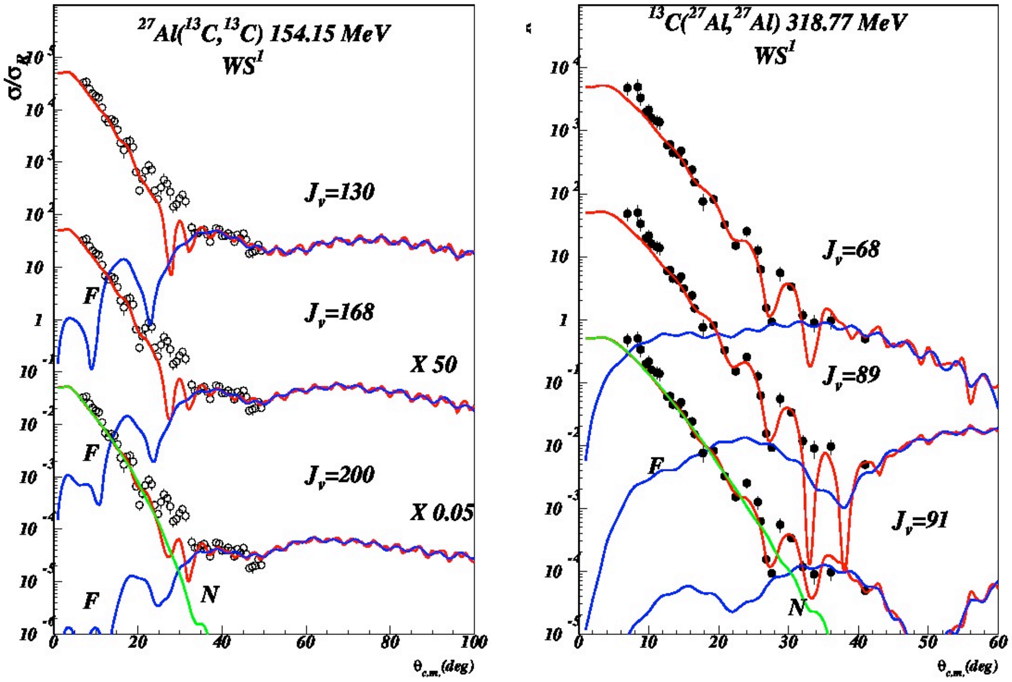

FIG. 2. Optical model fits for the elastic cross-section distributions obtained from the reactions, (left) ^{27}Al(^{13}C,^{13}C)^{27}Al, and (right) ^{13}C(^{27}Al,^{27}Al)^{13}C.

[1] H. Schatz, Prog. Part. Nucl. Phys. **66**, 277 (2011).
[2] H. Schatz and K. Rehm, Nucl. Phys. **A777**, 601 (2006).

Commissioning the Penning trap for the TAMUTRAP facility

B. Fenker, D. Melconian, and P.D. Shidling

The TAMUTRAP facility has a planned program in measuring the β decay of superallowed $T=2$ β-delayed proton transitions, starting with ^{32}Ar. En route to that goal, we have built and installed a prototype cylindrical Penning trap which has an inner diameter of 90 mm. While this prototype is already the worlds largest ion trap, we need one that is double the size to contain the β-delayed protons which have a Larmour radius of $R_L \leq 90$ mm.

The AutoCAD design of the trap as well as the final product are shown in Fig. 1. The electrode structure is based on our novel design [1] with a much larger radius-to-length ratio compared to typical cylindrical Penning traps. The trap was installed in the summer of 2016, and by the fall we demonstrated the ability to trap stable Potassium ions for long times, up to 30 s. The time-of-flight spectrum for different trapping times is shown in the left panel of Fig. 2 where one can see the effect of cooling the the ions with increased trapping times.

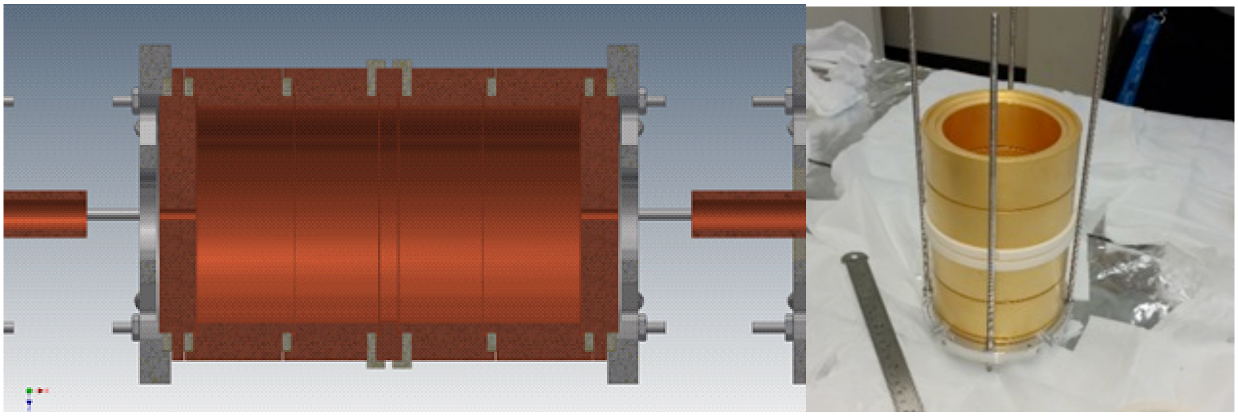

FIG. 1. Design (left) and the assembled prototype Penning trap for the TAMUTRAP facility (right). With an inner radius of 90mm, this is the world's largest cylindrical Penning trap. The time-of-flight (TOF) of the ions relative to ejection from the trap is made using a micro-channel plate situated outside of the superconducting solenoid (to the right of the trap).

We have since optimized injection of ions from the RFQ cooler and buncher, and characterized the trap's performance for different injection energies, trap depths, trapping times, etc. A major milestone was reached when we demonstrated the ability to manipulate the ion motion by exciting the magnetron motion of the trapped ions (typically used to remove contaminants at other Penning trap facilities). By applying rf at the appropriate frequency (420 Hz for ^{39}K) to the centre electrode, the trapped ions gain energy and are promoted to a larger radius. When ejecting these ions from the trap, ions that are excited do not make it through the 6 mm opening on the ejection (right) side of the trap.

We next applied dipole excitation to the ions at 2.7 MHz to excite the cyclotron motion of the ions As described in more detail in last year's report [2], the ions gain energy when in resonance with the cyclotron frequency with the net effect being a reduced TOF upon ejection relative to non-resonant frequencies. The first TOF vs frequency scan is shown in Fig. 2, where the ion rf was applied for just 10 ms. If the magnetic field of the magnet was precisely known, the frequency of the minimum TOF would represent a mass measurement. This frequency curve instead is actually a precise measurement of the magnetic field: B=7.019246 (4)T, better than a ppm precision. We have installed a 2nd offline ion source, this time Sodium, and are in the process of making a similar frequency scan. With the field calibrated to the ^{39}K ions, we will truly make a mass measurement of ^{23}Na. This is of course a well known quantity, but will serve to demonstrate our ability to make mass measurements at the ppm level and commission this aspect of the TAMUTRAP facilty.

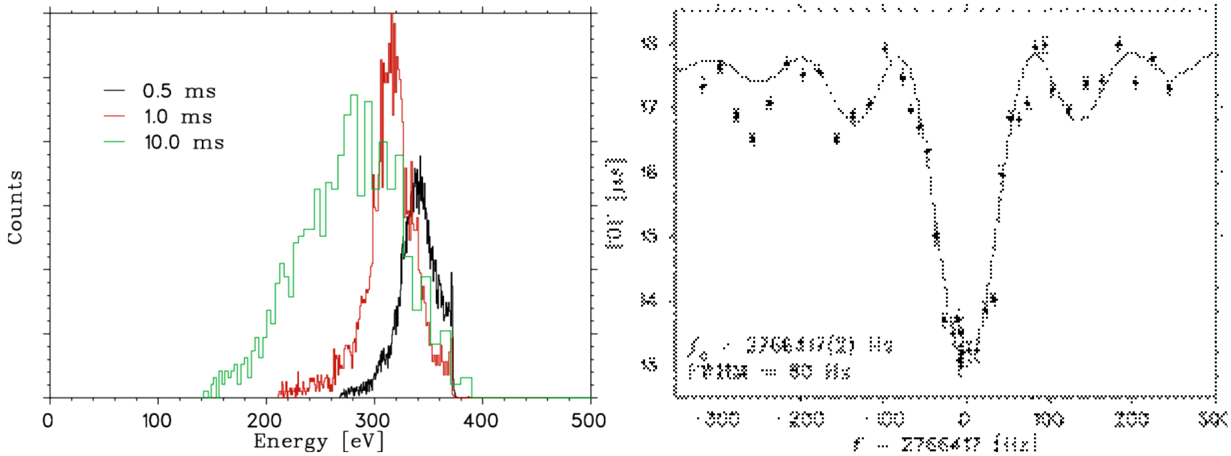

FIG. 2. TOF spectrum for the first trapped ions at TAMUTRAP (left), and the first cyclotron resonance curve of stable ^{39}K (right). The reduced average energy for longer trapping times demonstrates ion cooling from residual He atoms coming from the RFQ cooler/buncher. The resonance curve on the right is not perfect, but the width of the main drop in TOF is only ~20% larger than expected from the short (10 ms) rf excitation time. The mass-resolving power of this resonance curve corresponds to 30 ppm.

With the prototype trap commissioned and abiltiy to perform mass measurements demonstrated, we have started to design the full-sized Penning trap and expect to install it next year.

[1] M.Mehlman *et al.*, Nucl. Instrum. Methods Phys. Res. **A712**, 11 (2010).

[2] E. Bennett *et al.*, *Progress in Research*, Cyclotron Institute, Texas A&M University (2015-2016), p. I-62.

TRINAT status – precision polarization and beta-asymmetry

B. Fenker, D. Melconian, and P.D. Shidling

The TRINAT collaboration is utilizing magneto-optical trapping and optical pumping techniques to cool, confine and highly polarize ^{37}K atoms to provide an ideal source for precision β-decay experiments. Our goal is to measure parameters of the angular distribution to < 0.1% which would search for (or help constrain) physics beyond the standard model in a way that is competitive with and complementary to direct searches at high-energy colliders. Our particular focus at this point is a precision measurement of the β asymmetry parameter, A_β, which characterizes the correlation between the initial nuclear spin and the momentum of the daughter positron.

In order to be able to extract A_β from an asymmetry measurement (which goes like PA_β), we need to know the nuclear polarization of the atoms that are decaying. As described in last year's report [1], we use optical pumping to polarize the atoms along the same axis defined by the β detectors. We are able to reverse the direction of the polarization by simply reversing the polarization of the optical pumping laser light. Our result, recently published in Ref. [2], is $P_\uparrow = +0.9913(7)(5)$ and $P_\downarrow = -0.9912(6)(5)$ where the first uncertainty is statistical and the second systematic. The largest systematic uncertainty comes from an uncertainty in the initial distribution of the atoms amongst the possible sublevels. The overall uncertainty arising from our knowledge of the polarization is 0.08% which is precise enough to allow us to reach our goal of 0.1% in A_β.

Fig. 1 shows a drawing of the detection chamber. Two β telescopes, each consisting of a double-sided Si-strip (ΔE) and plastic scintillator (E) detectors, are positioned along the polarization axis. Electrostatic hoops generate an electric field which sweeps shake-off electrons and recoils to corresponding micro-channel plate detectors (MCPs); a coincidence with the shake-off MCP helps ensure that βs observed in the telescopes originated from decays that occurred within the trapping region and not, e.g., from untrapped atoms. On the right of Fig. 1, we show the observed asymmetry and the comparison

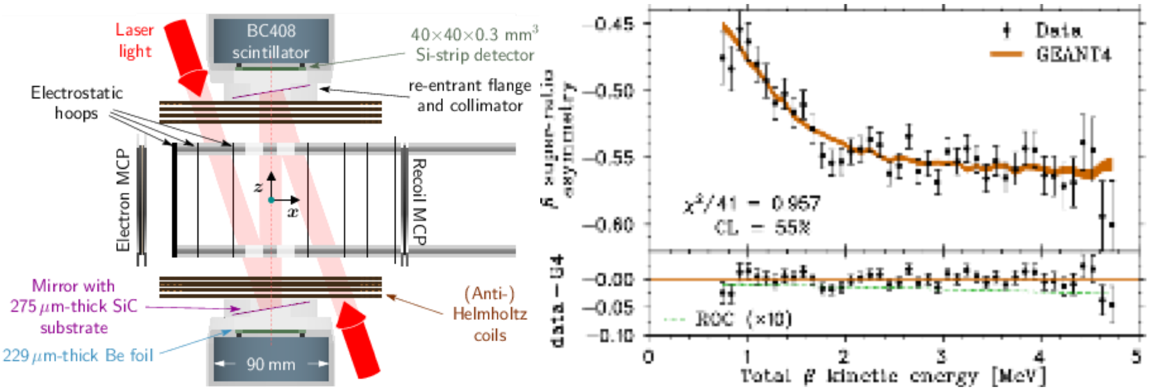

FIG. 1. The measurement chamber (left) and observed asymmetry (right) from part of the 2014 data set (filled circles). The super-ratio approach, which minimizes systematic effects, utilizes both β telescopes and both polarization states, and is compared to a GEANT4 simulation (filled band, with the width indicating it's statistical uncertainty) to extract A_β. Recoil-order effects introduce a very small correction, as shown by the dashed green line in the residual plot.

to our GEANT4 simulation. There is excellent agreement over the whole range of the β energies, requiring no background subtraction; the only free parameter of the fit was the value of $\rho = \frac{C_A M_{GT}}{C_V M_F}$ which determines the value of A_β.

$$A_\beta = -0.5707(12)_{\text{syst}}(13)_{\text{stat}}(5)_{\text{pol}},$$

where the dominant systematic is due to a small background: we apply a correction of 0.14% and assign a $\pm 0.08\%$ uncertainty to this correction. All other systematics are at or below the 0.05% level. This result is in good agreement with the standard model prediction $A_\beta^{SM} = -0.5706(7)$.

In terms of constraining physics beyond the standard model, this 0.3% measurement – with the smallest fractional uncertainty of any β-asymmetry measurement in a nucleus or the neutron – has been interpreted in two ways: to search for right-handed currents, and to improve the measurement of V_{ud} from this mirror decay. These results are shown in Fig. 2. Our results alone improve the mass limits on a new right-handed boson to be >352 GeV, a 42 GeV improvement over the previous best limit from ^{12}N and ^{107}In. In terms of CKM unitarity, our result represents a nearly $5\times$ improvement to the value of V_{ud} for ^{37}K and brings the average value from all mirror nuclei slightly more precise than that of the neutron.

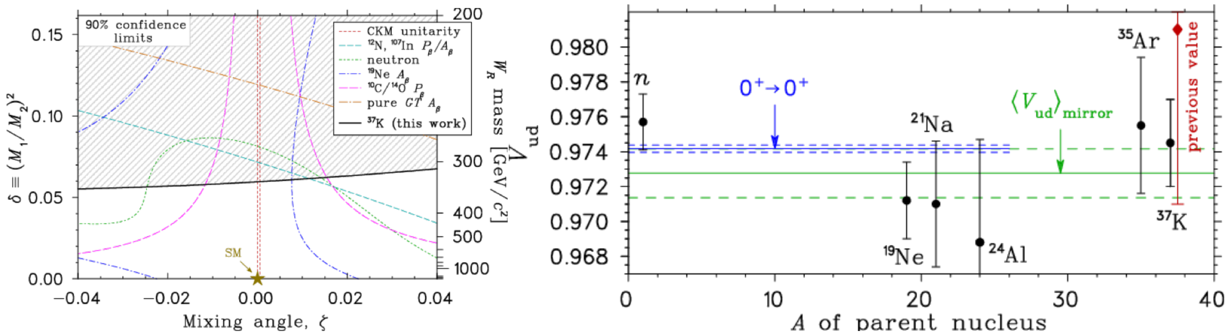

FIG. 2. Impact of the A_β measurement on physics beyond the standard model. On the left we compare our limit on right-handed current parameters to other nuclear experiments, where we provide the tightest constraint on the mass of a possible right-handed W boson, $\boldsymbol{M_W > 352\ GeV}$ at 90% confidence level. On the right, we use our present result with the *ft* value [4] to dramatically improve the value of $\boldsymbol{V_{ud}}$ for ^{37}K which, as can be seen, is now about as precise at the neutron and ^{19}Ne.

The A_β result has been submitted for publication [3] as we continue analyzing the energy-dependence to search for 2$^{\text{nd}}$-class currents and a non-zero Fierz interference parameter.

[1] D. Melconian *et al.*, *Progress in Research*, Cyclotron Institute, Texas A&M University (2016-2017) p.I-65.

[2] B. Fenker *et al.*, New J. Physics **18**, 073028 (2016).

[3] B. Fenker *et al.*, arXiv:1706.00414; Phys. Rev. Lett. (Submitted).

Clustering in ^{10}Be

S. Upadhyayula, G.V. Rogachev, E. Koshchiy, E. Uberseder, V.Z. Goldberg, J. Hooker,
H, Jayatissa, C. Hunt, and B.T. Roeder

There is a strong experimental evidence that some states in ^{10}Be exhibit molecular-like α:2n:α configuration [1,2,3]. Theoretically these exotic structures can be explored microscopically in the antisymmetrized molecular dynamics plus Hartree-Fock approach [4] or in Molecular Orbital model [5]. Based on these theoretical studies it appears that the 6.179 MeV 0^+ state in ^{10}Be has a pronounced α:2n:α configuration with an α-α inter-distance of 3.55 fm. This is 1.8 times more than the corresponding value for the ^{10}Be ground state. The 2^+ at 7.542 MeV in ^{10}Be is believed to be the next member of this rotational band [6]. The state at 10.2 MeV was identified as a 4^+ member [1, 3]. The algebraic model [7] predicts that a 6^+ state at around 13 MeV is the terminating member of this band. It would be of paramount importance to identify this 6^+ state experimentally and to conclusively establish the complete α:2n:α rotational band. This would become the most striking and well established case of molecular-like configurations in nuclei and an important step towards better understanding of clustering phenomena in atomic nuclei.

We performed an experiment to search for the 6^+ state in ^{10}Be at around 13 MeV excitation energy in the excitation function for ^{6}He+α scattering. The Cyclotron Institute Momentum Achromat Recoil Separator (MARS) facility was used to produce a secondary ^{6}He beam at 7.0 MeV/u from the production reaction of ^{7}Li(d,^{3}He). The sketch of the experimental setup is shown in Fig. 1. Modified thick target inverse kinematics approach [8] was used to measure the ^{6}He+α excitation function. Details of the experimental setup can be found in [9]. The energy of the ^{6}He beam was reduced down to 22 MeV by the thick scintillator foil located in front of the scattering chamber filled with Helium+CO_2 96:4 gas mixture at pressure of 1700 Torr.

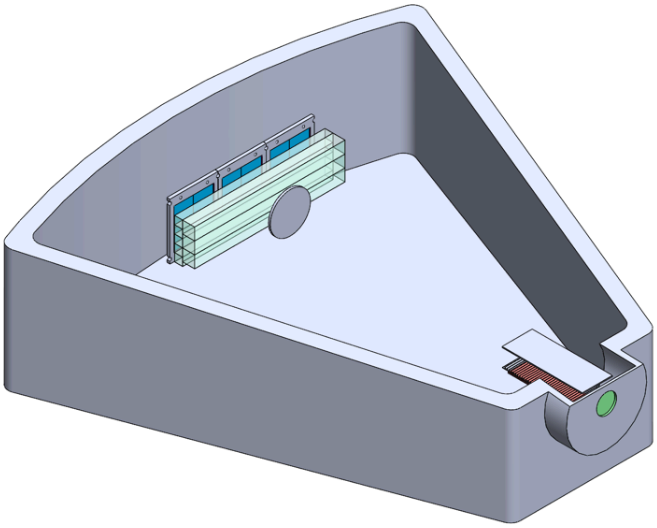

FIG. 1. Sketch of the experimental setup to measure the ^{6}He+α excitation function for resonance elastic scattering.

We have observed a distinct peak of α particles that could be a result of resonance in the ^{6}He+α excitation function which we were looking for (Fig. 2). It was verified that the peak in the α spectrum is associated with the incoming ^{6}He ions and not the other secondary beam components (the dominant of which is tritium). We expect that the highest energy α particles in the spectrum (from about 12 and 15 MeV) correspond to the pure elastic scattering. This is confirmed by sharp cut off in yield above 15 MeV (maximum energy of elastically scattered α particles). At lower energies admixtures from α particles due to inelastic scattering and breakup are possible. Based on the shape of the spectrum compared to Monte Carlo simulation (Fig. 3), the experimental yield and angular dependance of the cross section, we conclude that the α spectrum is dominated by the breakup of ^{6}He into α+2n at energies below 8 MeV.

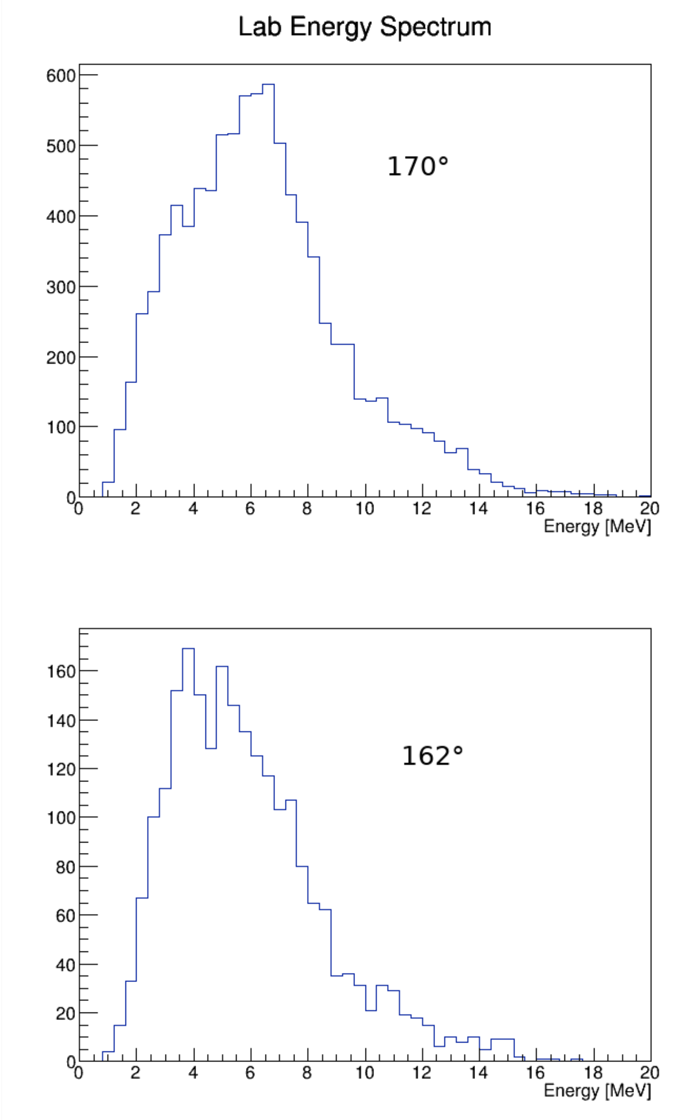

FIG. 2. Spectrum of α particles measured by the off-center Si detectors. The peak at 7 MeV is a result of ^{6}He decay into α + 2n (see text for details).

The peak in the α spectrum due to the hypothetical 6^+ state at 13.5 MeV [10] would appear in the vicinity of 10 MeV lab. energy of α-particles (Fig. 3). There is no indication for a resonance-like structure in our spectrum at that energy at any angle. The R-matrix calculations are being performed to put a qualitative limits on the existence of the hypothetical 6^+ resonance.

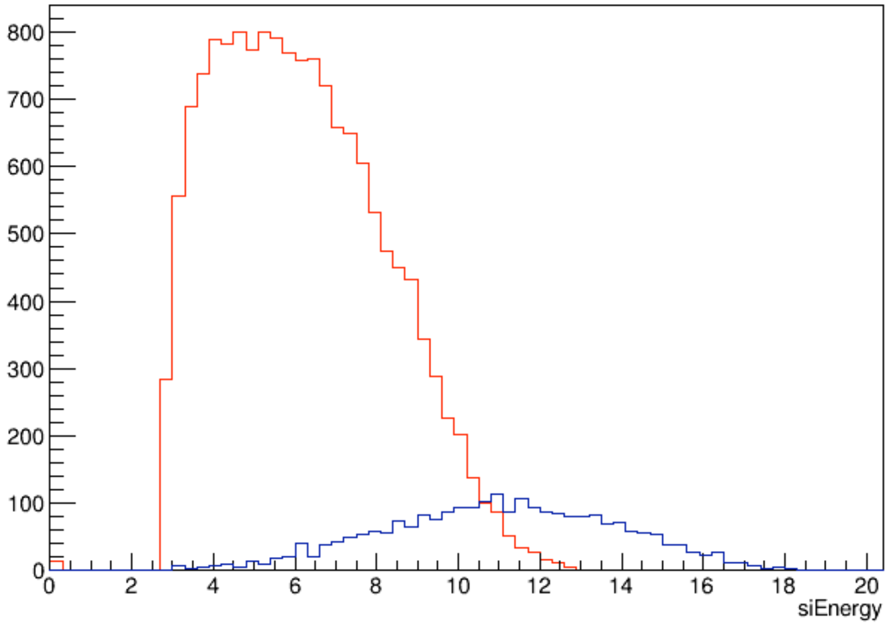

FIG. 3. Monte Carlo simulation of α particles spectrum due to breakup of ^{6}He. The (red) curve at lower energy shows α particles from ^{6}He decay. The (blue) curve at higher energy shows α particles due to inelastic scattering.

[1] M. Freer *et al.*, Phys. Rev. Lett. **96**, 042501 (2006).
[2] M. Milin *et al.*, Phys. At. Nucl. **69**, 1360 (2006).
[3] D. Suzuki *et al.*, Phys. Rev. C **87**, 054301 (2013).
[4] A. Doté, H. Horiuchi, and Y. Kanada-Enýo, Phys. Rev. C **56**, 1844 (1997).
[5] N. Itagaki and S. Okabe, Phys. Rev. C **61**, 044306 (2000).
[6] A.N. Kuchera *et al.*, Phys. Rev. C **88**, 054615 (2011).
[7] R. Wolsky *et al.*, Phys. At. Nucl. **73**, 1405 (2010).
[8] K. Artemov *et al.*, Sov. J. Nucl. Phys. **52** 408 (1990).
[9] S. Upadhyayula *et al.*, *Progress in Research*, Cyclotron Institute, Texas A&M University (2015-2016), p.I-31.
[10] D. Dell'Aquila *et al.*, Phys. Rev. C **93** 024611 (2016).

Experimental study of astrophysically important ^{22}Ne(α,n)^{25}Mg reaction via ^{22}Ne(^{6}Li,d)^{26}Mg at sub-Coulomb energies

H. Jayatissa,[1] G. V. Rogachev,[1] E. Uberseder,[1] E. Koshchiy,[1] O. Trippella,[2] J. Hooker,[1]
S. Upadhyayula,[1] C. Magana,[1] C. Hunt,[1] V. Z. Goldberg,[1] B.T. Roeder,[1] A. Saastamoinen,[1]
A. Spiridon,[1] and M. Dag[1]
[1]*Cyclotron Institute, Texas A&M University,College Station, Texas*
[2]*Department of Physics and Geology, University of Perugia, and Instituto Nationale di Fisica Nucleare, Section of Perugia, Via A. Pascoli, 06123 Perugia, Italy*

The ^{22}Ne(α.n)^{25}Mg reaction is one of the two main neutron source reactions for the slow neutron capture process (s-process) in Asymptotic Giant Branch (AGB) stars. The s-process is responsible for the formation of about half of the elements heavier than Iron [1]. The ^{22}Ne(α.n)^{25}Mg reaction is dominant for the weak component of the s-process during the helium burning and carbon-shell burning phases of an AGB star [2]. The present one-two orders of magnitude uncertainty in the ^{22}Ne(α.n)^{25}Mg reaction rate at 0.1-0.3 GK has significant implication on the final abundances of the s-process isotopes.

The direct measurement for this reaction is difficult to carry out due to its small cross section at energies relevant for nuclear astrophysics. The goal of this project is to constrain the ^{22}Ne(α.n)^{25}Mg reaction rate using α-transfer reaction ^{22}Ne(^{6}Li,d)^{26}Mg and ^{22}Ne(^{7}Li,t)^{26}Mg by measuring the partial α widths of the near α-threshold excited states in ^{26}Mg, that play a key role for the ^{22}Ne(α.n)^{25}Mg reaction. Performing the α-transfer reaction at sub-Coulomb energies for both the entrance and exit channels significantly reduces the model dependence of the extracted partial α widths

The experiment was carried out using 1.0 MeV/u ^{22}Ne beam produced by the K150 cyclotron and the Multipole-Dipole-Multipole (MDM) Spectrometer. We used a LiF target of thickness 30 ug/cm^{2} on a ^{12}C backing of thickness 10 ug/cm^{2}. The MDM Spectrometer was placed at 5^{0} from the beam axis and the magnetic field was set to measure the deuterons populating the 10.6 -11.5 MeV excitation energy range of ^{26}Mg corresponding to the Gamow energy window. These deuterons were observed using the focal plane detector (Oxford). This experiment had an energy resolution of around 100 keV.

Silicon detectors placed in the target chamber were used for monitoring the beam and for absolute normalization through the ^{6,7}Li+^{22}Ne elastic scattering. The focal plane Oxford detector was modified to measure the low energy deuterons by installing an array of 7 CsI (Tl) detectors (5x5 cm^{2} each) and removing the exit window. These modification (combined with energy losses and tracking in proportional wires of Oxford detector) allowed reliable identification of the α-transfer reaction events.

Fig. 1 shows the excitation energy spectrum for the state in ^{26}Mg populated in ^{22}Ne(^{6}Li,d)^{26}Mg reaction. The state at 11.3 MeV plays an important role for the ^{22}Ne(α.n)^{25}Mg reaction at astrophysical energies [3] and is the lowest excitation energy state that has been observed in direct ^{22}Ne(α.n)^{25}Mg measurements [3].

In order to verify that direct α transfer is the dominant reaction mechanism, two alpha-transfer reactions were carried out, the ^{22}Ne(^{6}Li,d)^{26}Mg and ^{22}Ne(^{7}Li,t)^{26}Mg. It was observed that the two reactions populate the same states and produce similar resonance strength for the populated states. The absolute normalization was performed using elastic scattering of ^{6}Li/^{7}Li by ^{22}Ne and augmented by direct measurements of the beam integral by the Faraday cup placed on the beam axis.

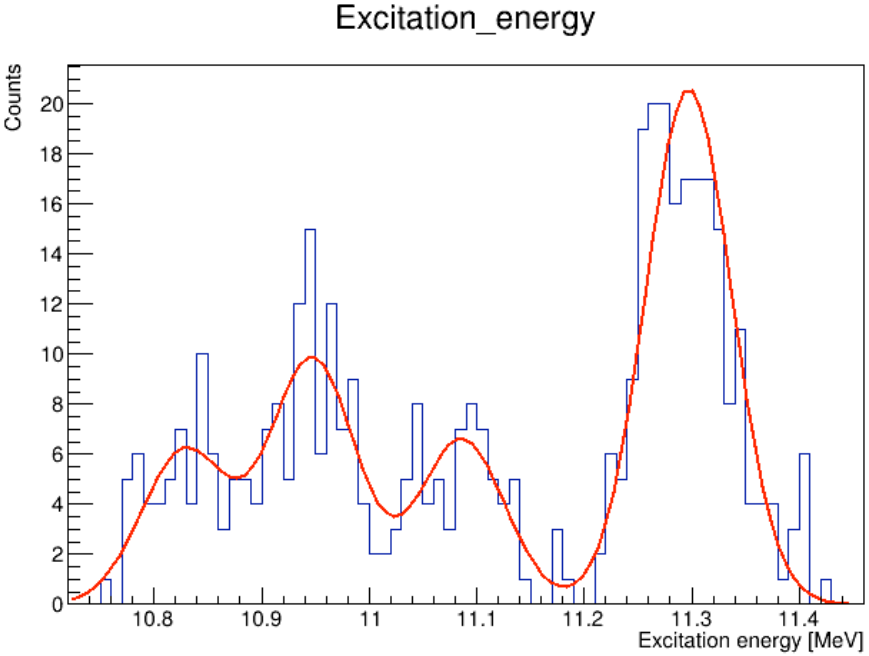

FIG. 1. Spectrum of ^{26}Mg excited states populated in ^{22}Ne(^{6}Li,d)^{26}Mg reaction.

All of the states populated in ^{22}Ne(^{6}Li,d)^{26}Mg reaction have been observed before [3,4,5]. However, there is no definitive spin-parity assignments for any of them. We assumed spin-parities of 0^{+}, 1^{-} and 2^{+} in order to evaluate an impact on the astrophysical reaction rate. It was observed that the upper and lower bounds for the reaction rate was obtained when a 0^{+} and 2^{+} assignment was given for all the resonances respectively. Even the upper limit that follows from our measurements is substantially below the ^{22}Ne(α.n)^{25}Mg reaction rate suggested in [4]. This is mostly because we do not see the strong resonance at 11.17 MeV observed in [4], indicating that this is most likely the high spin state that is readily populated at high energy [4], but cannot be populated at sub-Coulomb energy. The high spin state cannot have any significant impact on the reaction rate due to small penetrability factors. Fig. 2 demonstrates an impact of the lower ^{22}Ne(α.n)^{25}Mg reaction rate on the production of the isotopes formed by the s-process. The calculations were made using code NEWTON (Nucleosynthesis of Elements With Transfer Of Neutrons) for a stellar model of 1.5 solar mass and solar metallicity (low temperature and low neutron density). While these results are still preliminary, we believe that the presently accepted ^{22}Ne(α.n)^{25}Mg reaction rate is too high and reduction of this rated based on the results of the measurements described in this report has significant consequences on the final outcome of the s-process abundancies.

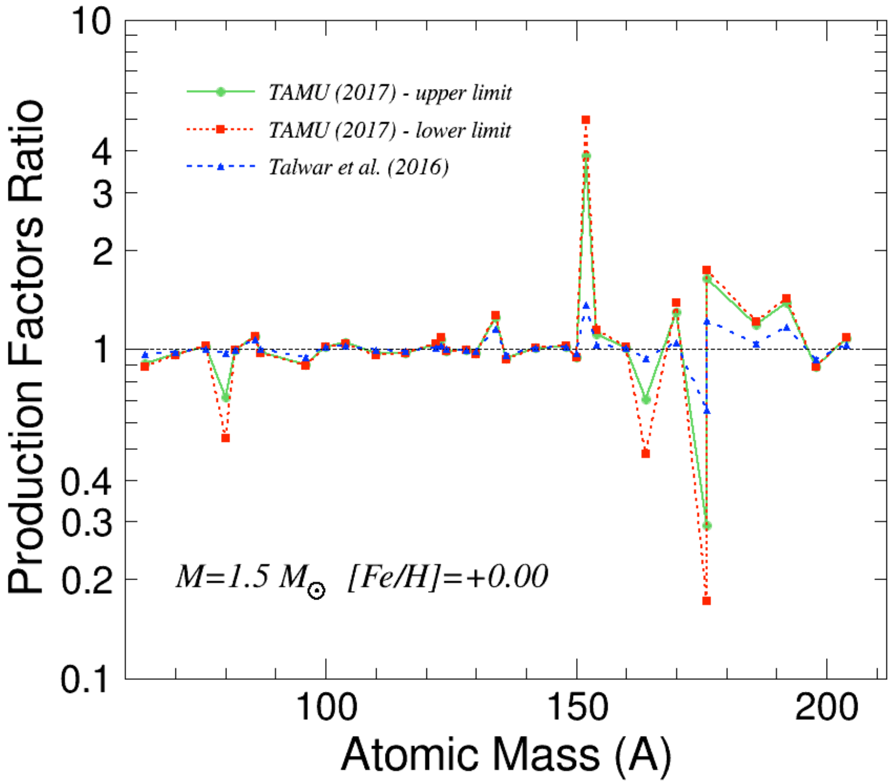

FIG. 2. The production factor for s-process only isotopes for the rates from the present work and of Talwar et. al [4] as a ratio to the production factors calculated using reaction rates of [2] for a stellar model of 1.5 solar mass and solar metallicity.

[1] M. Jaeger *et al.*, Phys. Rev. Lett. **87**, 202501 (2001).

[2] F. Kappeler *et al.*, Rev. Mod. Phys. **83**, 157 (2011).

[3] M. Jaeger *et al.*, Phys. Rev. Lett. **87**, 202501 (2001).

[4] R. Talwar *et al.*, Phys. Rev. C **93**, 055803 (2016).

[5] U. Giesen *et al.*, Nucl. Phys **A561**, 95 (1993).

Structure of ^{10}N via ^{9}C+p resonance scattering

J. Hooker, G.V. Rogachev, V.Z. Goldberg, E. Koshchiy, B.T. Roeder, H. Jayatissa, C. Hunt, C. Magana, S. Upadhyayula, E. Uberseder, and A. Saastamoinen

The new capabilities of rare isotope beams allowed the discovery of unusually large matter radii in some exotic nuclei by Tanihata, et al. [1]. The most famous example is ^{11}Li which has a nuclear matter root mean square radius as large as that of ^{208}Pb. This is due to the two- neutron halo of ^{11}Li where the wave function of two valence neutrons extends far beyond the ^{9}Li core. Important role in explaining the halo structure of ^{11}Li was played by three-particle models that describe ^{11}Li as a ^{9}Li-n-n system. These models rely on accurate knowledge of neutron-^{9}Li interaction, that can be established from the known states in ^{10}Li. However, in spite of much effort (see [2-9] and references therein), uncertainty in spin-parity assignments and excitation energies of some low-lying states in ^{10}Li still remains. Even less is known about the mirror nucleus ^{10}N. Only one experiment that claimed observation of the ground state of ^{10}N has been done. A broad resonance at 2.6(4) MeV with a width of 2.3(16) MeV was reported in ^{10}B(^{14}N,^{14}B)^{10}N reaction with rather low statistical significance [10]. The goal of this work is to provide a spin-parity assignment for the ground state and search for the excited states in this exotic, unbound nitrogen isotope - ^{10}N.

States in ^{10}N, including the ground state, were populated in resonance elastic scattering of ^{9}C on protons. The rare isotope beam of ^{9}C was produced by recoil spectrometer MARS using ^{10}B(p,2n) reaction. The TexAT-P1 time projection chamber (TPC) was placed at the end of the MARS beam line. The protons from ^{9}C+p elastic scattering events were identified using energy losses and energies in the TPC and array of Si detectors, assisted by tracking in TPC. A more detailed description of the experimental setup and the analysis procedures can be found in [11,12,13].

The excitation function for ^{9}C+p resonance scattering is shown in Fig. 1 [13]. The scattering angle is a function of excitation energy, the smallest angle (139^{o}) corresponds to the lowest energies. The excitation function has a sharp low energy rise vs. the Rutherford scattering shown as the red dash-dotted line in Fig. 1. This is characteristic for L=0 resonance(s). R-matrix analysis leads to the following conclusions. In order to reproduced the excitation function, it is necessary to add a 2^- L=0 ground state (g.s.) at 2.2 MeV and a 1^- L=0 state at 2.8 MeV. The corresponding fit is shown as the blue dashed line in Fig 1. It is also possible to fit the excitation function with a 1^- L=0 ground state at 1.9 MeV and a 2^- L=0 first excited state at 2.8 MeV (the green solid line in Fig. 1). The two fits are statistically identical. There is no conclusive evidence for any L=1 state(s) in the measured excitation function. However, an L=1 state placed at 3.3 MeV does not contradict the experimental data (the black dash-dotted line in Fig. 1). This location for the first L=1 state in ^{10}N was chosen since the most recent measurement on ^{10}Li observed a p-wave state at 0.45(3) MeV above the neutron threshold and a width of 680(30) keV [9]. This corresponds to 3.3 MeV above the proton threshold in ^{10}N.

The main result of this work is the first conclusive observation of ^{10}N – discovery of a new, most proton rich isotope of Nitrogen. The energy of the 2s shell in ^{10}N was measured to be 2.3 ± 0.2 MeV above the proton threshold in ^{10}N. We used simple potential model to calculate Thomas-Ehrman shift between ^{10}N-^{10}Li mirror pair and determined that the ^{10}Li ground state has to be the 2s shell state

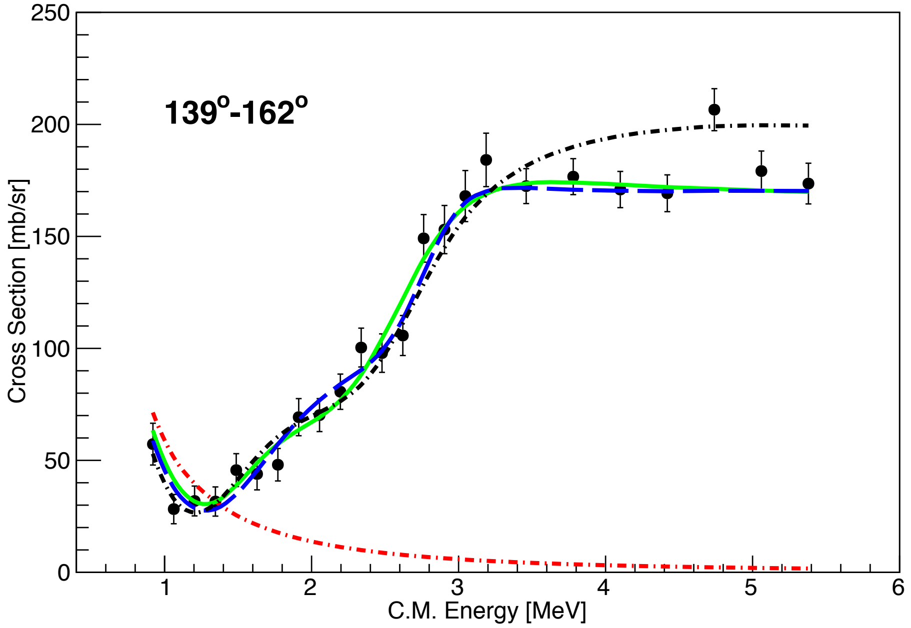

FIG. 1. Spectrum of protons from the ^{9}C+p resonance scattering. The red dash-dotted line is the Rutherford scattering cross-section, the blue dashed line is the best fit with the 2^- as the g.s. and a 1^- state as the 1st excited state. The green solid line is the best fit with a 1^- g.s. and 2^- 1st excited state. The black dash-dotted curve is the fit with a 2^- g.s., a 1^- 1st excited state and a 1^+ state at 3.3. MeV.

somewhere between 0 and 100 keV. This is consistent with breakup measurements [14]. Definitive spin-parity assignment (2^- or 1^-) for the ^{10}N ground state cannot be made solely on the basis of this experimental data. We also see no evidence for any L=1 state(s) in ^{10}N but cannot rule out existence of broad L=1 states at 3.3 MeV and above with respect to the proton decay threshold. We have also shown that the ^{10}Li ground state must be an L=0 state. These results are published in [13]

[1] I. Tanihata, H. Hamagaki, O. Hashimoto *et al.*, Phys. Rev. Lett. **55**, 2676 (1985).

[2] H.G. Bohlen, B. Gebauer, M. von Lucke-Petsch *et al.*, Z. Phys. A **344**, 381 (1993).

[3] B.M. Young, W. Benenson, J.H. Kelley *et al.*, Phys.Rev. C **49**, 279 (1994).

[4] M. Zinser, F. Humbert, T. Nilsson *et al.*, Phys. Rev. Lett. **75**, 1719 (1995).

[5] J.A. Caggiano, D. Bazin, W. Benenson *et al.*, Phys. Rev. C **60**, 064322 (1999).

[6] P. Santi, J.J. Kolata, V. Guimaraes *et al.*, Phys. Rev. C **67**, 024606 (2003).

[7] H. Jeppesen, F. Ames, U.C. Bergmann *et al.*, Nucl. Phys. **A738**, 511 (2004).

[8] B.A. Chernyshev, Yu.B. Gurov, V.S. Karpukhin *et al.*, Eur. Phys. J. A **49**, 68 (2013).

[9] M. Cavallero, *et al.*, Phys. Rev. Lett. **118**, 012701 (2017).

[10] A. Lepine-Szily, J.M. Oliveira, V.R. Vanin *et al.*, Phys. Rev. C **65**, 054318 (2002).

[11] G.V. Rogachev, J. Hooker *et al.*, *Progress in Research*, Cyclotron Institute, Texas A&M University (2014-2015), p. I-22.

[12] J. Hooker, G.V. Rogachev *et al.*, *Progress in Research*, Cyclotron Institute, Texas A&M University (2015-2016), p. I-38.

[13] J. Hooker, G.V. Rogachev *et al.*, Phys. Lett. B **769**, 62 (2017).

[14] H. Simon *et al.*, Nucl. Phys. **A791**, 267 (2007).

Structure of ^{20}Ne states in resonance ^{16}O+ α elastic scattering

V.Z. Goldberg, G.V. Rogachev, A.Volya,[1] D.K. Nauruzbayev,[2,4] A.K. Nurmukhanbetova,[2]
and M.S. Golovkov[3]
[1]*Department of Physics, Florida State University, Tallahassee, Florida*
[2]*National Laboratory Astana, Nazarbayev University, Astana, 010000, Kazakhstan*
[3]*Joint Institute of Nuclear Research, Dubna, Russian*
[4]*Saint Petersburg State University, Saint Petersburg, Russia*

^{20}Ne nucleus presents a famous example of the manifestation of the alpha-cluster structure, and therefore it makes this nucleus a touchstone for ab initio approaches [1]. The nucleus ^{20}Ne is also a benchmark case for the traditional shell model and its extension into algebraic and clustering domains. The well-established effective interaction Hamiltonians such as [2] not only shows an outstanding agreement with experimental data for *sd*-shell nuclei but also generates configuration mixing that shows transition to deformation and clustering.

The experimental aim of this work is to obtain new information on the structure of ^{20}Ne states, especially the broad 0^+, 2^+ states. Unlike other experimentalists, we used the Thick Target Inverse Kinematics method (TTIK) (see [3,4] and references therein) to study the excitation functions for the ^{16}O(α,α) ^{16}O elastic scattering in the ^{20}Ne excitation region of 5.5-9.6 MeV and in a broad angular

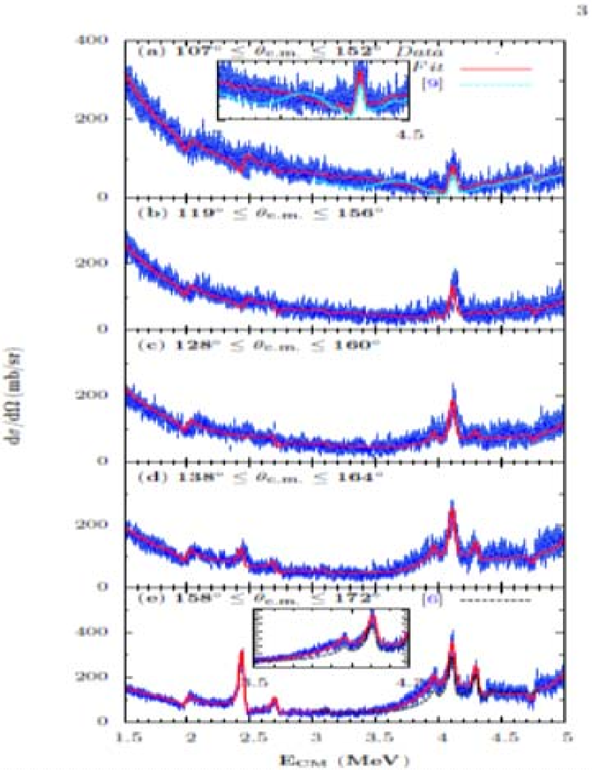

FIG. 1. Excitation functions for the ^{16}O(α,α) ^{16}O elastic scattering together with *R*-matrix fit and different parameters of the broad states.

interval. On the theoretical side, we also used a cluster-nucleon configuration interaction model (CNCIM) calculation to understand the limits of this approach in a description of the cluster states.

Fig.1 presents the excitation functions for the $^{16}O(\alpha,\alpha)\,^{16}O$ elastic scattering measured at DC-60 heavy ion cyclotron in Astana (Kazakhstan). Table I gives the resonance parameters obtained in this work using R-matrix fit in comparison with the available data and predictions of CNCIM.

Table I. ^{20}Ne levels.

N	**TUNL data** [6]			**H. Cheng** [5]		**This work**			**CNCIM**			
	E_x, (MeV)	J^π	Γ_α (keV)	E_x, (MeV)	Γ_α (keV)	E_x, (MeV)	Γ_α (keV)	γ_α	E_x (MeV)	J^π	SF_p.	SF_α
1	0	0^+_1		-	-	0	Large		0	0^+	0.36	0.73
2	1.63	2^+_1		-	-	1.63	Large		2.242	2^+	0.41	0.67
3	4.25	4^+_1		-	-	4.25	Large		4.58	4^+		0.62
4	5.78	1^-	$(28\pm3)\mathrm{x}\,10^{-3}$	-	-	4.45	0,03	1.4				
5	6.73	0^+_2	19±0.9	6.72	11	6.78	20.6	0.47	6.94	0^+_3	0.55	0.46
6	7.16	3^-	8.2±0.3	7.16	10	7.18	8.3	1.37				
7	7.19	0^+_3	3.4±0.2	7.19	5	7.20	3	0.019	6.27**	0^+_2	0.055	0.44**
8	7.42	2^+_2	15.1±0.7	7.43	7	7.44	14.3	0.19	7.39	2^+_3	0.01	0.12
9	7.83	2^+_3	2	7.83	1	***7.85***	***3.68***	0.01	7.15**	2^+_2	0.12	0.18**
10	8.45	5^-	0.013±0.004	8.45	0.02	8.45	0.013					
11	8.71	1^-	2.1±0.8			8.71	3.5					
12	***≈8.7***	***0^+_4***	***>800***	***8.62***	***1470***	***8.77±0.150***	***750±220***	~0.25	9.66**	***0+***$_4$	0.002	0.18**
13	8.78	6^+_1	0.11±0.02	-	-	8.78	0.14	0.5	9.49	6^+		0.51
14	8.85	1^-	19	8.84	27	8.85	18.0					
15	***9.00***	***2^+_4***	***≈800***	***8.87***	***1250***	***8.79±0.100***	***695±120***	0.86	8.36	***2^+_4***	0.02	0.02*
16	9.03	4^+_3	3	9.02		9.03	1.9	0.03	9.0	4^+		0.09
17	9.12	3^-	3.2	9.09	4	9.13	4.1					
18	9.19	2^+		-	-	(9.29)	≤10					
19	9.48	2^+	29±15	9.48	46	9.48	65±20	0.02?				
20	9.99	4^+_4	155±30	10,02	150	9.97	157	0.38	9.5	4^+		0.009
21*	10.26	5^-	145±40	10.26	190	10.26		1.9				
22	10.41	3^-	80	10.40	101	10.41						
23	10.58	2^+	24	10,56	15	10.58			10.2	***2^+***	0.005	0.04
24	10.80	4^+_4	350	10,75	400	10.80			10.7	4^+		0.04
25	10.97	0^+_5	580	10,99	700	10.97			11.9	0^+		
26	***11.24***	***1^-***	***175***	***11.19***	***85***	***11.24***						
27	11.95	8^+				11.95		0,35	11.50			0.40

*For the levels with numbers 21-27 the parameters of the present fit were fixed as in [6]

** Calculated in *psd* space. SF is to the first excited state in ^{16}O; SFs for the ground state in ^{16}O are ≤0.1

There is good overall agreement between theoretically predicted and observed spectra. Our theoretical approach describes very well the ground state band and the band built on the first 0^+ state.

Allowing cross shell excitations from the p-shell, it was possible to reproduce the band built on the second 0^+ state. For these states, all spectroscopic factors for alpha transitions to the ground state of ^{16}O and to the first excited state in ^{16}O as well as proton spectroscopic factors to the ground state of ^{19}F are well reproduced. The situation is not as good when it comes to resonances 1^- 3^- and 4th 0^+ and 4th 2^+, all of these states are broad and have exceptionally large alpha spectroscopic factors. Thus, inability of theoretical models to describe broad states exclusively while working well elsewhere suggests an additional coupling mechanism unaccounted for in the traditional shell model Hamiltonians.

This work was supported by Ministry of Education and Science of the Republic of Kazakhstan [grant number #0115PK03029 "NU-Berkeley", 2014-2018; grant number# 0115PK022465, 2015-2017]). This material is also based upon work supported by the U.S. Department of Energy Office of Science, Office of Nuclear Physics under Grant No. DE-SC0009883.

[1] G.R. Jansen *et al.,* Phys. Rev. C **94**, 11301 (2016).
[2] B.A. Brown and W.A. Richter, Phys. Rev. C **74**, 34315 (2006).
[3] K.P. Artemov *et al.*, Sov. J. Nucl. Phys. **52**, 408 (1990).
[4] G.V. Rogachev *et al.*, AIP Conference Proceedings **1213**, 137 (2010).
[5] H. Cheng *et al.*, Nucl. Instrum. Methods Phys. Res. **B85**, 47 (1994).
[6] D.R. Tilley *et al.*, Nucl. Phys. **A636**, 249 (1998).

T=3/2 isobaric analog states in ^{9}Be

C. Hunt, G.V. Rogachev, S. Almaraz-Calderon,[1] A. Aprahamian,[1] B. Bucher,[1] W. Tan,[1]
E.D. Johnson,[2] J. P. Mitchell,[2] M. Avila,[2] A. Kuchera,[2] and L.T. Baby[2]
[1]*Nuclear Science Laboratory, University of Notre Dame, Notre Dame, Indiana*
[2]*Department of Physics, Florida State University, Tallahassee, Florida*

The Thick Target and Inverse Kinematics (TTIK) approach [1] has been applied extensively to study the structure of exotic, proton rich nuclei [2,3]. The key advantages of TTIK, such as high efficiency, excellent energy resolution and well developed theoretical tools for analysis (R-matrix formalism) make it very attractive for such studies. It also inspires the application of this approach for neutron rich nuclei. Of course, direct implementation of TTIK for the neutron rich case would require neutron resonance scattering with radioactive beams though this is not possible at present. Instead, it has been suggested [4] to study neutron rich nuclei using TTIK through the corresponding isobaric analog states (IAS) populated in proton resonance scattering. The idea is 20 years old, but only few experiments have been performed. Specifically, structure of ^{9}He [5,6] and ^{13}B [7] have been studied through the corresponding IAS in ^{9}Li and ^{13}C populated in ^{8}He+p and ^{12}B+p resonance scattering. The progress is likely limited by complexities in R-matrix analysis, associated with the high density of T_{low} states. The main goal of this experiment is to benchmark the application of the TTIK technique for studies of neutron rich nuclei. The A=9 T=3/2 isobaric multiplet provides an ideal opportunity. Experimental data on proton resonances in ^{9}C and on structure of low lying states in ^{9}Li are available [8,9]. Therefore, direct comparison between ^{9}C, ^{9}Li and new data on T=3/2 states in ^{9}Be, populated using ^{8}Li+p resonance scattering is possible. The main goal of this experiment was to measure the excitation function for ^{8}Li+p resonance elastic scattering and compare the results to the available data for ^{9}C and ^{9}Li to benchmark the IAS TTIK method. Another goal was to locate the positive parity states (none are known in A=9 T=3/2 isobaric multiplet) to shed light on energy of the sd-shell in these nuclei.

The experiment was carried out at Florida State University using the RESOLUT radioactive beam facility. The ^{8}Li beam was produced using the ^{7}Li(d,p) reaction in a 4-cm long deuterium gas cell. The secondary beam ^{8}Li was momentum selected, bunched and separated from other contaminants by RESOLUT. The typical composition of the beam at the secondary polyethylene (C_2H_4) target was 95% of ^{8}Li and 5% of ^{7}Li. Three different target thicknesses were used, 5.5, 4.1, 2.8 mg/cm^2 with three ^{8}Li beam energies 25.0, 22.0 and 18.0 MeV.

The experimental setup is shown in Fig. 1. Three annular position sensitive detectors (S2, MicronSemiconductors) were used to detect the light and heavy recoils (eg., protons and ^{8}Li for elastic scattering) in coincidence. The kinematically complete measurement allowed for the unambiguous identification of the reaction and also made it possible to use the relatively thick target to simultaneously measure a significant energy region of the excitation function while still having excellent energy resolution (30 keV in c.m.).

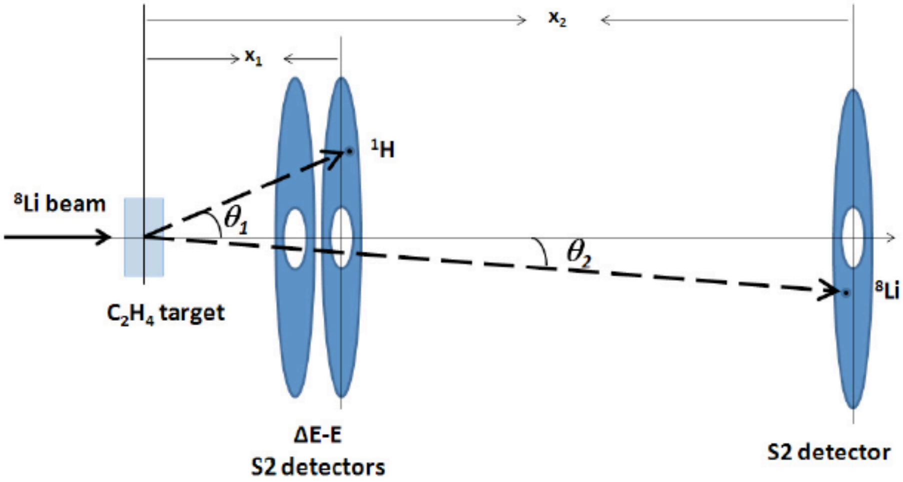

FIG. 1. The experimental set-up that include the thick target, dE detector and the light and heavy recoil detectors. Protons and ^{8}Li are measured in coincidence.

The excitation functions for ^{8}Li+p elastic scattering at different angles were reconstructed from measurements at the three beam energies. The 171° excitation function is shown in Fig. 2. An interesting feature of the measured excitation function is that it can be described very well by a single well known 5/2- T=3/2 state at 18.6 MeV in ^{9}Be (solid curve). The total width, and excitation energy for this state are taken from [10] and the ratio of the partial neutron to proton widths are determined using isospin Clebsch-Gordon coefficients and the corresponding penetrability factors. The best fit in Fig. 2 is achieved by varying the parameters of the optical model that is incorporated into the R-matrix formalism in the same way as suggested in [11] and is used to describe the statistical contribution of the T=1/2 states. The 5/2-

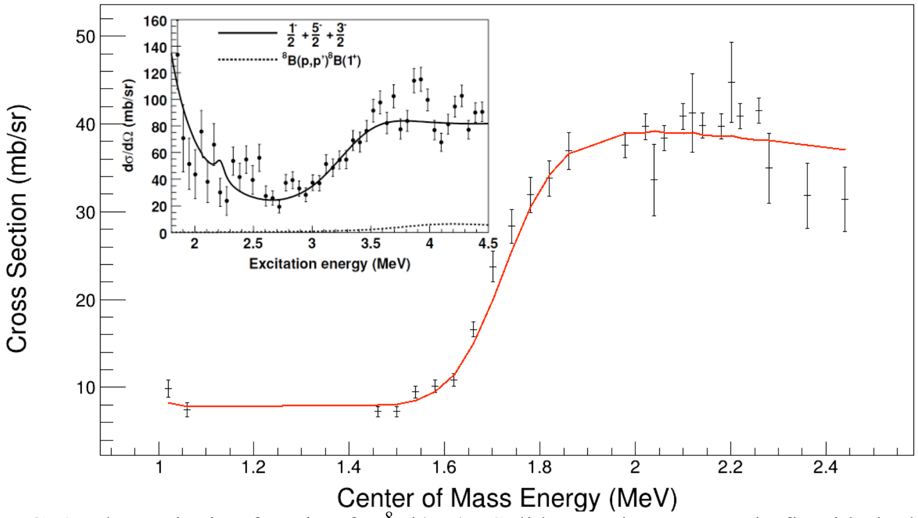

FIG. 2. The excitation function for ^{8}Li(p,p). Solid curve is an R-matrix fit with the known T=3/2 18.65 MeV, 5/2- excited state. Inset is the excitation function of ^{8}B(p,p) from [2].

state is also known to dominate the ^{8}B+p excitation function for resonance elastic scattering [8] which also has almost identical shape to the ^{8}Li+p excitation function (see inset in Fig. 2). This almost one-to-one correspondence provides a strong support for the IAS TTIK approach. It has to be noted, however, that the fit has strong dependence on the parameters of the optical potential and finding reliable and reproducible ways of constraining that potential is of paramount importance for future applications of this experimental technique.

[1] K.P. Artemov *et al.*, Sov. J. Nucl. Phys. **52**, 634 (1990).
[2] L. Axelson *et al.*, Phys. Rev. C **54**, R1511 (1996).
[3] J. Hooker *et al.*, Phys. Lett. B **769**, 62 (2017).
[4] V.Z. Goldberg, AIP Conference Proceedings **455**, 319 (1998).
[5] G.V. Rogachev *et al.*, Phys. Rev. C **67**, 041603 (2003).
[6] E. Uberseder *et al.*, Phys. Lett. B **754**, 323 (2016).
[7] B.B. Skorodumov *et al.*, Phys. Rev. C **78**, 044603 (2008).
[8] G.V. Rogachev *et al.*, Phys. Rev. C **75**, 014603 (2007).
[9] A.H. Wuosmaa *et al.*, Phys. Rev. Lett. **94**, 082502 (2005).
[10] D.R. Tilley *et. al.*, Nucl. Phys. **A745**, 155 (2004).
[11] D. Robson, Phys. Rev. **137**, 535 (1965).

Modification of the STAR FMS trigger for Drell-Yan detection

J.R. Pybus, Z. Chang, and C.A. Gagliardi and the STAR Collaboration

One of the STAR headline measurements during the 2017 RHIC run is the transverse single-spin asymmetry, A_N, for forward rapidity Drell-Yan di-electron production. It will test the prediction that measurements of the Sivers effect, a correlation between the spin of a proton and the transverse momentum of a quark or gluon within the proton, have opposite signs in Drell-Yan production and semi-inclusive deep-inelastic scattering. This sign change arises because the Sivers effect originates as a repulsive initial-state interaction in Drell-Yan production vs. an attractive final-state interaction in SIDIS. The STAR Drell-Yan measurement will sample the same quark x range, but very different Q^2, as sampled by complementary measurements of W and Z boson A_N that STAR is performing concurrently. In turn, these measurements will also provide crucial information necessary to quantify QCD evolution effects in transverse momentum dependent (TMD) distributions.

During the summer of 2016, we studied the trigger system of the STAR Forward Meson Spectrometer (FMS) to optimize the Drell-Yan detection capability. A large number of Drell-Yan di-electron events were simulated using PYTHIA, and cuts were made to restrict events to those where both the electron and the positron strike the FMS with $p_T > 1.0$ GeV/c. A model of the trigger system was used to identify those simulated events that satisfy the trigger requirements. We found that the existing FMS di-electron trigger had an efficiency of 86% and a spin-dependent Figure-of-Merit of 78.5% for Drell-Yan detection. A detailed investigation found that the reduced Figure-of-Merit arose because the trigger logic provided very good efficiency for Drell-Yan di-electrons with pair transverse momenta up or down, parallel or anti-parallel to the spin direction, but lower efficiency for pair transverse momenta perpendicular to the spin direction.

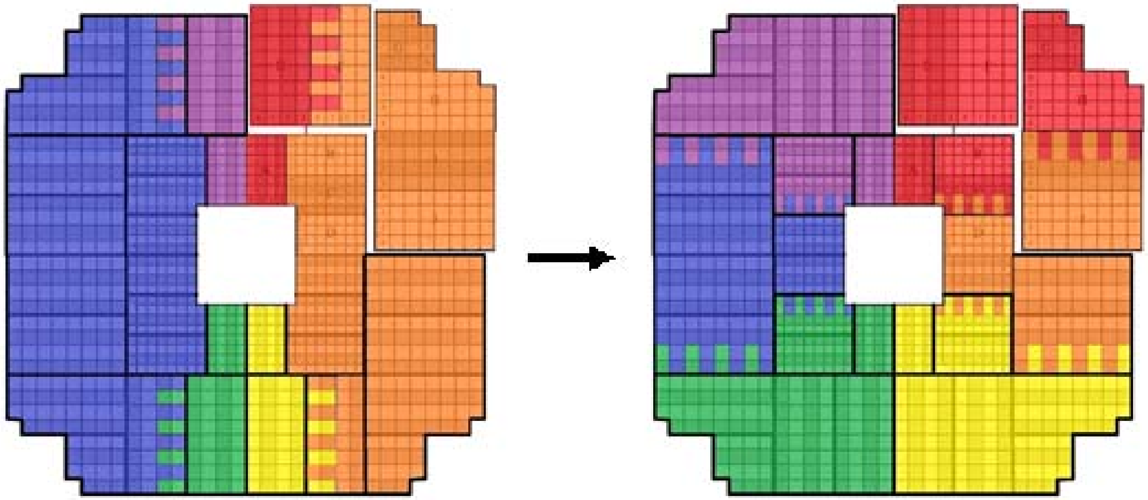

FIG. 1. The left panel shows the original FMS Drell-Yan trigger layout. The right panel shows the revised layout. In both cases, simultaneous hits on non-adjacent colored sections activate the trigger. Hatched sections are shared between sections.

Modifications were made to the trigger layout (Fig. 1) and the altered layout was used to analyze the same PYTHIA events. The modified layout was determined to have an efficiency of 94% and a Figure-of-Merit of 93.6% for Drell-Yan detection. The angular distribution of accepted events for each trigger layout can be seen in Fig. 2. The effects of the modification were also tested on similarly generated J/ψ events. The J/ψ efficiency was determined to increase from 76% to 86% and the Figure-of-Merit was determined to increase from 63% to 84%. Our proposed changes to the trigger logic were approved by the FMS group and adopted for the 2017 run of STAR.

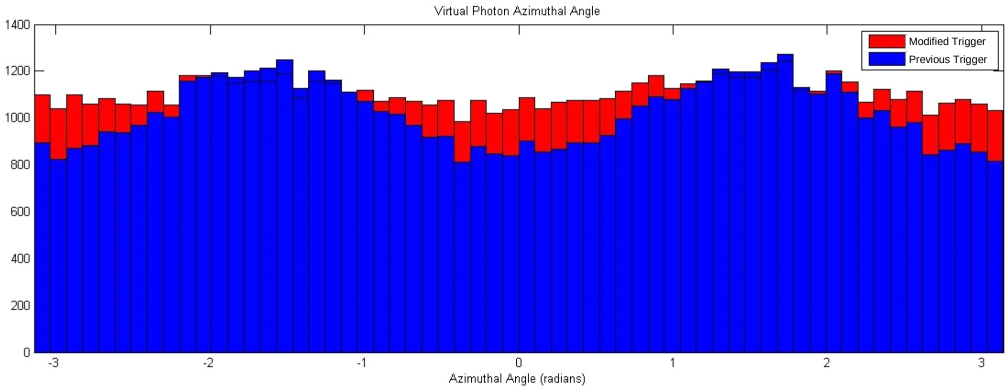

FIG. 2. Comparison of Drell-Yan accepted event angular distribution for each trigger when the p_T-threshold for individual electrons is 1.0 GeV/c.

The p_T-threshold for the individual electrons was initially intended to be set to 1.0 GeV/*c*. However, it was determined early in the run that the corresponding data rates were higher than acceptable. We reanalyzed the PYTHIA samples using different p_T-thresholds. The resulting Figures-of-Merit are given in Table I. Approximately 2/3 of the 2017 Drell-Yan data was recorded with the threshold at 1.3 GeV/*c*. This provided a compromise between sampling a large fraction of the delivered luminosity and concurrent acceptance for J/ψ. The J/ψ cross section is much larger than that for Drell-Yan. So for the final 1/3 of the 2017 run, the threshold was raised to 1.4 GeV/*c*, which allowed the Drell-Yan trigger to sample the full delivered luminosity while sacrificing the ability to collect additional J/ψ data efficiently.

Table I. Figures-of-Merit as a function of the electron trigger threshold.

p_T Threshold (GeV/c)	Drell-Yan Figure-of-Merit	J/ψ Figure-of-Merit
1.0	94%	85%
1.3	82%	42%
1.4	78%	29%

Spin physics with STAR at RHIC

Z. Chang, C.A. Gagliardi, R.E. Tribble, and the STAR Collaboration

Our group continues to play major roles in STAR investigations of both longitudinal and transverse spin phenomena in polarized *pp* collisions at RHIC. A major goal of the RHIC spin program is to determine the gluon polarization in the proton over a wide range of momentum fraction x. The longitudinal double-spin asymmetry, A_{LL}, for inclusive jet production is an ideal tool in this effort because the cross section is large and dominated by quark-gluon and gluon-gluon scattering processes, both of which have large partonic asymmetries.

For the past several years, we have been working on the analysis of A_{LL} for inclusive jets at $\sqrt{s}$ = 510 GeV, based on data that STAR recorded during 2012. In last year's *Progress in Research*, we described the improvements that we had developed in jet reconstruction, notably including an underlying event subtraction procedure. We also described the development of a new PYTHIA tune that provides a much better reproduction of jet data at RHIC energies.

During the past year, we performed the companion Monte Carlo analyses that were needed to estimate the corrections for the jet energy scale distortions and trigger and reconstruction bias, together with the corresponding systematic uncertainties. We found that the underlying event subtraction provided a much better match between jets observed in the detector and the parent hard-scattered parton jets of interest to determine the gluon polarization. We also developed new procedures to estimate the trigger and reconstruction bias and the PYTHIA tune uncertainties. In both cases, the new procedures led to substantially smaller systematic uncertainties than we would have obtained if we had used our previous procedures.

We have now completed the analysis of the 2012 data. Overall, our new analysis procedures reduce the systematic uncertainties by factors of 2~3 compared to those with our previous methodology. The new results are in very good agreement with the predictions from DSSV'14 [1] and NNPDFpol1.1 [2]. They also extend the range of x_T (= 2 $p_T/\sqrt{s}$) down to 0.026, compared to x_T = 0.056 for the 2009 measurements at 200 GeV [3]. We have not performed a full reweighting of either DSSV'14 or NNPDFpol1.1 to assess the impact of the new 2012 results. However, extrapolating from a reweighting of NNPDFpol1.1 to factor in other recent data [4], we expect the new results will provide a sizable reduction in the uncertainty in the gluon polarization uncertainty in the region $0.02 < x < 0.1$.

At present, we are writing the final article describing the 2012 inclusive jet analysis and results. We are combining the 2012 inclusive jet analysis that we've performed at Texas A&M together with the companion di-jet A_{LL} analysis of the same data set that is currently being finalized by collaborators at the University of Kentucky. We hope to submit the article for publication before the end of this year.

[1] D. DeFlorian *et al.*, Phys. Rev. Lett. **113**, 012001 (2014).

[2] E.R. Nocera *et al.* (NNPDF Collaboration), Nucl. Phys. B **887**, 276 (2014).

[3] STAR Collaboration, Phys. Rev. Lett. **115**, 092002 (2015).

[4] E.R. Nocera, arXiv:1702.05077

SECTION II

HEAVY ION REACTIONS

HIPSE calculations of alpha conjugate systems in the reactions of 35 MeV/u Si + C and implications in the search for toroidal configurations

X.G. Cao, K. Schmidt, K. Hagel, S. Wuenschel, E.J. Kim, M. Barbui, J.B. Natowitz, H. Zheng, N. Blando, A. Bonasera, G. Giuliani, M. Rodrigues, R. Wada, M. Huang, C. Botosso, G. Liu, G. Viesti, S. Moretto, G. Prete, S. Pesente, D. Fabris, Y. El Masri, T. Keutgen, S. Kowalski, Z. Kohley, and A. Kumar

We have continued the analysis of the alpha conjugate systems that were studied with NIMROD and reported previously [1-6]. In a previous report we discussed the idea that heavy ion collisions induced by light α-conjugate nuclei may provide conditions to access toroidal isomers with high excitation energies and angular momentum [7]. Peaks in the excitation energy distributions near those predicted by Staszczak, and Wong [8] for high spin isomers of the different decay channels led us to the idea that the decay of toroidal isomers might be a component of those excitation energy distributions.

In order to ascertain whether peaks in excitation energy distributions may result from toroidal configurations predicted by Staszczak, and Wong [8], we have compared events generated by HIPSE [9] calculations to the experimental data. The HIPSE (heavy-ion phase-space exploration) calculation proceeds first by describing the approaching phase of the collision, then the partition formation phase and finally the exit channel and after-burner phase. The first two phases are performed with the HIPSE code and the last phase is accomplished using the evaporation code GEMINI [10]. In particular, HIPSE with an afterburner has been shown to provide a good simulation of the energy and particle distributions in intermediate heavy-ion reactions [9]. It does not have a component of the decay of high spin toroidal isomers, so comparisons of the model calculations to the experimental data can show whether observed peaks are the result of experimental acceptance or perhaps phenomena not included in the calculation.

In Fig. 1 we show excitation energy distributions of events where 7 alpha particles are detected and the detected alpha like mass (Almass) is 28, ie a ^{28}Si nucleus. The solid points in figure 1 show the excitation energy distributions of 7α events with cuts in delta and distance, d, as described in [7]. The red arrow shows the position of 143 MeV, the excitation energy predicted for a toroidal configuration of ^{28}Si. As noted in [7], we observe an enhancement in the data in the region of this prediction.

We have performed calculations using the HIPSE code. HIPSE was used to generate the primary distributions as described briefly above and in [9] and GEMINI [10] was used as an afterburner in order to compare the calculations to the experimental data. The events in which the products had and alpha-like mass (Almass) = 28 before being filtered are shown as the red histogram in Fig. 1. It is clear that HIPSE does not generate the peaks at 143 MeV that are observed in the experiment.

As we note that HIPSE does not generate a peak observed at 143 MeV for the 7α events, we are in the process of filtering the HIPSE-GEMINI events to ensure that the acceptance of the detector does not “manufacture” such events. Simple simulations with a “toy model” suggest that the excitation energy reconstructed after filtering should track with the primary excitation energy, but a definitive answer requires the filtering and analysis performed in the same way as the data. These investigations are underway.

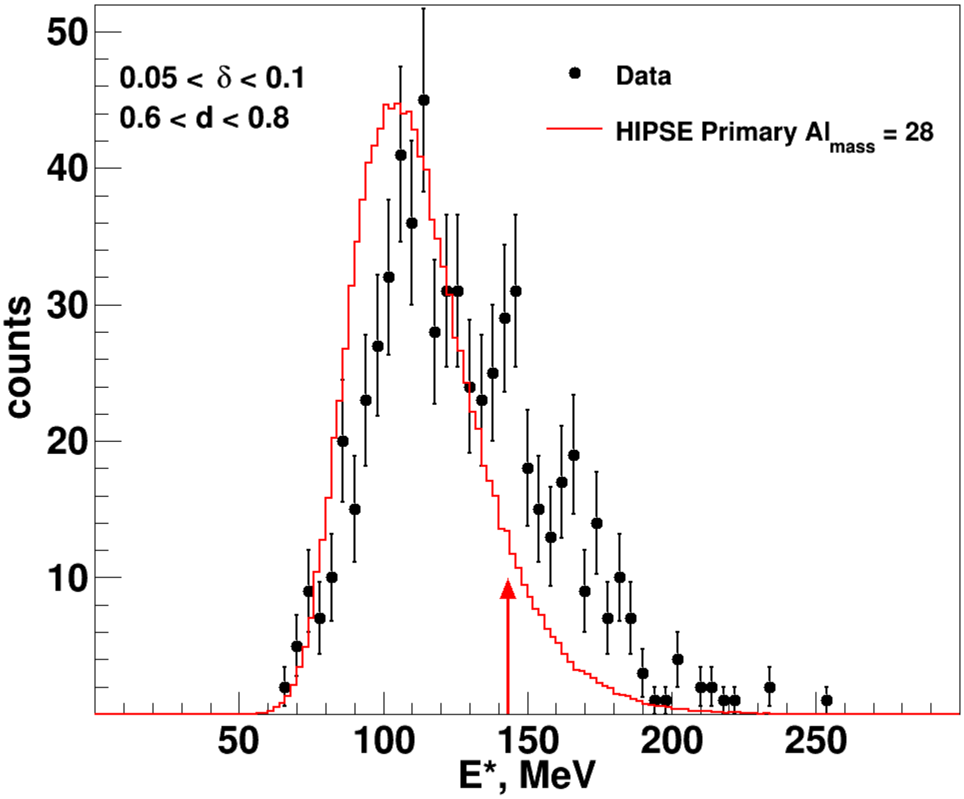

FIG. 1. Excitation energy distributions for 7α events where Almass = 28. The solid points represent the data. The red histogram shows the prediction of HIPSE events where the products produced by HIPSE have Almass = 28 after the GEMINI afterburner, but before filtering. The arrow at E*=143 MeV indicates the position of the prediction of [8] for a toroidal configuration of ^{28}Si.

[1] K. Schmidt *et al.*, *Progress in Research*, Cyclotron Institute, Texas A&M University (2011-2012), p. II-9.

[2] K. Schmidt *et al.*, *Progress in Research*, Cyclotron Institute, Texas A&M University (2012-2013), p. II-20.

[3] K. Schmidt *et al.*, *Progress in Research*, Cyclotron Institute, Texas A&M University (2012-2013), p. II-9.

[4] K. Schmidt *et al.*, J. Phys. Conference Series **420**, 012088 (2013).

[5] K. Schmidt *et al.*, *Progress in Research*, Cyclotron Institute, Texas A&M University (2013-2014), p. II-18.

[6] K. Schmidt *et al.*, Eur. Phys. J. Web of Conferences **88**, 24 (2015).

[7] X. G. Cao *et al.*, *Progress in Research*, Cyclotron Institute, Texas A&M University (2015-2016), p. II-16.

[8] A. Staszczak and C.Y. Wong, Phys. Lett. B **738**, 401 (2014).

[9] D. Lacroix, A.V. Lauwe, and D. Durand, Phys. Rev. C **69**, 054604 (2004).

[10] R.J. Charity *et al.*, Nucl. Phys. **A483**, 371 (1988).

Ternary fission fragment yields analysis in ^{124}Sn+^{112,124}Sn at 26*A* MeV reaction

J. Gauthier, M. Barbui, X.G. Cao, K. Hagel, J.B. Natowitz, R. Wada, and S. Wuenschel

An analysis of the data set coming from 26*A* MeV ^{124}Sn on ^{112}Sn and ^{124}Sn targets acquired by the NIMROD heavy ion detector [1] is underway and almost ready for publication. These data are being used to perform studies of the emission sources [2] with emphasis on emission of fragments in ternary fission processes [3] at high temperature and excitation energy. A better understanding of this phenomenon should help to improve the characterization of the reaction dynamics [4], especially in the low density mid-rapidity region.

The data set is composed of 33 runs combining 26 000 000 events. Charge identification is achieved up to Z=42 and isotopic identification is achieved up to Z=14 with very low statistics of mass identified fragments for charges above Z=9. The energy calibration of the Si-CsI(Tl) is now done. We used the SRIM calculation [5] and a Si-Si punch-through-energy based calibration to fit the energy distributions in all detectors. The energies resulting from the calibration are in very good agreement with those predicted by the HIPSE event generator [6] which gives us additional confidence in the calibration technique. Unfortunately, the absence of light particle calibration points prevents us from calibrating the light particles (Z=1,2) in the CsI(Tl).

The starting point of this analysis is based on the work done in reference [3]. About 0.3% of heavy nucleus spontaneous fissions produce a third fragment coming from the low density neck region [7]. Most of those fragments are α particles. A high yield of tritons relative to protons is observed as shown in reference [8] and the yield of heavier fragments decreases with Z. To reproduce the yields, we have previously used a nucleation model together with the nuclear statistical equilibrium (NSE) code LIBNUCEQ [9]. The NSE model is based on the assumption that the chemical potential μ(Z,A) is governed by equation (1). The yields are then extracted by the use of equation (2) which takes into account the temperature, the density and the proton fraction number

$$\mu(Z,A) = Z\mu_p + (A-Z)\mu_n, \qquad (1)$$

$$\mu(Z,A) = m(Z,A)c^2 + kT\ln\left\{\frac{\rho N_A Y(Z,A)}{G(Z,A)}\left[\frac{h^2}{2\pi m(Z,A)kT}\right]^{3/2}\right\}. \qquad (2)$$

This approach is in good agreement with experimental yields of light ternary fragments from spontaneous fission of ^{241}Pu but overestimates the yields of heavier isotopes as we can see in reference [3]. The inclusion of the nucleation process [10] allows us to modulate the approach to equilibrium. The nucleation uses surface tension constraints and the chemical potential to grow or diminish cluster size by accepting or emitting a single nucleon as time evolves. The nucleon absorption/emission process is driven by the critical cluster size A_c that is viewed as the mass threshold at which the clusters grow or break down. The inclusion of this process, which takes into account the reaction time and is described by equations 3, 4 and 5, greatly improves the agreement with the experimental data as it is shown in reference [3].

$$Y(A,\tau) = \frac{1}{2}\rho \exp\left[-\frac{G(A)}{T}\right] \times \mathrm{erfc}\left\{B(T,\sigma)\frac{[(A/A_c)^{1/3} - 1] + \left(1 - A_c^{-1/3}\right)\exp(-\tau)}{\sqrt{1-\exp(-2\tau)}}\right\} \qquad (3)$$

$$B(T,\sigma) = 2R_0\left(\frac{\pi\sigma}{T}\right)^{1/2} A_c^{1/3} \qquad (4)$$

$$\tau = \frac{3.967c\rho}{A_c^{2/3}\sqrt{T}}t \qquad (5)$$

.

In order to pursue such studies at higher temperature we turned to symmetric nuclear reactions. The mid-rapidity emission in the 26*A* MeV ^{124}Sn + $^{112,\ 124}$Sn system collisions allows us to prepare heavy systems similar to those which undergo spontaneous fission, thus to probe the neck emission process at higher temperature. In this analysis, the ternary-like-fragments are selected using the relative angle between the fragment of interest and the Z_{max} in the center of mass reference frame (see drawing in Fig. 2). To select mid-peripheral and peripheral collision, we apply a cut on $Z_{max} > 20$ as shown in Fig. 1.

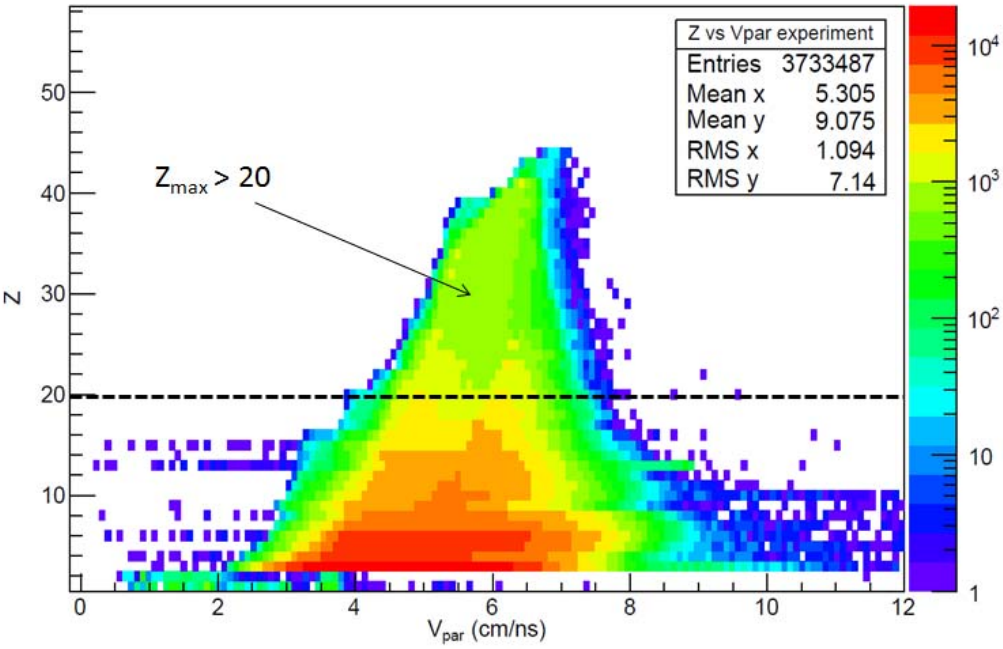

FIG. 1. Z_{max} selection as a function of the parallel velocity.

The ternary-like-fragment relative angle has to be as close as possible to 90^o in the center of mass frame but since the statistics are limited, we need to do a compromise between the relative angle selection and the number of events within this selection. To do so, we select the relative angle interval for which the average energy of the particles in the center of mass stops decreasing. This should exclude projectile-like emission sources. Fig. 2 shows these distributions for Z=3, 4 and 5. The compromise relative angle selection chosen corresponds to 50-130^o.

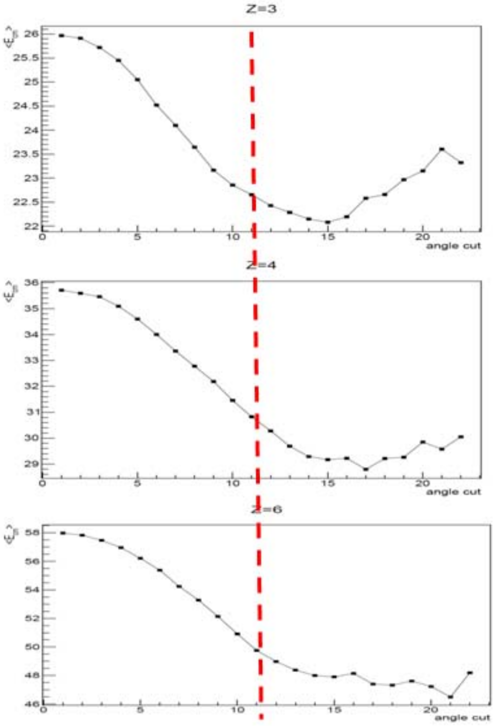

Cut #	rel. angle min	rel. angel max
1	0	180
2	5	175
3	10	170
4	15	165
5	20	160
6	25	155
7	30	150
8	35	145
9	40	140
10	45	135
11	50	130
12	55	125
13	60	120
14	65	115
15	70	110
16	75	105
17	80	100
18	82	98
19	84	96
20	86	94
21	88	92
22	89	91

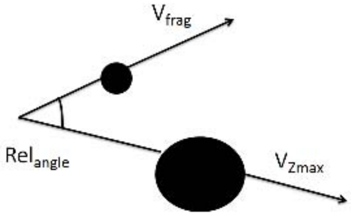

FIG. 2. (left) Average energy in the center of mass for several relative angle selections. The selection (cut) numbers are described in the table (middle). The best compromise is the 50-130^o range. (right) Graphical representation of our relative angle definition.

After normalization, we can compare the results of the NSE+nucleation calculation with the experimental data by using the fit metric described in equation (6), which is an average of the discrepancy between the experimental and theoretical *P(Z, A)* points and tells us how well the model reproduces the experimental values.

$$\text{Fit Metric} = \quad M^2 = \sum_j \{\ln[P_{\mathrm{TF}}^{\exp}(Z_j, A_j)] - \ln[P_{TF}(Z_j, A_j)]\}^2 / n \qquad (6)$$

In reference [3], The Fit Metric for spontaneous fission with NSE only (without nucleation) is 4.28 and the one with nucleation included is 1.18. With the NIMROD data presented in Fig. 3, we achieved a M^2 equal to 0.92 for the^{124} Sn and 0.94 for the ^{112}Sn target. However, these NIMROD fit metric numbers don't take into account the charges above 9 since the number of particles coming from

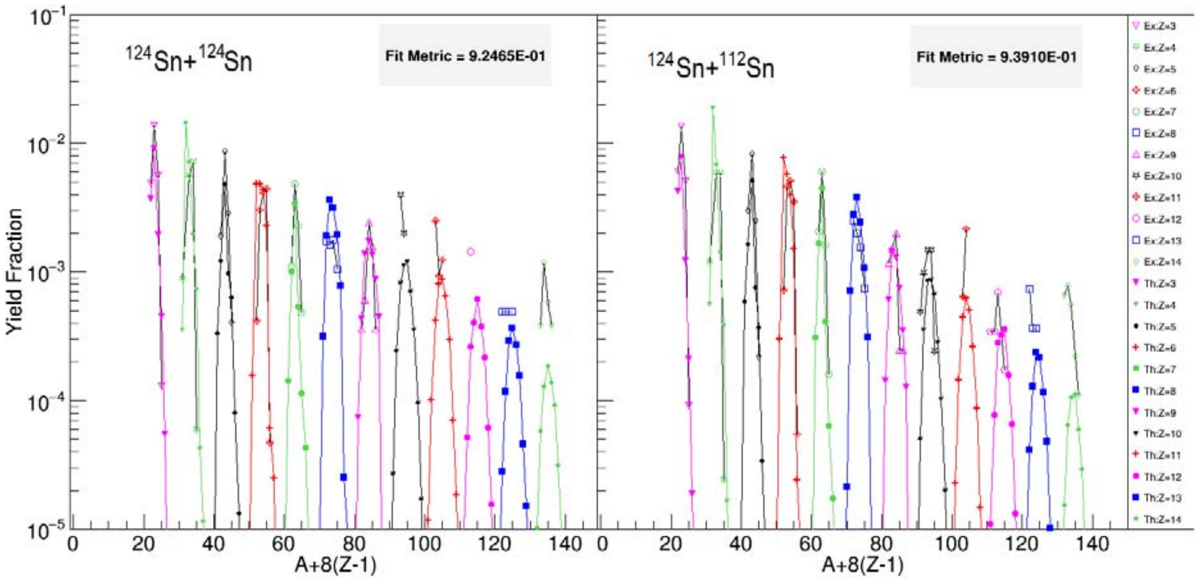

FIG. 3. Fitting results with NIMROD data for both systems with isotopic identification.

the mass identified set is too low for those elements and are then statistically irrelevant. If we don't take into account the isotopic information, meaning that we assign an average mass to each fragment not isotopically identified, the statistics gets much higher and we can reach an even better fit metric value(including all elements) as shown in Fig. 3. In Table I, we present a summary of the fit parameters used to achieve the optimized metric. The temperatures and densities are, as expected, higher than those in reference [3]. In order to achieve the best fit, we have to greatly increase the critical cluster size. The large discrepancies for the heavier isotopes is due to the very low statistics in the mass identified fragments for Z > 9. The discrepancies and values in table 1 still need to be interpreted.

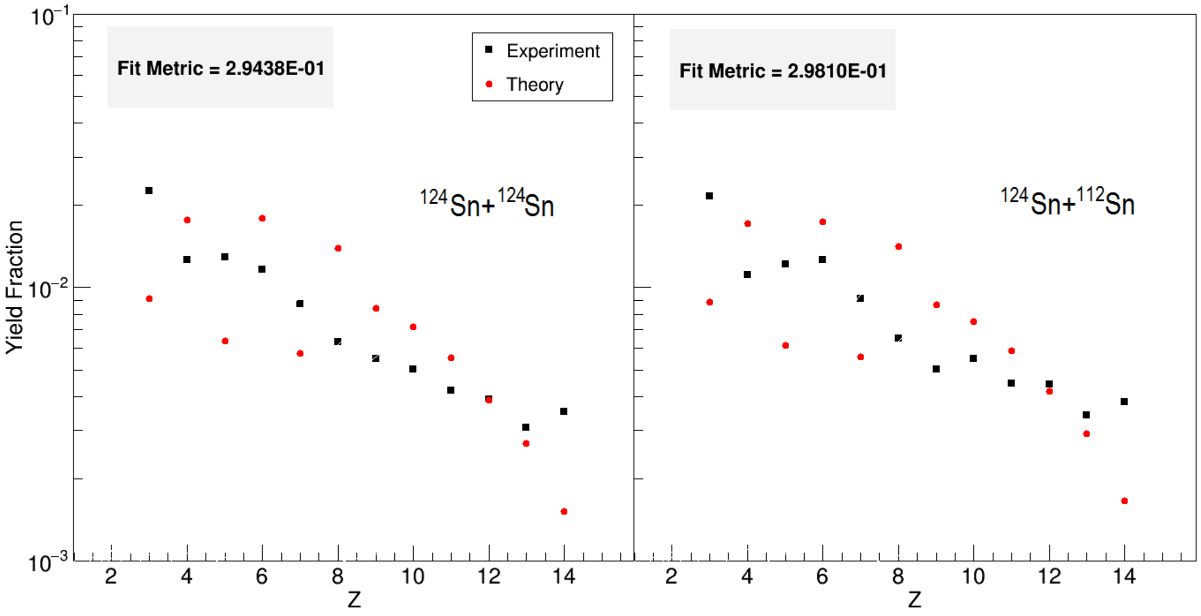

FIG. 4. Fitting results with NIMROD data for both systems with charge identification only.

Table I. Fit parameters for both studied systems including isotopic and Z only selections. The spontaneous fission of ^{241}Pu parameters from reference [3] are also added for comparison. For clarification, the last column, labeled *A,* is a fit performed with the mass only without taking Z into account (still from reference [3]).

System	^{124}Sn+^{124}Sn		^{124}Sn+^{112,}Sn		^{241}Pu	
selection	Isotopic	Z	Isotopic	Z	Isotopic	A
temperature (MeV)	2.49	2.30	2.45	2.30	1.4	1.4
density (10^{-4} fm^{-3})	13.0	13.4	12.6	13.7	4	4
time (fm/c)	9200	9300	8400	9400	6400	6400
A_c	16.0	16.0	15.8	16.0	5.4	5.4
proton ratio	0.41	0.41	0.44	0.41	0.34	0.34
fit metric	**0.925**	**0.294**	**0.939**	**0.298**	**1.18**	**0.561**

We would like to thank A.B. McIntosh and S.J. Yennello for the helpful discussions and comments about this work.

[1] S. Wuenschel *et al.*, Nucl. Instrum Methods Phys. Res. **A604**, 578 (2009).

[2] D.V. Shetty *et al.*, Phys. Rev. C **68**, 054605 (2003).

[3] S. Wuenschel *et al.*, Phys. Rev. C **90**, 011601, (2014).

[4] M.A. Famiano *et al.*, Phys. Rev. Lett. **97**, 052701 (2006).

[5] J.F. Ziegler *et al.*, Nucl. Instrum. Methods Phys. Res. **B268**, 11 (2010).

[6] D. Lacroix et *al.*, Phys. Rev. C **69**, 054604, (2004).

[7] C. Wagemans, *The Nuclear Fission Process* (CRC Press, Boca Raton, 1991).

[8] A. Schubert *et al.*, Z. Phys. A **341**, 481 (1992).

[9] http://sourceforge.net/p/libnuceq

[10] P. Demo and Z. Kozisek, J. Phys. G **23**, 971 (1997).

Alpha conjugate neck structures in the collisions of 35 MeV/nucleon ^{40}Ca with ^{40}Ca

K. Schmidt,[1,2] X.G. Cao,[3,1] E.-J. Kim,[1,4] K. Hagel,[1] M. Barbui,[1] J. Gauthier,[1] S.Wuenschel,[1] G. Giuliani,[1,5]
M.R.D. Rodrigues,[1,6] H. Zheng,[1,5] M.Huang,[1,7] N. Blando,[1] A. Bonasera,[1,5] R. Wada,[1] C. Botosso,[1]
G. Liu,[3] G.Viesti,[8] S. Moretto,[8] G. Prete,[9] S. Pesente,[8] D. Fabris,[8] Y. El Masri,[10] T. Keutgen,[10]
S. Kowalski,[2] A. Kumar,[11] G. Zhang,[1,3] and J.B. Natowitz[1]
[1]*Cyclotron Institute, Texas A&M University, College Station, Texas 77843, USA*
[2]*Institute of Physics, University of Silesia, 40-007 Katowice, Poland*
[3]*Shanghai Institute of Applied Physics, Chinese Academy of Sciences, Shanghai 201800, China*
[4]*Division of Science Education, Chonbuk National University, Jeonju 561-756, Korea*
[5]*Laboratori Nazionali del Sud, INFN, via Santa Sofia, 62, 95123 Catania, Italy*
[6]*Instituto de Física, Universidade de São Paulo,Caixa, CEP 05389-970, São Paulo, SP, Brazil*
[7]*College of Physics and Electronics information, Inner Mongolia University for Nationalities, Tongliao, China*
[8]*Dipartimento di Fisica dell'Università di Padova and INFN Sezione di Padova, I-35131 Padova, Italy*
[9]*INFN Laboratori Nazionali di Legnaro, I-35020 Legnaro, Italy*
[10]*Universite Catholique de Louvain, B-1348 Louvain-la-Neuve, Belgium*
[11]*Nuclear Physics Laboratory, Department of Physics, Banaras Hindu University, 221005 Varanasi, India*

In 2016 the de-excitation of alpha-conjugate nuclei produced in reactions of 35 MeV/nucleon 40Ca with 40Ca was investigated. The results of the study were published in [1]. Particular emphasis has been placed on examining the dynamics of collisions leading to projectile-like fragment exit channels. A general exploration of the reaction systematics reveals the binary dissipative character of the collisions and a hierarchy effect similar to that seen for heavier systems. Investigation of the subset of events characterized by a total alpha-conjugate mass (alpha particles plus alpha-conjugate fragments) equal to 40 and atomic number equal to 20 reveal a dominance of alpha-conjugate exit channels. The hierarchy effect for these channels leads to the production of alpha-clustered neck structures with potentially exotic geometries and properties.

In general nuclei have compact near spherical topologies. Nuclei with high excitation energies, high angular momenta or very high atomic numbers have been predicted to assume bubble or toroidal configurations [2-4]. A great deal of theoretical effort has been devoted to the investigation of such shapes, and to delineating the conditions under which they might occur. Both macroscopic and microscopic models have been employed [2-9]. The most recent work by Ichikawa et al. [5, 6] and by Wong and Staszczak [7-9] has led to specific predictions of highly excited, shell stabilized, high angular momentum toroidal states in light nuclei. Both models employ constrained cranked Hartree-Fock techniques but they differ in starting conditions, interactions utilized and wave function descriptions. Figure 1 indicates the excitation energies predicted for such states. While our experiment cannot determine the angular momenta of these states, the observed mass and excitation energy systematics of these states might provide evidence for the states predicted. The analysis is ongoing. Among the events with alpha-like mass equals to 40 and events with total mass equals to 40 and total charge equals to 20 we search for the candidates for toroids with the use of observables which represent the shape of the momentum flow during the decay. Encouraged by the results obtained for the 28Si, we will continue the study.

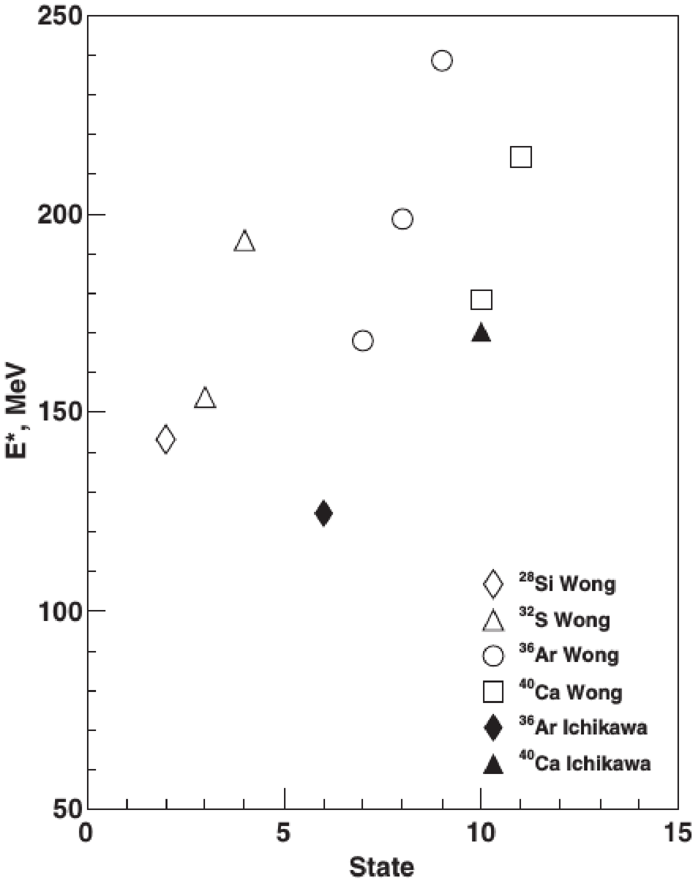

FIG. 1. Predicted excitation energies for stabilized toroidal states in light alpha-conjugate nuclei.

[1] K. Schmidt et al, Phys. Rev. C **95**, 054618 (2017).

[2] C.Y. Wong, Phys. Lett. **B41**, 446 (1972).

[3] C.Y. Wong,, Ann. Phys. **77**, 279 (1973).

[4] C.Y. Wong, in Superheavy Elements, edited by Lodhi M. A. K. (Pergamon Press, New York, 1978), p. 524.

[5] T. Ichikawa *et al.*, Phys. Rev. C **86**, 031303(R) (2012).

[6] T. Ichikawa *et al.*, Phys. Rev. C **109**, 232503 (2012).

[7] A. Staszczak and C.Y. Wong, Phys. Lett. B **738**, 401 (2014).

[8] A. Staszczak and C.Y. Wong, Acta Phys. Pol. B **46**, 675 (2015).

[9] A. Staszczak and C.Y. Wong, Phys. Scr. **90**, 114006 (2015).

Exploring exotic α-like emission from α conjugate nuclei collisions with the NIMROD-ISiS array

X.G. Cao, K. Schmidt, E.-J. Kim, K. Hagel, M. Barbui, J. Gauthier, R. Wada, S. Wuenschel,
M. Huang, G.Q. Zhang, H. Zheng, N. Blando, A. Bonasera, G. Giuliani, M. Rodrigues,
C. Botosso, G. Liu, and J.B. Natowitz

J. A. Wheeler had many pioneering ideas. In the 1950s He suggested that the nuclear liquid can assume toroidal shapes under certain conditions, such as excessive charge, excessive angular momentum and shell effects [1]. Early work of C. Y. Wong predicted there was a region of toroidal ground state nuclei near A~330 and Z~ 130 due to the large Coulomb energy [2]. Then Wong extended these investigations to light nuclear systems and predicted that, given sufficient angular momentum, toroidal configurations were also possible for high spin light nuclei [3]. Most recently, various sophisticated Hartree-Fock methods were used to re-examine the possibility of toroidal configurations in light nuclei [4]. From these theoretical studies, we learn that the excitation energy increases with the increase of nuclear quadrupole moment. Spin zero toroids may appear above a threshold excitation energy and potential minima exist for specific higher angular momenta due to internal shell effects.

For toroidal configurations in the heavy region, one can perhaps detect the fission fragments to check the fission fragmentation configuration and see whether there are toroidal potential minima. For light toroidal isomers with large spin and excitation energy investigation of the fragmentation pattern is more difficult.

Macroscopic tori fragment as a result of the development of Plateau-Rayleigh instabilities [5]. This decay mode is dominated by symmetric fragmentations into pieces with equal size. Nuclear toroids might also manifest Plateau-Rayleigh instabilities. However, the nuclear torus is more complicated compared to the macroscopic torus due to the following factors: 1) temperature dependent viscosity of the disassembling nucleus, 2) the existence of Coulomb forces, and 3)shell effects and variations in the fragment binding energies. In addition, the subsequent de-excitations, will smear the signature of the Plateau-Rayleigh instability. Fortunately, α particles can be regarded as quite inert units compared with it's neighbors and quartetting is dominant over deuteron formation at low density and moderate temperature. An experimental exploration with special attention and methodology into observing fragmentation into α particles or α conjugate nuclei offers some possibilities of observing toroidal de-excitations.

A series of experiments were carried out at the Texas A&M University Cyclotron Institute with ^{40}Ca and ^{28}Si beams at 15, 25, 35 MeV/u, provided by the K500 superconducting cyclotron, incident on C, Si, Ca and Ta targets [6], respectively. The reaction products were detected using the 4π array, NIMROD-ISiS (Neutron Ion Multi detector for Reaction Oriented Dynamics with the Indiana Silicon Sphere). The preliminary analysis of the raw data was accomplished by C. Bottosso, E-J Kim and K. Schmidt et al. [6]. Recently, some interesting results regarding α-conjugate neck structures have been obtained for ^{40}Ca+^{40}Ca [7]. In this report, We focus on α-like cluster decay from ^{28}Si+ C@35MeV/u. Binary configurations of excited projectile-like and target-like nuclei dominate in this energy range. Similar results are observed for ^{28}Si+Si and ^{28}Si+Ta, showing that the target effect may be negligible for our exit channel choices. However, the statistics for the ^{28}Si+Ta reaction is much lower than for the other two systems.

For the ^{28}Si+^{12}C reaction, a total of 17 million events were recorded and a significant proportion of events have significant α-conjugate mass emission. The definitions of α-like mass and α-like multiplicity can be found in ref. [8]. There are 7 α-like decay channels for mass 28. For the 7 α exit channel, more than 10 thousand events were obtained. The α-like event composition is shown by Fig. 1.

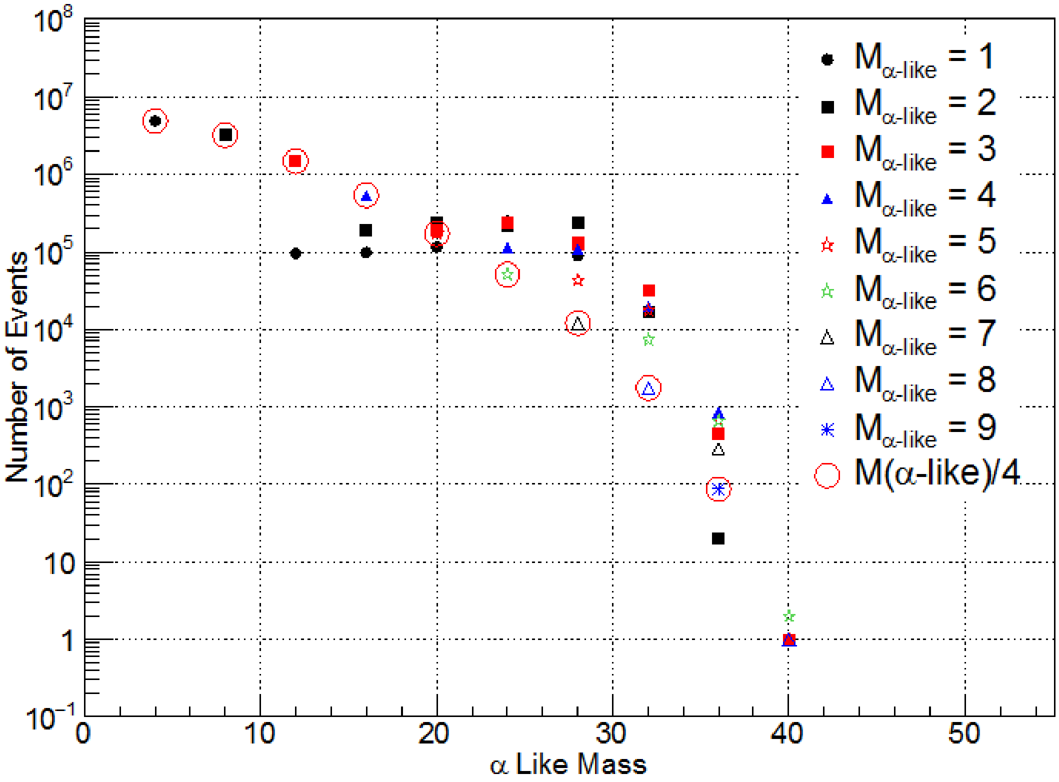

FIG. 1. The α-like event composition from ^{28}Si+^{12}C @ 35MeV/u.

What is the source of these α-like fragments? There is a possibility that these α-like fragments come from some exotic states, such as rod, toroid or disk shapes, or from Bose Einstein condensation.

A hierarchy effect is seen when heavier fragments have larger parallel velocity than the lighter fragments. A hierarchy effect is seen for these α decay channels, indicating lack of complete equilibrium of all degrees of freedom of the α-like emission source [7]. The parallel velocity of α-like fragments of the 7 α-conjugate exit channels from ^{28}Si is shown in Fig. 2.

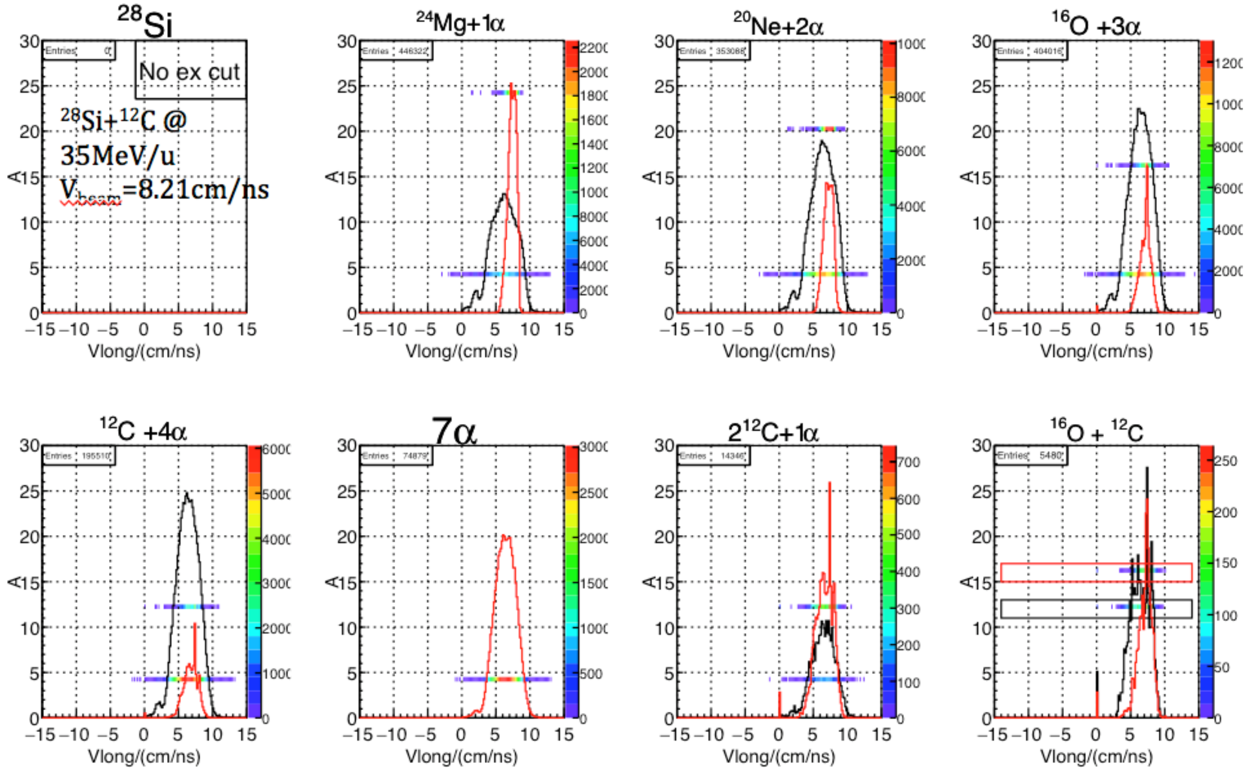

FIG. 2. The parallel velocity of α-like fragments of 7 interesting exit channels from ^{28}Si+^{12}C @ 35MeV/u.

The left panel of Fig. 3 shows that most of the exit channels are far from equilibrium. The right panel shows that the most interesting 7α decay channel has the largest absolute value of Ex_{peak} /Q, which supports the strong dynamical emission of the 7 αs.

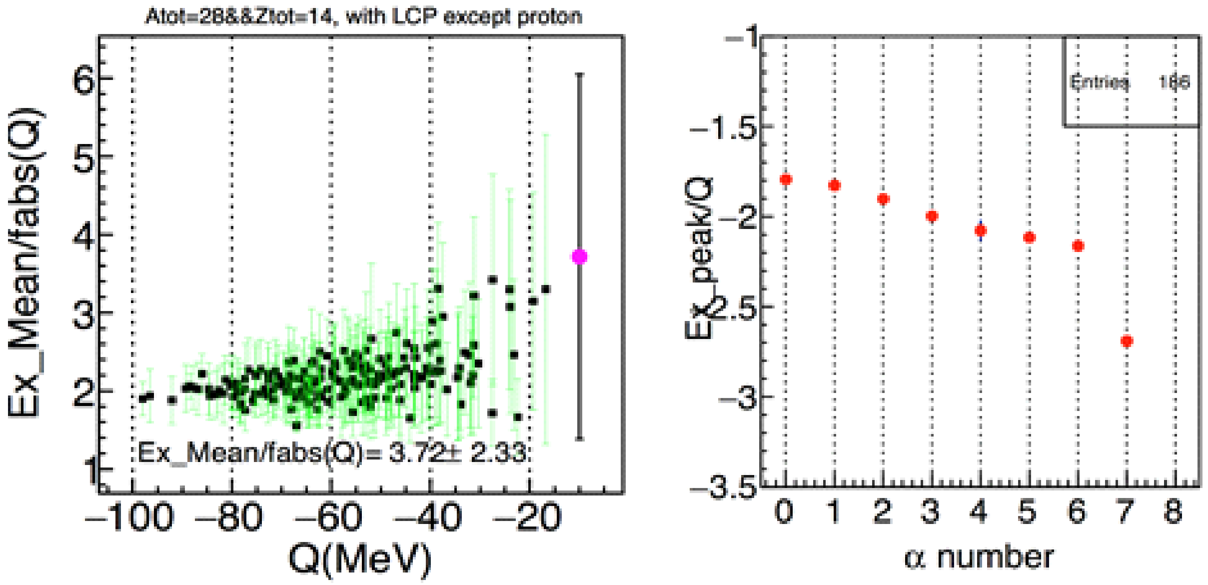

FIG. 3. Left panel: the mean value of excitation energy over absolute value of reaction Q as a function of Q value for all the exit channels satisfying the windows shown in the panel. Right panel: the peak value of excitation energy divided by reaction Q value as a function of number of α particles for the 7 α-like decay channels of ^{28}Si.

Antisymmetrized molecular dynamics (AMD) simulations shown by Fig. 4 help us to confirm that most nucleons in α-like fragments come from the projectile , (colors show the parallel velocity). Further comparison of the results for interesting exit channels such as 7α channel with those of AMD-3.4+Gemini, AMD-New(with cluster correlation) + Gemini and HIPSE + Gemini simulations are in progress.

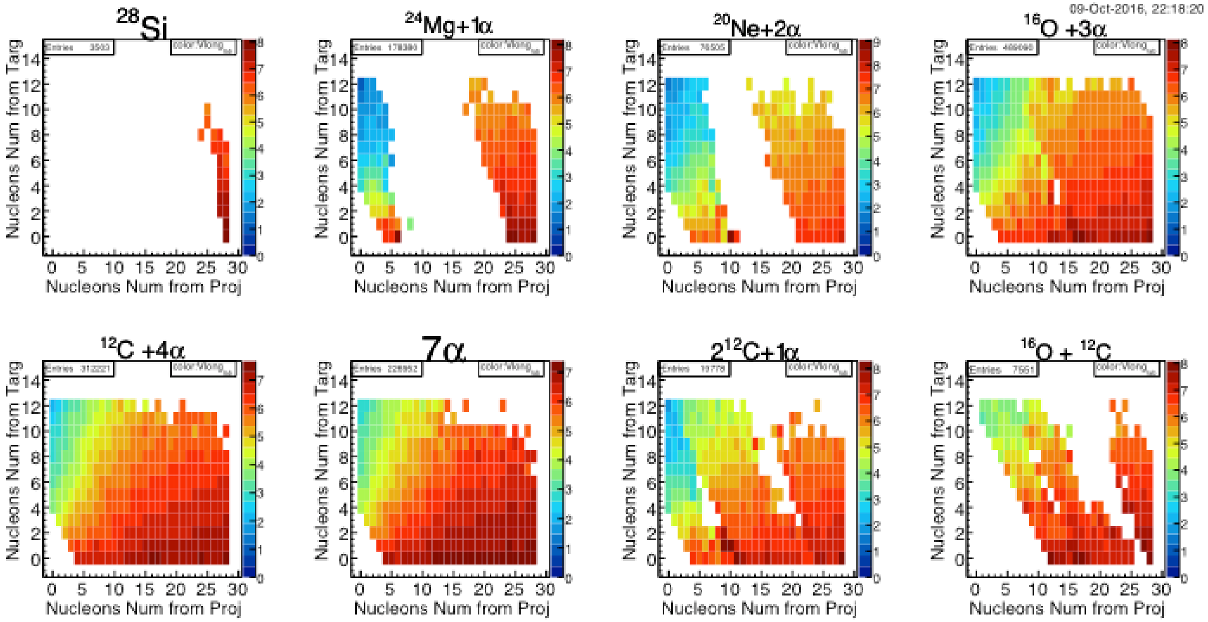

FIG. 4. Nucleon number from target v.s. nucleon number from projectile for α-like channels of ^{28}Si in antisymmetrized molecular dynamics (AMD) calculations.

[1] G. Gamow, Biography of Physics (Harper & Brothers Publishers, New York, 1961) p. 297.

[2] C.Y. Wong, Phys. Lett. **B41**, 446 (1972); C.Y. Wong, Ann. Phys. **77**, 279 (1973); C.Y. Wong, Phys. Rev. C **17**, 331 (1978).

[3] C.Y. Wong, Phys. Rev. Lett., **55**, 197 (1985).

[4] A. Staszczak, C.Y. Wong, Phys. Lett. B **738**, 401 (2014); A. Staszczak, C.Y. Wong, Phys. Scripta 90 114006 (2015); A. Staszczak, C.Y. Wong, arXiv:1510.04610 (2015); Zhang Wei *et al.* Chin. Phys. Lett. **27**, 10 (2010); A.S. Umar *et al.*, Phys. Rev. Lett. **104**, 212503 (2010); T. Ichikawa *et al.*, Phys. Rev. Lett. **107**, 112501 (2011); T. Ichikawa *et al.*, Phys. Rev. Lett. **109**, 232503 (2012).

[5] J. Plateau, Annual Report of the Regents, Smithsonian Institution, 207 (1863); E. Pairam and A. Fernández-Nieves, Phys. Rev. Lett., **102**, 234501 (2009).

[6] C. Bottosso *et al.*, *Progress in Research*, Cyclotron Institute, Texas A&M University (2008-2009), p.II-7; K. Schmidt *et al.*, *Progress in Research*, Cyclotron Institute, Texas A&M University (2010-2011), p. II-8; K. Schmidt *et al.*, *Progress in Research*, Cyclotron Institute, Texas A&M University (2011-2012), p. II-7; K. Schmidt *et al.*, *Progress in Research*, Cyclotron Institute, Texas A&M University (2012-2013), p. II-17; K. Schmidt *et al.*, *Progress in Research*, Cyclotron Institute, Texas A&M University (2013-2014), p. II-18.

[7] K. Schmidt et al., Phys. Rev. C **95**, 054618 (2017).

[8] X.G. Cao *et al., Progress in Research*, Cyclotron Institute, Texas A&M University (2014-2015), p. II-16; X.G. Cao *et al.*, *Progress in Research*, Cyclotron Institute, Texas A&M University (2015-2016), p. II-16.

Investigation of the use of multi-nucleon transfer reactions between very heavy nuclei for heavy element synthesis

S.Wuenschel, K. Hagel, M. Barbui, J. Gauthier, X.G. Cao, R. Wada, Z. Majka, Z. Sosin, A. Weiloch, S. Kowalski, K. Schmidt, C. Ma, G. Zhang, and J.B. Natowitz

Previous tests with a plastic scintillator array demonstrated that the use of a time filtering device to search for alpha decay following reactions between 7.5 MeV/nucleon ^{197}Au and ^{238}U with ^{232}Th was feasible even in the harsh environment encountered in such experiments.

While fast plastics provide the optimum in time resolution, the quenching of the light-output inherent In solid scintillators meant that, within the scintillator itself, discrimination between high energy alpha particles and spontaneous-fission fragments could be difficult. Since the active catcher has a much higher inherent efficiency than the ionization chamber array we decided to explore the use of scintillator materials offering pulse shape discrimination possibilities.

A second active catcher array was constructed using YAP scintillating detectors coupled to Hamamatsu PMTs via Lucite light guides. The YAP scintillators, obtained from Proteus, were chosen because of the fast rise time and light decay properties (t1=~14ns, t2=~140ns) that provide access to pulse shape discrimination based particle identification. An example of the typical separation achievable is provided in Fig. 1 with labeled gated regions.

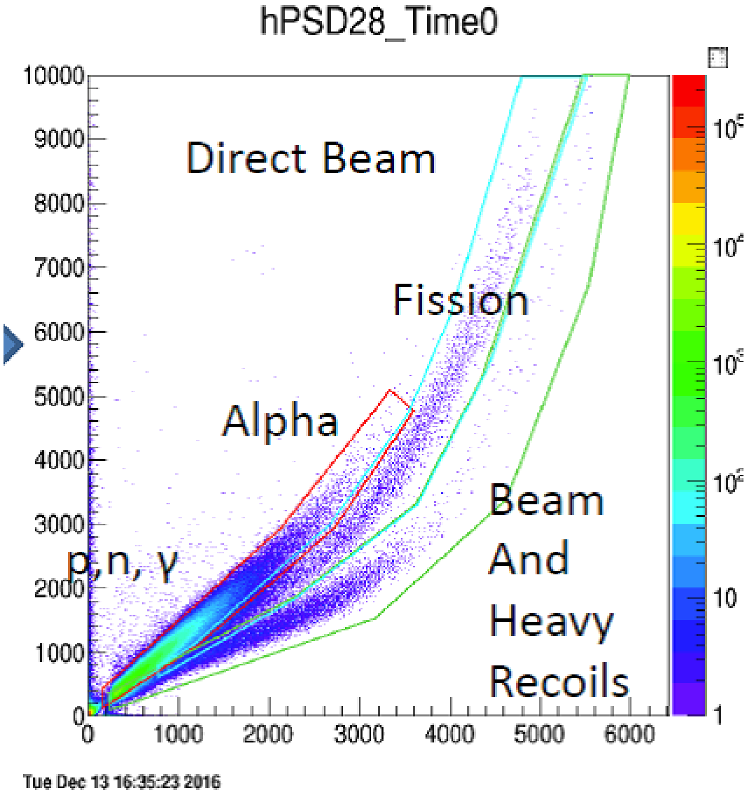

FIG. 1. Pulse shape discrimination of YAP active catcher ,7.5 MeV/nucleon ^{197}Au +^{232}Th direct beam.

It is important to note that the PSD (fast vs slow light output) shown in Figure 1 is sufficient to separate alpha decays from fission fragments, degraded beam and heavy residues.

The time decay constants inherent in YAP scintillators are notably slower than the fast plastic utilized previously. Thus, the dedicated, custom-made electronics and trigger scheme employed for the plastic scintillator array could not be easily adapted to these detectors. For this reason we turned top commercially available electronics for the YAP array. An experimental set-up triggering and signal acquisition scheme based upon the Struck SIS3316 250MHz Flash ADC modules was developed. These modules provide flexible digital triggering mechanisms. The trigger scheme utilized in the experiment was based on three operational considerations.

1. The experiment was carried out in a pulsed beam mode with variable beam on/beam off times.
2. The backward angle silicon detector modules generated triggers at a relatively low rate and very high quality.
3. While the SIS3316 modules could trigger in a mode very similar to the first-generation analog electronics. Such operation required vetoing ~40% of the time due to the convolution of 4ns FADC bins with the broader YAP decay times (relative to the plastic).

To avoid the problems associated with the last point, we decided to allow the forward angle YAP detectors to trigger acquisition only during the beam off periods.

The triggering scheme was divided into two primary modes, beam on and beam off. During the beam on periods, only the silicon detectors triggered the acquisition. The active catcher array was read in slave mode and a 2us waveform stored for each active catcher module. The synchronization between Si and YAP was set so that a coincident exit peak in an active catcher module would appear at ~800ns into the 2us waveform. During the beam off periods, the active catcher detectors were permitted to trigger the acquisition. Two microsecond waveforms were stored only for modules that triggered during the event. Because the trigger was generated entirely digitally, the beam on/off trigger mode was swapped using beam on/off bits provided to the acquisition system.

A third overarching trigger was also built into the logic. This intermittent trigger was applied to the silicon detectors. The threshold for this trigger was set to 8-8.5 MeV energy in the silicon detectors. For events generating the second, high energy trigger signal, the beam was pulsed off for 20 seconds and the acquisition set into the beam off trigger mode. Additionally, the stored waveforms were modified to be 160us long.

In August 2016, Experimental data were taken using the YAP active catcher array coupled to the backward angle IC-Si detector modules. Beams of ^{197}Au and ^{238}U of 7.5 meV/nucleon were incident on ^{232}Th targets. The digital triggering worked very well in conjunction with the now YAP based active catcher array.

The data are currently under analysis.

Search for an Hoyle state analogous state in ^{16}O using the thick target inverse kinematics technique

M. Barbui,[1] K. Hagel,[1] J. Gauthier,[1] S. Wuensche,[1] R.T. deSouza,[2] S. Hudan,[2]
D. Fang,[3] and J.B. Natowitz[1]
[1]*Cyclotron Institute, Texas A&M University, MS3366 College Station, TX*
[2]*Indiana University, Bloomington, IN, USA*
[3]*Shanghai Institute of Applied Physics (SINAP), Chinese Academy of Sciences, Shanghai, China*

Searching for alpha cluster states analogous to the ^{12}C Hoyle state in heavier alpha-conjugate nuclei can provide tests of the existence of alpha condensates in nuclear matter. Such states are predicted for ^{16}O, ^{20}Ne, ^{24}Mg, ^{28}Si etc. at excitation energies slightly above the multi-alpha particle decay threshold [1-3].

The Thick Target Inverse Kinematics (TTIK) [4] technique can be used to study the breakup of excited self-conjugate nuclei into many alpha particles. The reaction ^{20}Ne+α at 12 AMeV was studied at Cyclotron Institute at Texas A&M University. A picture of the experimental setup is shown in Fig. 1.

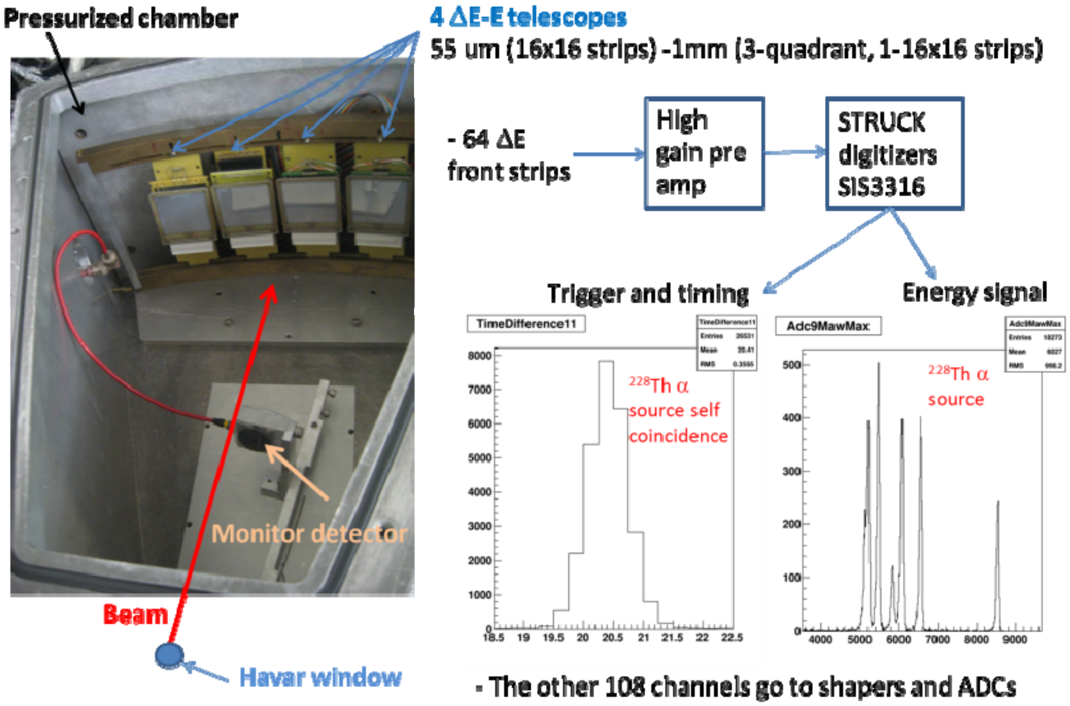

FIG. 1. Experimental setup and scheme of the electronics. Good energy and time resolution are obtained by using the STRUCK digitizers SIS3316.

The TTIK method was used to study both single α-particle emission and multiple α-particle decays. The analysis of the three α - particle emission data allowed the identification of the Hoyle state and other ^{12}C excited states decaying into three alpha particles. Some results are reported in ref [5, 6] and compared with other data available in the literature. In this report we update the results of the analysis of the events with alpha multiplicity four. In order to minimize accidentals, only events in which the four alpha particles arrive to the detectors in a time window of 30 ns are selected. Due to the very low beam intensity used during this run we estimate one beam particle per beam burst. To eliminate events that erroneously appear as multiplicity four, but are indeed lower multiplicity, we required that if more one alpha particle is detected in a given telescope, they should be detected by different quadrants in the E detectors. With this additional condition in the event selection the number of events with multiplicity four is reduced.

Two reconstruction algorithms are used to determin the position of the interaction point. One is based on a recursive procedure using the reaction kinematics, energy and momentum conservation. This reconstruction is based on the assumption of having, in the exit channel, ^{8}Be in the ground state (undetected) and ^{16}O (with enough excitation energy to decay into 4 alpha particles). The other is based on the average time of flight of the four alpha particles.

The excitation function of ^{16}O is shown in Fig. 2. The left panel shows the result obtained with the first reconstruction method, the right panel shows the excitation function obtained with the reconstruction based on the time of flight. The two excitation functions in Fig. 2 are qualitatively similar. Funaki *et al.* [8] predicted a state in ^{16}O at 15.1 MeV (the state) with the structure of the “Hoyle” state in ^{12}C coupled to an alpha particle. Our excitation function shows few events at about 15 MeV, but the statistics is too low to make any claim.

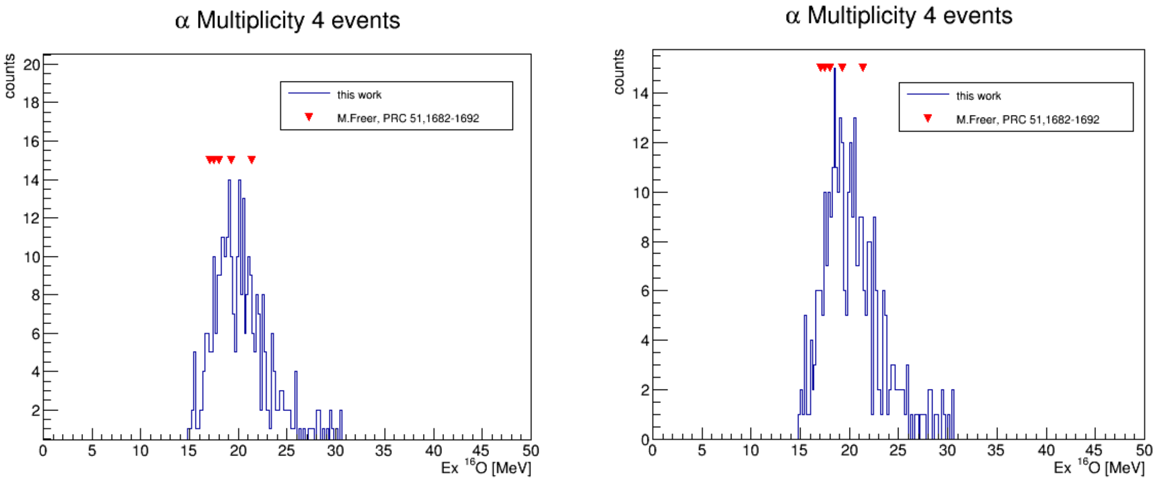

FIG. 2. Reconstructed excitation energy of ^{16}O obtained from the events with multiplicity 4. The arrows mark the position of known states in ^{16}O decaying into alpha particles [7].

[1] K. Ikeda, N. Takigawa, and H. Horiuchi, Prog. Theor, Phys. Suppl. Extra Number, 464 (1968).
[2] W. von Oertzen, M. Freer, and Y. Kanada-Enýo, Phys. Rep. **432**, 43 (2006).
[3] C. Beck, J. Phys. Conference Series **436**, 012014 (2013).
[4] K. Artemov *et al.*, Sov. J. Nucl. Phys. **52**, 406 (1990).
[5] M. Barbui *et al.*, Eur. Phys. J. Web of Conferences **66**, 03005 (2014).
[6] M. Barbui *et al.*, Eur. Phys. J. Web of Conferences **117**, 07013 (2016).
[7] M. Freer *et al.*, Phys Rev C **51**,1682
[8] Y. Funaki *et al.*, Phys. Rev. Lett. **101**, 082502 (2008).

Indium and thallium extraction into a betainium-based ionic liquid

M.F. Volia, E.E. Tereshatov, M.Yu. Boltoeva,[1, 2] and C.M. Folden III
[1]*Université de Strasbourg, IPHC, Strasbourg, 67037 France*
[2]*CNRS, Strasbourg, 67037 France*

Previously, our group has reported the extraction of indium (In) into imidazolium-based ionic liquids [1] and extraction of thallium (Tl) into several imidazolium-based and pyrrolidinium-based ionic liquids [2] using the liquid-liquid extraction (LLE) technique. This study is intended to provide the basis for a potential future chemistry study of nihonium, the heaviest homolog of In and Tl, with a focus on developing an effective and efficient separation of In and Tl.

The LLE technique used in this study is based on the distribution of the solute in two immiscible phases, an aqueous and an organic phase [3]. Our previous results showed that Tl was effectively extracted into the ionic liquids in the form of a negatively charged complex TlX_z^{3-z}, where X is either Cl^- or Br^-, and thus enabled effective separation with In, as the latter mainly remains in the aqueous phase. In the current work, we explore the ability of the ionic liquid betainium bis(trifluoromethylsulfonyl)imide ($[HBet][Tf_2N]$) to extract In and Tl from hydrochloric acid (HCl) media.

Unlike the previous ionic liquids that have been studied, $[HBet][Tf_2N]$ is not commercially available. The $[HBet][Tf_2N]$ ionic liquid was synthesized in our laboratory according to a procedure in the literature [4]. Betaine hydrochloride solution was mixed with lithium bis(trifluoromethylsulfonyl)imide solution with a 1:1 molar ratio. The mixture was stirred for 1 h at room temperature. Upon mixing, the solution was allowed to sit until it formed two distinct phases. Subsequently, the aqueous phase was dispensed and the organic phase was washed with deionized water several times to remove chloride impurities. The final product was used as a water-saturated ionic liquid to avoid uncontrollable water uptake during the extraction.

Betaine, which is also known as 1-carboxy- N,N,N-trimethylmethanaminium hydroxide, N,N,N-trimethylglycine, N-trimethylglycine, or trimethylglycine, is a zwitterion, and thus possesses both positive and negative charges within its molecule (Fig. 1) [3]. The zwitterionic form has a strong coordination site on the carboxylate group and this makes it a potential extractant to the metal ions [5].

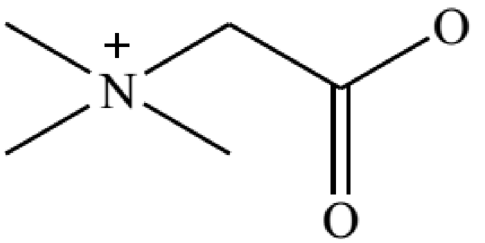

FIG. 1. The structure of zwitterionic betaine.

The mechanism of metal extraction into [HBet][Tf_2N] can occurs via several pathways, i.e., complex formation, ion exchange, or ion-pair formation. This extraction mechanism will be one of the subjects of a future study. Extraction experiments were performed following the previous procedure used in our work [6]. The result of extraction is presented in the form of a distribution ratio, that is, the ratio of activity of the solute in the organic phase to that of in the aqueous phase. Preliminary results of the current study indicate that the distribution ratios of In and Tl extraction are affected by several factors such as the acid concentration and the speciation of metal complexes in the aqueous solution.

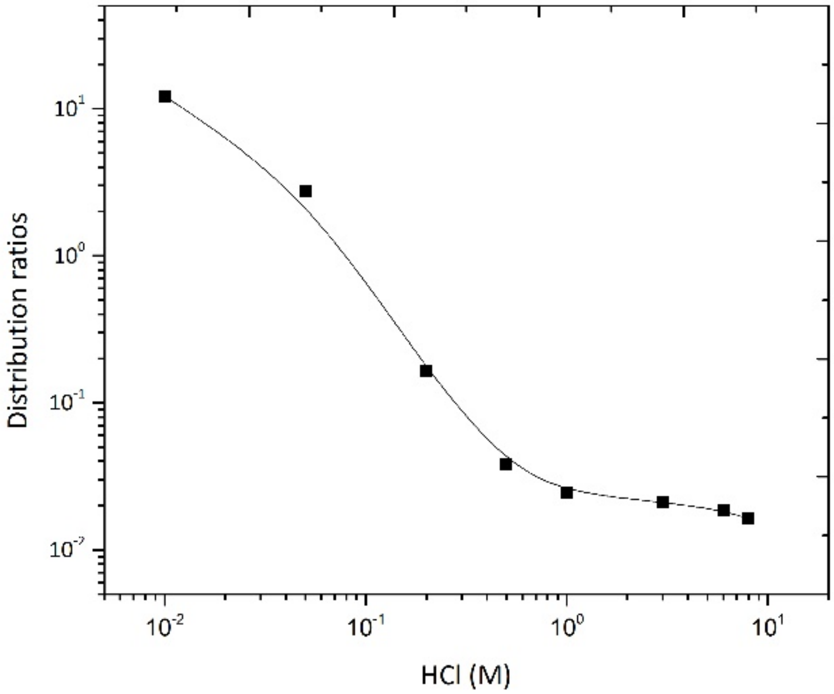

FIG. 2. Indium extraction into [HBet][Tf_2N].

As shown in Fig. 2, the distribution ratios of In extraction decrease as the HCl concentration increases. Also the distribution ratios of Tl(I) and Tl(III) decrease with the same trend (Fig. 3). Considering the pKa of betaine is 1.82 [7], deprotonation of $[HBet]^+$ may occur in 0.01 M HCl and enable the formation of zwitterion betaine compound in the organic phase. Indium is known to form $InCl_2^+$, $InCl_3$, and $InCl_4^-$ in chloride solution, depending on the chloride ion concentration [1, 8]. It is likely that at lower chloride concentrations (HCl concentration < 0.05 M), In is extracted as an $InCl_2^+$ complex, while at higher chloride concentrations (>0.5 M), the speciation of In is $InCl_3$ or $InCl_4^-$, resulting in much poorer extraction.

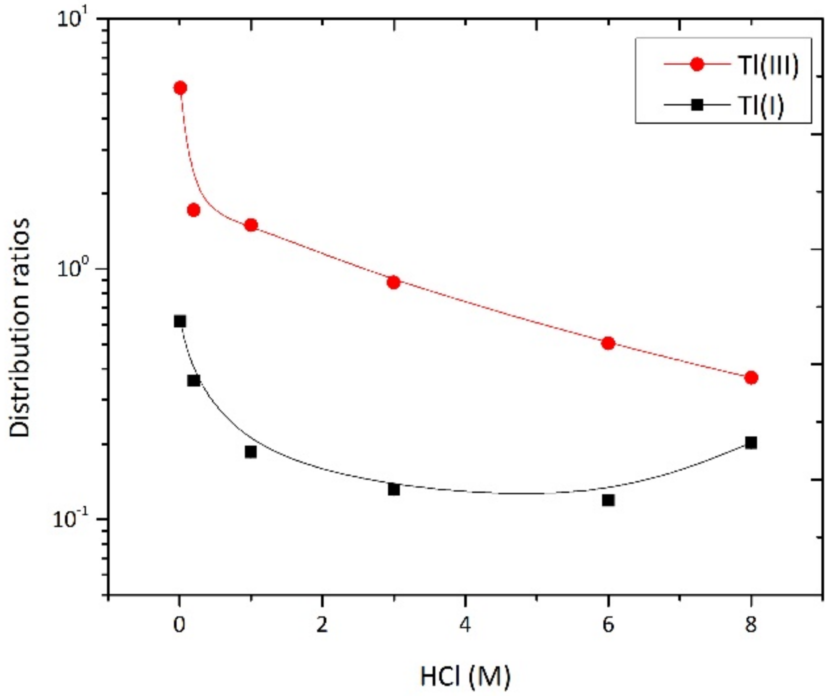

FIG. 3. Thallium extraction into [HBet][Tf_2N].

In the case of Tl(I), Tl^+ is the dominant species in dilute HCl, while it may present in the form of TlCl or $TlCl_2^-$ at higher acid concentrations [2]. Based on Fig. 3, the extraction curves of Tl(I) and Tl(III) show a similar trend, although Tl(I) mostly remains not extracted. This phenomena suggests that the extraction mechanism of Tl(I) and Tl(III) follow the same pathways (specifically at HCl concentrations < 3 M), but further experiments will be performed to test this assumption.

These preliminary results provided good indication of the ability of [HBet][Tf_2N] ionic liquid to extract In and Tl from HCl media. Based on these findings, potential separation of In and Tl can be achieved by controlling the acid concentration and the speciation of the metal ions. Further experiments will be conducted to confirm these results as well as to elucidate the extraction mechanisms. In addition, future experiments will be aiming toward improving the extraction efficiency by introducing an additional extractant into the existing chemical system.

[1] E.E. Tereshatov, M.Y. Boltoeva, and C.M. Folden III, Solv. Extr. Ion Exc. **33**, 607 (2015).

[2] E.E. Tereshatov, M.Y. Boltoeva, V. Mazan, M.F. Volia, and C.M. Folden III, J. Phys. Chem. B **120** 2311 (2016).

[3] T.V. Hoogerstraete, B. Onghena, and K. Binnemans, Int. J. Mol. Sci. **14**, 21353 (2013).

[4] P. Nockemann, B. Thijs, S. Pittois, J. Thoen, C. Glorieux, K. van Hecke, L. van Meervelt, B. Kirchner, and K. Binnemans, J. Phys. Chem. B **110**, 20978 (2006).

[5] B. Onghenaand K. Binnemans, Ind. Eng. Chem. Res. 54, 1887 (2015).

[6] M.F. Volia, E.E. Tereshatov, M.Y. Boltoeva, and C.M. Folden III, *Progress in Research*, Cyclotron Institute, Texas A&M University (2015-2016) p. II-3. https://cyclotron.tamu.edu/progress-reports/2015-2016/cyclotron_progress_2016.pdf.

[7] R.M.C. Dawson, D.C. Elliott, W.H. Elliott, and K.M. Jones, *Data for biochemical research* (Oxford University Press: New York, 1986) p. 8-9.

[8] E.A. Burns and D.N. Hume, J. Am. Chem. Soc. **79**, 2704 (1957).

Radioimpurity in medical ^{111}In isotope

E.E. Tereshatov and C.M. Folden III

Analysis of gamma-spectra of ^{111}In medical radioisotope samples has revealed the presence of a radioimpurity. This previously non-documented radioisotope does not have any detectable gamma-lines in the range up to 2000 keV. In previous experiments devoted to indium extraction into hydrophobic deep eutectic and low-temperature-transition mixtures,[1] an automated gamma-ray counter equipped with a low-resolution NaI detector was used to monitor ^{111}In activity.[2] Studying indium transfer into these green organic media, we found that the new radioimpurity represents another chemical element (not another indium isotope). Fig. 1 shows the activity distribution between the aqueous and organic phases, and it can be easily seen that the ^{114m}In isotope was successfully transferred to the organic medium. At the same time, the aqueous phase spectrum still shows the presence of an X-ray peak, which must be attributed to another element. It should be noted that the ^{111}In manufacturer declares ^{114m}In and ^{65}Zn activity presence at time of calibration at a level of not more than 0.075% combined. Although both ^{114m}In and ^{65}Zn have easily detectable gamma-lines, the radioimpurity list provided is not complete. In order to identify the new radioisotope, a long-term series of measurements was taken to determine its half-life. An aliquot of a stock solution was measured for over 300 d and the net area of the corresponding X-ray peak (~18 keV) was estimated. The measurement was initiated approximately 2 months after the ^{111}In ($T_{1/2}$ = 2.80 d) was

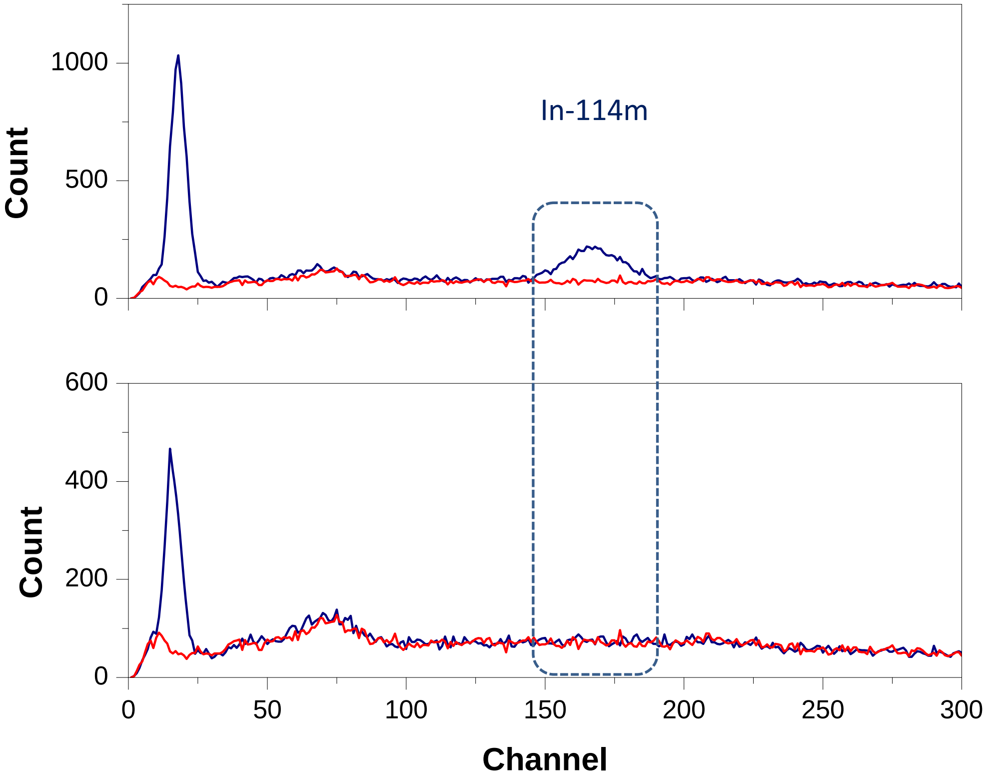

FIG. 1. Indium extraction from 5x10^{-4} M HCl to DL-menthol-lauric acid deep eutectic solvent: top – organic phase, bottom – aqueous phase.

produced. Fig. 2 shows the measured decay curve. The calculated half-life of the new radioisotope is $T_{1/2} = 468 \pm 18$ days. The identification was done based on such parameters as half-life, absence of any gamma-ray lines, and non-In-like behavior. Taking this into account, we believe that the radioimpurity found can be attributed to ^{109}Cd, which has a half-life of 462.6 days. The nuclear reaction used to produce the medical indium isotope is ^{112}Cd(p,2n)^{111}In. Most likely the enriched ^{112}Cd target material still contains small amounts of other stable cadmium isotopes. A possible reaction to produce this radioisotope is ^{110}Cd(p,2n)^{109}In followed by beta decay to ^{109}Cd.

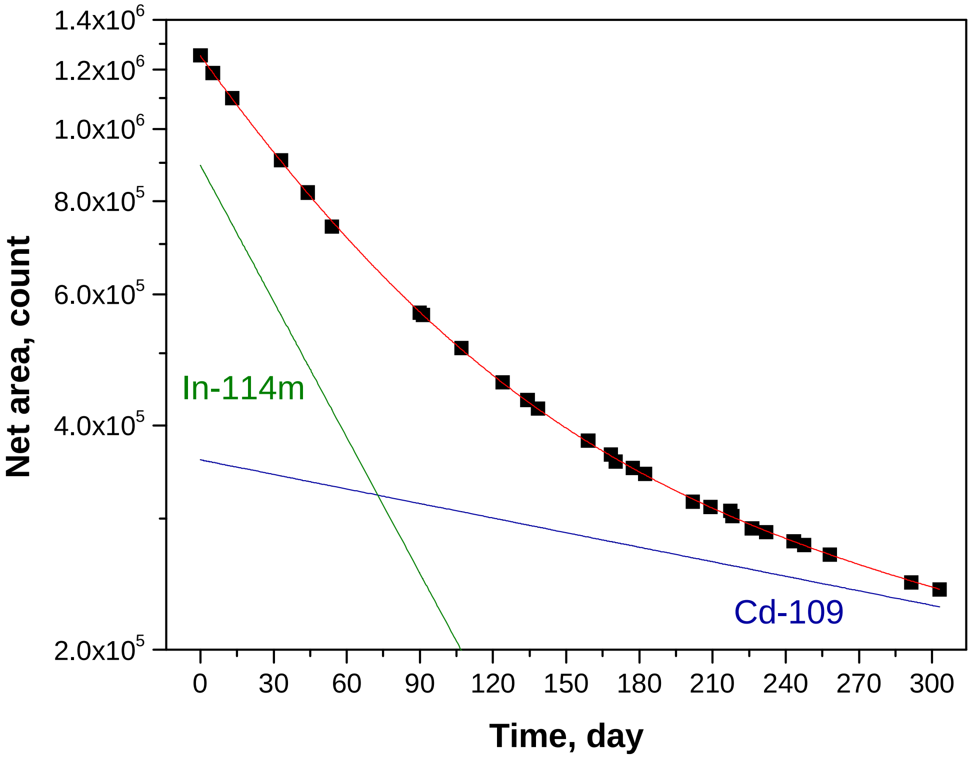

FIG. 2. Decay curve of ^{114m}In and ^{109}Cd.

[1] E.E. Tereshatov, M.Y. Boltoeva, and C.M. Folden III, Green Chem., **18**, 4616 (2016).

[2] E.E. Tereshatov and C.M. Folden III, *Progress in Research*, Cyclotron Institute, Texas A&M University (2015-2016) p. IV-66; DOI: 10.13140/RG.2.1.4682.9927.

Development of niobium electroplating for a future radioactive ^{93}Nb^{m} target

E.E. Tereshatov and C.M. Folden III

In preparation for a future experiment using a ^{93}Nb^{m} target ($t_{1/2}$ = 16.12 y), the heavy elements group has conducted experiments using stable Nb. The molecular plating technique was chosen for niobium electrodeposition. It is well known that organic solvents have larger electrochemical window (over which the electrolyte is stable) than aqueous solutions and isopropanol is the most popular organic medium for target preparation. In our experiments, an ICP-MS standard niobium solution (1 mg/mL) was used as a stock solution. A 1.3 mL aliquot of the stock solution was evaporated down to ~50 μL, diluted in 10 mL of isopropanol and transferred to the target cell. A high voltage supply capable of providing up to 1250 V and 20 mA was connected to the target cell and operated in constant voltage mode. The high voltage unit was upgraded to be controlled via PC. A GPIB interface was installed and LabVIEW software was created to monitor and record voltage/current data. Also, the new software allows for a constant current mode, although this was not utilized. In order to avoid solution overheating, a sine pulse mode was utilized. Niobium electrodeposition on aluminum foil (cathode) was carried out and the results obtained are shown in Fig. 1. The maximum current was set to 14 mA. Periodically (every hour) 0.3 – 0.5 mL of isopropanol was added to the cell to compensate for alcohol evaporation and to keep the solution volume at the same level. Approximately 5 min after that, a 100 μL aliquot was taken from the target cell solution and 100 μL of pure isopropanol was added to the cell. The niobium concentration in the isopropanol solution was determined by neutron activation analysis. The results obtained indicate that

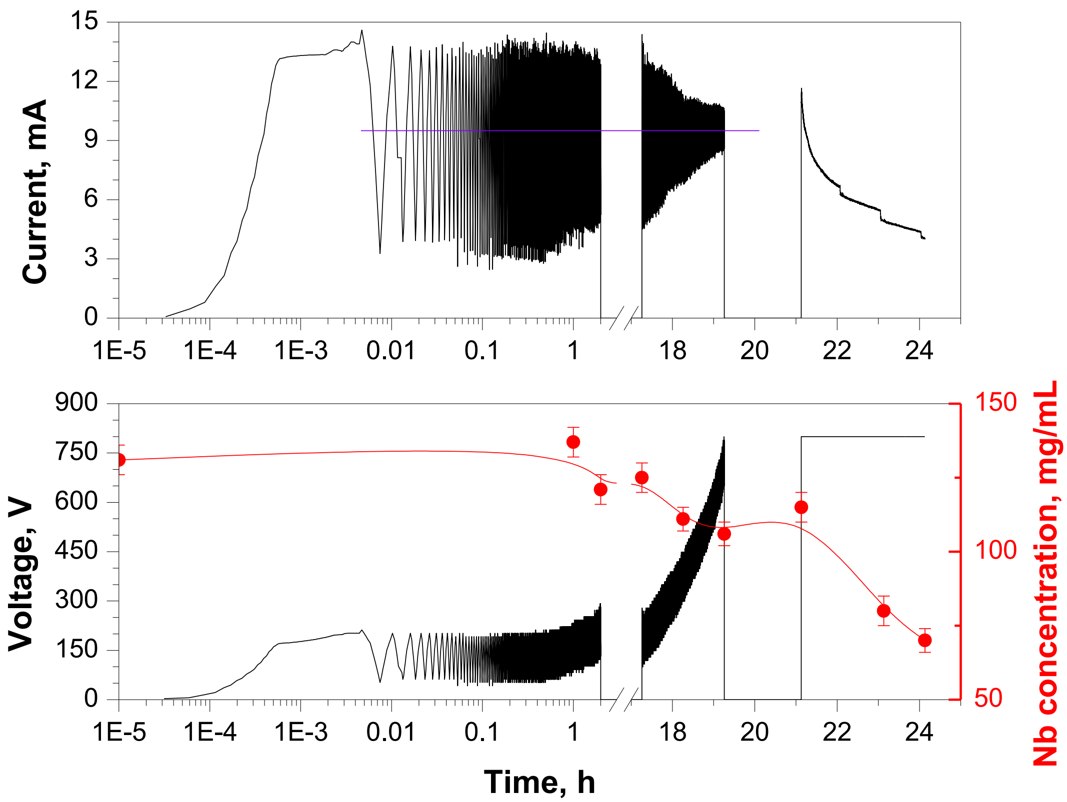

FIG. 1. Niobium electroplating from isopropanol solution.

there is no Nb deposition within the first hour of electroplating. During the second hour, the voltage was automatically increased a little bit due to the metal deposition. After 2 h, the high voltage was turned off and the isopropanol solution with niobium was left in the target cell overnight. The next day, a new aliquot was taken from the target cell before the high voltage was applied, to see if there was any dissolution of deposited material. As can be seen in Fig. 1, there is no significant loss of Nb. After that, the voltage was increased up to 800 V within the next 2 hours and the Nb concentration in the isopropanol decreased by 25%. A new 2 h pause was taken, and then the deposition mode was changed from sine pulse to constant voltage, because the system would have reached 1000 V within several minutes and we decided not to exceed this limit. Three more hours of electroplating resulted in almost 50% overall niobium deposition. Despite the presence of trace amounts of hydrofluoric acid in the ICP-MS standard (which leads to formation of a very stable oxyfluoro $NbOF_3$ complex and might be an obstacle for niobium electroplating), EDS and XPS analyses of the deposited layer (performed at the TAMU Materials Characterization Facility) indicate that niobium was electrodeposited mostly in the form of niobium oxide Nb_2O_3. The next step of this procedure development will be optimization of electrodeposition conditions.

PUREX separation of plutonium and uranium from fission products to measure elemental decontamination factors

K.J. Glennon[1,2] and C.M. Folden III[1]
[1]*Cyclotron Institute, Texas A&M University*
[2]*Department of Chemistry, Texas A&M University*

^{239}Pu is produced as a byproduct of UO_2 irradiation in a nuclear reactor, among other actinides and many fission products (FPs). These FPs are mostly elements of the 5th and 6th rows of the periodic table. The distribution of FPs relative to ^{239}Pu in the material is dependent upon multiple factors, including the burnup of the fuel and the neutron spectrum within the reactor. Therefore, by measuring the FP:^{239}Pu ratios within a spent fuel sample, we can learn more about the history of its irradiation [1]. This is an important analysis for nuclear security because Pu is fissile and may be used to make nuclear weapons.

It is likely, however, that any intercepted Pu will have already been chemically separated from the FPs. The most common process for Pu purification is the PUREX process, which employs typically 30% tributyl phosphate in kerosene or n-dodecane to selectively extract Pu and U from the other species present in spent fuel. If the decontamination factor (DF) of each FP is known throughout the PUREX process, the original FP:^{239}Pu ratio before purification may be obtained. It is rare, however, for reprocessing facilities to publish the DFs of each FP throughout their process [2]. Recent work this year has focused on obtaining the DFs for attribution elements like Cs and Eu throughout the PUREX process used at the Barnwell Nuclear Fuel Plant (BNFP), which was built in South Carolina but never operated commercially.

The process employed at the BNFP consists of 11 major steps. Within these steps, the facility would have accomplished codecontamination (purification of Pu and U together), partitioning of the feed into separate Pu and U streams, and then final purification of each stream. The first challenge in the current work was downsizing the 11-step industrial process to a smaller scale experiment that could be completed in the laboratory. The source for the process characterizes the Ru-Rh decontamination through each step [3], which serves as a benchmark to ensure the lab-scale process matches the specifications of the industrial reprocessing plant. Afterwards, experiments were performed to maximize the oxidation of Pu(III) to Pu(IV) using sodium nitrite. This is a crucial oxidation for the first step of the process. Experiments confirmed the optimal conditions from a Hanford study to be elevated temperatures (70 ^{o}C), low mass loading (4:1 Pu:$NaNO_2$), and an hour-long reaction time in 3 M HNO_3 [4]. The second challenge to overcome was the difference in U loading between the lab-scale and industrial-scale process. Because the sample of irradiated UO_2 in possession here is quite small (approximately 13 mg), the concentration of U in solution is roughly 1000 times less than in the industrial plant. This difference in concentration is expected to impact the DFs of the FPs. As a result, a study was performed to determine the magnitude of this impact. An initial control experiment was performed for the first step of the PUREX process as designed by the BNFP using our unaltered irradiated UO_2 sample. The DFs for several elements were obtained, as seen in Table I. A second experiment where depleted UO_2 will be added to our sample, such that the concentration of U in solution matches that used in the BNFP process, will be completed shortly hereafter and compared to the preliminary results in Table I.

Table I. Decontamination factors (DFs) for elements in step one of the control study. The U concentration in the initial aqueous solution was 0.93 mM.

Nuclide	**Decontamination factor**
^{241}Am	7.6 ± 0.9
^{144}Ce	11.2 ± 0.7
^{154,155}Eu	6.1 ± 0.5
^{125}Sb	62 ± 11
^{106}Ru	5.6 ± 0.6
^{134,137}Cs	3500 ± 1300

In most cases, errors may be improved with longer counting times. For Cs, the error is quite high because the DF is very large and the element reaches its detection limit easily. The DF of each element will continue to increase as further steps of the process are performed. Pu recovery was measured by alpha spectrometry and meets the expected 98% recovery through step one.

The results so far present new elemental DFs for step one of the BNFP process with one thousandth of the U concentration. Future work will include the elemental DFs for all 11 major steps of the BNFP process with the proper U concentration.

[1] S.S. Chirayath, J.M. Osborn, and T.M. Coles, Sci. Glob. Secur. **23**, 48 (2015).

[2] P.M. Mendoza, S.S. Chirayath, and C.M. Folden III, Appl. Radiat. Isot. **118**, 38 (2016).

[3] M. Benedict, T.H. Pigford, and H.W. Levi: Nuclear Chemical Engineering, Second Edition. Fuel Reprocessing, Section 10.4. (McGraw-Hill Professional, 1981).

[4] C.A. Colvin, U.S. Department of Energy. Report Number HW-79354

Pionic fusion of ^{4}He + ^{12}C using the ParTI array

A. Zarrella, A. Bonasera, J. Gauthier, L. Heilborn, A. Jedele, A.B. McIntosh,
A. Rodriguez Manso, and S.J. Yennello

Pionic fusion is the process by which two nuclei fuse and then deexcite by the exclusive emission of a pion. The resulting compound nucleus is left in or near its ground state [1]. The process requires that nearly all of the available kinetic and potential energy in the colliding system be concentrated into two degrees of freedom - the rest mass and kinetic energy of the emitted pion. Thus, the energy of the emitted pion is limited by the number of available final states of the fusion residue [2]. The combination of limited available energy and the extreme coherence required in the process ensures that the pionic fusion channel is greatly suppressed. Indeed, the measured pionic fusion cross sections range from hundreds of nanobarns for the lightest systems (He + He) to hundreds of picobarns as one moves to larger systems ($A_{tot} = 6 - 24$) [2-12].

An experimental effort to measure the pionic fusion process at the Cyclotron Institute was undertaken in August of 2016 when the Momentum Achromat Recoil Spectrometer (MARS) [13] and the Partial Truncated Icosahedron (ParTI) phoswich array [14] were used to perform a coincidence measurement of pionic fusion from the ^{4}He + ^{12}C reaction. Pionic fusion events of interest will produce a π^{+} which will potentially be detected in the ParTI array and a ^{16}N residue which will potentially be detected at the back of MARS. The analysis for that experiment is currently underway. In addition to the pionic fusion experiment, four ParTI phoswich detectors were transported to the Paul Scherrer Institute (PSI) facility in Switzerland where the detector response from incident charged pions was characterized. Using the data from the PSI experiment and the data from the phoswich calibration experiment from 2015, a calibration method was developed for the ParTI array [14].

For the pionic fusion experiment, the K500 Superconducting Cyclotron at the Texas A&M University Cyclotron Institute was used to produce a beam of 55 MeV/u ^{4}He particles which was impinged on a ^{12}C target in the MARS beamline. MARS was used to separate reaction products produced around 0° and transport them to the focal plane where they were detected using a silicon stack. The front silicon in the stack was a 5 cm x 5 cm position-sensitive strip detector and the second silicon was a 5 cm x 5 cm single area detector. MARS was tuned to 4 different magnetic rigidities which sampled energy windows inside the kinematically allowed range of pionic fusion residues. Also, background data was taken directly above and below the allowed rigidity range.

During the course of the experiment, it was determined that the position-sensitive silicon detector's thickness varied substantially over the active area. As a result, at the end of the experiment an ^{17}O beam was transported to the back of MARS and scanned across the face of the detector in order to map the thickness by measuring the energy loss of the beam as a function of position on the detector. The result of that measurement can be seen in Fig. 1 which shows the 3-dimensional detector thickness map. Using this information, the two silicons in the stack were energy-calibrated. Fig. 2 shows the E_{tot} vs. Y-position particle separation at the back of MARS. Due to the nature of MARS, the Y-position is a measurement of the particle's mass-to-charge ratio. On the detector are spots corresponding to the A = 2Q

+ 1 line (where A is the number of nucleons and Q is the charge state of the fragment) and the A = 2Q + 2 line. The A = 2Q + 1 line begins with A = 7, Q = 3 at around 17 MeV and ends with A = 15, Q = 7 at around 45 MeV. The A = 2Q + 2 line begins with A = 12, Q = 5 at around 29 MeV and ends with A = 18, Q = 8 at around 49 MeV.

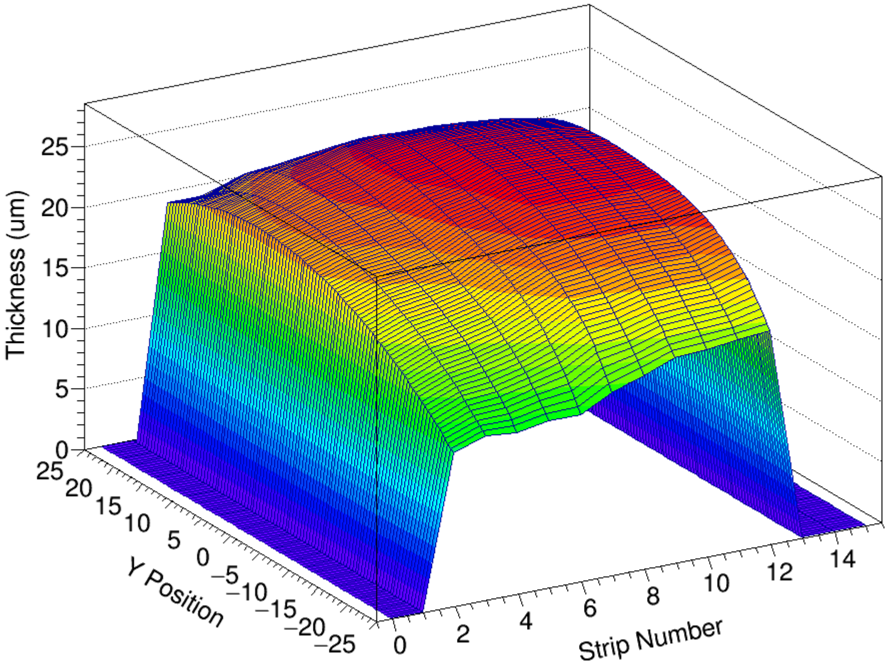

FIG. 1. The measured thickness over the face of the strip silicon detector used in the pionic fusion experiment. On the x-axis is the strip number of the X1 type detector, on the y-axis is the y-position along each strip of the detector. Along the z-axis is the thickness in microns measured at that detector position.

The separation in Fig. 2 is not sufficient, however, to identify specific particle species due to charge state ambiguity. The $^{16}N^{7+}$ particles of interest, for instance, are indistinguishable from $^{16}O^{7+}$ in this particle identification space. In order to solve this problem, the dE (energy deposited in the strip silicon) can be plotted as a function of the sampled thickness of the detector from the detector map in Fig. 1 for particles in a single E_{tot} vs. Y-position spot where E_{tot} = dE + E. Fig. 3 is an example of this process for the A = 12, Q = 5 spot. A clear separation between $^{12}B^{5+}$ and $^{12}C^{5+}$ can be seen. The current state of the MARS analysis is concentrated on incorporating the various efficiencies and uncertainties necessary for producing production cross sections for the detected species.

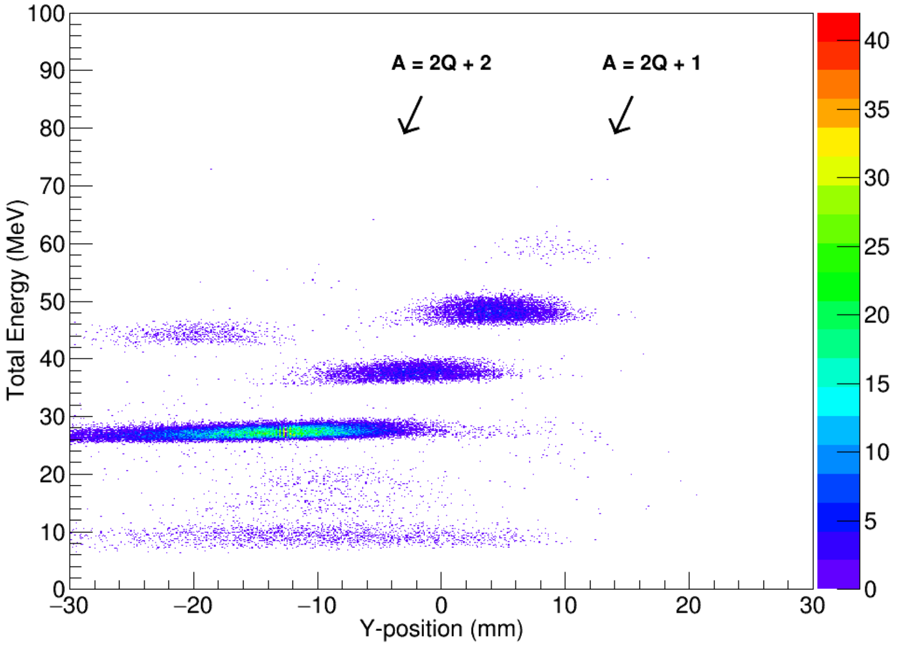

FIG. 2. The total energy vs. y-position plot produced by residues at the back of MARS. The spots correspond to single mass and charge species.

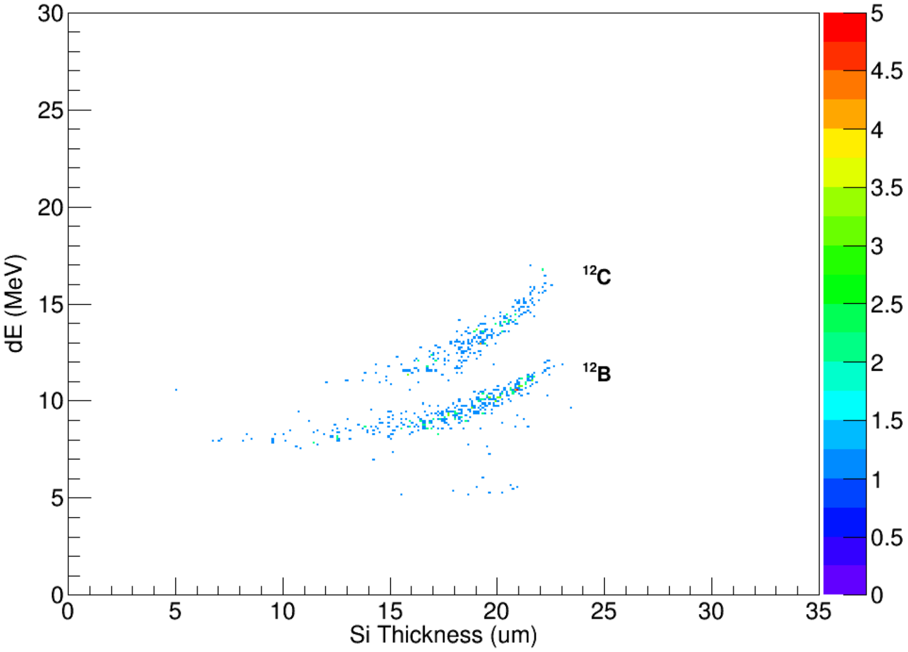

FIG. 3. A plot of the energy deposited in the strip silicon vs. the thickness sampled by the particle for only particles inside the A = 12, Q = 5 spot from Fig. 2. This plot separates particle species by atomic number.

The second major experimental effort from the last year was the ParTI phoswich characterization experiment which was conducted at PSI. The ParTI array was designed for use in the pionic fusion experiment for the purpose of identifying charged pions. It is comprised of 15 plastic/CsI(Tl) phoswiches arranged on the faces of a truncated icosahedron geometry. The phoswiches were mounted at the back of the πM1 beamline where charged pions were degraded by a variable-thickness copper degrader array and impinged on the ParTI detectors. The detector responses were recorded using the SIS3316 digitizer [15]. These charged pion events are the first examples of charged pion implantations in the ParTI phoswiches. Fig. 4 shows digitized waveforms from the PSI experiment – a π^+ event in panel (a) and a π^- event in panel (b). Both of these waveforms display the characteristic muon decay pulses following the initial implantation pulses which identify them as pion primary events.

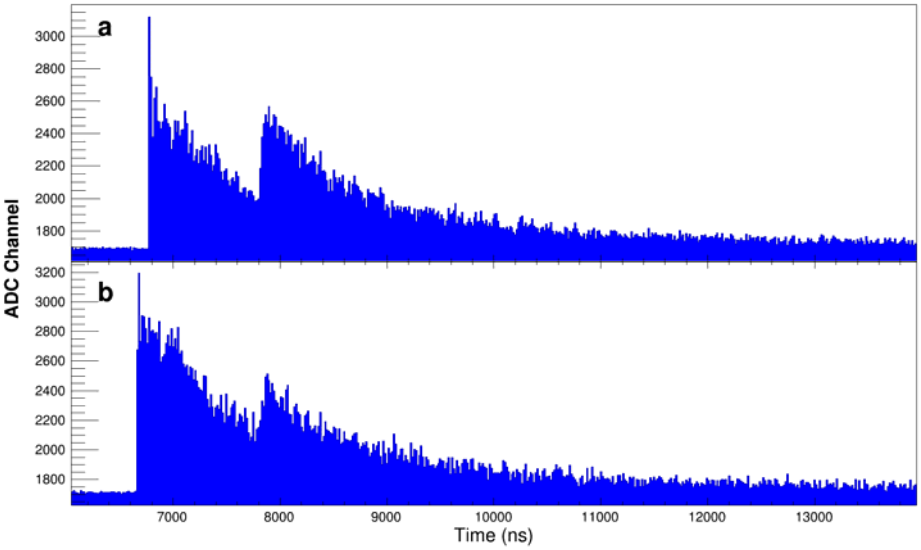

FIG. 4. Examples of phoswich response waveforms with a muon decay secondary pulse for a π+ (a) and π- (b) event. On the horizontal axis is time in nanoseconds and the vertical axes are the digitized channel recorded by the SIS3316. The initial response is due to the implantation of the charged particle in the phoswich. The second peak in the response is produced by the decay of the muon implanted in the detector and is a characteristic of a pion primary event.

Independent of the presence of the muon decay peak, a fast vs. slow pulse shape analysis can be performed on the charged particle implantation pulses to produce particle identification lines. Fig. 5 shows these particle identification lines from the PSI experimental runs. On the vertical axis is the integrated fast signal from the phoswich response which is proportional to the energy deposited in the plastic scintillator component of the phoswich. The horizontal axis is the integrated slow signal which is proportional to the energy deposited in the CsI(Tl) component of the phoswich. In both panels, lines can be seen corresponding to pion, proton, and deuteron events (labeled π, p, and d, respectively). In panel (a), the pion line is produced by a π^+ beam and in panel (b) the pion line is produced by a π^- beam. The dearth of events in the π^- line is impacted by the absorption of the pions by nuclei in the detector. The effectiveness of the muon decay trigger system that was developed for the SIS3316 was also explored during the PSI experiment. It was found that the muon decay trigger increased the ratio of pion events to background events by approximately an order of magnitude.

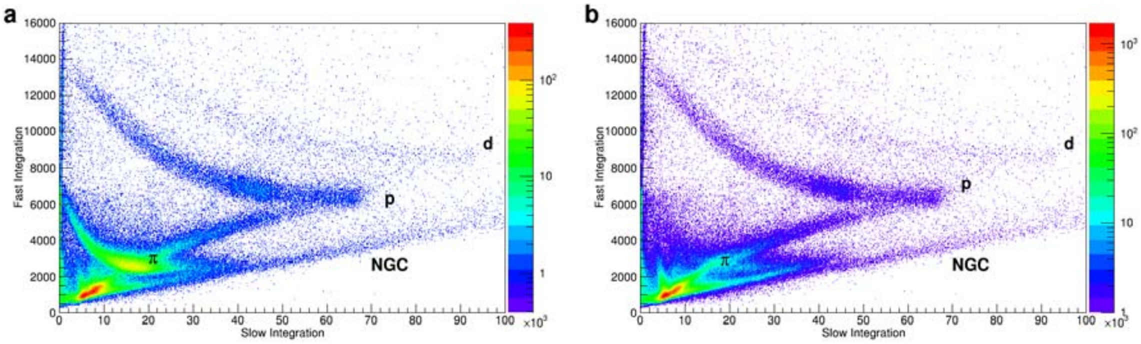

FIG. 5. Data for proton and π^+ beams (a) and proton and π^- beams (b) collected during the PSI experiment. The vertical axes are the fast integrations of the waveforms from the implantation of the charged particles in the phoswich. The horizontal axes are the slow integrations of the waveforms. Moving upward from 0 on the fast integration axis is the neutron/gamma/cosmic (NGC) line, a region corresponding to position (electron) events in panel a (b), a line corresponding to charged pions, the line corresponding to protons, and the line corresponding to deuterons.

Over the course of the next year, the analysis of residues collected at the back of MARS will continue through the inclusion of various detection and instrument efficiencies. This will result in measured cross sections for all species identified. The data collected by the ParTI array during the pionic fusion experiment will be calibrated using the PSI data and the method detailed in reference [14]. The search will then begin for pionic fusion coincidences - a ^{16}N fusion residue at the back of MARS in the same event as a charged pion in the ParTI array.

[1] P. Braun-Munzinger and J. Stachel. Ann. Rev. Nucl. Part. Sci. **37**, 97 (1987).
[2] D. Horn, *et al*. Phys. Rev. Lett. **77**, 2408 (1996).
[3] Y. Le Bornec, *et al*. Phys. Rev. Lett. **47**, 1870 (1981).
[4] L. Joulaeizadeh, *et al.* Phys. Lett. B **694**, 310 (2011).
[5] W. Schott, *et al*. Phys. Rev. C **34**, 1406 (1986).
[6] M. Andersson, *et al.* Nucl. Phys. **A779**, 47 (2006).
[7] M. Andersson, *et al.* Phys. Lett. B **481**, 165 (2000).
[8] M. Andersson, *etal.* Phys. Scr. **T104**, 96 (2003).
[9] L. Bimbot, *et al.* Phys. Rev. C **30**, 739 (1984).
[10] L. Bimbot, *et al.* Phys. Lett. B **114**, 311 (1982).
[11] J. Homolka, *et al.* Phys. Rev. C **38**, 2686 (1988).
[12] N. Willis, *et al.* Phys. Lett. B **136**, 334 (1984).
[13] R.E. Tribble, *et al*. Nucl. Instrum. Methods Phys. Res. **A285**, 441 (1989).
[14] A. Zarrella, *et al.* Physics Procedia (Accepted).
[15] http://www.struck.de/sis3316.html.

Detailed characterization of neutron-proton equilibration in dynamically deformed nuclear systems

A. Rodriguez Manso, A.B. McIntosh, A. Jedele, K. Hagel, L. Heilborn, Z. Kohley, L.W. May,
A. Zarrella, and S.J. Yennello

We extend the study of neutron-proton (NZ) equilibration in dynamically deformed nuclear systems presented in [1] by investigating further the correlations between the two largest fragments produced in semi-peripheral collisions of ^{70}Zn+^{70}Zn, ^{64}Zn+^{64}Zn, ^{64}Ni+^{64}Ni and ^{64}Zn+^{64}Ni at 35 MeV per nucleon measured at the Cyclotron Institute at Texas A&M University. The extent of NZ equilibration is investigated using the rotation angle as a clock for the equilibration. Fragments which are initially dissimilar in NZ composition converge exponentially with consistent rate constants across a wide variety of reaction partners and systems, indicating the equilibration follows first order kinetics. The statistical and dynamical components are separated on average. The equilibration curve for the purely dynamical is consistent with the overall equilibration curve, indicating the robustness of the method to statistical contamination. A small systematic effect in the composition is observed for reactions of a relatively neutron poor projectile with a neutron-rich target, consistent with physical expectations. Equilibrium composition and rate constant values are extracted from the data. No significant differences in the rate constants are noted between systems of different initial composition. This work was recently published[2].

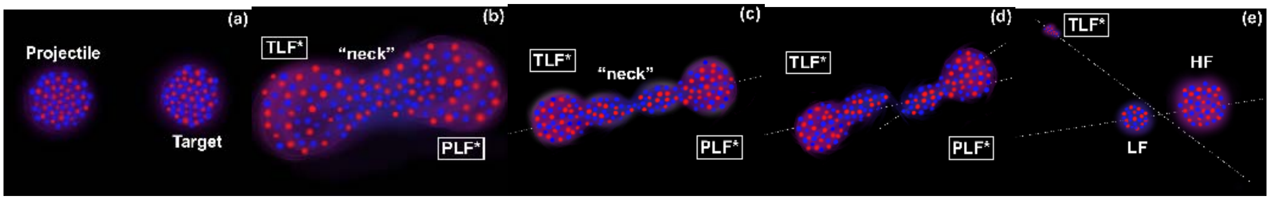

FIG. 1. Illustration of dynamical deformation and decay following a heavy-ion collision. Panel (a) shows a projectile approaching target. In panel (b), the projectile has rotated around the target forming a low-density "neck" region. In panel (c), the excited PLF* and TLF* have moved further away from each other and stretched into a "string of pearls" with the smallest fragments forming out of the neck region. Panel (d) represents the breaking of the nuclear system with the PLF* separating from the TLF*. Panel (e) shows the subsequent separation of the PLF* into HF and LF [3].

The general features of heavy-ion reactions near the Fermi energy proceeding through extremely deformed intermediate states are illustrated in Fig. 1[3]. Initially, there are the target and projectile, in panel(a), and a deeply penetrating contact between them with slight compression. As the excited Projectile-Like Fragment (PLF*) and excited Target-Like Fragment (TLF*) begin to separate from each other, in panel(b), a low-density neck of nuclear material is formed between them due to, in a classical description, nuclear viscosity and surface tension. Neutrons are driven preferentially to the low-density neck due to the density dependence of the asymmetry energy. This is illustrated in the figure by the excess of neutrons (in blue) in the neck and the relatively higher concentration of protons (in red) in the PLF* and TLF* regions. The velocity gradient stretches the system and the competition of the velocity gradient with surface tension amplifies instabilities, panel(c); until the velocity gradient stretches the system beyond the capabilities of the nuclear force to hold it together and the system ruptures, panel(d). After one rupture of the neck, the now separated PLF* and TLF* are likely to be strongly deformed along the separation axis and, because of their deformation, they are likely to break again. The subsequent breakup of the PLF* into two pieces (the heavy fragment, HF, and the light fragment, LF) is illustrated in panel(e). If some time elapses between the PLF*-TLF* scission and the HF-LF scission, the angular momentum of the PLF* causes rotation through an angle so that the relative velocity of HF and LF makes a non-zero angle with the PLF*-TLF* separation axis, the center-of-mass velocity of the PLF*. If the angular velocity can be deduced and the breakup timescale is short relative to the rotational period, the rotation angle can be used as a clock. Since the neck is neutron rich at the time of the first scission, nucleon flow between regions of the deformed PLF* allow NZ equilibration to occur between the developing HF and LF. Thus measuring the composition of HF and LF as a function of the rotation angle allows direct observation of the time dependence of NZ equilibration.

Some highlights of the work involve the study of the PLF*'s deformation alignment. Representative angular distributions, α, are illustrated in the left panel of Fig. 2, for the ^{70}Zn+^{70}Zn system.

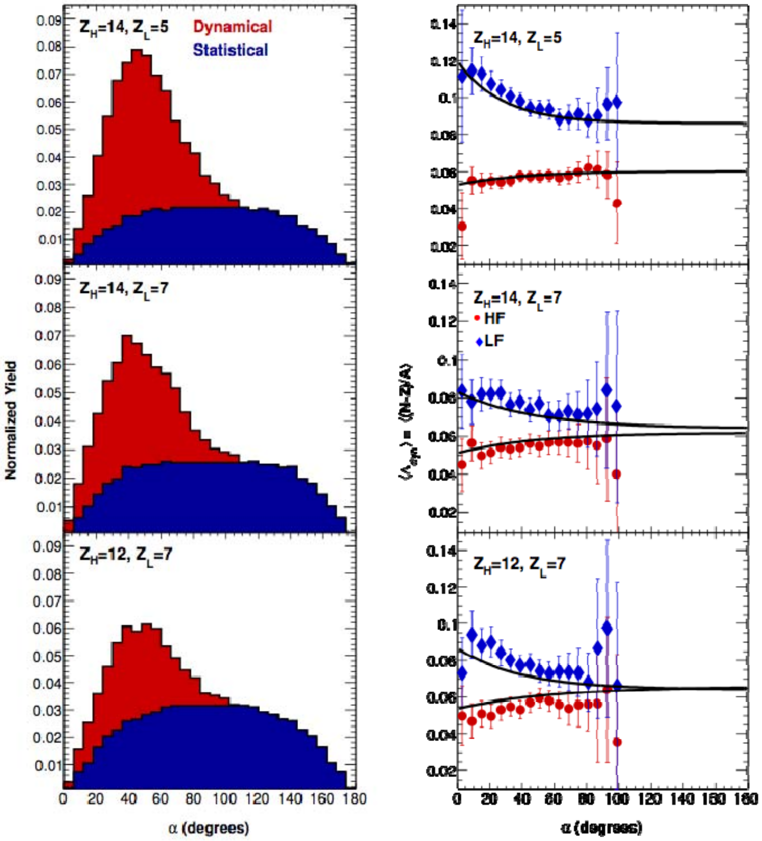

FIG. 2. System ^{70}Zn+^{70}Zn, where three representative combinations of HF and LF are shown: $Z_H=14$, $Z_L=5$ (upper panel), $Z_H=14$, $Z_L=7$ (middle panel) and $Z_H=12$, $Z_L=7$ (lower panel). Left panel: normalized angular distribution α where the blue area represents the statistical contribution and the remaining area (red) represents the dynamical contribution. Right panel: Average dynamical composition, $<\Delta_{dyn}>$, as a function of the decay alignment α. The black lines correspond to the exponential fit of the average composition as a function of the decay alignment.

Three representative combinations of HF and LF are shown. They are strongly peaked with $\alpha<90^0$. The distributions fall toward 0 at $\alpha=0^0$ and $\alpha<180^0$, a consequence of the geometry of the detector array which gives a reduced detector efficiency due to double hits. This impacts particles at a particular angle α the same regardless of the mechanism of their origin. The total yield can be understood as arising from two different mechanisms of production: statistical decay and dynamical decay. The observed yield for $\alpha>90^0$ comes primarily from statistical decays from a rotating source which produces an angular distribution that is symmetric about 90^0. The excess observed yield for $\alpha<90^0$ is consistent with dynamical decay, most probable at the smallest angles and steadily decreasing in probability with increasing angle.

In order to disentangle dynamical from statistical decay contributions to the yield, we describe the total yield as the sum of the statistical and dynamical components $Y_{total}=Y_{dyn} + Y_{stat}$. We assume the statistical yield is symmetric at about 90^0 and that the yield at large α (above 108^0) is entirely statistical. Modeling the precise shape of the statistical component requires a detailed knowledge of the angular distribution of intermediate-mass fragments statistically emitted from a large nucleus for a range of angular momenta. We use instead our estimate of the statistical yield based on the measured yield at large α to show that our subsequent equilibration results are quite insensitive to the accounting of statistical decay. Our estimates of the statistical (in blue) angular distribution are shown in the left panel of Figure(2). The red area corresponds to the dynamical contribution.

Furthermore, we present a method to extract the dynamical composition as a function of α, describing the observed composition as a combination of the composition of the dynamical component and the statistical component, each weighted by their fractional yield as $<\Delta>= <\Delta_{stat}>f_{stat} + <\Delta_{dyn}>f_{dyn}$. We observe that the composition of the statistical component is independent of the angle for $\alpha>100^0$, and assume that this is true also for $\alpha<100^0$. This enables us to calculate $<\Delta_{dyn}>$ as a function of α, presented in the right panel of Fig. 2. Exponential fits from the overall composition are represented as black lines for easier visual comparison.

The LF (HF), which originates close to (far from) the neck region and therefore is neutron-rich (neutron-poor), starts off with a large (small) initial composition $<\Delta>$ for small alignment angles. As the angle of rotation increases, surface tension drives the system towards sphericity, keeping the HF and LF in contact longer, resulting in more time to exchange nucleons. The opportunity to exchange nucleons allows the asymmetry energy to drive a net neutron flow out of the LF and into the HF to equilibrate the chemical potentials of the two nascent fragments. This gives rise to similar values of the composition for the LF and the HF at higher alignment values. The $<\Delta_L>$ changes by a larger amount than the $<\Delta_H>$. This is a consequence of mass conservation, considering that the HF is larger than the LF and thus, the exchange of nucleons affects the composition of the latter more. The dynamical yield generally follows the same trend as the overall yield. The compositions are slightly more extreme for the purely dynamical component (i.e. the LF is slightly more neutron-rich and the HF is slightly more neutron-poor). It is not surprising that a statistical “background" of constant composition would mute the signal present in the purely dynamical. Applying this correction to isolate the dynamical component results in significantly larger uncertainties. The rate of change of the composition is essentially unaffected by the correction and the precise values of the composition are modified slightly. We continue the analysis on the inclusive composition rather than the dynamical, with the knowledge that the rates extracted are minimally impacted by the statistical contribution, and our resulting uncertainties are minimized by avoiding the systematic uncertainty introduced by the subtraction.

We expanded our study to other projectiles and targets. The fits of $<\Delta>$ as a function of α are performed for thirty-two pairings of Z_H, Z_L for the ^{70}Zn+^{70}Zn, and ^{64}Zn+^{64}Zn systems, for twenty-five pairings for the ^{64}Ni+^{64}Ni and for sixteen pairings for the ^{64}Zn+^{64}Ni asymmetric system. Fig. 3 shows the average composition $<\Delta>$ as a function of the decay alignment α for the $Z_H=12$, $Z_L=7$ pair in all the systems studied. From the comparison of the different panels it is observed that HF and LF for the ^{70}Zn+^{70}Zn and ^{64}Ni+^{64}Ni systems have $<\Delta>/\alpha$ correlations that are essentially the same. The ^{64}Zn+^{64}Zn is less neutron-rich than the other two symmetric systems. We see that the $<\Delta>/\alpha$ correlation is shifted to lower values (i.e. lower equilibrium composition) but the rate constant and the change from initial to final values are essentially the same. The comparison between the ^{64}Zn+^{64}Zn and the ^{64}Zn+^{64}Ni systems is quite interesting. The initial composition for the HF is essentially the same for the two, but the composition of the LF is significantly more neutron rich for the system with the more neutron-rich target. For both systems, the composition of HF and LF approach a common value, but this value is more neutron rich for the system with the neutron-rich target. While the magnitude of these shifts is not far from the statistical errors on each individual point, the systematic shift of all the points from one system to the other is consistent with the expected effects of changing the neutron richness of the target. More details on these results have been published in [3].

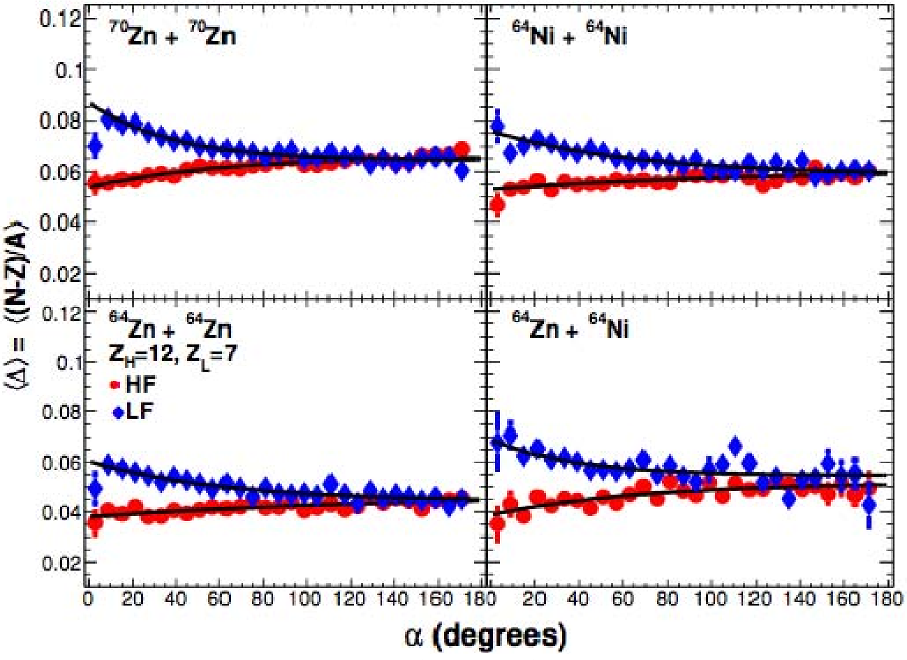

FIG. 3. Average composition $<\Delta>$ as a function of the decay alignment α for the $Z_H=12$, $Z_L=7$ pair in all systems studied (i.e. ^{70}Zn+^{70}Zn, ^{64}Zn+^{64}Zn, ^{64}Ni+^{64}Ni and ^{64}Zn+^{64}Ni. The HF is represented in red circles and the LF in blue rhombi. The black lines correspond to the exponential fits of the data.

[1] A. Jedele *et al.*, Phys. Rev. Lett **118**, 062501 (2017).
[2] A. Rodriguez Manso *et al.*, Phys. Rev. C **95**, 044604 (2017).
[3] A. Poulsen, oxidantshappencomics.wordpress.com, 2016.

Neutron-proton equilibration in dynamically deformed nuclear systems: multifragmentation

A. Rodriguez Manso, A.B. McIntosh, J. Gauthier, L. Heilborn, A. Jedele,
A. Zarrella, and S.J. Yennello

Recently we have been studying neutron-proton equilibration between the largest two fragments produced when beams of ^{70}*Zn*, ^{64}*Zn* and ^{64}*Ni* are accelerated to *35* MeV per nucleon by the *K500* Cyclotron at Texas A&M University and focused onto thin foils of ^{70}*Zn*, ^{64}*Zn* and ^{64}*Ni* to obtain symmetric and asymmetric collisions [1,2]. The rotation angle has been used as a clock for the equilibration of the neutron-proton composition where the initially dissimilar fragments converge exponentially with consistent rate constants across a wide variety of reaction partners and systems, indicating that the equilibration follows first-order kinetics.

Of further interest is the investigation of neutron-proton equilibration between the three largest fragments coming from the excited Projectile-Like Fragment (PLF*) [3,4]. The physical idea is depicted in Fig. 1, where the (PLF*) breaks into a heavy fragment (HF), a light fragment (LF) and a third lighter fragment (3F).

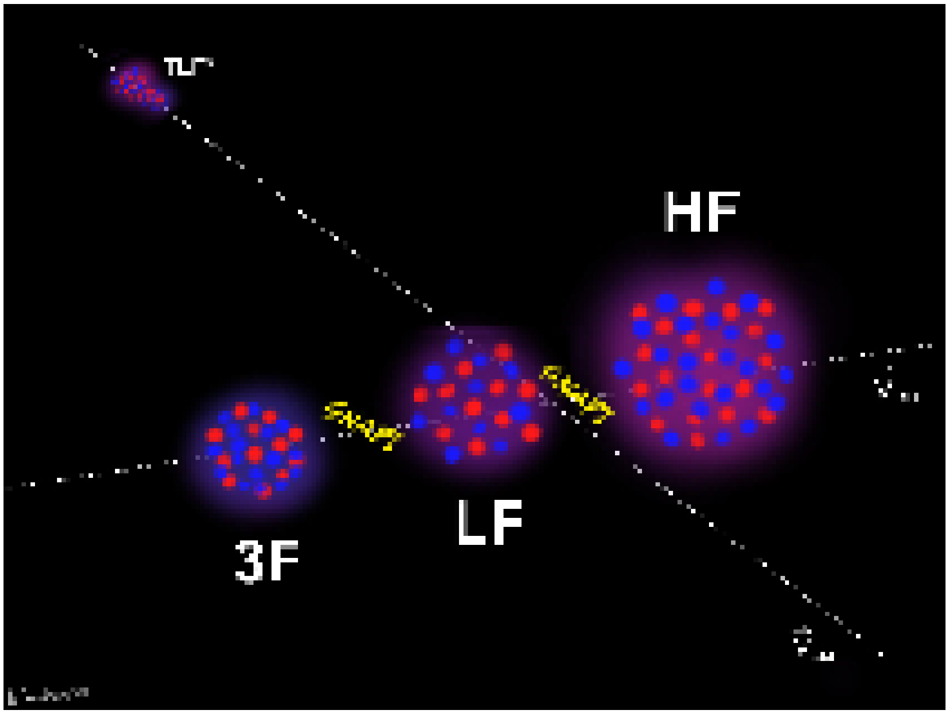

FIG. 1. Illustration of the last phase of dynamical deformation and decay after a heavy ion collision [5]. The excited PLF* and TLF* have broken apart and moved further away from each and the PLF* have subsequently separated into HF, LF and 3F.

The three body system's Z correlation can be studied using symmetrized Dalitz plots like the one shown in Fig. 2. The left panel of the figure is a cartoon that depicts how the events fill in the space of the triangle. The center of the triangle corresponds to three approximately equal sized fragments. The edges of the triangle, between two vertices, corresponds to one small fragment and two large ones approximately equally sized. Finally, if the vertices of the triangle are filled in, this hints to large cross sections for two small plus one large fragments. The right panel of Fig. 2, shows our data for all the *Z's* included in the analysis. The region where the data is peaked corresponds to one large and two smaller, equally sized fragments.

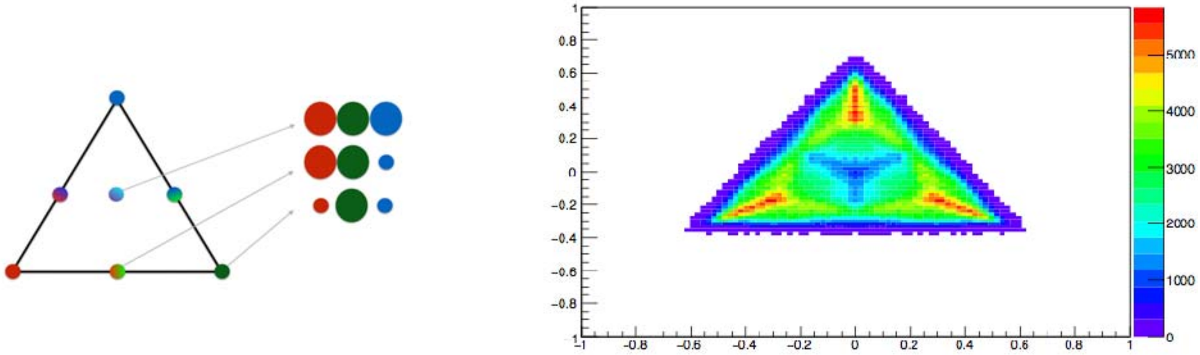

FIG. 2. *Z* correlation for the HF, LF and 3F studied using symmetrized Dalitz plots.

The fragments' velocity distributions in the direction of the beam are used to establish the specific fragments that correspond to the PLF* daughters. Fig. 3 illustrates the normalized yield as a function of the velocity distributions for the HF (in red), the LF (in blue) and the 3F (in green), in the direction of the beam. The distributions shown are from the symmetric $^{70}Zn+^{70}Zn$ system for three representative combinations of HF, LF and 3F: $Z_H = 14$, $Z_L = 5$, $Z_3 = 3$ (upper panel), $Z_H = 14$, $Z_L = 7$, $Z_3 = 3$ (middle panel), and $Z_H = 12$, $Z_L = 7$, $Z_3 = 3$ (lower panel). The dashed lines (from right to left) correspond to the beam velocity (i.e., $v = 0.27c$) and half of the beam velocity (i.e., $v = 0.13c$), respectively. The 3F is produced at velocities higher than mid-velocity and lower than both the LF and HF. The LF is produced at velocities higher than mid-velocity and lower than the HF, which is produced closer to the beam velocity. As the fragments get smaller, the velocity distribution broadens. HF, LF and 3F are peaked above mid-velocity which indicates that the three of them originate from the PLF*.

There seems to be a hierarchy in the velocity distributions that is strongly correlated to the charge sorting: the HF is, on average, the fastest one in the beam direction and appears to be forward with respect to the LF and 3F, while the second heaviest (LF) is the second fastest fragment in the beam direction and appears to be forward with respect to 3F. The three body study is currently ongoing.

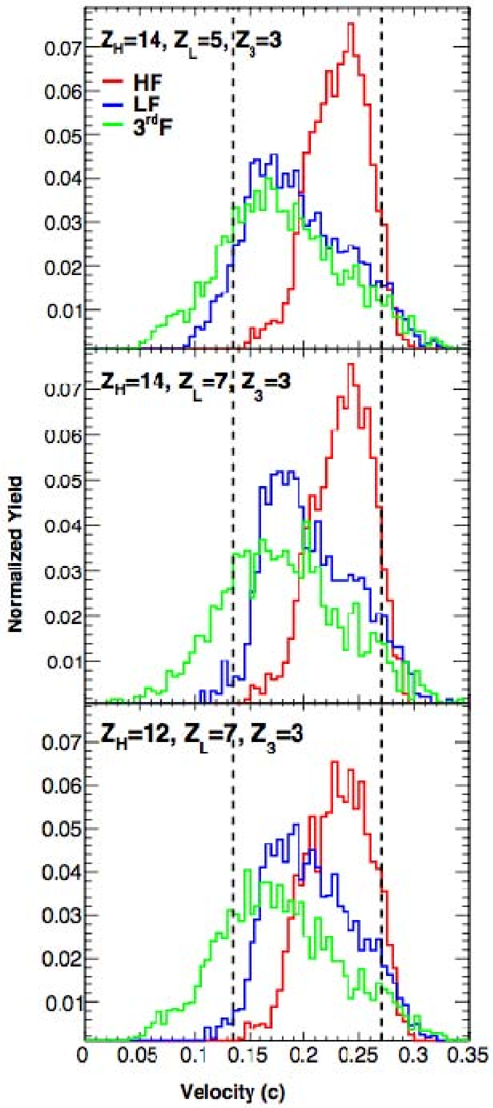

FIG. 3. Normalized velocity distributions for the HF, LF and the 3F in the direction of the beam. The HF is represented in red, the LF in blue and the 3F in green. The distributions correspond to the ^{70}Zn+^{70}Zn system for three representative combinations of HF, LF and 3F: $Z_H = 14$, $Z_L = 5$, $Z_3 = 3$ (upper panel), $Z_H = 14$, $Z_L = 7$, $Z_3 = 3$ (middle panel), and $Z_H = 12$, $Z_L = 7$, $Z_3 = 3$ (lower panel). The dashed lines (from right to left) correspond to the beam velocity (i.e., v = 0. 27c) and mid-velocity (i.e., v = 0.13c), respectively.

[1] A. Jedele *et al.*, Phys. Rev. Lett **118**, 062501 (2017).

[2] A. Rodriguez Manso *et al.*, Phys. Rev. C **95**, 044604 (2017).

[3] C. Colin *et al.*, Phys. Rev. C **67**, 064603 (2003).

[4] S. Hudan *et al.*, Phys. Rev. C **80**, 064611 (2009).

[5] A. Poulsen, oxidantshappencomics.wordpress.com, 2016

Neutron-proton equilibration in dynamically deformed systems at E=15, 25, 35 and 45 MeV/nucleon

A. Jedele, A.B. McIntosh, J. Gauthier, L. Heilborn, A. Rodriguez Manso, A. Zarrella, and S.J. Yennello

Recent work [1,2] has shown NZ equilibration follows first-order kinetics within excited projectile-like fragments (PLF*) in ^{70}Zn, ^{64}Zn and ^{64}Ni reaction systems at 35MeV/nucleon. Future experiments have been proposed to examine the characteristics of NZ equilibration in ^{40}Ca+^{64,70}Zn at 15A, 25A, 35A and 45MeV/nucleon with the NIMROD array [3].

Constrained Molecular Dynamics (CoMD) [4] simulations were performed for ^{40}Ca+^{64,70}Zn reaction systems at 45MeV/nucleon and the ^{40}Ca+ ^{64}Zn reaction system at 35MeV/nucleon. For each reaction system 10,000 events were analyzed and fragments were sorted based on atomic number and velocity. The heaviest fragment (HF) from the excited projectile-like fragment was required to have a HF>6 and a velocity greater than 0.12c (~30% of v_{beam} for 45 MeV/nucleon systems). For the second heaviest fragment (LF), LF>3 and v_L>0.08c. The velocity requirement was to ensure fragments are

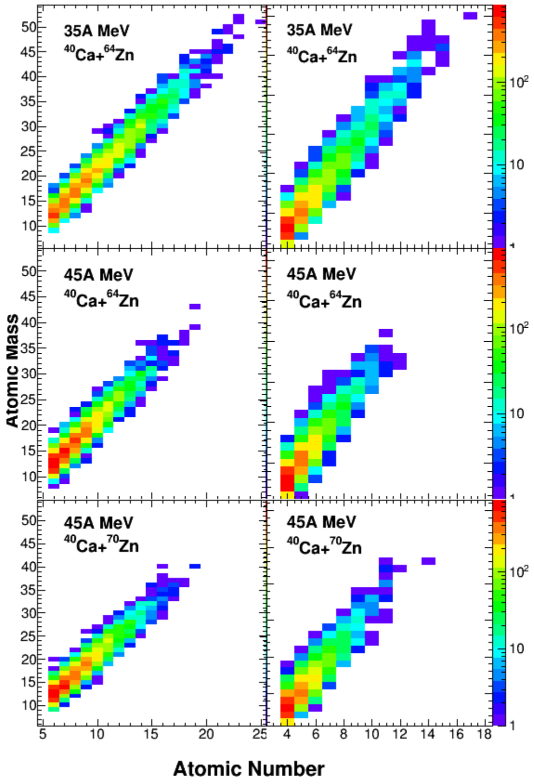

FIG. 1. The mass number vs. atomic number of the HF (left) and LF (right) for the three reaction systems. The ^{40}Ca+^{64}Zn at 35 MeV/nucleon is on the top row; ^{40}Ca+^{64}Zn at 45 MeV/nucleon in the middle and ^{40}Ca+^{70}Zn at 45 MeV/nucleon in the bottom. For all 6 distributions, the greatest yield is seen at low Z (Z=7 for HF and Z=4 for LF). The 35 MeV/ nucleon system has a greater atomic number and mass number distribution.

primarily originating from the PLF*. Approximately 5% of events passed the above cuts for all three reaction systems. The mass number versus the atomic number for both fragments and all reaction systems is shown in Fig. 1. The largest yield is shown at low Z, especially for the higher energy systems. The lower energy system has a greater range in atomic number for both HF and LF. The multiplicity distribution for all fragments including those originating from the TLF* ranges from 10-70 and is peaked at 55 for the 45MeV/nucleon systems. For the 35MeV/nucleon system, the multiplicity distribution ranges from 10-60 and is peaked at 45.

For detector design, the angular distribution and energy as a function of angle were considered. The energy as a function of angle is shown in Fig. 2. For both HF and LF, the energy is centered significantly lower than beam energy. The angular distributions for both the 35 and 45 MeV/nucleon reaction systems are very similar. The lab angles ranges from 0-40° for HF and 0-60° for LF. The vast majority of particles were located below 20° for HF and below 40° for LF. Based on the angular distribution, rings 2-9 (3.6-45.0°) in NIMROD will be of highest priority. Looking at the energy, the majority of HF is located between 100-600 MeV for 45 MeV/nucleon. The majority of HF for 35 MeV/nucleon is lower at 100-500 MeV. For both energies, there are particles with much greater energies, above 1200 MeV for 45 MeV/nucleon and above 1000 MeV for 35 MeV/nucleon. The majority of the LF distribution is lower between 25-250 MeV and extends up to approximately 600 MeV for 45 MeV/nucleon. For 35 MeV/nucleon, the majority of LF is lower energy at 25-200 MeV and the distribution goes as high as approximately 600 MeV.

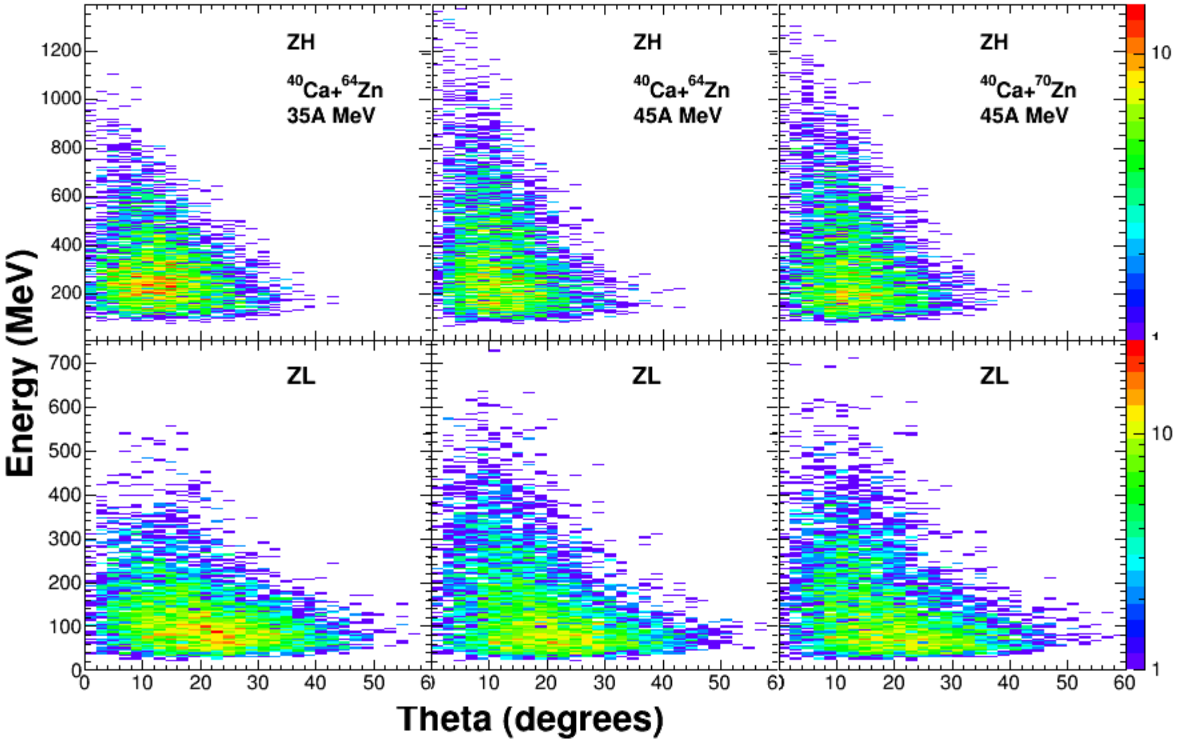

FIG. 2. Energy vs. theta. The top row corresponds to HF; bottom to LF. For HF, the energy distribution ranges from 100-600 MeV for 45 MeV/nucleon and 100-500 MeV for 35 MeV/nucleon. The angular distribution is between 0-40°. The energy distribution for LF ranges from 25-250 MeV for 45 MeV/nucleon and is slightly lower at 25-200 MeV for 35 MeV/nucleon. The angular distribution is between 0-60°.

Energy loss calculations were performed. CycSrim was used to calculate the energy loss in the target, a Si1, Si2 and CsI. The thickness of the Si2 was 500 μm and the thickness of the CsI was 6.0 cm (thinnest CsI in NIMROD). Two different Si thicknesses were tested for the front Si (100 μm and 150 μm). Results showed most particles were detected in either the ΔE-E or E-CsI/ΔE-CsI. For LF, 17-29% stopped in the ΔE and approximately 5-20% of HF stopped in the ΔE. The ΔE-E and E-CsI for HF and LF are shown in the middle and right part of Fig. 3. The left-hand side of Figure 3 is the ΔE vs. Z for all fragments stopping in the 1st Si.

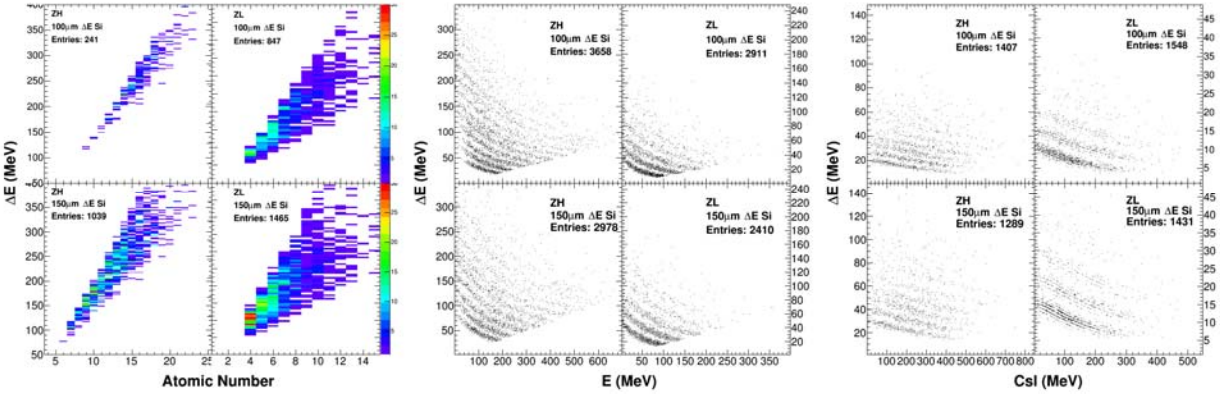

FIG. 3. From left to right: ΔE vs. Atomic number for fragments that stopped in the 1st Si, ΔE vs. E, and ΔE vs. CsI for 35 MeV/nucleon. For each 4 panel, the top row corresponds to the 100 μm 1st Si. The bottom row has a 1st Si thickness of 150 μm. The HF is on the left-hand side and LF is on the right. The number of events per identification method is shown in the upper right-hand side of each panel. Most of the fragments are identified with the 1st and 2nd Si detector.

Future work will focus on examining the equilibration between ^{48}Ca+^{64,70}Zn at 15A, 25A, 35A and 45A using COMD simulations. Results will help further determine which rings of NIMROD will be needed for the experiment. NIMROD will be outfitted with more supertelescopes in strategic locations to improve the chances of measuring with isotopic resolution the two heaviest daughters of the PLF*.

[1] A. Jedele, *et al*. Phys. Rev. Lett **118**, 062501 (2017).
[2] A. Rodriguez Manso, *et al*. Phys. Rev. C **95**, 044604 (2017).
[3] S. Wuenschel, *et al*. Nucl. Intrum. Methods Phys. Res. **A604**, 578 (2009).
[4] M. Papa, T. Maruyama, and A. Bonasera, Phys. Rev. C **64**, 024612 (2001).

Cluster-cluster correlation in intermediate heavy ion collisions

R. Wada, G. Tian, W. Lin, and A. Ono

Fragments and light clusters are copiously produced in various kinds of nuclear reactions such as in heavy-ion collisions. Formation of fragments and clusters is one of the essential features of these reactions, since they are produced in most of the events in these reactions with the participation of most of the nucleons in the system. Here we apply AMD-CC, an antisymmetrized molecular dynamics with cluster-cluster correlation [1], to the experimental results of the ^{12}C + ^{12}C reaction at 95MeV/nucleon [2].

In the implementation of two-nucleon collisions in most transport models, only the states of the two nucleons are changed under the assumption that these two nucleons are not correlated with the other nucleons in the system. On the other hand, if the correlations exist in the final states between the scattered nucleons and other nucleons, it is more reasonable to construct the final states, taking account of the correlations. Here the correlations mean that clusters with A = 2, 3 and 4 can propagate in the medium if it is allowed by the Pauli principle. In AMD, if several wave packets (with different spins and isospins) are placed at the same phase space point, these wave packets will tend to move together as a cluster by the equation of motion. On the other hand, if the wave packets are placed randomly in the phase space, the chance for these nucleons to form a cluster after propagation is small. Therefore, in order to respect the possibility of forming a cluster in the final state of a two-nucleon collision, the set of final states should be suitably constructed. In the early version of AMD-CC, these correlations are incorporated only for light clusters with $A \leq 4$ in the code. In the latest version of AM-CC, used in this work, the cluster correlations are extended to clusters with $A \leq 10$.

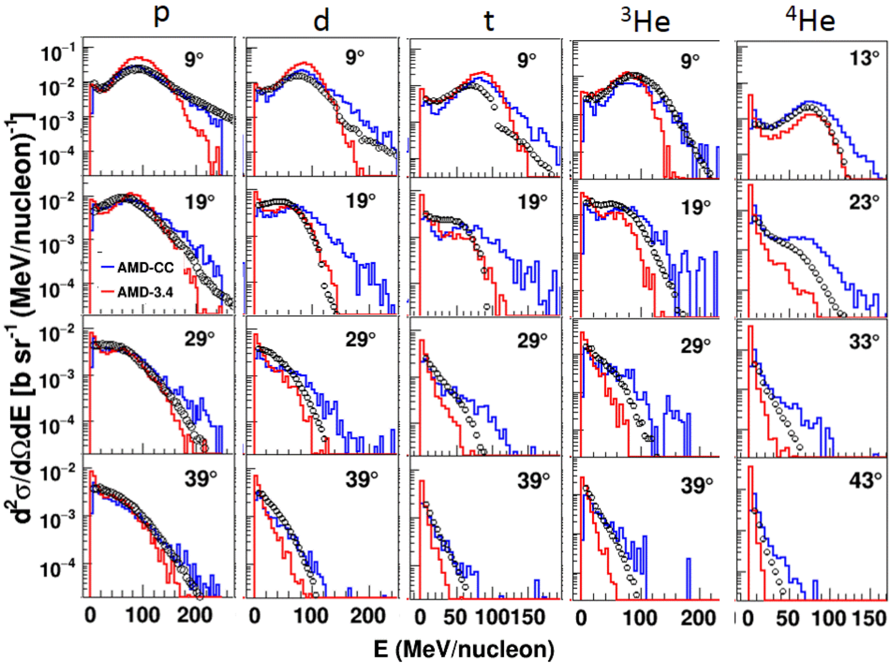

FIG. 1. Calculated energy spectra for LCPs from AMD-CC (blue histograms) and AMD (red histograms) are compared with the experimental data of ^{12}C+^{12}C at 95 A MeV [2] at four selected angles. From left to right column, p, d, t, ^{3}He and ^{4}He are plotted. The comparisons are made in an absolute scale.

The calculated results with AMD-CC (blue histograms) are compared to those of AMD without the correlations (red histograms) together with the experimental data (circles) for LCP in Fig.1 and IMFs in Fig.2 at selected angles. One can clearly see significant improvements in the reproduction of the most of the energy spectra by AMD-CC, especially for those of IMFs.

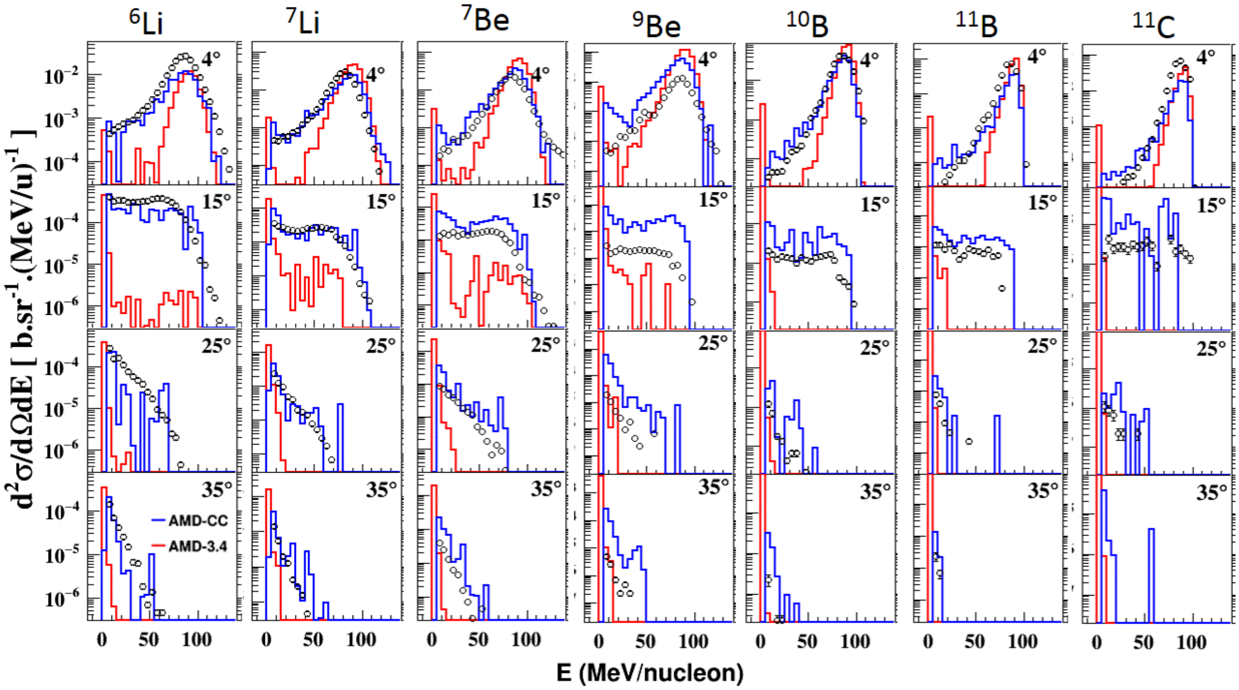

FIG. 2. Calculated energy spectra for IMFs from AMD-CC and AMD are compared with the experimental at four selected angles. Symbols and curves are same as those of Fig.1. The selected isotopes are indicated in the figure.

[1] A. Ono, Eur. Phys. J. Web of conference **122**, 11001(2016).

[2] J. Dudouet *et al.*, Phys. Rev. C **88**, 024606 (2013).

Three nucleon interaction in heavy ion collisions at intermediate energies

R. Wada

High energy proton emission were studied experimentally by Germain et al. in ^{36}Ar+^{181}Ta at 94A [1] MeV and by Coniglione *et al.* in ^{36}Ar+^{51}V at 44A MeV [2]. In their experiments proton energy often exceeds 3-4 times the incident energy per nucleon. In our recent study [3], we demonstrated that a careful treatment of the Fermi motion in a transport model, especially for the high momentum distribution of the Fermi motion in hot nuclear matter, is crucial for the production of high energy protons. In the present work, theoretical studies are performed, based on an antisymmetrized molecular dynamics (AMD) [4]. In the extended AMD [5,6], the Fermi motion is taken into account as a quantum fluctuation, a quantum branching of the wave packets called a diffusion process in the nucleon propagation in a mean field. In our work in Ref. [3], we also take into account the quantum fluctuation in each collision process and the modified code is called AMD-FM. These treatments are quite different from that in most other transport models, in which the Fermi motion is added to nucleons only once in the initial nuclei, whereas in AMD-FM, a new Fermi motion is assigned as a momentum fluctuation in the diffusion process and each collision process, thus many times throughout the calculation. The AMD-FM significantly improves the reproduction of the high energy protons in above available experimental data. We extend this study to include a 3N collision term at higher incident energies in this study.

The importance of the 3N collision term at intermediate heavy ion collisions was first pointed out by Mrowczy´nski [7]. Bonasera et al. studied it in detail and put it into a transport model formalism [8–10]. The 3N collision term was applied in the experimental data, using a perturbed calculation based on a BNV transport model in Ref.[1]. A 3N collision term is incorporated into AMD-FM following the description in Ref. [10]. We will refer this version of AMD as AMD-FM(3N). The 3N interaction is simply calculated by a succession of three binary collisions where one couple of nucleons interacts twice when three nucleons are in the collision distance each other. In each collision, the same treatment as in Ref. [3] is made for each nucleon momentum to take into account the Fermi motion and avoid double counting with the diffusion process. The effect is called ”Fermi boost”.

The AMD-FM(3N) is applied for the ^{40}Ar +^{51} V reactions at 100, 200, 300 and 400A MeV, to overview the 3N collision effect on the high energy proton emission. The calculated results (histograms) are compared AMD-FM (circles) in Fig. 1. At 100A MeV on the left, the energy spectra are very similar at different angles between two calculations, but the yields of AMD-FM(3N) are slightly larger, by a factor of 2 at most. When the incident energy increases to 200A MeV, the shape of the energy spectra show a distinct difference, that is, the energy slope of AMD-FM(3N) show much harder slopes than those of AMD-FM. Similar differences are also observed at higher incident energies. One should note that the slope of the spectra barely depend on the impact parameter range, because they originate essentially from the 2N or 3N collisions. One can also see broader peaks at the lower proton energy in the forward spectra for the AMD-FM(3N) simulations. This can be explained as follows: At the low energy side, the spectra of AMD-FM show a semi-Gaussian distribution. The contribution from the 3N collisions also becomes a Gaussian distribution, because of the Fermi boost for the third nucleon, and thus they are overlaid on top of each other, which causes a broadening of the distribution. In the high energy side, on the other hand, the spectra of AMD-FM show an exponential fall off and the 3N contribution becomes visible only in the higher energy side.

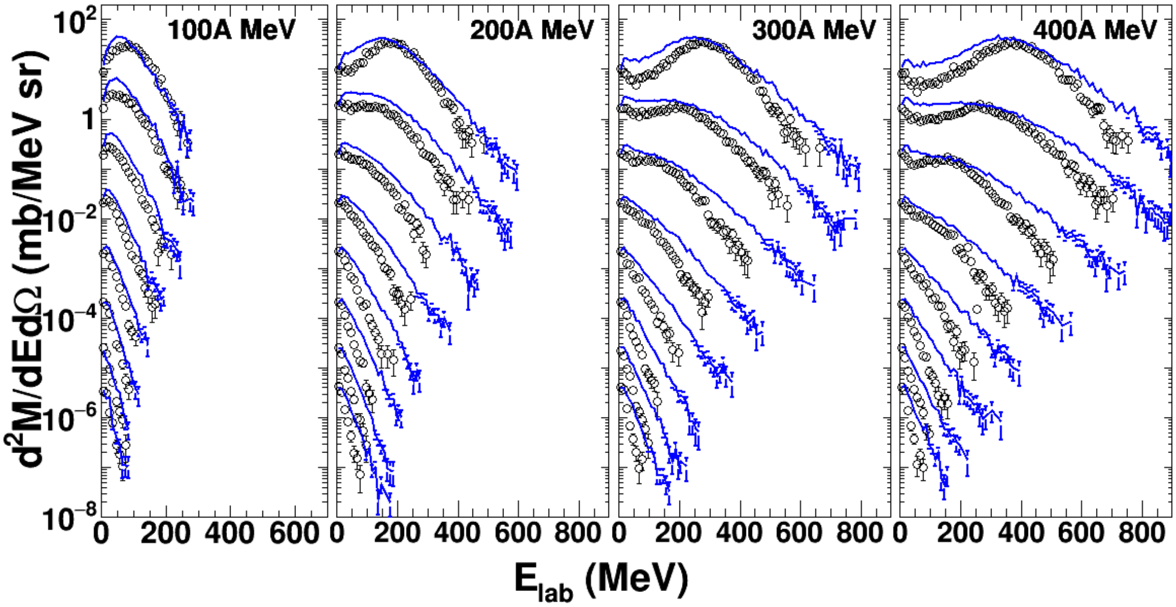

FIG. 1. Simulated results of proton energy distributions for ^{40}Ar +^{51} V at different incident energies. Histograms represent the results of AMD-FM(3N) and circles are from AMDFM. The spectra in each column are plotted every 20◦ from θ = 10° (x1) at the top to θ = 170◦ (x10^6) at the bottom.

In the insert in Fig. 2, the number of collisions is plotted as a function of reaction time for attempted collisions and Pauli-allowed collisions at 100A MeV in (a) and 300A MeV in (b). At both energies, the maximum number of collisions per time occurs at the time of overlap between the projectile and target. Around this time period, the shape of the collision distributions are very similar between attempted and Pauli-allowed collisions. When the peaks are fit by a Gaussian distribution, the width for the 3N collisions is less than half of that of the 2N collisions, indicating that the 3N collisions are more localized in time, at the time of the maximum density. This is what is expected from Eq. (1). This width difference in the numbers between the 2N and 3N collisions indicates how quickly the overlap region expands in time.

In Fig. 2 a summary of the number of collisions is plotted as a function of the incident energy. The number of collisions is calculated around the peak, using a Gaussian fit as shown in the insert. Collisions at later stages are not included. The number of the 2N collisions decreases rapidly as the incident energy increases from 44A to 100A MeV, whereas the number of the 3N attempted collisions increases rapidly in this energy range. The number of the Pauli-allowed 3N collisions below 60A MeV is small and increases very slowly. At 100A MeV, about 50% of the attempted 2N collisions are blocked by the Pauli exclusion principle. The blocking is more significant for the 3N collisions, where nearly 90% of the collisions are blocked. At 300A MeV, about 40% of the 2N collisions are Pauli-blocked, whereas for the 3N collisions about 75% are blocked. These numbers of blocking indicate that, even above 100A MeV, a careful treatment of the Pauli blocking is still very important, especially for the 3N collisions.

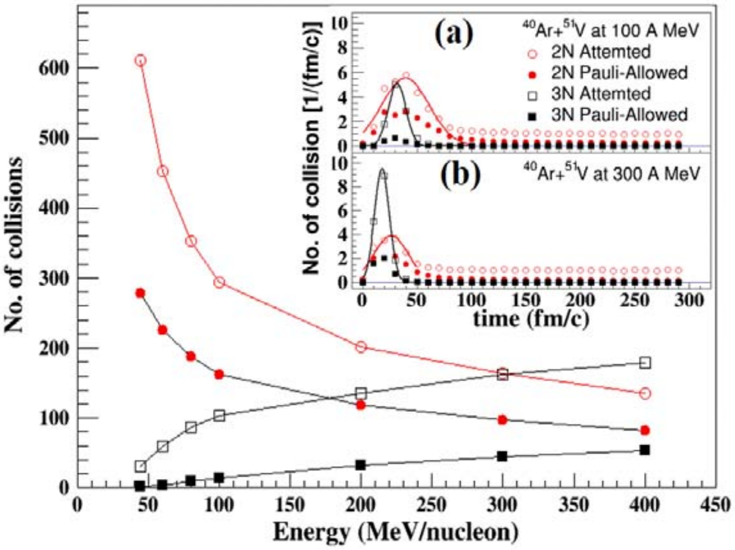

FIG. 2. Summed number of 2 body (circles) and 3 body (squares) collisions are plotted as a function of incident energy. Lines are guides of eyes. Insert: Number of 2N and 3N collisions are plotted as a function of reaction time. (a) $^{40}Ar+^{51}V$ at 100*A MeV*. The density in the overlap region becomes maximum at $t = 30 fm/c$ at this energy. (b) $^{40}Ar+^{51}V$ at 300*A MeV*. The density becomes maximum at $t = 20 fm/c$ at this energy. The sigma of the Gaussians are 21.7 (15.9) for 2N and 8.0 (6.8) for 3N attempted collisions at 100A (300A) MeV, respectively.

[1] M. Germain *et al.*, Nucl. Phys. **A620**, 81 (1997).
[2] R. Coniglione *et al.*, Phys. Lett. B **471**, 339 (2000).
[3] W. Lin *et al.*, Phys. Rev. C **94** 064609 (2016).
[4] A. Ono *et al.*, Prog. Theo. Phys. **87**, 1185 (1992).
[5] A. Ono, Phys. Rev. C **53**, 2958 (1996).
[6] A. Ono, Phys. Rev. C **59**, 853 (1999).
[7] St. Mrøwczyński, Phys. Rev. C **32**, 1784 (1985).
[8] A. Bonasera *et al.*, Phys. Lett. B **259**, 331 (1991).
[9] A. Bonasera *et a*l., Phys. Lett. B **275**, 24 (1992).
[10] A. Bonasera *et al.*, Phys. Rep. **243**, 1 (1994).

Toward understanding relativistic heavy-ion collisions with the STAR detector at RHIC

D.M. Anderson, Y. Liu, S. Mioduszewski, N. Sahoo, and the STAR Collaboration

This project is a study of high-energy heavy-ion collisions at the Relativistic Heavy Ion Collider (RHIC). The focus of the study is on two probes of the dense, partonic matter created in these collisions: 1) direct-photon-triggered jets (and their correlations) and 2) heavy-quarkonium production and suppression.

1. Investigating Energy Loss through Photon-Triggered Jet Measurements

The hard production of a direct photon back-to-back with a jet (γ-jet) is a probe of the parton energy loss in heavy-ion collisions [1]. In the "γ-jet" coincidence measurement, the measured energy of the trigger particle (the photon) serves as a calibrated baseline for the total energy of the jet particles on the recoil side (i.e. opposite in azimuth) of the trigger. The mean-free path of the γ in the medium is large enough so that its momentum is preserved, regardless of the position of the initial scattering vertex. Thus it does not suffer from the geometric biases, i.e. the non-uniform spatial sampling of hadron triggers due to energy loss in the medium, of e.g. π^0 triggers. Because of the difference in path length traversed, on average, between a direct-γ and a π^0 trigger, comparisons of γ-jet to hadron(π^0)-jet measurements can provide insight into the path-length dependence of the energy loss.

As the dominant background to direct photons are π^0 (decaying to two photons), the Barrel Shower Maximum Detector (BSMD) has provided the capability of distinguishing direct photons from neutral pions via the transverse shower shape. Our group has used this method in the measurement of direct photon+hadron correlations [2]. The γ-hadron correlation studies can be extended to studies of γ-triggered jet reconstruction measurements (as has been done at the LHC [3, 4]). The away-side jet will then be reconstructed in coincidence with triggers selected as direct photon candidates or (for p_T<20 GeV using the shower shape with the BSMD) identified π^0 triggers. The advantage of this should be the ability to reach lower energy fragments in the jet to study jet-shape modification and possible redistribution of energy.

First, we carried out a charged-jet reconstruction analysis on the available 2011-Run Au+Au collisions. Here, only charged tracks are included in the jet reconstruction. The result, presented at Quark Matter 2017 [5], is shown in the left panel of Fig. 1.

The 2014-Run "L2Gamma"-triggered events (events with a high-energy calorimeter signal) in Au+Au collisions were recently reconstructed. We have begun the quality assurance of the 2014-Run L2Gamma triggers and plan to carry out the γ-jet analysis on this data set.

In addition, we carried out some studies of full-jet reconstruction (including both charged tracks and neutral energy measured with the electromagnetic calorimeter) on the 2009-Run p+p collisions. A result of the raw, uncorrected spectra of charged jets vs. full jets is shown in the right panel of Fig. 1.

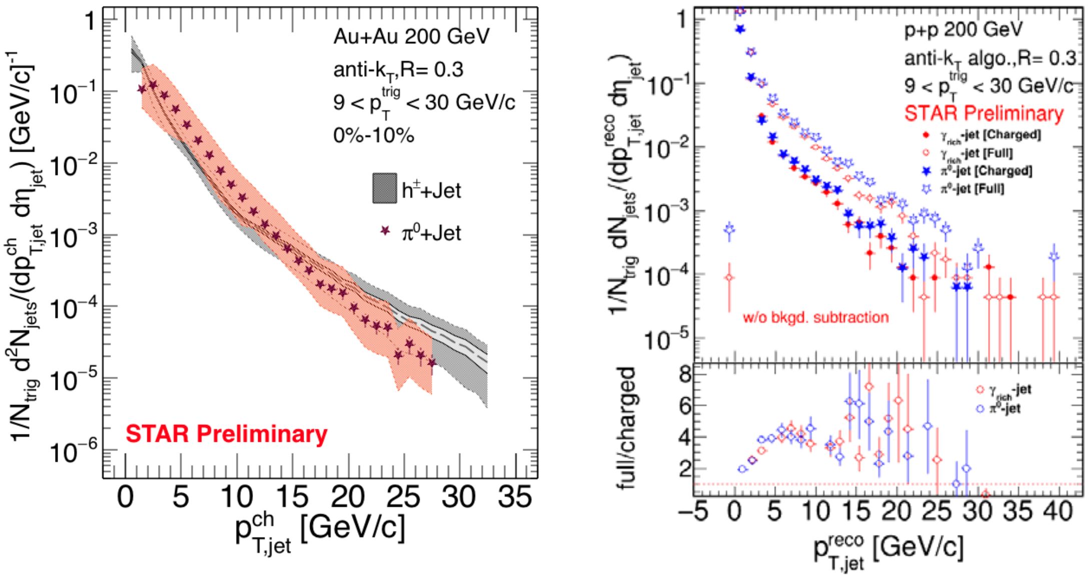

FIG. 1. (Left) Preliminary π^0-triggered charged-jet measurement compared to recently published result of charged-hadron-triggered charged-jet measurement [6]. (Right) Studies of charged-jet reconstruction vs. full-jet reconstruction in Run-9 p+p data (uncorrected for efficiencies and background fluctuations).

2. Unraveling Cold Nuclear Matter Effects in J/Ψ Suppression

The J/ψ has long been considered one of the most promising direct probes of deconfinement. According to theoretical predictions in 1986 [7], the produced $c\bar{c}$ pair will not be able to form a J/ψ bound state in the QGP, if a sufficiently high temperature is reached where the screening radius is smaller than the binding radius of the J/ψ resonant state. The "Debye" screening radius is the distance at which the color charges of two quarks are screened from one another, so that the confinement force is not able to hold the quarks together. A suppression in the yield of J/ψ was first observed in Pb+Pb collisions by the NA50 experiment at the CERN SPS (see, for example, [8]).

At RHIC, the predicted suppression of J/ψ due to screening in the QGP is much larger than the suppression observed at the SPS due to the higher initial density of the produced medium [9]. The RHIC measurements, however, show a level of suppression similar to NA50 at mid-rapidity [10], which is significantly smaller than expectations due to color screening effects alone. This can be understood in a scenario where charmonium is regenerated due to the large initial production of charm + anti-charm quarks at $\sqrt{s_{NN}}$= 200 GeV, in conjunction with their possible thermalization in the created medium [11]. If charm quarks (partially) thermalize in RHIC collisions, then the coalescence of $c\bar{c}$ could lead to a smaller than expected suppression [12].

With counteracting effects, it is a challenge to disentangle the suppression from the regeneration. Further complicating this task is that the J/ψ-particle yields that are measured are not all primordial; some ~40% are feed-down from χ_c (approximately 30%) and ψ′ (approximately 10%) decays. Since the survival rate of different charmonium states may be different, due to the different sizes, it is important to know these feed-down fractions precisely. In addition, there are cold nuclear matter effects [13], including modification of the parton distribution functions ("shadowing") and partonic multiple scattering, that also lead to suppression of heavy quarkonium and need to be disentangled from QGP suppression. In order to quantify effects of deconfinement, cold nuclear matter effects (via p+A collisions) must be measured and disentangled.

We have worked on the quality assurance and a centrality determination for the 2015 p+Au data set. The (raw) distributions of numbers of primary tracks, shown in Fig. 2, are for the classification of events into "centrality" or "event activity". They don't yet include corrections due to trigger efficiency, luminosity, and vertex dependence. However, the data are compared to event-generator simulations with the experimental conditions and efficiencies imposed, showing good agreement. These results were also presented the Quark Matter 2017 conference in a poster. Once finalized, we will be able to build on this event classification to carry out quarkonium studies in p+Au collisions.

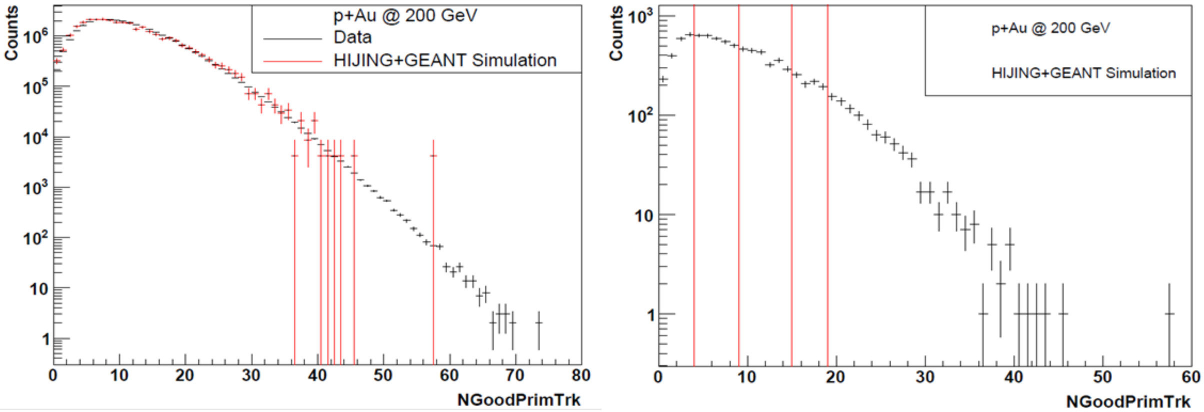

FIG. 2. Number of good primary tracks. (Left) Data vs. HIJING with trigger conditions applied. (Right) Centrality cuts, shown as red vertical lines on un-biased HIJING distribution, selecting 0-10% (<Ncoll>=8.3), 10-20% (<Ncoll>=7.1), 20-50% (<Ncoll>=6.0), and 50-80% (<Ncoll>=4.1) of the total cross section.

[1] X.N. Wang, Z. Huang, and I. Sarcevic, Phys. Rev. Lett. **77**, 231 (1996).
[2] L. Adamczyk *et al.* [STAR Collaboration], Phys. Lett. B **760**, 689 (2016).
[3] S. Chatrchyan *et al.* [CMS Collaboration], Phys. Lett. B **718**, 773 (2013).
[4] [ATLAS Collaboration], ATLAS-CONF-2012-121.
[5] N.R. Sahoo for the STAR Collaboration, arXiv:1704.04814 [nucl-ex].
[6] L. Adamczyk *et al.* [STAR Collaboration], arXiv:1702.01108v1 [nucl-ex].
[7] T. Matsui and H. Satz, Phys. Lett. B **178**, 416 (1986).
[8] M.C. Abreu *et al.* [NA50 Collaboration], Eur. Phys. J. C **39**, 335 (2005).
[9] L. Grandchamp, R. Rapp, and G.E. Brown, Phys. Rev. Lett. **92**, 212301 (2004); A. Capella and E.G. Ferreiro, Eur. Phys. J. C **42**, 419 (2005).
[10] A. Adare *et al.* [PHENIX Collaboration], Phys. Rev. Lett. **98**, 232301 (2007).
[11] P. Braun-Munzinger and J. Stachel, Phys. Lett. B **490**, 196 (2000).
[12] L. Grandchamp and R. Rapp, Phys. Lett. B **523**, 60 (2001).
[13] R. Vogt, Phys. Rev. C **71**, 054902 (2005).

SECTION III

NUCLEAR THEORY

A novel method for determining the effect of short range correlations on single particle density: Application to the charge density difference between the isotones ^{206}Pb – ^{205}Tl

G. Bonasera[1] and S. Shlomo[1,2]
[1]*Cyclotron Institute, Texas A&M University, College Station, Texas 77843, USA*
[2]*Department of Elementary Particles and Astrophysics, the Weizmann Institute of Science, Rehovot 76100, Israel*

The relation between shell model wave functions and the real nuclear ones is rather complicated. Important information about it may be gleaned from the measurement of the charge distribution of the proton $3s_{1/2}$ orbit. This is given by the measured charge density difference, $\Delta\rho_c(r)$, between charge density distributions of the isotones ^{206}Pb – ^{205}Tl. The experimental data of the charge density shows a clear maximum at the center of ^{206}Pb with two additional maxima. This seems to be the shape obtained from a $3s_{1/2}$ single proton wave-function, in agreement with the simple shell model. It was pointed out in the literature that commonly used central potentials, such as the Wood-Saxon potential, lead to a $3s_{1/2}$ charge density in disagreement with experimental data. In particular, the central density obtained from the Woods-Saxon potential is too large by 40%. This difference between data and the Woods-Saxon results was considered earlier in the literature resulting with the statement that it is accounted for by the effect of two-body short range correlations (SRC) on the shell model wave functions. In this work [1] we take a closer look at the effect of SRC on the nuclear density.

Using the Jastrow many-body correlated wave function, with a two-body correlation factor, and employing the single pair approximation we derive a simple and accurate method (within few percent) for calculating the effect of (SRC) on the single particle density. Adopting the harmonic oscillator single particle wave functions we determined the effect of (SRC) on the charge densities of ^{206}Pb and ^{205}Tl. In Fig. 1 we show the results for the $3s_{1/2}$ single proton wave-function and compare with experiment. We have thus demonstrated that although the effect of SRC is to reduce the $3s_{1/2}$ single proton charge density at r = 0 by 30%, the calculated density disagrees with the experimental data by more than a factor of 2, particularly in the region of r = 2 – 4 fm.

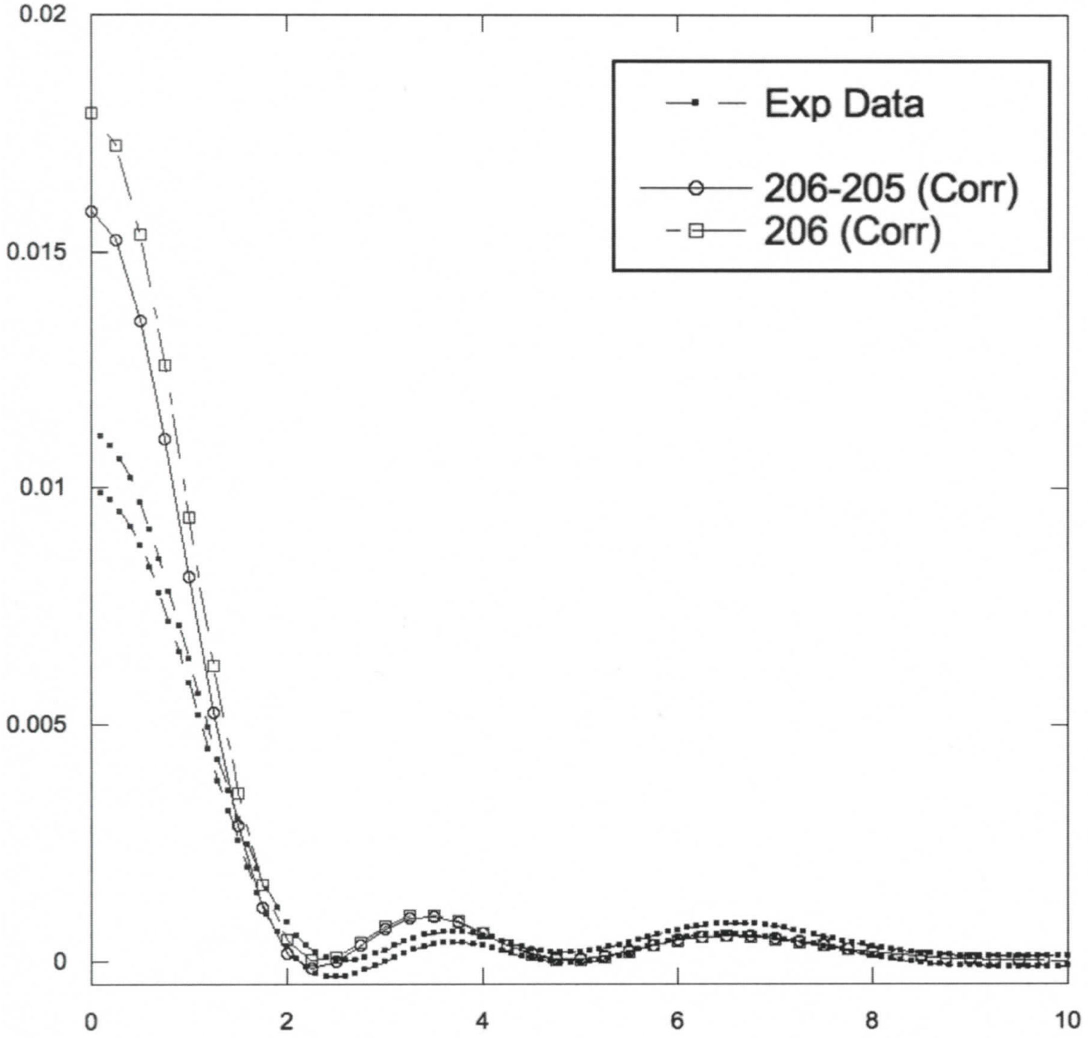

FIG. 1. Calculated (solid line) and experimental (dotted lines) difference, $\Delta\rho_c(r)$ between ^{206}Pb and ^{205}Tl charge distributions. The dashed dotted line is for the $3s_{1/2}$ proton orbit in ^{206}Pb.

[1] G. Bonasera and S. Shlomo, to be published.

Bulk and isospin instabilities in hot nuclear matter

V.M. Kolomietz[1] and S. Shlomo [2,3]
[1]*Institute for Nuclear Research, 03680 Kiev, Ukraine*
[2]*Cyclotron Institute, Texas A&M University, College Station, Texas 77843, USA*
[3]*Department of Elementary Particles and Astrophysics, the Weizmann Institute of Science, Rehovot 76100, Israel*

We have considered [1] the appearance and the development of instabilities in an asymmetric nuclear matter in both the isoscalar and the isovector channels. Our analysis is based on the equations of motion for the quantum Fermi liquid in the presence of the Fermi-surface distortion effects and the relaxation processes. We point out that a realistic description of the unstable modes in a homogeneous nuclear matter requires the extension of the equation of state by taking into consideration the gradient corrections to the total energy functional. The presence of the gradient corrections leads to the anomalous dispersion term in the equation of motion and influences significantly the behavior of the instability growth rate.

Studying the appearance of the bulk and isospin instabilities, we have performed numerical calculations of the dependence of the incompressibility coefficient, $K(\rho_0)$, and the symmetry energy coefficient, $C_{\mathrm{sym}}(\rho_0)$, on the nuclear density, ρ_0. To evaluate the values of $K(\rho_0)$ and, $C_{\mathrm{sym}}(\rho_0)$, at non-equilibrium density, $\rho_0 \neq \rho_{\mathrm{eq}}$, we have applied the cranking approach. The external cranking field was used in the form which excludes the direct contribution of the cranking field to the incompressibility coefficient $K(\rho_0)$ for the Skyrme interactions SkM*, KDE0v1 and Sly230b for different temperatures and particle densities, we have established the critical temperature $T_{\mathrm{crit}} = 14\ to\ 15$ MeV where the nuclear matter becomes unstable at the equilibrium density $\rho_{\mathrm{eq}}(T)$. A peculiarity of the isovector mode is that the instability of nuclear matter with respect to isovector density fluctuation, i.e. regime $C_{\mathrm{sym}}(T) < 0$, can occur in the superdense nuclear matter only and depends significantly on the choice of the Skyrme interaction parameterization, such as the case of SkM*.

We have shown that the Fermi-surface distortion effects strongly hinder the development of instabilities in nuclear matter. The dependence of the instability growth rate $\Gamma_+(q)$ on the wave number q has a specific non-monotonic behavior which is caused by the anomalous dispersion term. Different slopes of the curve $\Gamma_+(q)$ reflect different regimes (fission or multifragmentation) of instability. To illustrate this fact, we have considered the behavior of instability growth rate $\Gamma_+(q)$ in the finite nucleus ^{208}Pb for different multipolarities L of particle density fluctuations and different temperatures T. The results presented in Fig. 1 show that the fission mode (low L) is preferable at low temperatures. The instability with respect to multifragmentation (high L) increases with temperatures. Moreover, one can expect that the yield of small fragments, which correspond to the highest values of L, is strongly increasing for high temperatures, see corresponding lines $4, 6$ and 8 MeV in Fig. 1.

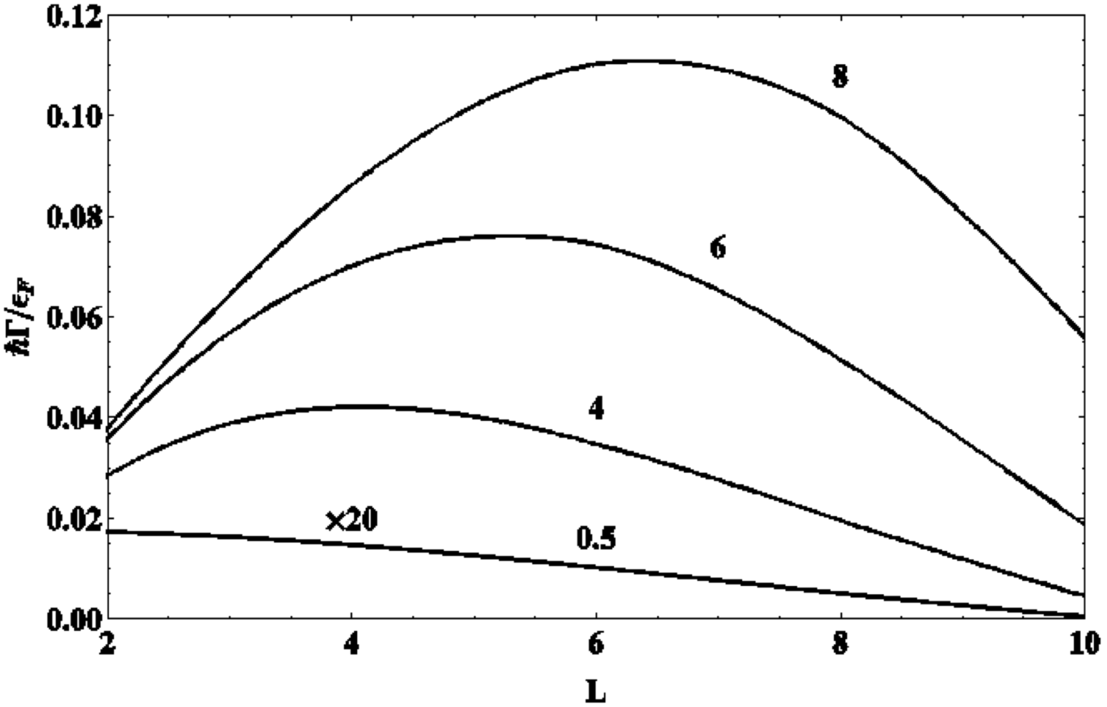

FIG. 1. The dependence of the isoscalar instability growth rate $\boldsymbol{\Gamma_{+}(L)}$ on the multipolarity $\boldsymbol{L}$ of the particle density fluctuations for the nucleus ^{208}Pb for different temperatures. 0.5, 4, 6 and 8 **MeV** which are shown near the curves. The calculations were performed for KDE0v1 [2] interaction.

[1] V.M. Kolomietz and S. Shlomo, Phys. Rev. C **95**, 054614 (2017).
[2] B.K. Agrawal, S. Shlomo, and V.K. Au, Phys. Rev. C **72**, 014310 (2005).

Equation of state and radii of finite nuclei in the presence of a diffuse surface layer

V.M. Kolomietz,[1] S.V. Lukyanov,[1] A.I. Sanzhur,[1] and S. Shlomo[2,3]
[1]*Institute for Nuclear Research, 03680 Kiev, Ukraine*
[2]*Cyclotron Institute, Texas A&M University, College Station, Texas*
[3]*Department of Particles and Astrophysics, the Weizmann Institute of Science, Rehovot 76100, Israel*

We have applied [1] the approach proposed earlier by Gibbs-Tolman-Widom for a classical liquid drop in presence of the liquid-vapor interface to the derivation of actual size of a nucleus in presence of finite surface diffuse layer. The basic idea of the Gibbs-Tolman-Widom approach is the introduction of a sharp dividing surface, $\mathcal{S}$. The dividing surface is arbitrary but located within the surface diffuse layer. The actual (physical) equimolar surface and thereby the actual nuclear surface are fixed by the requirement that the contribution to the surface energy $E_S[R] \sim A^{2/3}$ from the bulk energy $E_{\text{bulk}} \sim A$ should be eliminated. The bulk density, ρ_0, of neutrons and protons inside the sharp equimolar surface is obtained using the experimental data for the separation energy s_q for each kind of nucleon.

The Gibbs-Tolman-Widom conception of sharp equimolar surface allows one to derive the nuclear volume and, as a consequence, the pressure $P(\rho_0)$ and the equation of state for finite nuclei. In our consideration, we have performed the calculations of well-defined equation of state for spherical nuclei and some nuclear characteristics such as the nuclear radius, the surface tension, the pressure, etc. Our numerical calculations are based on the direct variational method, the extended Thomas-Fermi approximation and the effective Skyrme nucleon-nucleon interaction. Applying the Gibbs-Tolman-Widom approach, we redefine the surface and symmetry energies. Note that we do not use the traditional leptodermous approximation and evaluate the Coulomb energy taking into consideration the finite diffuse layer of the proton density distribution.

Performing the analysis of the equation of state $P = P(\rho_0)$, we have extracted from $P(\rho_0)$ the partial contributions which occur due to the different sources: the A- and $X = (N - Z)/A$-independent bulk pressure $P_{\text{vol}}(\rho_0)$ caused by the bulk energy of a symmetric nuclear matter; the surface (capillary) pressure, $P_{A,\text{capil}}(\rho_0, X) \sim A^{-1/3}$; the contribution from the symmetry energy, $P_{A,\text{sym}}(\rho_0, X) \sim X^2$ and the Coulomb force contribution $P_{A,\text{C}}(\rho_0, X)$. The corresponding numerical results are given in Ref. [1]. The inclusion of surface (capillary) term $P_{\text{capil}}(\rho_0, X)$ shifts the equilibrium point $\rho_{0,\text{eq}}$ to larger values with respect to the ones in a nuclear matter. Also the capillary pressure $P_{A,\text{capil}}(\rho_0, X)$ is connected to the surface tension coefficient $\sigma(A, X)$ by the classical Laplace relation. The action of the Coulomb pressure $P_{A,\text{C}}(\rho_0, X)$ is opposite to the capillary pressure $P_{A,\text{capil}}(\rho_0, X)$ and shifts the equilibrium point to the smaller values of $\rho_{0,\text{eq}}$.

The use of the Gibbs-Tolman-Widom equimolar radius R_e allowed us to give a more realistic procedure for an extraction of the nuclear surface tension coefficient from the experimental data. The equimolar radius R_e determines the equimolar surface area S_e in absence of a diffuse layer. This fact allows us to evaluate both the surface energy, E_{S_e}, and the surface tension coefficient, $(A, X) = E_{S_e}/S_e$. Using the experimental data within the wide interval of mass number $40 \leq A \leq 220$ and the corresponding values of equimolar radii, we have established the following A-expansion for the surface tension coefficient $\sigma(A, X^*) = \sigma_0 + \sigma_1 A^{-1/3}$ with $\sigma_0 = (0.98 \pm 0.03)\ \mathrm{MeV\ fm^{-2}}$ and $\sigma_1 = (0.75 \pm 0.16)\ \mathrm{MeV\ fm^{-2}}$. The obtained result for the curvature correction $\sigma_1 A^{-1/3}$ allows one to estimate the Tolman length, ξ, in nuclei which is $\xi = (-0.41 \pm 0.07)$ fm.

We have evaluated the partial pressure $P_{A,\mathrm{sym}}(\rho_0, X)$ caused by the symmetry energy. The partial pressure $P_{A,\mathrm{sym}}(\rho_0, X)$ induces the polarization effect on the particle density $\rho_{0,X}$ beyond beta-stability line. We have shown that the partial pressure $P_{A,\mathrm{sym}}(\rho_{0,\mathrm{eq}})$ is positive and reduces the particle density $\rho_{0,X}$ with respect the corresponding equilibrium density $\rho_{0,\mathrm{eq}}$ on the beta-stability line. The partial pressure $P_{A,\mathrm{sym}}$ and the polarization effect are rather sensitive to the Skyrme interaction parameterization such as the SkM*, SLy230b and KDE0v1 interactions. We point out that the evaluated equimolar radius R_e of the nuclei does not necessary obey the saturation condition $R_e = r_0 A^{1/3}$. That is caused by the fact that we use the experimental data for the chemical potentials to derive the bulk density within the equimolar surface in agreement with the Gibbs-Tolman-Widom method. The corresponding experimental chemical potentials (separation energy of nucleons) include the quantum shell effects, the pairing correlation effects, etc., and give rise to the non-monotonic behavior of the nuclear equimolar radii $R_e(A)$. Also that the average interparticle distance r_0 becomes slightly A-dependent.

Using the partial equimolar radii $R_{e,q}(A)$ separately for both kind of nucleons, we have evaluated the corresponding nucleon rms radii $\sqrt{\langle r_q^2 \rangle}$ and the neutron-skin thickness $\Delta r_{np} = \sqrt{\langle r_n^2 \rangle} - \sqrt{\langle r_p^2 \rangle}$. The evaluated values of the proton rms radius $\sqrt{\langle r_p^2 \rangle}$ for the Na isotopes show a slightly non-monotonic behavior of $\sqrt{\langle r_p^2 \rangle}$ which is caused by the above mentioned fluctuations of $R_{e,p}$. Also the presence of the significant shift up of the proton rms $\sqrt{\langle r_p^2 \rangle}$ caused by the surface layer corrections. The influence of the pairing and shell effects on the neutron-skin thickness Δr_{np} is illustrated in Fig. 1 for the Na isotopes. As seen from Fig. 1 the Gibbs-Tolman-Widom concept of the sharp equimolar surface allows one to describe a fine non-monotonic structure of the isovector shift Δr_{np}. The saw-like behavior of Δr_{np} (see the open circles connected by the dotted line in these figures) reflects the even-odd and shell effects in the nuclear binding energy and thereby in the nuclear radii. In general, the value of the isovector shift Δr_{np} is the sum of two contributions: the one, $\Delta r_{np,R}$, is due to the different radii (skin effect) and the other, $\Delta r_{np,a}$, is due to the different shape (surface layer) of neutron and proton distributions (halo effect) [1]. One can expect that the neutron halo effect appears more significantly in light nuclei far away from the stability line.

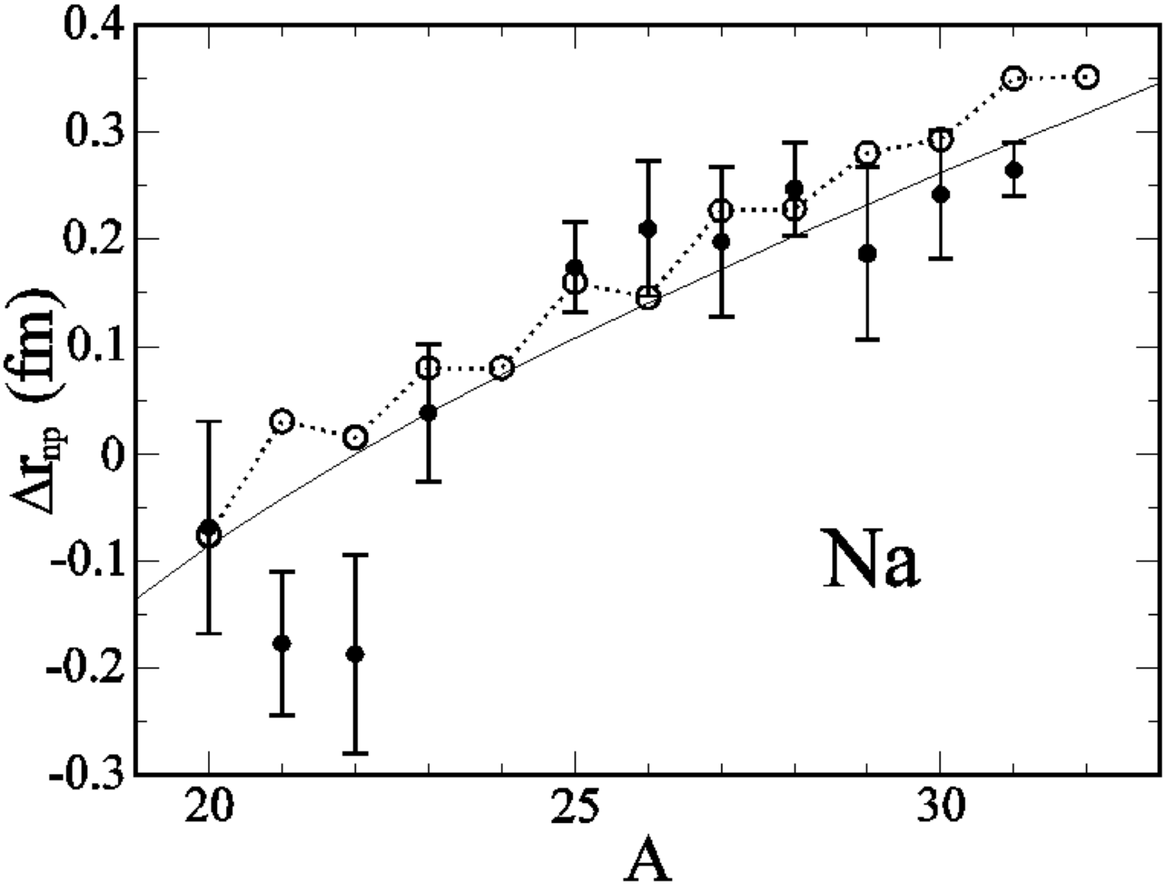

FIG. 1. Isovector shift of nuclear rms radius $\boldsymbol{\Delta r_{np}} = \sqrt{\langle r_n^2 \rangle} - \sqrt{\langle r_p^2 \rangle}$ in Na isotopes. The solid points are the experimental data, the open circles (connected by dotted line) have been obtained using the Gibbs-Tolman approach described in text and the solid line is obtained using the extended Thomas-Fermi approximation with the $\mathbf{SkM}^*$ Skyrme interaction.

[1] V.M. Kolomietz, S.V. Lukyanov, A.I. Sanzhur, and S. Shlomo, Phys. Rev. C **95**, 054306 (2017).

Isovector giant quadrupole resonances in ^{40,48}Ca, ^{68}Ni, ^{90}Zr, ^{116}Sn, ^{144}Sm, and ^{208}Pb and the energy weighted sum rule enhancement factor

G. Bonasera, M.R. Anders, and S. Shlomo

We have performed fully self-consistent Hartree-Fock (HF)-based random phase approximation (RPA) calculations of the centroid energies for the isovector resonances up to L=3 multi-polarity for several spherical nuclei over a wide range of mass. The calculations were done using 33 different Skyrme-type effective nucleon-nucleon interaction commonly adopted in the literature.

The Pearson Correlation coefficient is calculated for every nuclear matter (NM) property. We then compare our theoretical calculation to the available experimental data and in the cases where we have high correlation we can set limiting values on the NM properties. Here we report on a strong correlation between the Centroid Energies of the Isovector Giant quadrupole Resonances and the energy weighted sum rule enhancement factor, κ. In Fig. 1 we show that the centroid energies, of the isovector giant quadrupole resonance associated with each Skyrme interaction and every resonance, as a function of κ, have a strong Pearson correlation coefficient for all nuclei shown. Using the experimental data, we can limit the value of κ to be between 0.25 and 0.65. Similar results were found for the isovector resonance with L=1 and 3. Analysis is performed for all the resonances and nuclei [1] and other nuclear matter quantities. These results will be used to determine the next generation nuclear energy density functional with improved predictive power for properties of nuclei and nuclear matter.

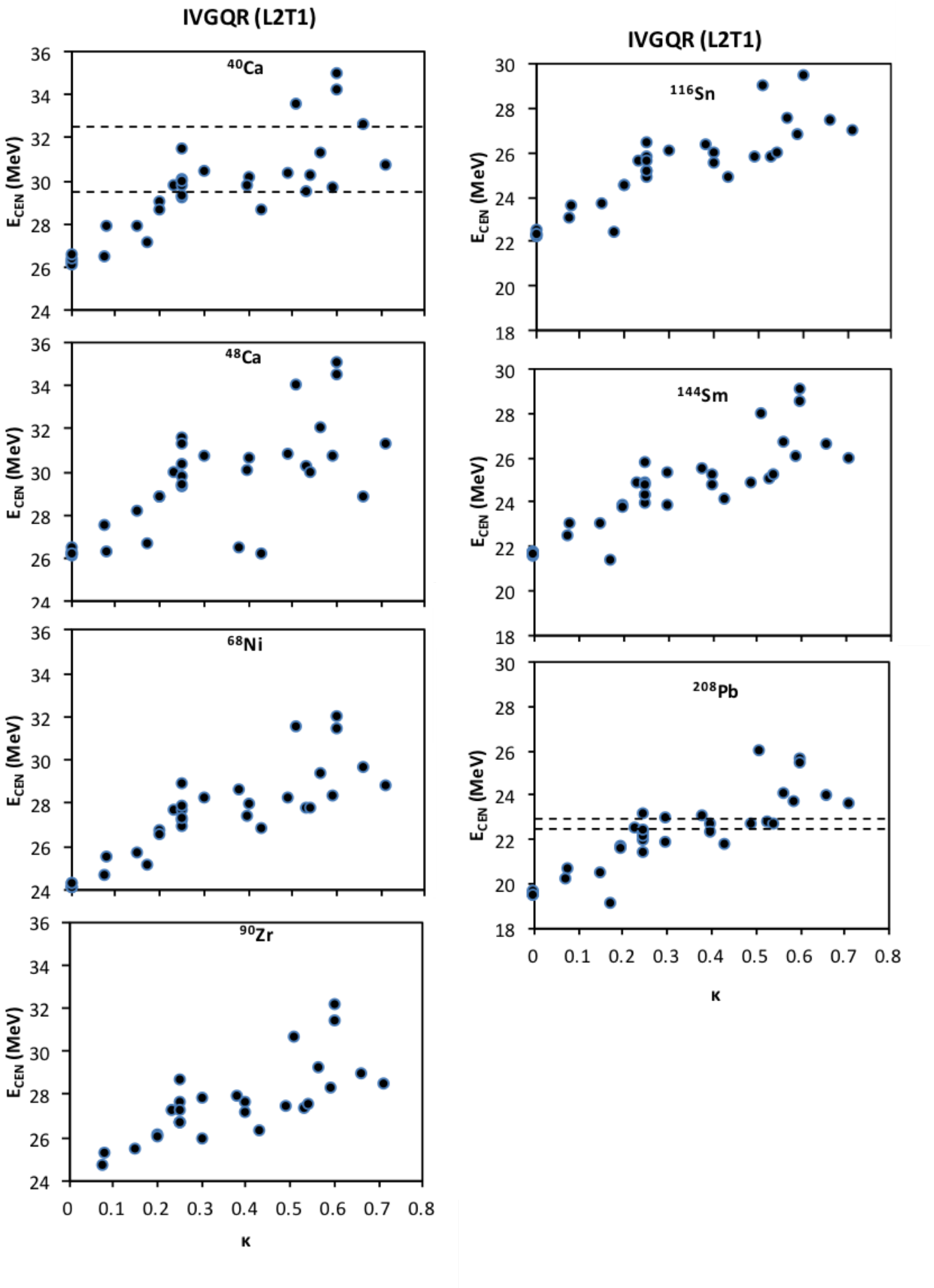

FIG. 1. Calculated Centroid Energies in MeV (full circle) of the isovector giant quadrupole resonance, for the different interactions, as a function of the energy weighted sum rule enhancement factor, κ. Each nucleus has its own panel and the experimental uncertainties are contained by the dotted lines.

[1] G. Bonasera *et al.*, in preparation for publication.

On unitarity of the particle-hole dispersive optical model

M.L.Gorelik,[1] S. Shlomo,[2,3] B.A. Tulupov,[4] and M.H. Urin[5]
[1]*Moscow Economic School, Moscow 123022, Russia*
[2]*Cyclotron Institute, Texas A&M University, College Station, TX 77843, USA*
[3]*Department of Elementary Particles and Astrophysics, the Weizmann Institute of Science, Rehovot 76100, Israel*
[4]*Institute for Nuclear Research, RAS, Moscow 117312, Russia*
[5]*National Research Nuclear University "MEPhI", Moscow 115409, Russia*

The particle-hole (p-h) dispersive optical model (PHDOM) was developed recently to describe simultaneously the main relaxation modes of high-energy (p-h)-type excitations in medium-heavy mass spherical nuclei. These modes include the p-h strength distribution (Landau damping), coupling to the single-particle (s-p) continuum and to many-quasiparticle configurations (the spreading effect). The model, formulated with the use of the Fermi-system Green functions, is, actually, an extension of the continuum-RPA version to the description (phenomenological and in average over the energy) of the spreading effect. This effect is considered in terms of the specific p-h interaction (polarization operator, or p-h self-energy term) responsible for the spreading effect. After energy averaging, the strength of this interaction is properly parameterized to satisfy a statistical assumption concerned with independent spreading of different p-h states. This allows one to get in a closed form the expression for the PHDOM basic quantity – the "free" p-h Green function (p-h response function, or p-h propagator). Being the direct extension of the discrete-RPA p-h propagator, this expression contains the imaginary and real parts of the strength of the energy-averaged p-h self-energy term. The imaginary part determines the real one via the proper dispersive relationship, which follows from the spectral expansion of the 2p-2h Green function (2p-2h configurations are the doorway-states for the spreading effect). The "free" p-h propagator corresponds to the model of non-interacting independently damping quasiparticles. Within the PHDOM, the s-p continuum is taken into account with the use of an approximate spectral expansion for the Green function of the Schrodinger equation involving the imaginary and (dispersive) real additions to the mean field. The imaginary part of the combined s-p potential is relatively small (as compared with the imaginary part of the potential used for the optical-model description of nucleon-nucleus scattering) due to a (destructive) interference between the spreading effect on particles and holes.

The methods used within the PHDOM for the description of the spreading effect lead to weak violations of the model unitarity. The sources of unitarity violations are an energy dependence of the energy-averaged p-h self-energy term, and also the above-mentioned approximate spectral expansion of the optical-model Green function. Unitarity violation within the s-p optical model due to the mean-field energy dependence is discussed in Ref. [1]. The signatures of unitarity violations within the PHDOM are the appearance of: (i) nonzero values (markedly larger than uncertainties of numerical calculations) of the spurious strength function, corresponding to the unit external field; (ii) small negative values of the strength function of the isoscalar giant monopole resonance (ISGMR) at the energies much larger than the ISGMR energy. The last effect leads to an underestimation of the total ISGMR strength.

In this work [2], we investigate weak unitarity violations within the particle-hole dispersive optical model and propose a method for unitarity restoration by modifying the optical model green functions following the method of Ref. [1]. The method is illustrated by consideration of the isoscalar monopole excitations in the ^{208}Pb nucleus. In particular, we study the energy-averaged isoscalar monopole double transition density and strength functions in a wide excitation-energy interval that includes the isoscalar giant monopole resonance (ISGMR) and its overtone (ISGMR2).

In Fig. 1, the relative strength functions, $y_i^R(\omega)$, calculated within the PHDOM-UV for the ISGMR is given in a comparison with the respective quantities obtained within the PHDOM initial version. These results can be considered as an evidence of weak violation of model unitarity. Nevertheless, restoration of model unitarity allows one, in particular, to eliminate negative values of the ISGMR relative strength function.

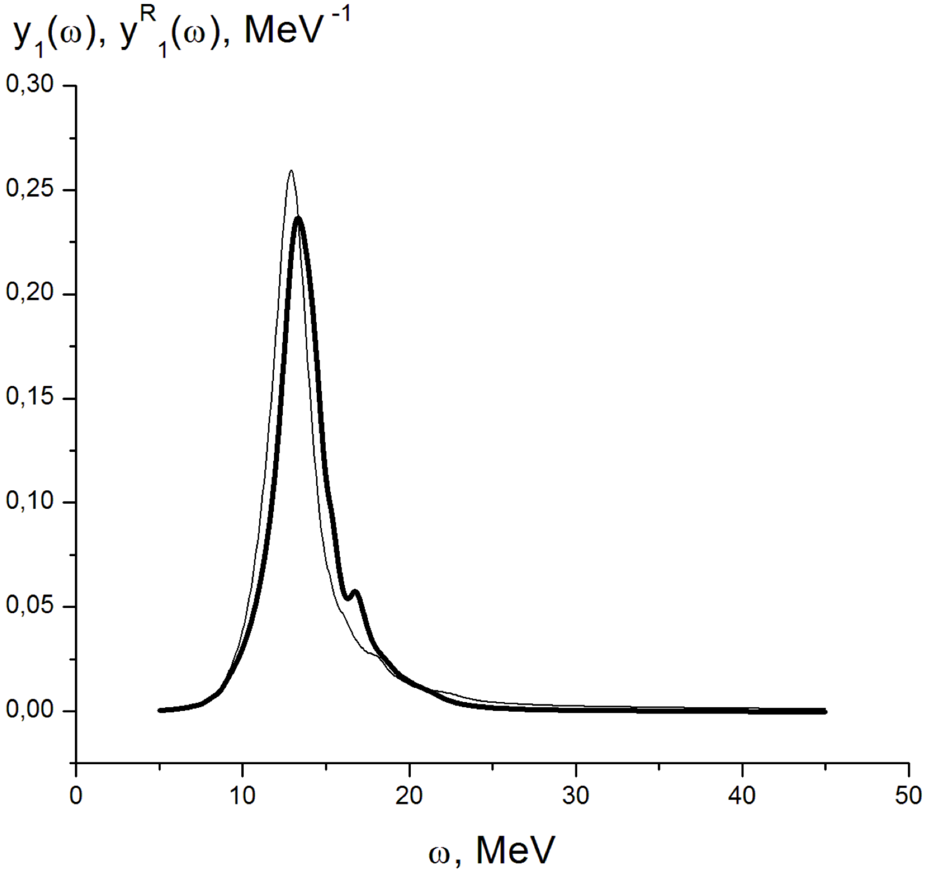

FIG. 1. The relative energy-weighted strength functions calculated for the ISGMR in ^{208}Pb within the initial $y_1(\omega)$ (thick line) and unitary $y_i^R(\omega)$ (thin line) versions of the PHDOM.

[1] S. Shlomo, V.M. Kolomietz, and H. Dejbakhsh, Phys. Rev. C **55**, 1972 (1997).

[2] M.L. Gorelick, S. Shlomo, B.A. Tulupov, and M.H. Urin, to be published.

Nuclear thermodynamic equation of state from chiral effective field theory

J.W. Holt

The equation of state of neutron-rich matter from sub- to supra-nuclear densities directly influences neutron star structure and evolution, the dynamics of core-collapse supernovae, r-process nucleosynthesis, as well as features of gravitational waves produced during the late inspiral and post-merger phases of binary neutron star coalescence. The major challenge is to model the free energy $F(n,T,Y_p)$ of baryonic matter over approximately eight orders of magnitude in density ($n \sim 10^8 - 10^{15}$g/cm^3), temperatures up to $T \sim 5{\times}10^{11}\,K$, and proton fractions $Y_p \leq 0.6$. Under this range of conditions (well below the chiral symmetry breaking scale of $\Lambda_\chi \approx 1$ GeV) effective field theory methods [1-3] are expected to provide a suitable framework for the description of strongly interacting matter. In anticipation of new observational campaigns of neutron stars (e.g., NICER) and searches for gravitational waves from binary neutron star mergers (Advanced LIGO), present efforts in our research group are focused on reducing theoretical uncertainties in the nuclear thermodynamic equation of state and refining phenomenological energy density functionals by imposing microscopic constraints from chiral effective field theory (chiral EFT).

Microscopic many-body calculations based on chiral EFT are now able to provide reliable predictions for properties of the nuclear equation of state through a multi-channel analysis of theoretical uncertainties. In the past year we studied [4] in particular the relationship between the nuclear isospin asymmetry energy, S_v, and its slope parameter, L (as shown in Fig.1). Even the most conservative

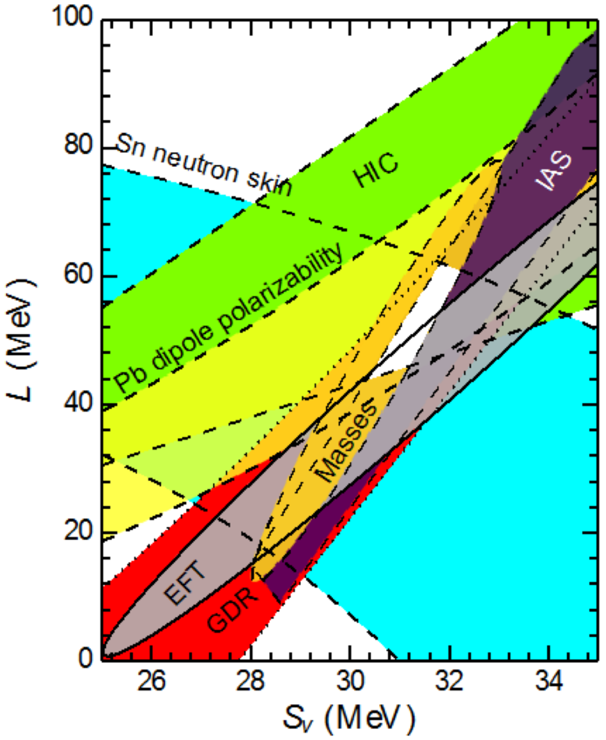

FIG. 1. Correlation between the nuclear symmetry energy, S_v, and its slope parameter, L, from chiral EFT (adapted from [4]).

theoretical uncertainty estimate on this correlation, shown as the "EFT" ellipse in Fig.1, yields a constraint on par with existing experimental investigations of the same quantity (shown as other bands in Fig. 1). This calculation utilized recent developments in perturbation theory [5] by our group that allowed for the inclusion of all third-order diagrams in the expansion of the nuclear equation of state.

More recently we have begun independent collaborations with Andrew Steiner and Shun Furusawa to develop new supernova equations of state that utilize the free energy of bulk nuclear matter obtained from chiral effective field theory in the Matsubara imaginary-time formalism. This expands on our previous finite-temperature studies [6-8] of the nuclear free energy for homogeneous nuclear and neutron matter. The free energy of bulk nuclear matter will be supplemented with a liquid-drop model formalism that accounts for the temperature- and composition-dependent surface energy. The inhomogeneous mixed phase of the supernova equation of state will then be constructed as in previous works [9,10].

Microscopic constraints on nuclear energy density functionals

The high-density ($\rho > 2\rho_0$) and high-temperature ($T > 50\ \mathrm{MeV}$) phase of nuclear matter plays only a small role in core-collapse supernovae. However, the construction of a universal equation of state suitable also for describing neutron star structure and binary neutron star mergers requires modeling in energy regimes beyond the scope of chiral effective field theory with coarse resolution nuclear potentials. This motivated our recent program to identify [11] existing energy density functionals and to construct new functionals [12] that are consistent with the low-energy constraints from effective field theory [4,6-8]. In Ref. [12] we derived new Skyrme interactions by fitting the bulk matter equation of state from chiral effective field theory as well as the binding energies of doubly magic nuclei, the latter to fix the density gradient coupling strengths. In the future, we plan to estimate the gradient terms microscopically from the density matrix expansion [13] at second order and via the static density-density response function.

Neutron star crusts constrained by chiral effective field theory

As a first application of the new Skyrme energy density functionals derived in Ref. [12], we computed properties of neutron star crusts, including the crust-core transition density and pressure, which have important implications for neutron star moments of inertia and the interpretation of pulsar glitches. We predicted a rather tight range in the transition density $0.084\ \mathrm{fm}^{-3} < \rho_t < 0.094\ \mathrm{fm}^{-3}$ by varying the microscopic force model and the treatment of surface contributions to the ground state energy in both the liquid-drop model and the Thomas-Fermi approximations. The full range of pasta phases was considered in both models and found to exist within a confined region in the inner crust of thickness 100m.

Nuclear dipole polarizability from mean-field models constrained by chiral EFT

The nuclear electric dipole polarizability has attracted much attention recently due to its strong correlation with neutron skin thicknesses and the density dependence of the nuclear isospin asymmetry energy. While ab initio many-body techniques have been used to investigate the dipole polarizability of medium-mass nuclei [14], only mean field theory methods can access the dipole response of heavy nuclei. We have recently computed [15] from new Skyrme mean field models constrained by chiral EFT the isovector dipole response of ^{48}Ca, ^{68}Ni, ^{120}Sn, and ^{208}Pb. The mean field models reproduce very well without additional fine tuning the peak positions of the giant dipole resonances in these nuclei as well as the associated dipole polarizabilities, which are proportional to an energy-weighted sum rule of the dipole response. The new Skyrme interactions are therefore useful for studying other isovector properties of atomic nuclei in regimes where ab initio many-body methods are not feasible.

[1] S. Weinberg, Physica A **96**, 327 (1979).
[2] E. Epelbaum, H.-W. Hammer, and U.-G. Meissner, Rev. Mod. Phys. **81**, 1773 (2009).
[3] R. Machleidt and D. R. Entem, Phys. Rpt. **503**, 1 (2011).
[4] J.W. Holt and N. Kaiser, Phys. Rev. C **9**5, 034326 (2017).
[5] L. Coraggio, J.W. Holt, N. Itaco, R. Machleidt, L.E. Marcucci, and F. Sammarruca, Phys. Rev. C **89**, 044321 (2014).
[6] C. Wellenhofer, J.W. Holt, N. Kaiser, and W. Weise, Phys. Rev. C **89**, 064009 (2014).
[7] C. Wellenhofer, J.W. Holt, and N. Kaiser, Phys. Rev. C **92**, 015801 (2015).
[8] C. Wellenhofer, J.W. Holt, and N. Kaiser, Phys. Rev. C **93**, 055802 (2016).
[9] A.W. Steiner, M. Hempel, and T. Fischer, Astrophys. J. **774**, 17 (2013).
[10] S. Furusawa, K. Sumiyoshi, S. Yamada, and H. Suzuki, Nucl. Phys. **A957**, 188 (2017).
[11] E. Rrapaj, A. Roggero, and J.W. Holt, Phys. Rev. C **93**, 065801 (2016).
[12] Y. Lim and J.W. Holt, Phys. Rev. C **95**, 065805 (2017).
[13] J.W. Holt, N. Kaiser, and W. Weise, Eur. Phys. J. A **47**, 128 (2011).
[14] G. Hagen, A. Ekström, C. Forssén, G.R. Jansen, W. Nazarewicz, T. Papenbrock, K. A. Wendt, S. Bacca, N. Barnea, B. Carlsson, C. Drischler, K. Hebeler, M. Hjorth-Jensen, M. Miorelli, G. Orlandini, A. Schwenk, and J. Simonis, Nature Phys. **12**, 186 (2016).
[15] Z. Zhang, Y. Lim, J.W. Holt, and C.M. Ko, arXiv:1703.00866.

Chemical freeze-out in relativistic heavy ion collisions

J. Xu and C.M. Ko

One surprising result in relativistic heavy-ion collisions is that the abundance of various particles measured in experiments is consistent with the picture that they reach chemical equilibrium at a temperature much higher than the temperature they freeze out kinetically [1-3]. Using a multiphase transport model [4] to study particle production in these collisions, we find [5], as an example, that the effective pion to nucleon ratio, which includes those from resonance decays, indeed changes very little during the evolution of the hadronic matter from the chemical to the kinetic freeze-out, and it is also accompanied by an almost constancy in the specific entropy as shown in Fig.1. Starting from the chemical freeze-out state in the AMPT model, we have further studied the expansion and cooling of the system using the hadron resonance gas model, and found that only the scenario of an expanding and cooling hadronic matter with non-unity fugacities can lead to both constant specific entropy and effective pion/nucleon ratio. Our study shows that after chemical freeze-out in relativistic heavy-ion collisions, the system is no longer in chemical equilibrium, but the statistical model can still be used to extract the temperature and chemical potential at chemical freeze-out since the relative abundances of particle species remain constant during later hadronic evolution. The present study thus helps clarify our understanding of chemical freeze-out in relativistic heavy-ion collisions, and validate the use of the statistical model [1-3] in mapping out the phase diagram of the strong-interacting matter from relativistic heavy-ion collisions.

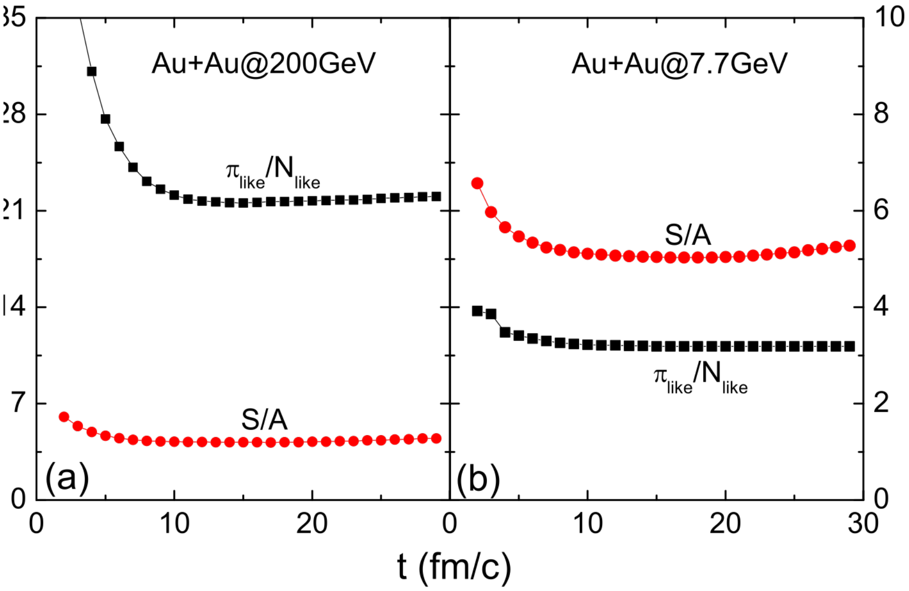

FIG. 1. Time evolution of the specific entropy (S/A) and the effective pion/nucleon ratio (π_{like}/N_{like}) in the hadronic phase of central Au+Au collisions at √sNN = 200 (a) and 7.7 GeV (b).

[1] A. Andronic, P. Braun-Munzinger, and J. Stachel, Nucl. Phys. **A772**, 167 (2006).

[2] J. Cleymans, H. Oeschler, K. Redlich, and S. Wheaton, Phys. Rev. C **7**3, 034905 (2006).

[3] A. Andronic, P. Braun-Munzinger, and J. Stachel, Nucl. Phys. **A83**4, 237c (2010).

[4] Z.-W. Lin, C. M. Ko, B.-A. Li, B. Zhang, and S. Pal, Phys. Rev. C **72**, 064901 (2005).

[5] J. Xu and C. M. Ko, Phys. Rev. C (Submitted).

Three-particle correlations in a multiphase transport model

Y.F. Sun and C.M. Ko

Using the AMPT model [1] with parameters for the Lund string fragmentation and parton scattering taken from Ref.[2], we have calculated the centrality dependence of three-particle correlations mixed harmonic correlations in relativistic heavy ion collisions by considering the observable $Cm,n,m+n = \langle\langle \cos(m\varphi_1 + n\varphi_2 - (m+n)\varphi_3)\rangle\rangle$, where $\varphi_{1,2,3}$ are azimuthal angles of all particle triplets, in Au+Au collisions at $\sqrt{s_{NN}} = 200$ GeV [3]. We have found that our results for C_{112}, C_{224} and C_{235} generally agree with experimental data both in their magnitude and dependence on the participant number of collisions as shown in the left window of Fig. 1. In particular, our results for C_{224} agree very well with the data, although our results for the elliptic and quadrupolar flows differ slightly from the data. For C_{123}, our results show that for mid-central collisions there is a weaker correlation between the angles of the reaction plane for the directed, elliptic and triangular flows for mid-central collisions in AMPT model than in the experimental data. We have further studied the dependence of three-particle correlations on the relative pseudorapidity $|\eta_1-\eta_2|$ and $|\eta_1-\eta_3|$ between first and second particles as well as between first and third particles. Our results, shown in the right window of Fig.1, are seen to agree with experimental data for C_{123} and C_{224}, and indicate that the boost invariance is weakly broken in the angles of the reaction planes for the elliptic and quadrupolar flows but strongly broken in those for the directed and triangular flows. These results have led us to conclude that the AMPT model with its fluctuating initial conditions and strong partonic scatterings can capture the essential collision dynamics of relativistic heavy ion collisions as revealed in the measured anisotropic flows and three-particles correlations.

[1] Z.-W. Lin, C.M. Ko, B.-A. Li, B. Zhang, and S. Pal, Phys. Rev. C **72**, 064901 (2005).
[2] J. Xu and C.M. Ko, Phys. Rev. C **84**, 014903 (2011).
[3] Y. Sun and C.M. Ko, Phys. Lett. B **769**, 219 (2017).
[4] L. Adamczyk *et al.* (STAR Collaboration), arXiv:1701.06497 [nucl-ex].

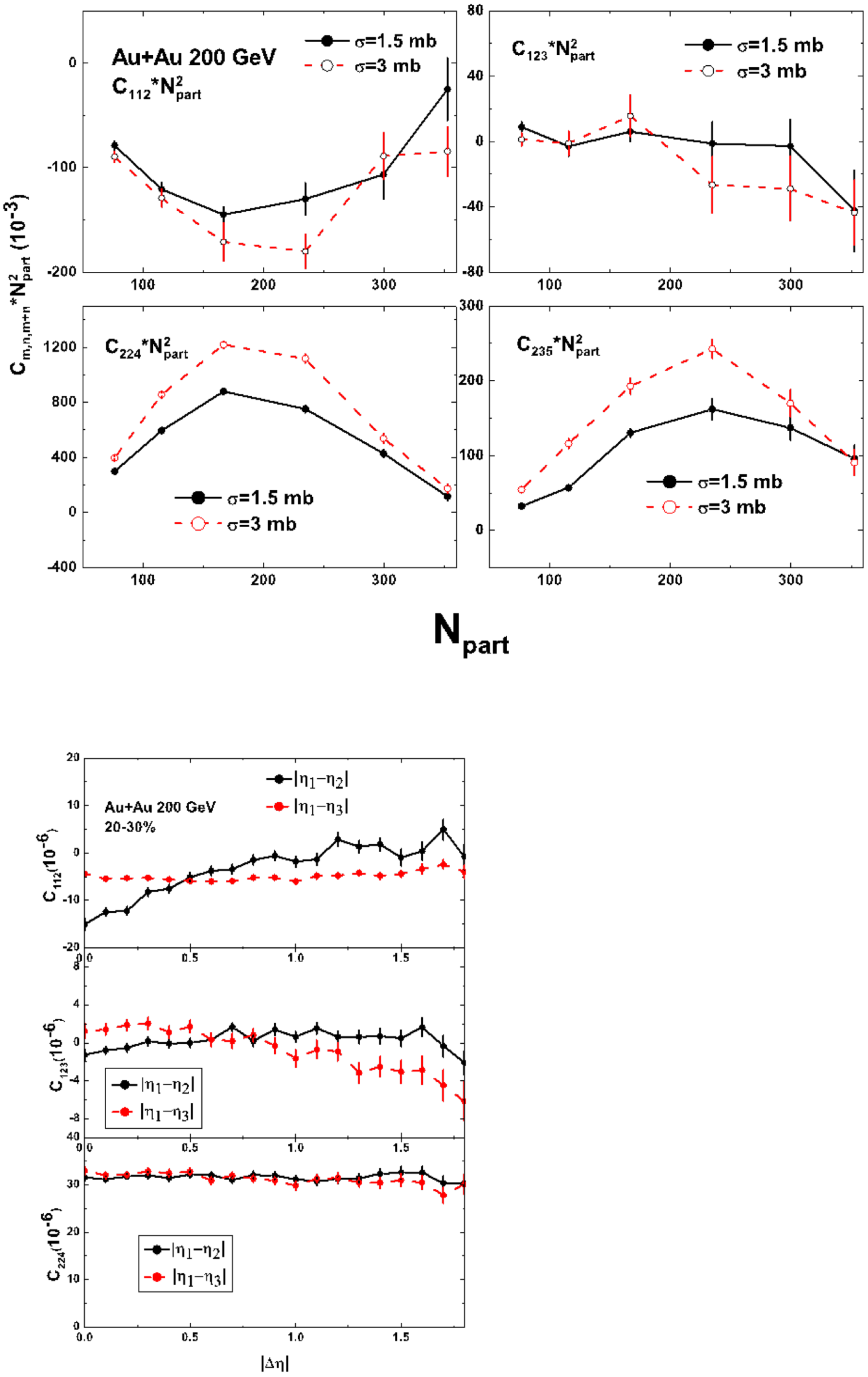

FIG. 1. Centrality (left window) and relative pseudorapidity |Δη| (right window) dependence of $C_{m,n,m+n}N_{part}$ for mid-pseudorapidity (|η|<1) charged particles of transverse momentum p_T>0.2 GeV/*c* in Au+Au collisions at s_{NN} = 200 GeV. Open circles are experimental data from [3].

Elliptic flow of light nuclei

X. J. Yin,[1] C.M. Ko, Y. Sun, and L.L. Zhu[1]

[1]*Department of Physics, Sichuan University, Chengdu 610064, China*

Using the coalescence model based on the nucleon phase-space distribution function from a blast-wave model, we have studied the transverse momentum spectra and elliptic flows of light nuclei in relativistic heavy-ion collisions [1]. Assuming that the spatial distribution of nucleons in the system is independent of their momenta and fitting the parameters to the experimental measured proton transverse momentum spectrum and elliptic flow by the STAR collaboration at RHIC, we have obtained a good description of the measured transverse momentum spectra of deuteron (antideuteron) and triton (helium-3) as shown in the top window of Fig.1 but have failed to reproduce the measured elliptic flows of these nuclei, particularly at large transverse momenta. We have attributed this failure of the coalescence model to the neglect of possible preference of nucleons of large transverse momenta to be more spread in space if their momenta are along the reaction plane than perpendicular to it. Allowing a nucleon phase-space distribution that includes such space-momentum correlations in the blast-wave model indeed leads to a good description of the elliptic flows of deuteron (anti-deuteron) and triton (helium-3) as shown in the bottom window of Fig. 1. Our study thus indicates that the elliptic flows of light nuclei are sensitive to the space- momentum correlations of nucleons at kinetic freeze-out and are thus a possible probe of the nucleon emission source in relativistic heavy ion collisions.

[1] X.J. Yin, C.M. Ko, Y. Sun, and L.L. Zhu, Phys. Rev. C **95**, 054913 (2017).

[2] B.I. Abelev *et al.* (STAR Collaboration), Phys. Rev. Lett. **97**, 152301 (2006).

[3] S.S. Adler et al. (PHENIX Collaboration), Phys. Rev. Lett. **94**, 122302 (2005).

[4] B. I. Abelev *et al.* (STAR Collaboration) (2009), arXiv:0909.0566 [nucl-ex].

[5] L. Adamczyk *et al.* (STAR Collaboration), Phys. Rev. Lett. **116**, 062301 (2016).

[6] L. Adamczyk *et al.* (STAR Collaboration), Phys. Rev. C **94**, 034908 (2016).

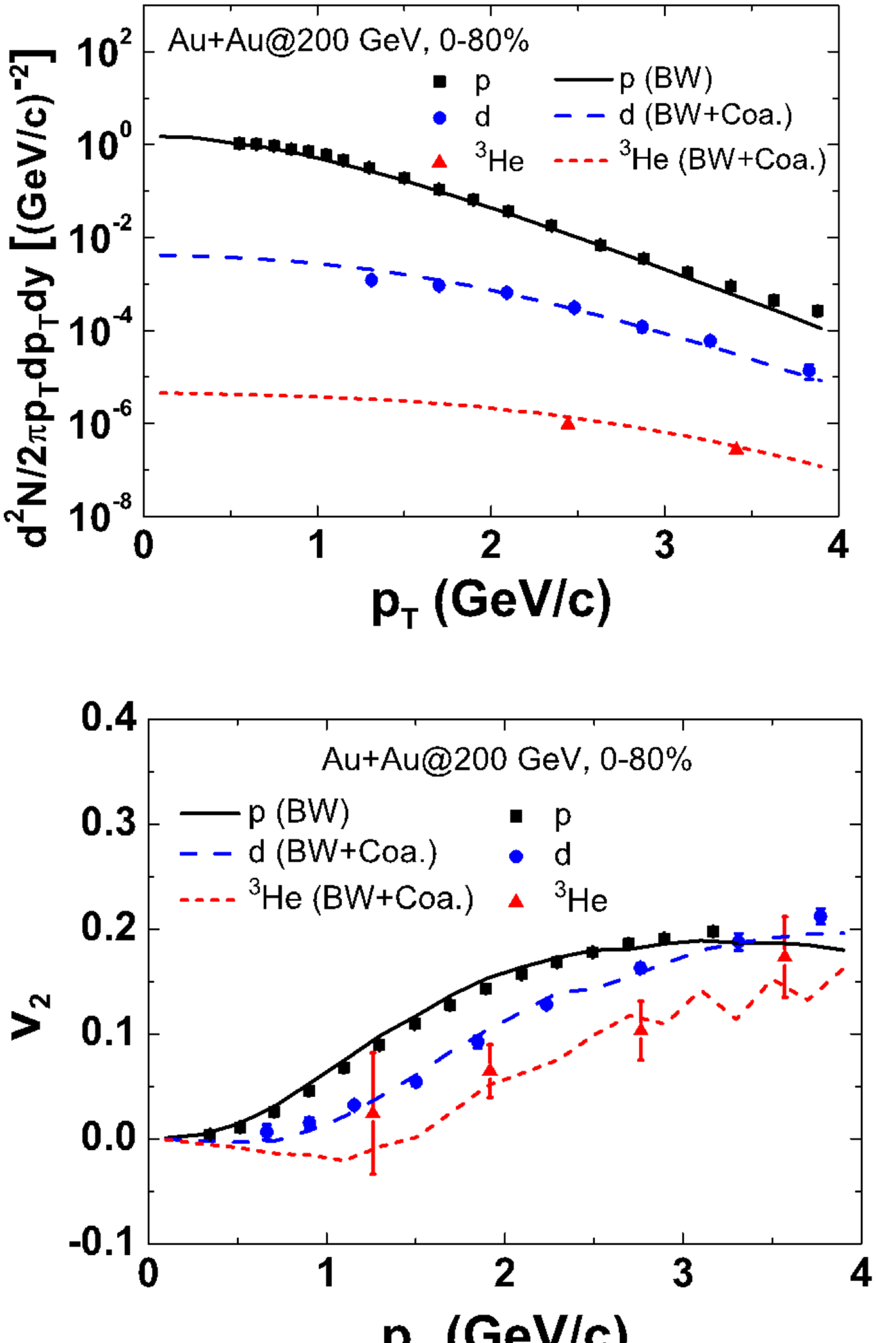

FIG. 1. Transverse momentum spectra (top) and elliptic flows (bottom) of midrapidity proton (black solid line), deuteron (anti-deuteron) (blue long-dashed line), and triton (helium-3) (red short-dashed line) from the coalescence model based on a blast-wave model with space-momentum correlation for Au+ Au collisions at $\sqrt{s_{NN}}$ = 200 GeV and centrality of 0- 80%. Data for transverse momentum spectra are from Refs.[2] for proton, Ref. [3] for deuteron (anti-deuteron), and Ref. [4] for triton (helium-3), while those for elliptic flows are from Ref.[5] for proton and Ref. [6] for deuteron (anti-deuteron) and triton (helium-3).

Collision energy dependence of elliptic flow splitting between particles and their antiparticles from an extended multiphase transport model

J. Xu and C.M. Ko

Based on an extension to the AMPT model [1] that includes mean-field potentials in both the partonic and the hadronic phase, uses the mix-event coalescence for hadronization, and ensures the charge conservation during the hadronic evolution, we have studied the energy dependence of elliptic flow splitting between particles and their antiparticles at RHIC-BES energies [2]. The density evolutions of particles and their antiparticles in both the partonic and hadronic phases are illustrated. The elliptic flow splitting from the contribution of the partonic phase and the further modification in the hadronic phase at various collision energies is observed. As shown in Fig. 1, our model can describe reasonably well the elliptic flow splitting at lower collision energies and can describe qualitatively but not quantitatively that at higher beam energies. In particular, our model underestimates the elliptic flow splitting between nucleons and antinucleons at higher collision energies. The present study thus calls for other mechanisms in addition to the mean-field potentials that may contribute to the elliptic flow splitting between particles and their antiparticles.

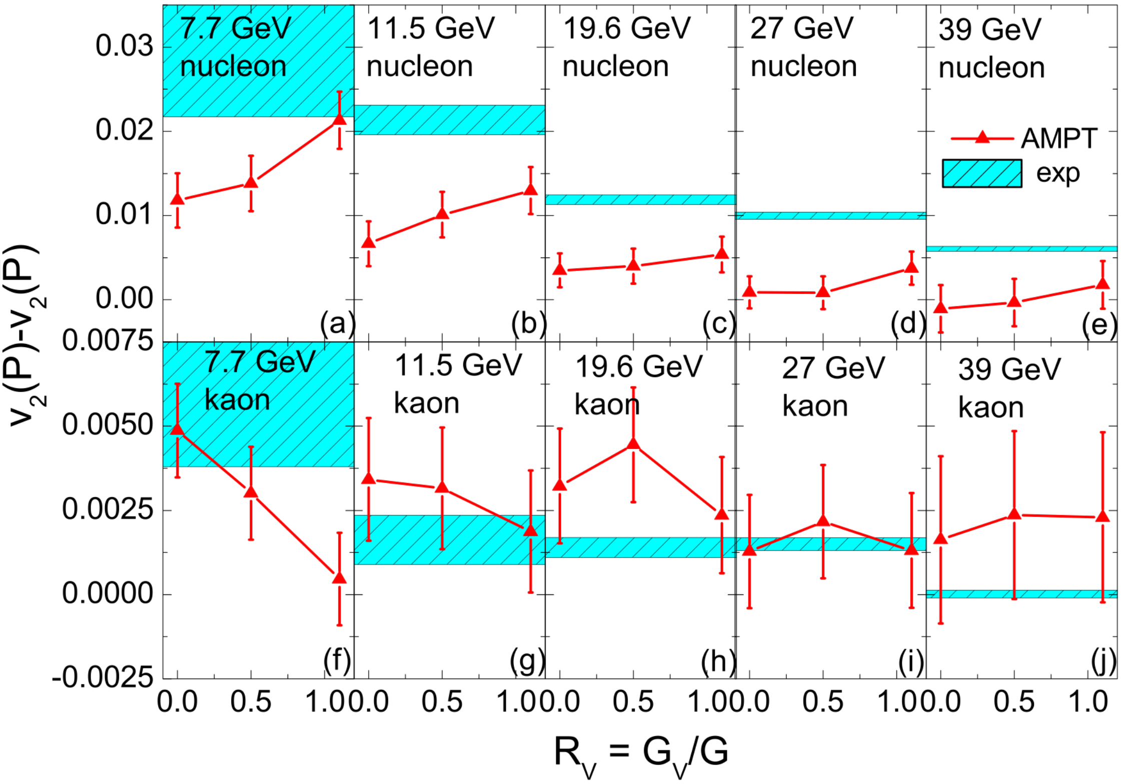

FIG. 1. Elliptic flow difference between midrapidity nucleons and antinucleons (upper panels) and that between midrapidity K^+ and K^- (lower panels) in the final stage of mini-bias (0%–80%) Au + Au collisions at $\sqrt{s}$= 7.7, 11.5, and 39 GeV, with the quark vector to scalar couplings R_V = 0, 0.5, and 1.1. Experimental data are from Ref.[3].

[1] Z.-W. Lin, C.M. Ko, B.-A. Li, B. Zhang, and S. Pal, Phys. Rev. C **72**, 064901 (2005).
[2] J. Xu and C.M. Ko, Phys. Rev. C **94**, 054909 (2016).
[3] L. Adamczyk *et al.* (STAR Collaboration), Phys. Rev. Lett. **110**, 142301 (2013).

Thermal production of charm quarks in heavy ion collisions at future circular collider

Y. Liu[1] and C.M. Ko
[1]*Department of Physics, Tianjin University, Tianjin 300072, People's Republic of China*

We have studied charm quark production from the quark-gluon plasma (QGP) produced in heavy ion collisions at 39 TeV in the future circular collider (FCC) [1]. Using the charm production cross section in quark-antiquark and gluon–gluon scattering calculated in the next-to-leading order in QCD [2,3] and assuming that the produced QGP expands boot invariantly, we have found that charm production from the QGP is not negligible. Depending on the formation time of the QGP, its contribution can be near to 50% for a formation time of 0.2 fm. Such an enhanced production of charm quarks than that produced from initial hard scattering is expected to have a significant effect on not only open charm but also charmonium production in heavy ion collisions at this energy [4].

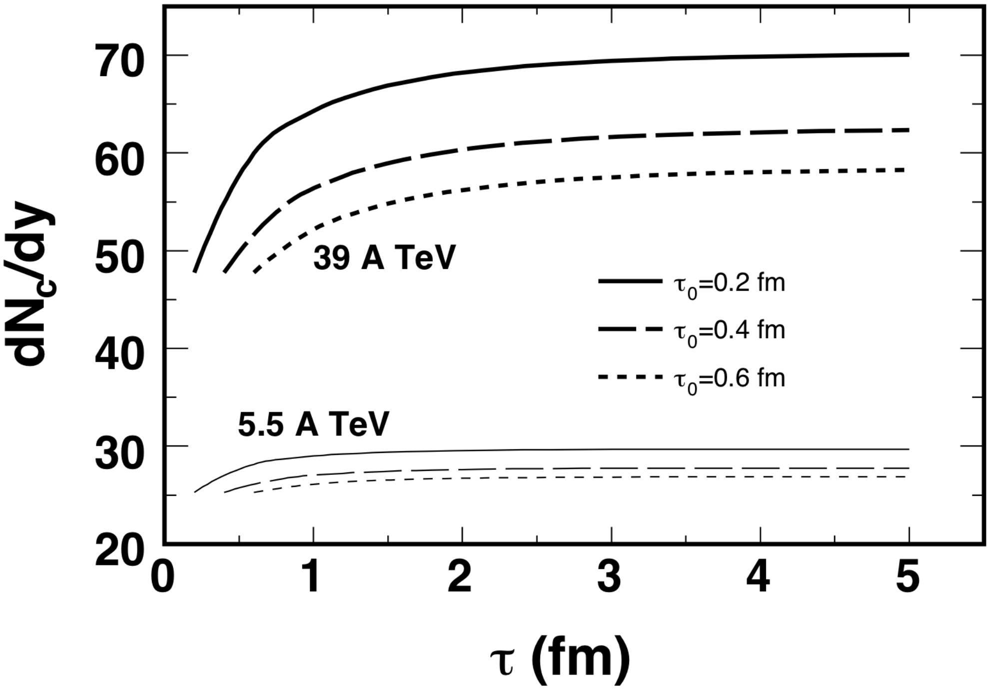

FIG. 1. Time evolution of the number of charm quarks with different QGP formation time τ_0.

[1] Y. Liu and C.M. Ko, J. Phys. G **43**, 125108 (2016).
[2] P. Nason, S. Dawson, and R. K. Ellis, Nucl. Phys. **B303**, 607 (1988); Nucl. Phys. **B327**, 49 (1989).
[3] B.W. Zhang, C.M. Ko, and W. Liu, Phys. Rev. C **77**, 024901 (2008).
[4] K. Zhou, Z. Chen, C. Greiner, and P. Zhuang, Phys. Lett. B **758.** 434 (2106).

Anomalous transport model study of chiral magnetic and vertical effects in heavy ion collisions

Y.F. Sun and C.M. Ko

Based on the anomalous transport model, which includes the propagation of massless quarks and antiquarks according to the chiral kinetic equation [1-3] and allows the change of chiralities during the scattering between positively and negatively charged partons, we have studied the elliptic flow of charged particles in non-central relativistic heavy ion collisions [4,5]. Using initial conditions from a blast wave model and assuming the presence of a strong and long-lived magnetic field, we have obtained an appreciable charge quadrupole moment in the transverse plane of the collision, which then leads to different elliptic flows for particles of negative and positive charges, shown in the upper window of Fig.1, as the system expands. The elliptic flow difference shows a linear dependence on the total charge asymmetry $A_{\pm}= (N_{+}-N_{-})/(N_{+}+N_{-})$ of the partonic matter, where N_{+} and N_{-} are the total number of positively and negatively charged particles, with a slope that is negative unless the Lorentz force is neglected. Compared to the experimental data, ours is, however, much smaller. Similar results are obtained if we also assume the presence of a vorticity field, which is modeled according to that from the AMPT model [6], except the appearance of a positive intercept at zero charge asymmetry, as shown in the lower panel of Fig.1, which is, however, larger than the experimental value [7]. With only the vorticity field, no elliptic flow splitting of negatively and positively charged particles is present when the charge asymmetry of the partonic matter is nonzero. As shown by dashed lines in Fig.1, the inclusion of the Lorentz force cancels the chiral effects due to the magnetic and vorticity fields and leads instead to a negative slope parameter in the charge symmetry dependence of the elliptic flow splitting of negatively and positively charged particles, contrary to that observed in experiments. Understanding this experimental result in terms of the chiral effects thus remains a challenge.

[1] M.A. Stephanov and Y. Yin, Phys. Rev. Lett. **109**, 162001 (2012).

[2] J.-H. Gao, Z.-T. Liang, S. Pu, Q. Wang, and X.-N. Wang, Phys. Rev. Lett. **109**, 232301 (2012).

[3] J.-W. Chen, S. Pu, Q. Wang, and X.-N. Wang, Phys. Rev. Lett. **110**, 262301 (2013).

[4] Y. Sun, C.M. Ko, and F. Li, Phys. Rev. C **94**, 045204 (2016).

[5] Y. Sun and C.M. Ko, Phys. Rev. C **95**, 034909 (2017).

[6] Z.-W. Lin, C.M. Ko, B.-A. Li, B. Zhang, and S. Pal, Phys. Rev. C **72**, 064901 (2005).

[7] G. Wang, Nucl. Phys. **A904-905**, 248c (2013).

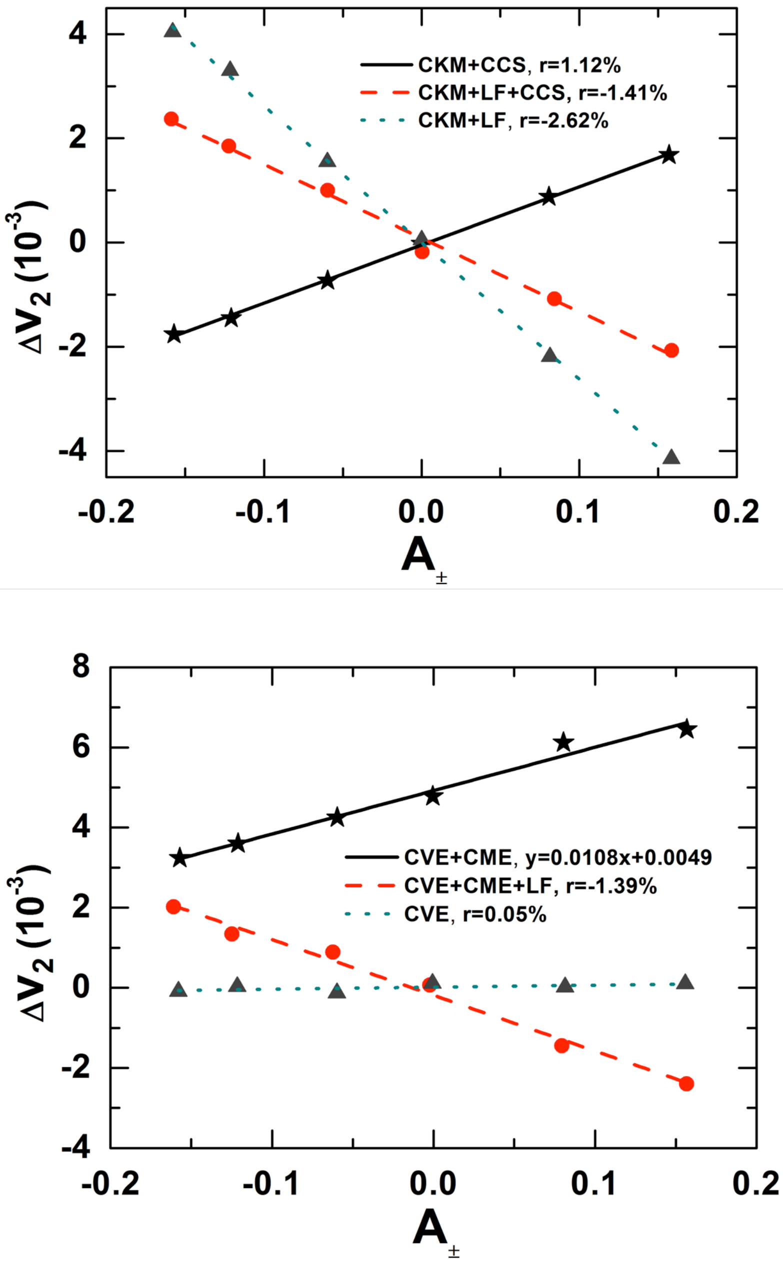

FIG. 1. Elliptic flow difference as a function of charge asymmetry $A_\pm$ for different scenarios of parton dynamics in ther presence of only a mganeitc field (left window) and both the magnetic and vorticity fields (right window).

Nuclear dipole polarizability from mean-field models constrained by chiral effective field theory

Z. Zhang, Y. Lim, J.W. Holt, and C.M. Ko

We have constructed three extended Skyrme interactions [1] by fitting the EOSs of nuclear matter with various isospin asymmetric as predicted by chiral effective field theory [2,3] together with the binding energies of selected closed shell doubly-magic nuclei. Using these interaction, we have then studied the isovector dipole response of ^{48}Ca, ^{68}Ni, ^{120}Sn, and ^{208}Pb in the random-phase approximation (RPA). We have found that although the RPA calculations using the three extended Skyrme interactions slightly underestimate the peak energy of the giant dipole resonance, they nevertheless well reproduce the experimental data on the electric dipole polarizability as shown in Fig.1. We have further investigated the correlation between the neutron skin thickness and the product of the electric dipole polarizability and symmetry energy at saturation density. The predicted results from the three extended Skyrme interactions are found to be consistent with the linear relations extracted from RPA calculations using a representative set of energy density functionals. The predicted neutron skin thickness of ^{208}Pb from our study is also consistent with the experimental values [4-6]. Our results thus confirm the usefulness of these extended Skyrme interactions in studying the isovector properties of nuclei in regimes where *ab initio* calculations with chiral nuclear forces have not been feasible.

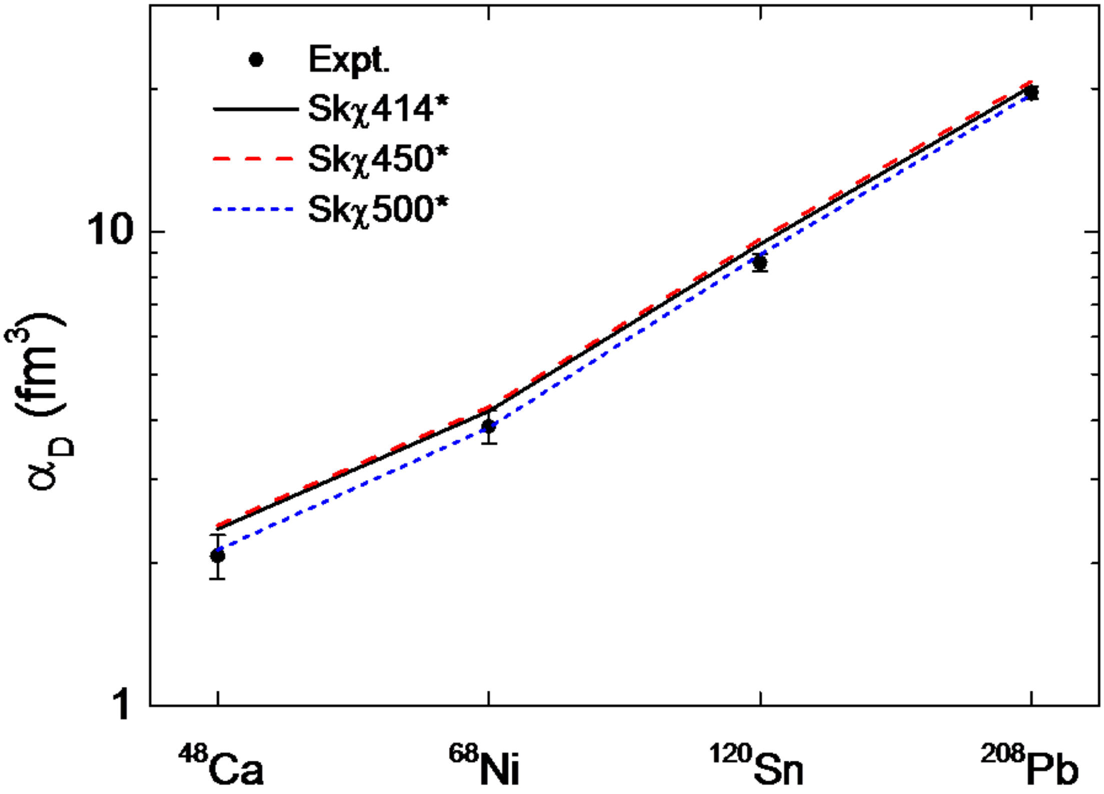

FIG. 1. Electric dipole polarizabilities of ^{48}Ca, ^{68}Ni, ^{120}Sn, and ^{208}Pb predicted by Skχ414*, Skχ450* and Skχ500*. For comparison, experimental data [4-7] are shown as black solid circles.

[1] Z. Zhang, Y. Lim, J.W. Holt, and C.M. Ko, Phys. Lett. B (Submitted).

[2] C. Wellenhofer, J.W. Holt, and N. Kaiser, Phys. Rev. C **93**, 015801 (2015).

[3] C. Wellenhofer, J.W. Holt, and N. Kaiser, Phys. Rev. C **93**, 055802 (2016).

[4] C.M. Tarbert *et al.*, Phys. Rev. Lett. **112**, 242502 (2014).

[5] C.J. Horowitz *et al.,* Phys. Rev. C **85**, 032501(R) (2012).

[6] S. Abrahamyan *et al.*, Phys. Rev. Lett. **108**, 112502 (2012).

Spinodal instabilities of baryon-rich quark matter in heavy ion collisions

F. Li and C.M. Ko

Using the test-particle method to solve the transport equation derived from the Nambu-Jona-Lasino (NJL) model, we have studied how phase separation occurs in expanding quark matter like that in a heavy ion collision [1]. To test our method, we have first investigated the growth rates of unstable modes of quark matter in a static cubic box and found them to agree with the analytical results that were previously obtained using the linear response theory [2]. In this case, we have also studied the higher-order scaled density moments in the quark matter, which have values of one for a uniform density distribution or a distribution where the nonzero density regions all have same value, and they are found to increase with time and saturate at values significantly larger than one after the phase separation. The skewness of the quark number event-by-event distribution in a small subvolume of the system is also found to increase, but this feature disappears if the subvolume is large. For the expanding quark matter, two cases have been considered: one using a blast-wave model for the initial conditions and the other using initial conditions from a multiphase transport (AMPT) model [3]. In both cases, we have found that the expansion of the quark matter is slowed down by the presence of a first-order phase transition. Also, density clumps appear in the system and the momentum distribution of partons becomes anisotropic, which can be characterized by large scale density moments and nonvanishing anisotropic elliptic and quadrupolar flows, respectively. The large density fluctuations further lead to an enhancement in the dilepton yield. In the case with the AMPT initial conditions, the presence of a first-order phase transition also results in a narrower distribution of partons in rapidity. These effects of density fluctuations can be regarded as possible signals for a first-order phase transition that occurs in the baryon-rich quark matter formed in relativistic heavy ion collisions.

[1] F. Li and C.M. Ko, Phys. Rev. C **95**, 055203 (2017).
[2] F. Li and C.M. Ko, Phys. Rev. C **93**, 035205 (2016).
[3] Z.-W. Lin, C.M. Ko, B.-A. Li, B. Zhang, and S. Pal, Phys. Rev. C **72**, 064901 (2005).

Medium effects on pion production in heavy ion collisions

Z. Zhang and C.M. Ko

We have extended the relativistic Vlasov-Uehling-Uhlenbeck (RVUU) model based on the nonlinear relativistic NLρ mean-field model [1] by including the isospin-dependent pion *s*-wave and *p*-wave potentials in nuclear medium [2], which are obtained from calculations based on the chiral perturbation theory [3] and the Δ-hole model [4,5], respectively. Their effects on the π^-/π^+ ratio in Au + Au collisions at E/A = 400 MeV have been studied in following six different cases: i) without the threshold and pion in-medium effects (free), namely, nucleons, Δ resonances and pions are treated as free particles in all reactions; (ii) with only the threshold effect (Th); (iii) with the threshold effect and the pion s-wave potential (Th+S); (iv) with the threshold effect and the pion p-wave potential (Th+P); (v) with the threshold effect and both the pion s-wave and p-wave potentials (Th+S+P); (vi) same as case (v) but with the coupling constant for the isovector-vector ρ meson to nucleon in the NLρ model reduced. It is seen from Fig. 1 that while the π^-/π^+ ratio is enhanced by the pion *p*-wave potential, it is significantly suppressed by the pion *s*-wave potential. As a result, the pion potentials in nuclear medium lead to a significant reduction (about 10 %) of the π^-/π^+ ratio, which is comparable to that due to the stiffness of nuclear symmetry energy at high densities. After including both the threshold effect and the pion in-medium effect, the π^-/π^+ ratio obtained from the RVUU model based on the relativistic NLρ model, which has a value of L = 84 MeV for the slope parameter of nuclear symmetry energy, is slightly larger than the experimental upper value from the FOPI Collaboration [6]. Using a softer symmetry energy of L=59 MeV, which is consistent with currently known empirical value [7,8], by reducing the ρ-nucleon coupling constant in the NLρ model can, however, well reproduce the experimental data on the charged pion ratio.

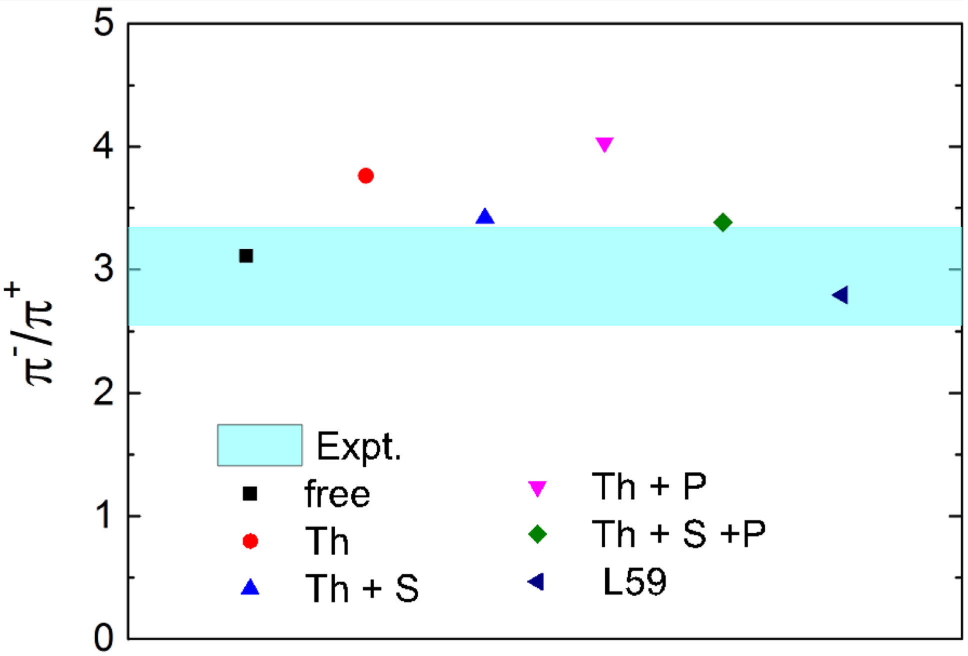

FIG. 1. The π^-/π^+ ratio in Au+Au collisions at impact parameter of 1.4 fm and energy of E/A = 400 MeV from the NLρ model in different cases (see text for details). Experimental data from the FOPI collaboration [6] are shown as the cyan band.

[1] T. Song and C.M. Ko, Phys. Rev. C **91**, 014901 (2015).

[2] Z. Zhang and C.M. Ko, Phys. Rev. C **95**, 064604.

[3] N. Kaiser and W. Weise, Phys. Lett. B **512**, 283 (2001).

[4] G.E. Brown and W. Weise, Phys. Rep. **22**, 279 (1975).

[5] L. Xiong, C.M. Ko, and V. Koch, Phys. Rev. C **47**, 788 (1993).

[6] W. Reisdorf *et al.*(FOPI Collaboration), Nucl. Phys. **A848**, 366 (2010).

[7] M. Oertel, M. Hempel, T. Klähn, and S. Typel, Rev. Mod. Phys. **89**, 015007 (2017).

[8] B.-A. Li, arXiv:1701.03564 [nucl-th].

Subthreshold resonances and resonances in the R-matrix method for binary reactions and in the Trojan Horse method

A.M. Mukhamedzhanov, Shubhchintak, and C.A. Bertulani

In this work we discuss the R-matrix approach to treat the sub-threshold resonances for the single-level and one channel, and for the single-level and two channel cases. In particular, the expression relating the ANC with the observable reduced width, when the sub-threshold bound state is the only channel or coupled with an open channel, which is a resonance, is formulated. Since the ANC plays a very important role in nuclear astrophysics, these relations significantly enhance the power of the derived equations. We present the relationship between the resonance width and the ANC for the general case and consider two limiting cases: wide and narrow resonances. Different equations for the astrophyical S-factors in the R-matrix approach are presented. After that we discuss the Trojan Horse Method (THM) formalism. The developed equations are obtained using the surface-integral formalism and the generalized R-matrix approach for the three-body resonant reactions. It is shown how the Trojan Horse (TH) double differential cross section can be expressed in terms of the on-the-energy-shell astrophysical S-factor for the neutron generator $^{13}C(\alpha,n)^{16}O$ in low-mass AGB stars. At astrophysically relevant energies this astrophysical S-factor is controlled by the threshold level $1/2^+$, $E_x = 6356$ keV. Here, we reanalyzed recent TH data taking into account more accurately the three-body effects and using both assumptions that the threshold level is a subthreshold bound state or it is a resonance state.

This work has been submitted to Phys. Rev. C.

Internal and external radiative widths in the combined R-matrix and potential-model formalism

A.M. Mukhamodzhanov, Shubbchintak, C.A. Bertulani, and T.V. Nhan Hao

By using the R-matrix approach we calculate the radiative width for a resonance decaying to a bound state through electric-dipole E1 Transitions. The total radiative width is determined by the interference of the nuclear internal and external radiative width amplitudes. For a given channel radius the external radiative width amplitude is model independent and is determined by the asymptotic normalization coefficient (ANC) of the bound state to which the resonance decays. It also depends on the partial resonance width. To calculate the internal radiative width amplitude we show that a single-particle-potential model is appropriate. We compare our results with a few experimental data.

The work was published in Phys. Rev. C **95,** 024616 (2017).

The cosmological lithium problem revisited

C.A. Bertulani, A.M. Mukhamedzhanov, and Shubhchintak

A brief review of the cosmological lithium problem is presented. We also report a few recent attempts to find theoretical solutions by out group at Texas A&M University (Commerce & College Station). We discuss our studies on the theoretical description of electron screening, the possible existence of parallel universes of dark matter, and the use of non-extensive statistics during the Big Bang nucleosynthesis epoch. Last but not least, we discuss possible solutions within the nuclear physics realm. The impact of recent measurements of relevant nuclear reaction cross sections for the Big Bang nucleosynthesis based on indirect methods is also assessed. Although our attempts may not be able to explain the observed discrepancies between theory and observations, they suggest theoretical developments that can be useful also for stellar nucleosynthesis.

The talk published in AIP Conference Proceedings **1753**, 040001 (2016); doi: 10.1063/1.4955357

Assessing the near threshold cross section of the ^{17}O(n, α)^{14}C reaction by means of the Trojan Horse method

G.L. Guardo, C. Spitaleri, L. Lamia, M. Gulino, M. La Cognata, X. Tang, R. deBoer, X. Fang, V. Goldberg, J. Mrazek, A. Mukhamedzhanov, N. Notani, R.G. Pizzone, G.G. Rapisarda, M.L. Sergi, and M. Wiescher

The study of the ^{17}O(n, α)^{14}C reaction has been performed by means of the Trojan horse method (THM) applied to the quasifree ^{2}H(^{17}O, α^{14}C)^{1}H reaction induced at a beam energy of 43.5 MeV. The THM allowed us to study the 8121-keV 180* resonant level, for which the previous THM investigation pointed out the ability of the method to overcome the centrifugal barrier suppression effects in the entrance channel. Here, in view of the developments of the method for resonant reactions, the detailed analysis of the performed experiment will be discussed, focusing on the extraction of the 8121-keV resonance strength for which no information is present in scientific literature. Moreover, the experimental results clearly show the excitation of the subthreshold level centered at -6keV in the center-of-mass system, which is fundamental to determine the ^{17}O(n, α)^{14}C reaction rate of astrophysical interest. Finally, a new recommended reaction rate is presented for future astrophysical application.

The work was published in Phys. Rev. C **85**, 025807 (2017).

Measurement of the $^{10}B(p, \alpha_0)^7Be$ cross section from 5 keV to 1.5 MeV in a single experiment using the Trojan Horse method

C. Spitaleri, S.M.R. Puglia, M. La Cognata, L. Lamia, S. Cherubini, A. Cvetinovic, G. D'Agata, M. Gulino, G.L. Guardo, I. Indelicato, R.G. Pizzone, G.G. Rapisarda, S. Romano, M.L. Sergi, R. Spart'a, S. Tudisco, A. Tumino, M. Gimenez Del Santo, N. Carlin, M.G. Munhoz, F.A. Souza, A. Szanto de Toledo, A. Mukhamedzhanov, C. Broggini, A. Caciolli, R. Depalo, R. Menegazzo, V. Rigato, I. Lombardo, and D. Dell'Aquila

For the first time the astrophysical factor of the $^{10}B(p, \alpha_0)^7Be$ reaction has been measured over a wide energy range, from 5 keV to 1.5 MeV, via the Trojan horse method (THM) applied to the quasifree $^2H(^{10}B, \alpha^7Be)n$ reaction. Therefore, the S(E) factor has been recast into absolute units by scaling in the energy range 200 keV- 1.2 MeV to a recent measurement using the activation method, leading to a normalization uncertainty of 4%. An R-matrix fit of the THM data was performed, to parametrize the S factor, obtain spectroscopic information on the populated resonances, and compare with other recent experiments. Finally, a new determination of the screening potential U_e has been obtained, U_e= 240 ± 50eV, with a much smaller error than our previous measurement.

This work was published in Phys. Rev. C **95**, 035801 (2017).

Radiative nucleon capture with quasi-separable potentials

Schubhchintak, C.A. Bertulani, A.M. Mukhamedzhanov, and A. Kruppa

We study radiative capture reactions using quasi-separable potentials. This procedure allows an easier treatment of non-local efforts that can be extended to three-body problems. Using this technique, we calculate the neutron and proton radiative capture cross sections on 12C. The results obtained are shown to be in good agreement with the available experimental data. The experimental phase shifts are also well reproduced and can be straightforwardly be extended to multi-channel problems.

This work was published in Journal of Physics G: Nuclear and Particle Physics, **43**, 125203 (2016).

Primordial α+d → ^{6}Li+γ reaction and second lithium puzzle

A.M. Mukhamedzhanov, Shubhchintak, and C.A. Bertulani

During the Big Bang, ^{6}Li was synthesized via the ^{2}H(α,γ)^{6}Li reaction. After almost *25* years of the failed attempts to measure the ^{2}H(α,γ)^{6}Li reaction in the laboratory at Big Bang energies, just recently the LUNA Collaboration presented the first successful measurements at two different Big Bang energies [1]. In this paper we will discuss how to improve the accuracy of the direct experiment. To this end the photon's angular distribution is calculated in the potential model. It contains contributions from electric dipole and quadrupole transitions and their interference, which dramatically changes the photon's angular distribution. The calculated distributions at different Big Bang energies have a single peak at ~50°. These calculations provide the best kinematic conditions to measure the 2H(α,γ)6Li reaction. The expressions for the total cross section and astrophysical factor are also derived by integrating the differential cross section over the photon's solid angle. The LUNA data are in excellent agreement with our calculations using a potential approach combined with a well established asymptotic normalization coefficient for ^{6}Li → α + d. Comparisons of the available experimental data for the astrophysical factor and different calculations *are* presented. The Big Bang lithium isotopic ratio ^{6}Li/^{7}Li following from the LUNA data and the present analysis are discussed in the context of the disagreement between the observational data and the standard Big Bang model, which constitutes the second lithium problem.

This work published in Phys. Rev. C **93**, 045805 (2016).

[1] Anders *et al.*, Phys. Rev. Lett. **113**, 042501 (2014).

Description of charged particle pseudorapidity distributions in Pb+Pb collisions with Tsallis thermodynamics

G. Yuan,[1] H. Zheng,[2] L.L. Zhu,[3] and A. Bonasera[2, 4]
[1]*School of Information Engineering, Hangzhou Dianzi University, Hangzhou, China*;
[2]*Laboratori Nazionali del Sud, INFN, I-95123 Catania, Italy*;
[3]*College of Physical Science and Technology, Sichuan University, Chengdu, China*;
[4]*Cyclotron Institute, Texas A&M University, College Station, Texas*

The centrality dependence of pseudorapidity distributions for charged particles produced in Au+Au collisions at sqrt(s)$_{NN}$ = 130 GeV and 200 GeV at RHIC, and in Pb+Pb collisions at sqrt(s)$_{NN}$ = 2.76 TeV at LHC are investigated in the fireball model, assuming that the rapidity axis is populated with fireballs following one distribution function. We assume that the particles in the fireball fulfill the Tsallis distribution. The theoretical results are compared with the experimental measurements and a good agreement is found as shown in Fig. 1. Using these results, the pseudorapidity distributions of charged particles produced in Pb+Pb central collisions at sqrt(s)$_{NN}$ = 5.02 TeV and 10 TeV are predicted.

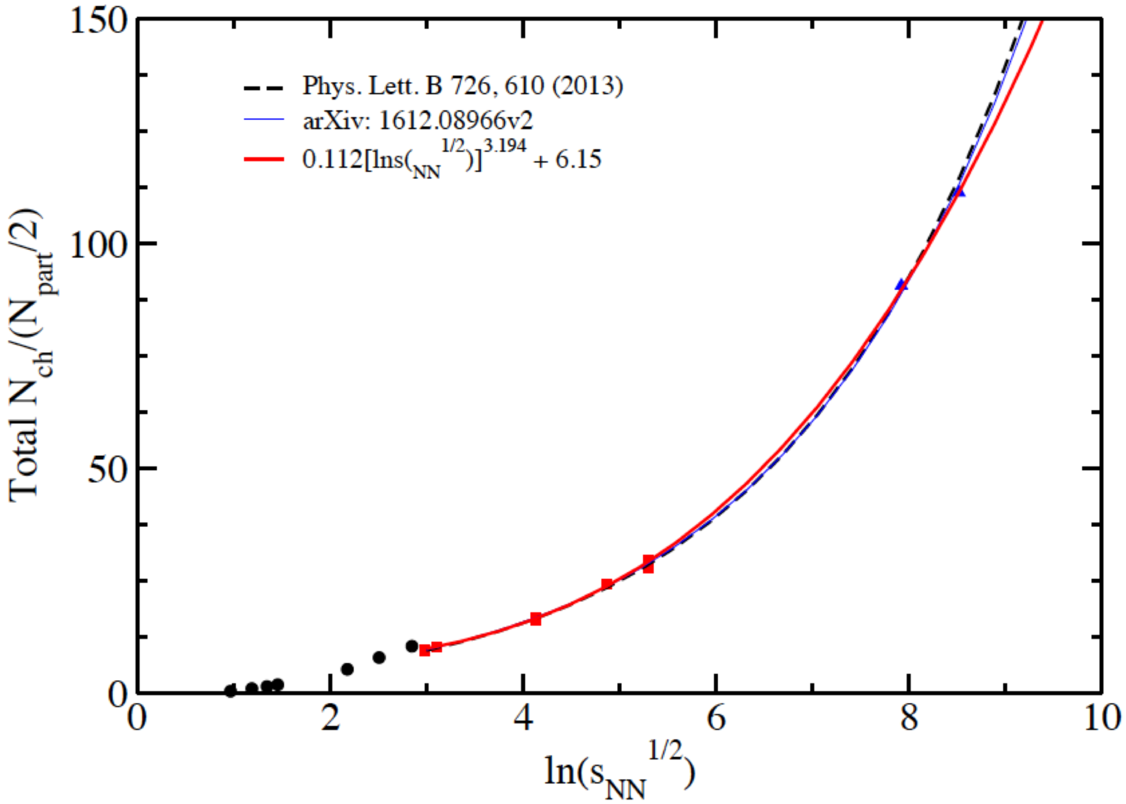

FIG. 1. The total number of charged particles per participant pair produced in the most central collisions versus ln(sqrt(s)$_{NN}$). The experimental data at AGS (0-5% Au+Au), SPS (0-5% Pb+Pb), RHIC (0-6% Au+Au and 0-6% Cu+Cu) and LHC (Pb+Pb 0-5%) are taken from Refs. In the inset. The curves are our fitting results and the ones from Refs. In the inset.

Highly compressed and *not* so hot plasma at the SGII laser facility

A. Bonasera (Proposal for the INFN, SGII, SIOM, SINAP, TAMU, and IMUM collaboration)

Our recent experiment at the SGII laser facility using 8 lasers impinging on a solid CD_2 target of different thicknesses indicates that high compression is reached in some shots. The reached density is three orders of magnitude higher than the initial plastic density but the temperature at the time when fusions occur is not so high (of the order of 1 KeV or less). Energetic neutrons and protons coming from ternary reactions: $d+t\rightarrow\alpha$+n (14MeV) and $d+{}^3He\rightarrow\alpha$+p (14.7MeV) are slowed down in the compressed plasma. This can be considered as an 'attempt' to ignite the plasma, see Fig. 1.

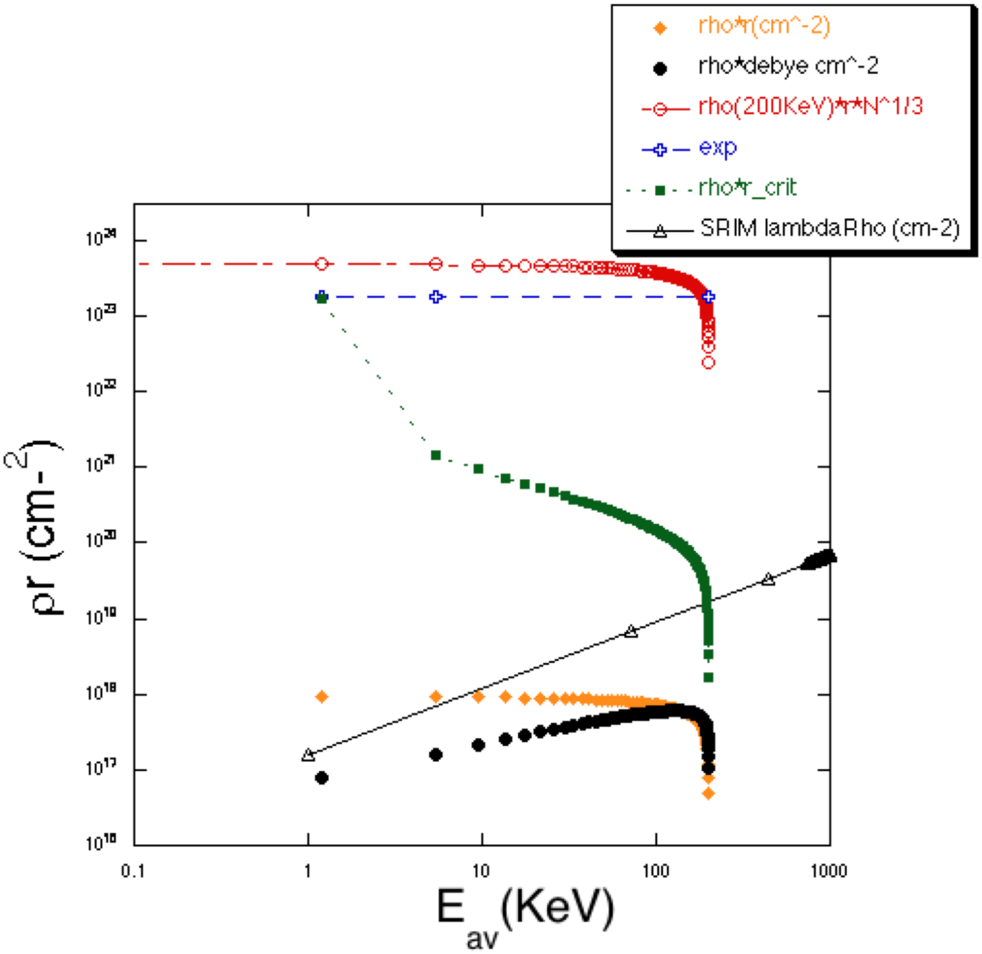

FIG. 1. The product of density times the range of the ions in the hot and compressed plasma. The dashed+cross symbol refers to the ratio of 3 to 2 body fusion reaction obtained at SGII. Other symbols refer to theoretical calculations using simplified CD_2 equation of state and different assumption for the ion range in the plasma.

In medium energy levels of light cluster

S. Zhang,[1] M. Huang,[1] H. Zheng,[2], A. Bonasera,[2,3], Z. Kohley,[2,4] and S.J. Yennello[2,4]
[1]*College of Physics and Electronics information,*
Inner Mongolia University for Nationalities, Tongliao, 028000, China
[2]*Laboratori Nazionali del Sud, INFN, via Santa So_a, 62, 95123 Catania, Italy*
[3]*Cyclotron Institute, Texas A&M University, College Station, Texas*
[4]*Chemistry Department, Texas A&M University, College Station, Texas*

We explore the possibility of deriving energy levels of nuclei from fragmentation reaction. In particular, we investigate the geometry configurations of triple *α*, *t*+2p and ^3He+2p resonances measured in $^{70}Zn+^{70}Zn$, $^{64}Zn+^{64}Zn$ and $^{64}Ni+^{64}Ni$ at 35 MeV/nucleon using the hyper-spherical method. The experimental results are successful compared to microscopic CoMD calculations. In particular the model calculations show that 3α particle correlation functions are mostly determined by direct 3α and α+^{8}Be production in the fragmentation reaction with the contribution from ^{12}C decay negligible. We derive the three-body correlation function from the knowledge of the one-body and two-body correlations. The rate of α+^{8}Be→^{12}C reaction is studied as well. The possibility of Bose Einstein Condensate/Fermion Quenching is addressed.

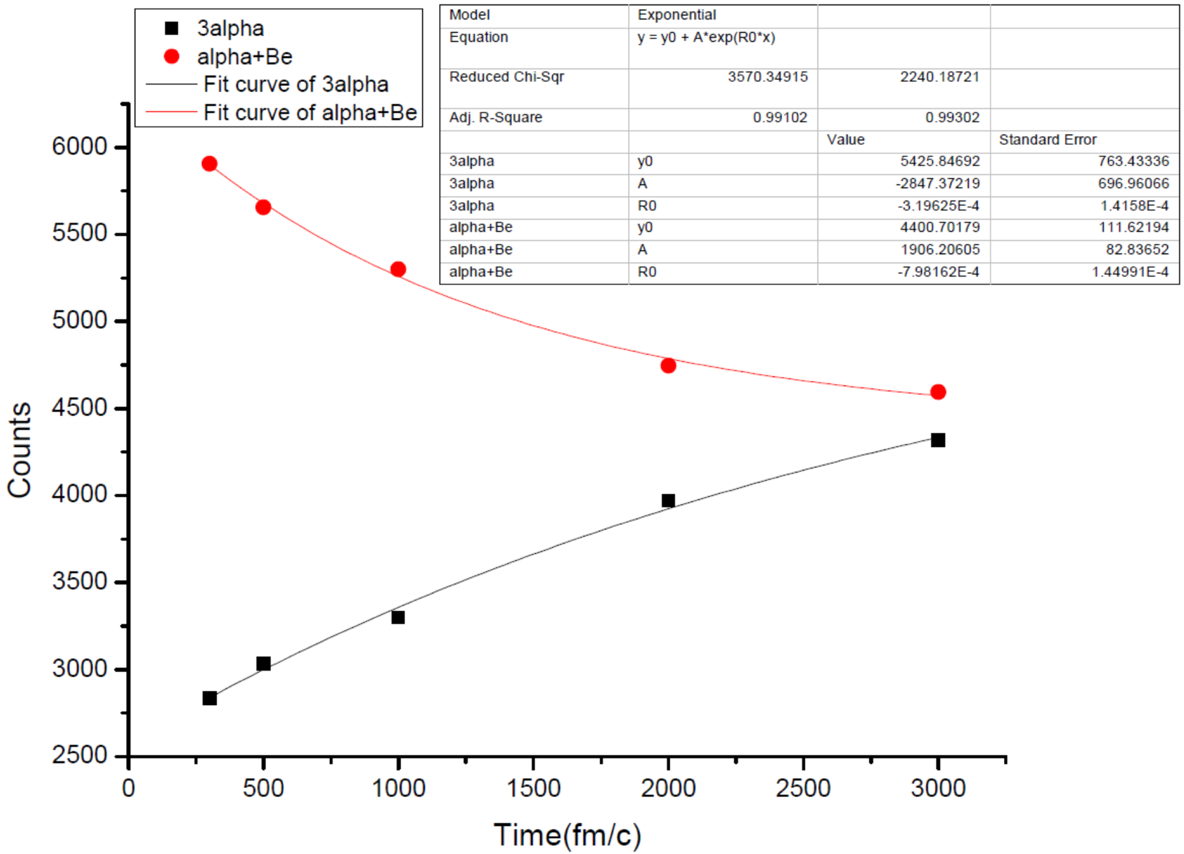

Model	Exponential		
Equation	y = y0 + A*exp(R0*x)		
Reduced Chi-Sqr	3570.34915	2240.18721	
Adj. R-Square	0.99102	0.99302	
		Value	Standard Error
3alpha	y0	5425.84692	763.43336
3alpha	A	-2847.37219	696.96066
3alpha	R0	-3.19625E-4	1.4158E-4
alpha+Be	y0	4400.70179	111.62194
alpha+Be	A	1906.20605	82.83652
alpha+Be	R0	-7.98162E-4	1.44991E-4

FIG. 1. Number of 3α and α+^{8}Be production vs time in the CoMD approach. ^{12}C production is negligible as compared to these channels.

Neutron enhancement from laser interaction with a critical fluid

H.J. Quevedo,[1] G. Zhang,[21*] A. Bonasera,[2,3] M. Donovan,[1] G. Dyer,[1] E. Gaul,[1] G.L. Guardo,[3] M. Gulino,[3,4] M. La Cognata,[3] D. Lattuada,[3] S. Palmerini,[5,6] R.G. Pizzone,[3] S. Romano,[3] H. Smith,[2], O. Trippella,[5,6] A. Anzalone,[3] C. Spitaleri[3], and T. Ditmire[1]
[1]*Center for High Energy Density Science, C1510, University of Texas at Austin, Austin, Texas,*
[2]*Cyclotron Institute, Texas A&M University, College Station, Texas*
[3]*Laboratori Nazionali del Sud-INFN, via S. Sofia 64, 95123 Catania, Italy*
[4]*Libera Universita' Kore, 94100 Enna, Italy*
[5]*Department of Physics and Geology, University of Perugia, Via A. Pascoli, 06123 Perugia, Italy*
[6]*Istituto Nazionale di Fisica Nucleare, Section of Perugia, Via A. Pascoli, 06123 Perugia, Italy*

We discuss neutron production from a system prepared near the liquid-gas critical point. The petawatt laser at the University of Texas-Austin was focused on a cluster gas producing a hot plasma. Using deuterated methane, it is possible to prepare the system very close to its critical temperature and pressure. We let the fluid expand through a conical nozzle and irradiate it with the laser. After the ionization, the clusters explode and the collision of two energetic ions might produce neutrons from fusion reactions. We showin Fig. 1 that the critical fluctuations present in the nozzle before the expansion

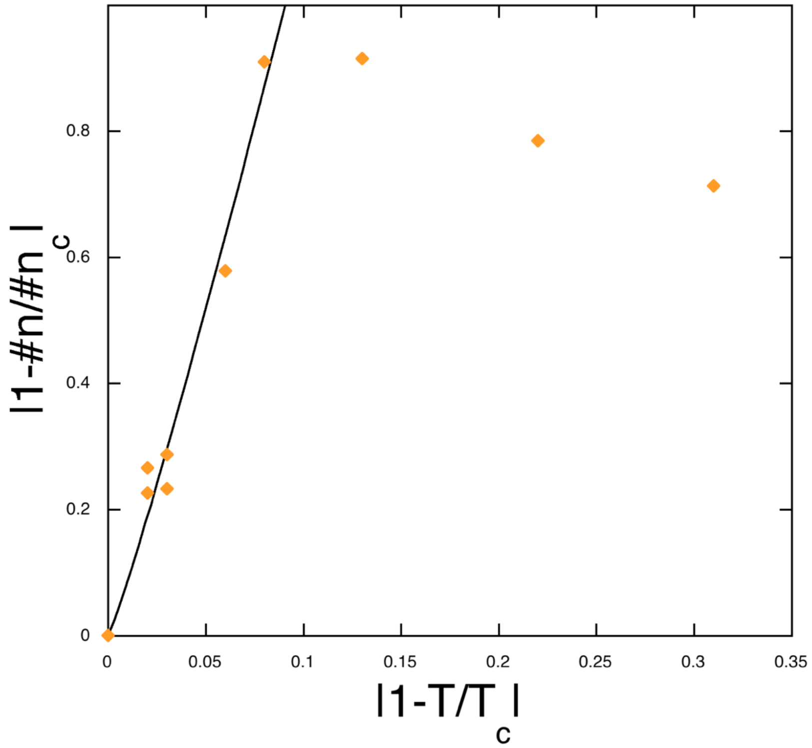

FIG. 1. "Critical distance" of the neutron number as function of the distance from the critical temperature. The power law fit (full line) gives: $|1-\#n/\#n_c|=14.1 \cdot |t|^{1.1}$.

---

[*] On leave from SINAP, Shanghai, China.

influence the dynamics of neutron production. Neutron production near the critical point follows a power law, which is a signature of a second order phase transition and it is consistent with the Fisher model. This result might be relevant for energy production from fusion reactions.

Competition between fermions and bosons in nuclear matter at low densities and finite temperatures

J. Mabiala,[1] H. Zheng,[2] A. Bonasera,[2,3] Z. Kohley,[4] and S.J. Yennello[3,5]
[1]*INFN, Laboratori Nazionali di Legnaro, Italy*
[2]*Laboratori Nazionali del Sud, INFN, via Santa Sofia, 62, 95123 Catania, Italy*
[3]*Cyclotron Institute, Texas A&M University, College Station, Texas*
[4]*National Superconducting Cyclotron Laboratory, Michigan State University, East Lansing, Michigan*
[5]*Chemistry Department, Texas A&M University, College Station, Texas*

We derive the free energy for fermions and bosons from fragmentation data. Inspired by the symmetry and pairing energy of the Weizsacker mass formula, we obtain the free energy of fermions (nucleons) and bosons (alphas and deuterons) using Landau's free energy approach. We confirm previously obtained results for fermions and show that the free energy for alpha particles is negative and very close to the free energy for ideal Bose gases and in perfect agreement with the free energy of an interacting Bose gas under the repulsive Coulomb force. Deuterons behave more similarly to fermions (positive free energy) rather than bosons, which is probably due to their low binding energy. We show that the alpha particle fraction is dominant at all temperatures and densities explored in this work. This is consistent with their negative free energy, which favors clusterization of nuclear matter into alpha particles at subsaturation densities and finite temperatures.

Introduction

Dilute mixed systems composed of fermions and bosons exhibit a large variety of interesting features that have been the subject of several theoretical and experimental works. Although generally considered as made of strongly interacting fermions (protons and neutrons), nucleonic systems have been observed to display some properties relevant of bosons. Some of these aspects are the alpha decay in heavy nuclei, preformed alpha particles in the ground state of nuclei, and the cluster structure of N = Z = even light nuclei. While the tunneling through the Coulomb barrier is well understood, the preformation of the alpha particle is still a difficult task for theoretical model descriptions. Recently, ab initio lattice simulations have shown that, depending on the form of the interaction between nucleons, the ground states of certain light nuclei lie near a quantum phase transition between a Bose-condensed gas of alpha particles and a nuclear liquid [1].

We report on experimental free energy (density) for fermions and bosons from the fragmentation of quasiprojectiles by application of Landau’s free-energy approach [2]. The temperature and density of the produced quasiprojectile systems are determined using the quantum fluctuation method. We notice, and it is an important result, that the free-energy density for alphas is negative. In contrast, it is positive for deuterons and close to that for fermions. The free-energy density for ideal Bose gases gives results similar to those for alphas but has opposite sign for those of deuterons. This demonstrates that alphas behave indeed as bosons while deuterons do not and are suppressed, probably due to their low binding energy. The fact that the free-energy density is negative means that if N = Z = even systems will “live” long enough, all the particles will cluster into alphas while deuterons will disappear.

Results

The experiment was performed at the Cyclotron Institute, Texas A&M University. Beams at 35 MeV/A of ^{64}Zn, ^{70}Zn, and ^{64}Ni from the K-500 superconducting cyclotron were used to respectively irradiate self-supporting targets of ^{64}Zn, ^{70}Zn, and ^{64}Ni.

We have analyzed fragment yield data to investigate the nuclear phase transition using the Landau free-energy technique. The temperatures and densities of the QP are determined from the fluctuations of the transverse momentum quadrupole, average multiplicities, and multiplicity fluctuations. These observables are used to correct for Coulomb effects as well.

Using the extracted Landau's fitting parameters, to determine the fragment free energy per nucleon, FA, for fermions. For bosons (deuterons and alphas), we adopt the parametrization FA = −apδ/A3/2 to easily derive the free energy [2]. Estimated statistical errors on FA for protons are 10% while those for deuterons and alphas are smaller than 3%. There is a strong correlation of increasing FA with increasing T and density for protons and deuterons. In contrast to protons and deuterons results, FA values for alphas are negative and weakly depend on T and density. In Fig. 1 the free energy density against T is examined. It is observed that f_A approaches zero in the limit T → 0 MeV, as expected. Both the f_A results obtained for an ideal Bose gas (dashed lines) and for a Coulomb corrected Bose gas (solid lines) are shown.

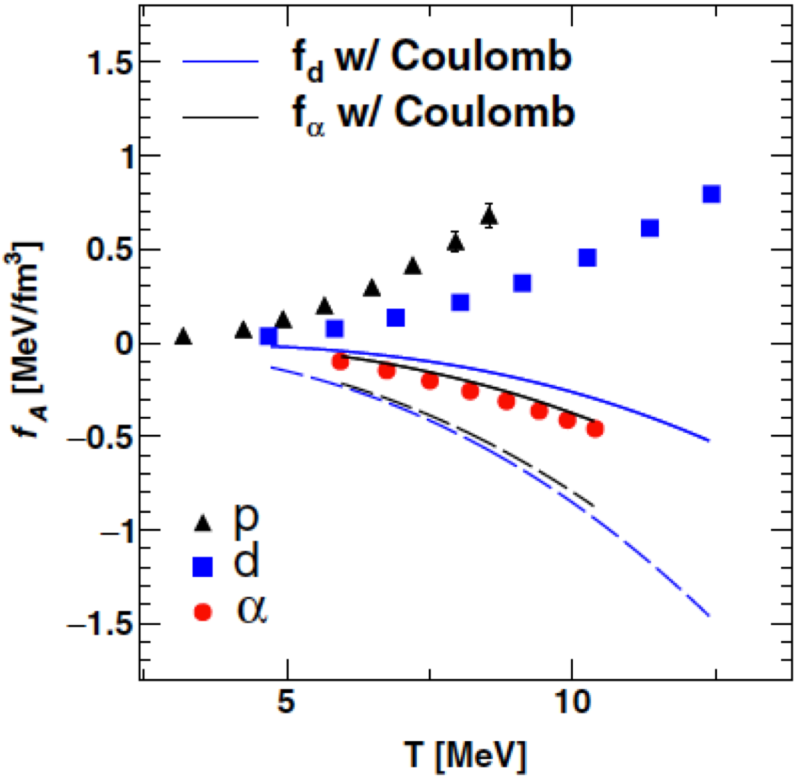

FIG. 1. Free-energy density as a function of temperature for the three light particles. Error bars are shown when statistical errors exceed the size of the symbols. Solid lines refer to the Coulomb corrected free-energy density for deuterons and alphas. The dashed lines are the corresponding ideal Bose gas limit.

The good agreement between the calculations and the experimental results is quite interesting since they have been obtained in completely different ways, one from the experimental yield distribution and the other from the Coulomb corrected free energy density for bosons. The ideal gas limit displays a similar behavior of the data but slightly shifted downwards. Notice also the different theoretical behavior of deuterons and alphas with and without Coulomb corrections. The positive experimentally derived fA values for deuterons indicate that these particles behave much like fermions, probably because of their low binding energy. For a system in equilibrium, this implies that the system of nucleons will predominantly coalesce into alpha particles.

In theoretical models cluster mass fractions are commonly used to characterize the degree of clusterization in low-density matter. We also investigate the mass fractions of the three light particles as a function of E*/A, derived directly from data. While a higher alpha-cluster fraction is seen for all E*/A values, protons and deuterons have similar mass fractions.

Conclusions

In summary, we have extracted the free energy (density) for fermions and bosons in finite nuclei at subsaturation densities and finite temperatures using the Landau free-energy technique. It was found that free-energy results for alpha particles are negative and close to those of ideal (and Coulomb corrected) Bose gases, whereas deuterons behave much like fermions. The alpha particle fraction was shown to be favored at all temperatures and densities explored in this work. The present results are consistent with the clusterization of nuclear matter into alpha particles. In the limit of zero temperature and ground-state density, the free energy discussed above reduces to the symmetry and pairing terms in the Weizsacker mass formula.

[1] S. Elhatisari *et al.*, Phys. Rev. Lett . **117**, 132501 (2016).
[2] J. Mabiala *et al.*, Phys. Rev. C **94**, 06461 (2016).

Range of plasma ions in cold cluster gases near the critical point

G. Zhang,[1*] H.J. Quevedo,[2] A. Bonasera,[1,3] M. Donovan,[2] G. Dyer,[2] E. Gaul,[2] G.L. Guardo,[3]
M. Gulino,[3,4] M. La Cognata,[3] D. Lattuada,[3] S. Palmerini,[5,6] R.G. Pizzone,[3] S. Romano,[3]
H. Smith,[2] O. Trippella,[5,6] A. Anzalone,[3] C. Spitaleri,[3] and T. Ditmire[2]
[1]*Cyclotron Institute, Texas A&M University, College Station, Texas*
[2]*Center for High Energy Density Science, C1510, University of Texas at Austin, Austin, Texas*
[3]*Laboratori Nazionali del Sud-INFN, via S. Sofia 64, 95123 Catania, Italy*
[4]*Libera Universita' Kore, 94100 Enna, Italy*
[5]*Department of Physics and Geology, University of Perugia, Via A. Pascoli, 06123 Perugia, Italy*
[6]*Istituto Nazionale di Fisica Nucleare, Section of Perugia, Via A. Pascoli, 06123 Perugia, Italy*

We measured the range of plasma ions in cold cluster gases by using the Petawatt laser at the University of Texas-Austin. The produced plasma propagated in all directions some hitting the cold cluster gas not illuminated by the laser. From the ratio of the measured ion distributions at different angles we can estimate the range of the ions in the cold cluster gas. It is much smaller than estimated using popular models, which take only into account the slowing down of charged particles in uniform matter. We discuss the ion range in systems prepared near a liquid-gas phase transition.

[1] G. Zheng *et al.*, Phys. Lett. A **381**, 1682 (2017).

---

[*] On leave from SINAP, Shanghai, China.

Superconductive behavior in two-neutron transfer reactions

C. Agodi,[1] G.Giuliani,[2] F. Cappuzzello,[1,2] A. Bonasera,[1,4] D. Carbone,[1] M. Cavallaro,[1] A.Foti,[2,5]
R. Linares,[3] and G. Santagati[1]
[1]*INFN - Laboratori Nazionali del Sud, Catania, Italy*
[2]*Dipartimento di Fisica e Astronomia, Università di Catania, Catania, Italy*
[3]*Instituto de Física, Universidade Federal Fluminense, Niteroi, RJ, Brazil*
[4]*Cyclotron Institute, Texas A&M University, College Station Texas*
[5]*INFN, Sezione di Catania, Catania, Italy*

The transfer yields mass spectra were measured[1] in ^{11}B,^{12,13}C,^{28}Si(^{18}O,^{17}O) and ^{11}B,^{12,13}C,^{28}Si(^{18}O,^{16}O) reactions at 84 MeV. The Two-Neutron Transfer (2NT) and the One-Neutron Transfer (1NT) cross sections were extracted for all the systems. The 2NT cross section is found comparable to 1NT and remarkably larger than that predicted assuming no correlations among the two transferred nucleons as shown in Fig. 1. Calculations based on the Constrained Molecular Dynamics (CoMD) model show that such superconductive behaviour is uniquely consequence of neutron pairing correlations (CoMD+NN) in the ^{18}O ground state.

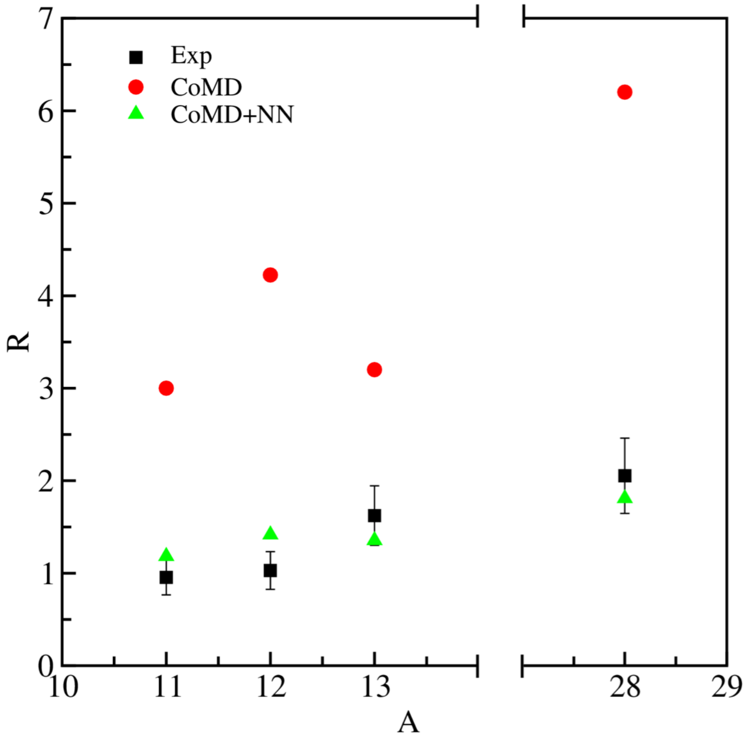

FIG. 1. R = $\sigma_{1NT}/\sigma_{2NT}$ for the considered targets. The squares refer to the experimental data, while the circles and the triangles to CoMD and CoMD+NN calculations respectively.

Initial angular momentum in high energy nuclear collisions

R.J. Fries, G. Chen, and S. Somanathan

The study of the effects of angular momentum in high energy nuclear collisions has intensified recently after the STAR collaboration reported non-vanishing polarization measured for Lambda baryons in collisions at the Relativistic Heavy Ion Collider (RHIC). The polarization effect decreases with beam energy and is compatible with zero within current error bars at top RHIC energies. In a recent study [1] we looked at the high energy limit of nuclear collisions, where color glass condensate (CGC) is expected to be the correct effective theory for the early phase of the collision. In the analytic framework developed by some of us with Kapusta and Li [2] it is possible to recursively solve the Yang-Mills equations for the initial gluon field, and to calculate event averages over color charge distributions in the framework of the McLerran-Venugopalan model.

We have studied the relativistic angular momentum tensor $M^{\mu\nu\lambda}$ calculated from the energy momentum tensor $T^{\mu\nu}$ of the initial classical gluon field. Since the setup is boost-invariant, a good approximation around midrapidity at the highest energies, we calculate $dL_2/d\eta$ and estimate it to be ~ $R_A Q_S^{-3} \varepsilon_0$ at a time ~ $1/Q_S$ at midrapidity. Here R_A is the nuclear radius, Q_S is the saturation scale, and ε_0 is the average initial energy density. The energy flow in the gluon field carrying this angular momentum is shown in Fig. 1 in the reaction plane (orthogonal to the y-axis). The nuclei after the collision are moving to the right in the upper half-plane and to the left in the lower half-plane, the vortex visible in Fig. 1 is

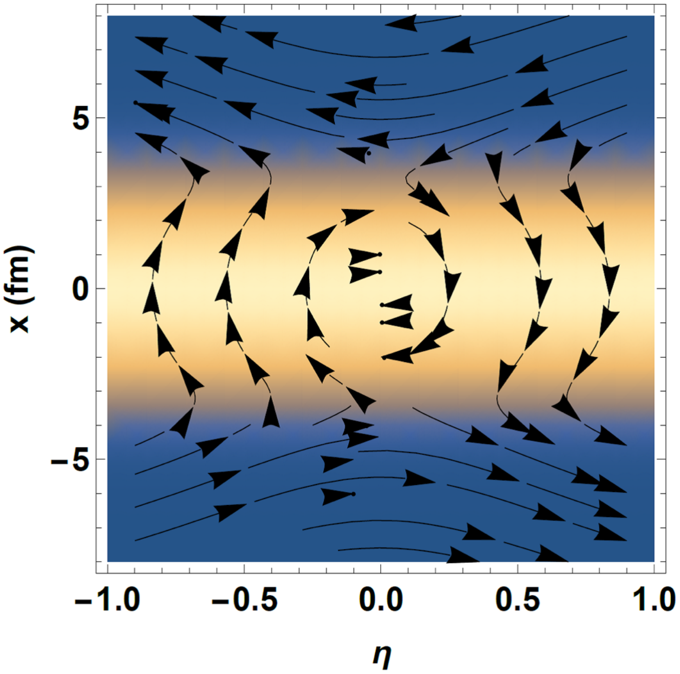

FIG. 1. Energy flow components (T^{01}, T^{03}) of the initial gluon field contributing to local angular momentum around midrapidity in the reaction plane of Pb+Pb collisions at time $\tau = 0.25$ fm/c. Flow not contributing to angular momentum (for example radial flow) is subtracted for clarity. Background shading shows the initial energy density in the reaction plane.Figure taken from Ref. [1].

thus aligned with the primordial angular momentum of the colliding nuclei. Note that energy flow not contributing to angular momentum is not shown. To be more precise, only rapidity-odd contributions of the flow T^{01} in x-direction (directed energy flow), and rapidity even contributions of the flow T^{03} in z-direction (longitudinal shear flow) contribute and are shown.

We further discuss the procedure to match results from the initial classical Yang-Mills phase to ideal and viscous fluid dynamics, with conservation laws for energy, momentum and angular momentum as guiding principles. We argue that dissipative stress calculated from the Yang-Mills phase has to be included when initializing fluid dynamics, or basic conservation laws are violated.

We find that in the fluid phase the angular momentum is initially carried by a longitudinal shear flow, i.e. an imbalance of longitudinal flow velocity between two sides of the reaction plane. This event-averaged picture will receive modifications when event-by-event fluctuations are taken into account. Angular momentum is also carried by the initial shear stress tensor. In a boost-invariant picture there is no rotational component to the flow field. Both the shear stress and longitudinal shear flow tend to dissipate in viscous fluid dynamics, leading to overall suppressed local angular momentum at midrapidity. This is consistent with the observation that particle polarization and directed flow at midrapidity decrease with increasing beam energy and increasing boost-invariance of the system.

[1] R.J. Fries, G. Chen, and S. Somanathan, Phys. Rev. C (Submitted);e-Print: arXiv:1705.10779 [nucl-th].
[2] G. Chen, R.J. Fries, J.I. Kapusta, and Y. Li, Phys.Rev. C **92**, 064912 (2015).

The JETSCAPE collaboration

R.J. Fries

July 2016 marked the starting point of the JETSCAPE Collaboration. JETSCAPE stands for *Jet Energy-loss Tomography with a Statistically and Computationally Advanced Program Envelope*. It is a collaboration funded with \$3.6M through the *Software Infrastructure for Sustained Innovation* (SI2) program of the U.S. National Science Foundation. R. J. Fries has been a PI on the proposal and is representing Texas A&M University in this multi-institutional effort. The other PIs are located at Duke University, Lawrence Berkeley National Laboratory, Lawrence Livermore National Laboratory, McGill University, MIT, Ohio State University, UC Berkeley and Wayne State University.

JETSCAPE is a naturally following up with efforts of the JET collaboration, however it focuses mostly on computational aspects. The goal of the collaboration is to devise the next generation of event generators to simulate the physics of ultra-relativistic heavy-ion collisions with a focus on high momentum probes and jets. It involves theoretical and experimental physicists, computer scientists, and statisticians.

The JETSCAPE Collaboration will develop a scalable and portable open source software package to replace a variety of existing codes. The modular integrated software framework will consist of interacting generators to simulate (i) wave functions of the incoming nuclei, (ii) viscous fluid dynamical evolution of the hot plasma, and (iii) transport and modification of jets in the plasma. Integrated advanced statistical analysis tools will provide non-expert users with quantitative methods to validate novel theoretical descriptions of jet modification, by comparison with the complete set of current experimental data. To improve the efficiency of this computationally intensive task, the collaboration will develop trainable emulators that can accurately predict experimental observables by interpolation between full model runs, and employ accelerators such as Graphics Processing Units (GPUs) for both the fluid dynamical simulations and the modification of jets. The collaboration will create this framework with a user-friendly envelope that allows for continuous modifications, updates and improvements of each of its components. The effort will serve as a template for other fields that involve complex dynamical modeling and comparison with large data sets. It will open a new era for high-precision extraction of the internal structure of the Quark-Gluon Plasma with quantifiable uncertainties.

The design of the software framework is well under way and a first version of the JETSCAPE package is expected for late summer 2017. In the meantime, the collaboration published first physics results [1] that test the coupling of different jet shower Monte Carlo (MC) codes. The partons initiating jets are produced far off shell, measured by their virtuality Q. Jet shower MC codes so far have either focused on the virtuality evolution from large to intermediate/small virtuality, or on the energy evolution for moderately off-shell particles. The MARTINI MC code by the McGill group and LBT by the Berkeley/CCNU group are examples of the latter, while MATTER, developed at Wayne State, and vacuum shower MCs used in High Energy Physics, like PYTHIA, compute the virtuality evolution. A comprehensive description in heavy ion collisions must reconcile the high-Q and intermediate/low-Q part of the evolution. Fig. 1 shows spectra resulting from matching MATTER and LBT, together with results obtained from running individual codes. Different matching scenarios are employed, see Ref. [1] for details. Interesting new effects have been observed in this work, most notably in the distributions of angles of partons with respect to the jet axis, which qualitatively agree with experimental observations.

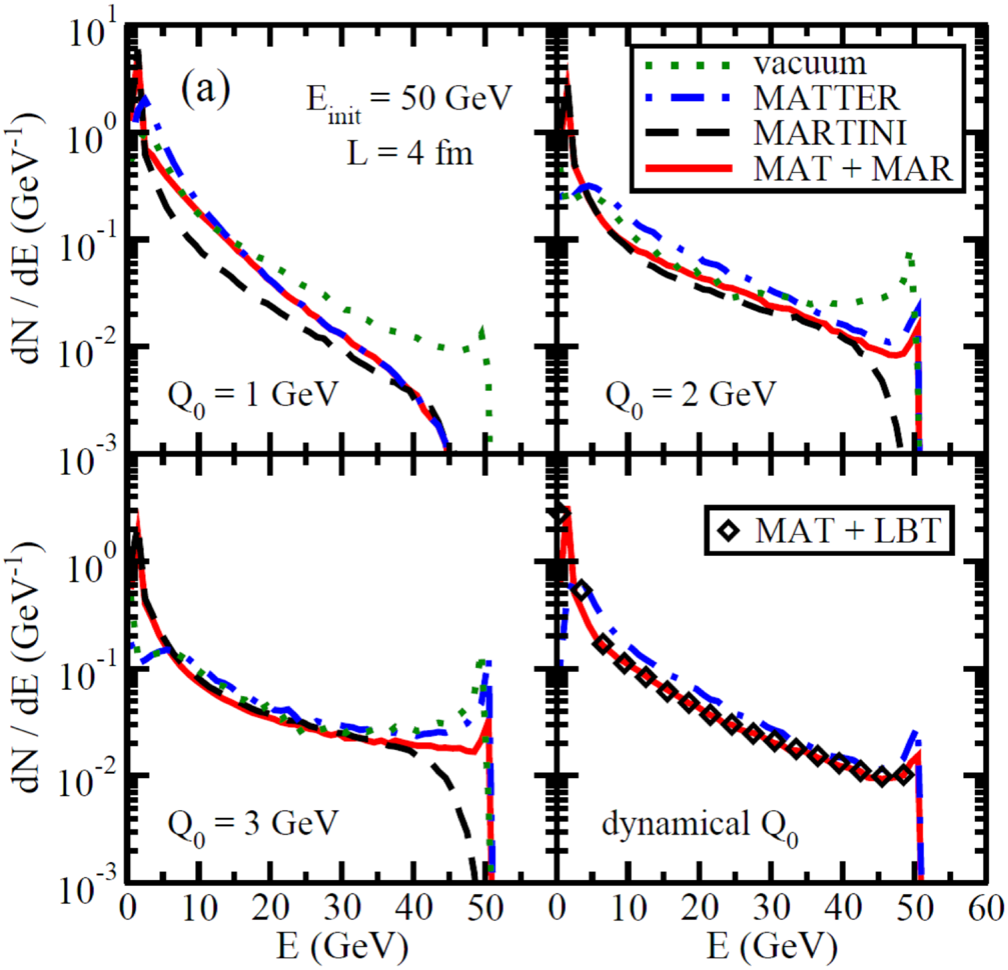

FIG. 1. Energy distribution dN/dE of partons in 50 GeV jets travelling through a brick of quark gluon plasma of size 4 fm and temperature 250 MeV. Results for vacuum jet shower evolution in MATTER (green dots), in-medium evolution with MATTER (blue dash-dots), in-medium evolution with vacuum shower plus MARTINI (black dashes) and the combination of in-medium MATTER showers with in-medium LBT evolution (black dots) are shown for 4 different matching scenarios. Q_0 denotes the virtuality scale at which vacuum or MATTER evolution ends, and MARTINI or LBT evolution starts. Figure taken from Ref. [1].

[1] S. Cao *et al.* (JETSCAPE Collaboration), Phys. Rev. C (Submitted); e-Print: arXiv:1705.00050 [nucl th].

Equation of state for strongly coupled systems with emerging bound states

Shuai Y.F. Liu and Ralf Rapp

The interplay of bound and continuum states is a key feature in a wide variety of quantum many-body systems, e.g., in cold atomic gases, electromagnetic and electron-hole plasmas, nuclear matter, and its transition to the quark-gluon plasma (QGP). A microscopic description of their equation of state (EoS) becomes particularly challenging when a strong coupling between the constituents mandates methods beyond the quasi-particle approximation. One such method is the Luttinger-Ward-Baym (LWB) formalism [1-3],

$$\Omega(G) = \mp \mathrm{Tr}\{\ln(-G^{-1}) + (G_0^{-1} - G^{-1})G\} \pm \Phi(G)$$

where the grand potential is evaluated in terms of Feynman diagrams with fully dressed in-medium single-particle propagators, G. The predictive power of this formalism hinges on including the relevant diagrams in the calculation of the Luttinger-Ward functional (LWF), $\Phi(G)$. Typically, $\Phi(G)$ is constructed to finite order in the ``skeleton diagram" expansion, from which the integral equation for G should be solved self-consistently. However, for strongly coupled system a non-perturbative resummation for $\Phi(G)$ is required. In our recent work [4-5], we developed a resummation method to evaluate the $\Phi(G)$ non-perturbatively via a generalized T-matrix formalism [5],

$$\Phi(G) = -\frac{1}{2}\int d^4\tilde{P}\,\mathrm{Tr}\left\{\mathbb{L}\mathrm{og}\left(1 - \mathbb{V}\mathbb{G}\mathbb{G}(\tilde{P})\right)\right\}$$

Here, $\mathbb{L}$og denotes a matrix-logarithm operation, and $\mathbb{V}$ and $\mathbb{G}$ are matrices in energy and momentum space after discretization of the interaction kernel V and propagator G. By self-consistently solving for the propagators G, we can calculate the EoS non-perturbatively including both in-medium bound and 1-particle states systematically.

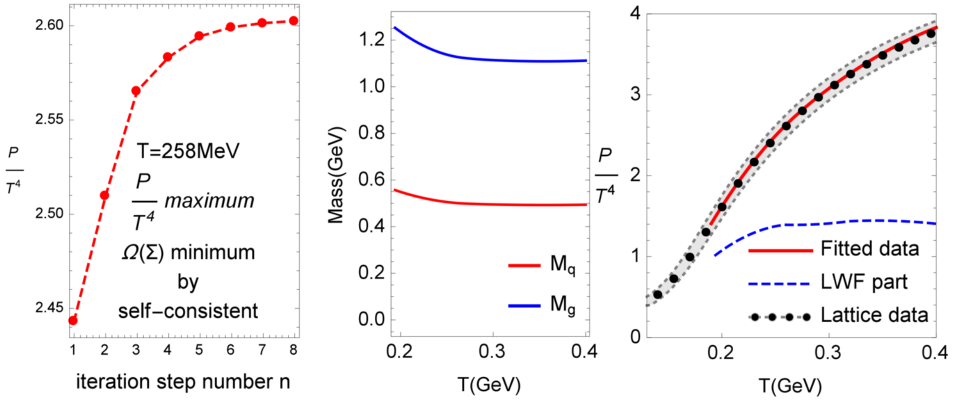

FIG. 1. Evolution of the pressure in the self-consistent iteration procedure (left panel), and temperature dependence of quark and gluon masses (middle panel) needed to fit lQCD data [7] for the scaled pressure, $\boldsymbol{P/T^4}$ (right panel).

We apply this method to evaluate the EoS of QGP. The starting point is an effective Hamiltonian where the interaction V is constrained by the static quark-antiquark free energy as computed in lattice QCD (lQCD) [6]. Tuning two fit parameters (the light parton masses), the EoS obtained through our approach can describe the lQCD data as shown in Fig.1; in the right panel, the LWF Φ contribution to the EoS, which encodes dynamical bound/resonance states, is found to dominate the pressure when the temperature approaches the pseudo-critical one. The resonance interactions, in turn, strongly distort the single-parton spectral functions, see Fig.2, which is a prediction of the approach.

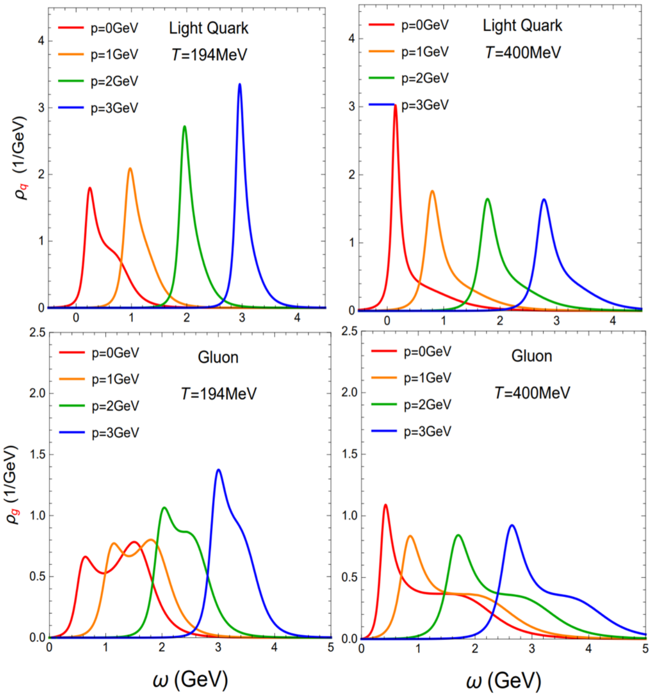

FIG. 2. In-medium spectral functions for quarks (left two panels) and gluons (right two panels) at $T = 194$ MeV and $T = 400$ MeV for 3-momenta $p = 0, 1,2,3$ GeV.

The spectral functions are broad and non-quasiparticle like at low momenta and low temperatures while they recover quasi-particle structures at high momenta and/or temperatures. This is a direct reflection of the remmants of the strong confining force in QCD at low energy scales and asymptotic freedom at high energy scales, as encoded in the potential V. The pertinent 2-particle T-matrices are shown in Fig. 3 in attractive channels, illustrating strong resonances at low temperature and their dissolution at higher temperatures.

In summary, utilizing a newly developed many-body method, we have unraveled a strongly coupled picture of QGP near the transition region where quantum effects play a key role: as the pseudocritical temperature is approached from above, broad single-parton spectral functions give way to dynamically formed bound states, driven by the confining force as constrained by lattice QCD.

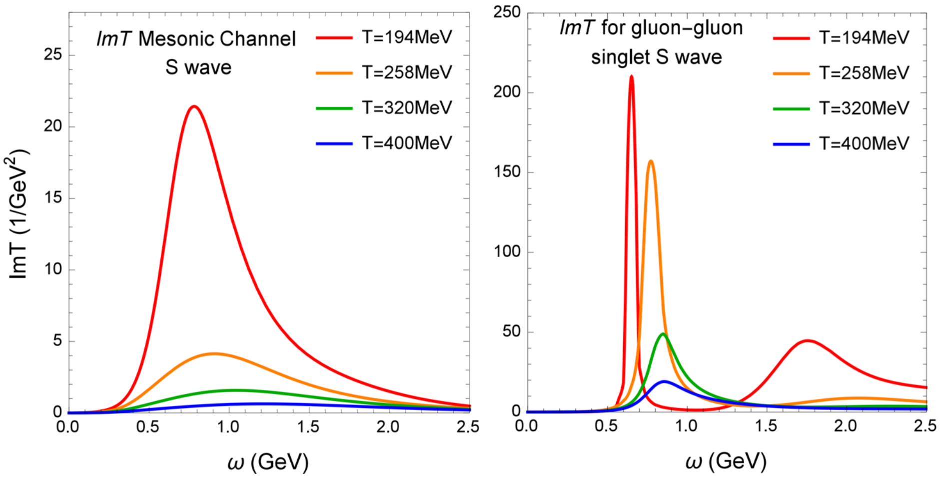

FIG. 3. Imaginary part of the in-medium T -matrix for $P = 0$ in the color-singlet $\boldsymbol{q\bar{q}}$ (left) and gg (right) channels.

[1] J.M. Luttinger and J.C. Ward, Phys. Rev. **118**, 1417 (1960).

[2] G. Baym and L.P. Kadanoff, Phys. Rev. **124**, 287 (1961).

[3] G. Baym, Phys. Rev. **127**, 1391 (1962).

[4] S.Y.F. Liu and R. Rapp, J. Phys. Conf. Ser. **779**, 012034 (2017).

[5] S.Y.F. Liu and R. Rapp, arXiv:1612.09138

[6] S.Y.F. Liu and R. Rapp, Nucl. Phys. **A941**, 179 (2015).

[7] A. Bazavov *et al*. (HotQCD collaboration), Phys. Rev. D 90, 094503 (2014).

The electric conductivity in hot hadronic matter

J. Atchison and R. Rapp

Transport coefficients are an important tool to characterize the properties of hot nuclear matter as they carry information about the long-wave length excitations of the medium [1]. In the present work we study the electric conductivity of hot nuclear matter which is of particular interest as it can be calculated from the same spectral function that determines the thermal emission rate of dileptons. We extract it within the theoretical framework of hadronic many-body theory which has been successful in describing low-mass dilepton production in heavy-ion collisions over a large range of energies, $\sqrt{s} \approx 2$-200 GeV [2]. Within the Vector Dominance Model electromagnetic interactions in hadronic matter proceed through the light vector mesons (ρ,ω,φ), with the primary contribution from the ρ-meson. Thus, one can extract the conductivity from the ρ-meson spectral function, in the zero-momentum low-energy limit. Recent calculations of the electric conductivity in hot nuclear matter have produced varying results [3].

We here focus on the effects on the ρ self-energy in a hot medium of pions which are the dominant degrees of freedom at low temperature. The Feynman diagrams necessary to obtain a gauge invariant self-energy in vacuum are shown in Fig. 1 [4].

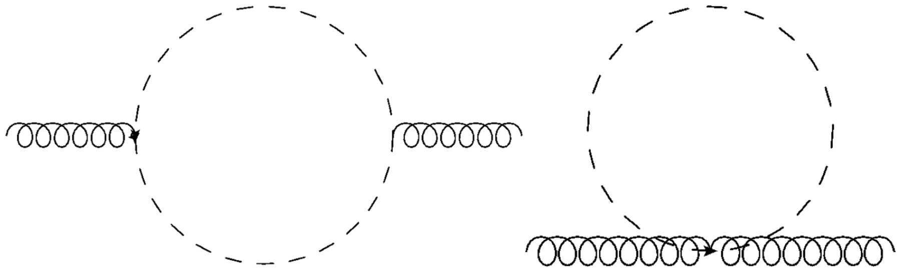

FIG. 1. Contributions to the ρ self-energy necessary for gauge invariance in vacuum.

The medium effects arise from a dressing of the pion propagators in the ρ's pion cloud (Fig. 1); this, however, upsets gauge invariance. Restoring it requires the calculation of medium-induced vertex corrections to the ρππ and ρρππ vertices, shown in Fig. 2.

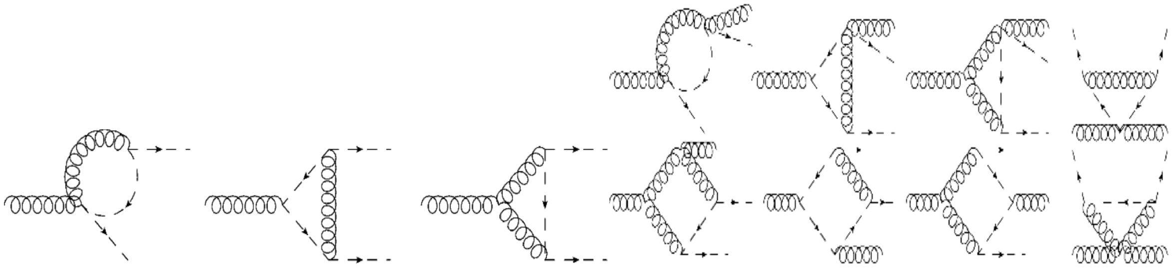

FIG. 2. Corrections to the ρππ vertex (left 3 diagrams) and ρρππ vertex (right 8 diagrams).

The vertex corrections contain intermediate π and ρ propagators. If these propagators are undressed the conductivity diverges (free-gas limit). Therefore, finite widths are introduced into these propagators, with the associated violation of gauge invariance being parametrically suppressed. Our preliminary results [5] suggest that the conductivity obeys the lower quantum bound set by conformal field theories in the strong-coupling limit, and that the pion gas is strongly coupled.

[1] G. Aarts *et al.*, JHEP **215**, 186 (2015).
[2] R. Rapp and H. van Hees, Eur. Phys. J. A **52**, 257 (2016).
[3] M. Greif, C. Greiner, and G. Denicol, Phys. Rev. D **93**, 096012 (2016), and refs. therein.
[4] M. Urban, M. Buballa, R. Rapp, and J. Wambach, Nucl. Phys. **A673**, 357 (2000).
[5] J. Atchison and R. Rapp, J. Phys. Conf. Series **832**, 012057 (2017).

Color screening and regeneration of bottomonia at RHIC and the LHC

Xiaojian Du, Min He, and Ralf Rapp

Heavy quarkonia are key probes of the medium effects on the fundamental QCD force in strongly interacting matter. Large experimental and theoretical efforts are devoted to measure charmonium and bottomonium observables in heavy-ion collisions (HICs) [1] and to interpret the results. Kinetic-rate equation approaches have proven a successful tool to unravel the interplay of suppression and regeneration mechanisms for charmonia [2]. For bottomonia, regeneration processes are expected to be less important, providing a more direct window on their dissolution mechanisms.

In this work [3], we investigate ϒ(nS) production in HICs at RHIC and LHC energies using a rate equation approach [4]. Improving on previous work [5], we implement in-medium binding energies from T-matrix calculations [6] to compute inelastic reaction rates, B-meson resonances in calculating ϒ equilibrium limits near T_c, a lattice-QCD equation of state in the fireball evolution, and realistic b-quark spectra from Langevin simulations [7] to compute transverse-momentum (p_T) spectra from coalescence processes [8]. The resulting centrality and p_T-dependent production yields are generally in good agreement with experiments at RHIC (√s=0.2TeV) and the LHC (√s=2.76 and 5.02 TeV).

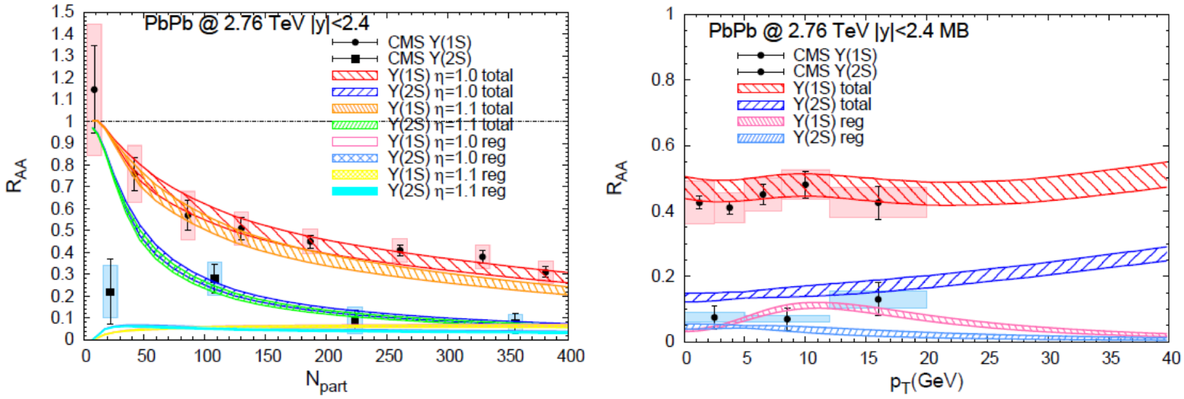

FIG. 1. Nuclear modification factor of ϒ(1S) and ϒ(2S) in 2.76TeV Pb-Pb collisions as a function of centrality (left) and p_T (right). Calculations with the baseline TBS (η=1.0) are compared to CMS data [9]; the orange band for the ϒ(1S) in the left panel includes a 10% stronger reduction of the TBS binding energies (η=1.1, encoded in the reaction rates).

In Fig. 1 we show the comparison to CMS data in Pb-Pb(2.76TeV) collisions. The ϒ(1S) nuclear modification factor (R_{AA}) shows a promising sensitivity to the in-medium binding energy, with the baseline T-matrix binding scenario (TBS) providing good agreement with data. Regeneration contributions are generally small, mostly limited by the strongly suppressed R_{AA} of the ϒ(2S). However, the p_T dependence of the ϒ(1S) R_{AA} shows a slight maximum structure due to regeneration which is not inconsistent with data. An assumption of thermalized b-quark spectra leads to discrepancies with the measured $R_{AA}(p_T)$'s for both ϒ(1S) and ϒ(2S) (not shown). The model predictions for 5.02 TeV Pb-Pb collisions are also in fair agreement with recent CMS data [10], cf. the left panel of Fig. 2.

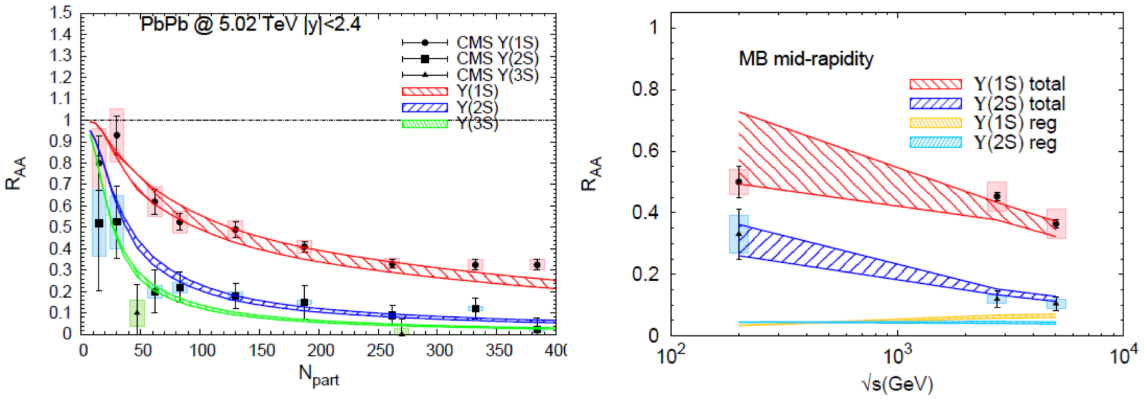

FIG. 2. Left: centrality-dependent R_{AA} for Υ(1S), Υ(2S) and Υ(3S) in 5.02 TeV Pb-Pb collisions in the baseline TBS, compared to CMS data [10]. Right: excitation function of Υ(1S) and Υ(2S) R_{AA} in MB AA collisions, compared to RHIC [11] and LHC [9,10] data.

The calculation of excitation functions of the R_{AA} for Υ(1S) and Υ(2S) are compared to minimum-bias (MB) data in the right panel of Fig. 2. From the suppression pattern of the Υ(2S) we conclude that the confining force, which is the main agent for Υ(2S) binding in vacuum, is screened at RHIC and fully suppressed at the LHC. On the other hand, the Υ(1S), which is mostly bound by the color-Coulomb force, survives up to temperatures of 500-600 MeV, indicating that color screening penetrates down to 0.1-0.2 fm at the LHC. Regeneration contributions are generally small, but possibly play a role in the flattening of Υ(2S) $R_{AA}(\sqrt{s})$ from 2.76 to 5.02 TeV.

[1] E. Scomparin, proceedings of Quark Matter 2017, arXiv:1705.05810.
[2] R. Rapp and X. Du, proceedings of Quark Matter 2017, arXiv:1704.07923.
[3] X. Du, M. He, and R. Rapp, arXiv:1706.08670; Phys. Rev. C (Submitted).
[4] L. Grandchamp *et al.*, Phys. Rev. C **73**, 064906 (2006).
[5] A. Emerick, X. Zhao, and R. Rapp, Eur. Phys. J. A **48**, 72(2012).
[6] F. Riek and R. Rapp, Phys. Rev. C **82**,035201 (2010).
[7] M. He, R.J. Fries, and R. Rapp, Phys. Lett. B **735**, 445 (2014) 445.
[8] V. Greco, C.M. Ko and P. Levai, Phys. Rev. C **68**, 034904(2003).
[9] V. Khachatryan *et al.* [CMS Collaboration], Phys. Lett. B **770**, 357 (2017).
[10] V. Khachatryan *et al.* [CMS Collaboration], CMSPAS-HIN16-0023.
[11] Z. Ye *et al.* [STAR collaboration], proc. of QM17, arXiv:1702.05651.

Thermal dileptons from coarse-grained transport as fireball probes at GSI-SIS energies

T. Galatyuk, P.M. Hohler, R. Rapp, F. Seck, and J. Stroth

The radiation of dileptons from the interacting fireballs as formed in heavy-ion collisions is a highly versatile tool to probe properties of the hot and dense QCD medium created in these reactions. At ultra-relativistic collision energies, dilepton spectra at low invariant masses, $M < 1\text{GeV}$, are mostly due to in-medium decays of the ρ(770) meson, which have revealed the mechanism of hadronic mass melting when approaching the QCD transition temperature into the quark-gluon plasma (QGP) [1,2]. At intermediate masses, $1<M/\text{GeV}<3$, thermal dilepton radiation is continuum-like, and the pertinent slope parameter yields the medium's temperature in its early phases, revealing the production of a QGP. In addition, the total yield of radiated low-mass dileptons gives an accurate measure of the fireball lifetime [2].

The concept of a thermalized medium is more controversial at lower heavy-ion collision energies. In the present work [3] we therefore adopt hadronic transport simulations from the UrQMD model [4], applying a "coarse-graining" procedure to define an average local temperature and baryon density over which thermal dilepton emission rates [5] can be convoluted (see also Ref. [6]). An ensemble of central Au-Au collisions at a bombarding energy of E_{lab}=1.23A GeV has been simulated and discretized into 21^3 cells of volume 1fm^3 each, from which the time evolution of their temperature (from pion spectra) and density in the local rest frame are extracted. The time evolution of a central 7^3 cube shows maximal temperatures and baryon densities of $T\approx90\text{MeV}$ and $\rho_B\approx3\rho_0$ in these reactions, cf. left panel of Fig. 1 (the extracted temperatures are about 20% larger when using nucleon spectra, which, however, carry a contamination from the initial motion).

A remarkable synchronicity of the dilepton emission and the build-up of collective transverse flow of nucleons emerges, cf. middle panel Fig. 1. This establishes a direct connection between two key but independent features of an interacting system, i.e., pressure and radiation. Our studies thus strongly support the formation of matter near local equilibrium. We also find that the radiation duration (or pressure-driven acceleration) lasts for only 12-14fm/c, much shorter than the ~20fm/c that the system spends at densities above nuclear saturation density, $\rho_0=0.16\text{fm}^{-3}$, but in line with the systematics of Ref. [2] at higher collision energies. Significant radiation sets in only near the maximal compression (or temperature) of the system, i.e., when most of the entropy has been produced; this is particularly welcome in view of the theoretical challenges in calculating pre-equilibrium emission. In the right panel of Fig. 1 we display the final dilepton radiation spectrum that can be compared to experimental data. The low-mass region predicts a near complete melting of the ρ-meson resonance structure, due to the high baryon densities reached in the simulations. The temperature extracted from the slope of the spectrum in the intermediate-mass region amounts to $T_{\text{slope}}=88\pm5\text{MeV}$, close to the maximal temperatures reached in the simulation. This confirms the validity of using intermediate-mass dilepton spectra as a thermometer [2].

In the future, it would be of high interest to push the coarse-graining approach to even lower energies, to extend the use of dileptons (or photons) as spectrometer, chronometer, thermometer and barometer.

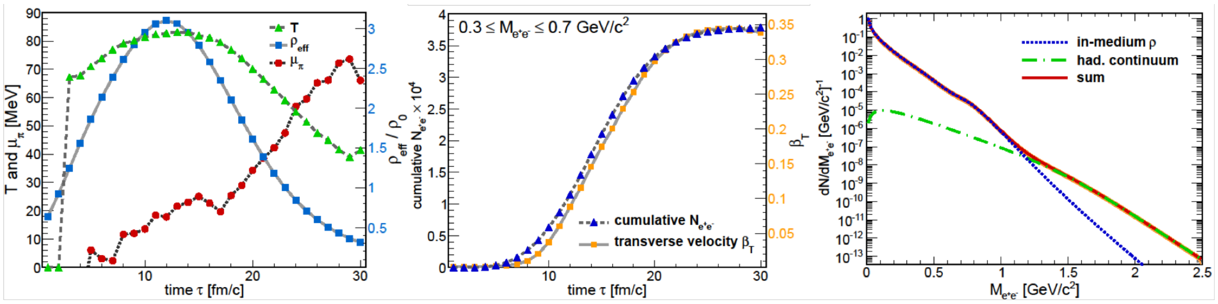

FIG. 1. Left panel: time evolution of temperature, effective baryon density, $\rho_{\mathrm{eff}} = \rho_N + \rho_\Delta$, and pion chemical potential extracted from ensemble-averaged UrQMD events for central Au-Au(1.23AGeV) collisions. Middle panel: pertinent time evolution of the integrated dilepton radiation yield and transverse collective expansion velocity of nucleons. Right panel: final dilepton spectra from in-medium ρ decays at low masses and hadronic continuum radiation prevalent at intermediate masses.

[1] R. Rapp, Adv. High Energy Phys. **2013**, 148253 (2013).

[2] R. Rapp and H. van Hees, Phys. Lett. B **753**, 586 (2016).

[3] T. Galatyuk, P.M. Hohler, R. Rapp, F. Seck, and J. Stroth, Eur. Phys. J. A **52**, 131 (2016).

[4] S.A. Bass *et al.*, Prog. Part. Nucl. Phys. **41**, 225 (1998).

[5] R. Rapp and J. Wambach, Eur. Phys. J. A **6**, 415 (1999).

[6] S. Endres, H. van Hees, J. Weil, and M. Bleicher, Phys. Rev. C **92**, 01491 (2015).

SECTION IV

SUPERCONDUCTING CYCLOTRON, INSTRUMENTATION AND RIB UPGRADE

K500 operations and development

D.P. May, G.J. Kim, B.T. Roeder, H.L. Clark, and F.P. Abegglen

Introduction

During the 2016-2017 reporting period a total of 23 different beams, including 5 newly developed beams, were used for experiments, and there were a total of 26 beam tunings for these experiments. The SEE program and the charge-breeding effort are treated separately in this progress report.

Ion Sources

During the shutdown ECR1 was opened for examination, and it was found that there had been no further deterioration in the damaged spot that had developed over a plasma flute on the aluminum wall.

Cyclotron Beams

New beams of ^{10}B at 17.2 AMeV, ^{14}N at 30 AMeV, ^{15}N at 31 AMeV, ^{16}O at 3.9 AMeV, and ^{17}O at 4.0 AMeV were developed for experiments.

Operations

For the period April 1, 2016 through March 31, 2017, the operational time is summarized in Table I, while Table II lists how the scheduled time was divided. Unscheduled maintenance was quite low, possibly due to the large amount of scheduled maintenance that occurred when the January shutdown was extended for the start of the installation of the new building air-conditioning system.

Table I. 2016-2017 operational time.

Time	Hrs.	%Time
Beam on target	6148	70
Beam development	772	9
Scheduled maintenance	1680	19
Unscheduled maint	136	2
Total	**8736**	**100.0**

Table II. 2016-2017 Scheduled Beam Time.

Time	**Hrs.**	**%Time**
Nuclear physics	1197	17.3
Nuclear chemistry	1212	17.5
Outside collaboration	167	2.4
Outside users	3572	51.6
Beam development	772	11.2
Total	**6920**	**100.0**

Texas A&M cyclotron radiation effects facility
April 1, 2016 – March 31, 2017

H.L. Clark, J. Brinkley, L. Chen, G. Chubarian, S. Gerlt, V. Horvat, B. Hyman,
B. Roeder, and G. Tabacaru

The activity of the Radiation effects facility increased over the previous reporting year. In this reporting period, the facility was used for 3,355 hours, which is a 10% increase over the 3,042 hours used in the 2015-2016 reporting period and is the highest usage year ever. Users of the facility (and hours used) over the past year were: Boeing Satellite Systems (331), NASA GSFC (265), Ryoei (245.5), Intersil Corp (191), Lockheed Martin (187.75), SEAKR (187), Radiation Test Solutions (176), NASA JPL (148), Northrop Grumman (137), Texas Instruments (120), Thales Alenia Space (105.5), Honeywell (102), International Rectifier (98.5), Sandia National Lab (92), NAVSEA (76), Cal Tech (70.5), ATMEL (64.5), Air Force (63), Cobham (56), Space X (52.5), TRAD (40), Harris Corp (35.5), Freebird (34), Ball Aerospace (33.5), VPT Inc (32), Frequency Management (31), Scientic (28.5), Colordao State University (24), JAXA (24), STEE-Satellite Systems (24), Microsemi Corp (22.5), L-3 Communications (21), Johns Hopkins APL (20), Vanderbilt University (18), BAE Systems (16), CoolCad (16), InnoFlight (16), Silicon Turnkey Solutions (16), Space Micro (16), T2 Research (16), Teledyne DALSA (16), Utah State SDL (16), Raytheon Corp (14.5), VPT Rad (12.5), NASA LRC (12), Aeroflex Corp (8), Data Device

Table I. Radiation effects facility usage by commercial and government customers for this and previous reporting years.

Reporting Year	Total Hours	Commercial Hours (%)	Government Hours (%)
2016-2017	3355	2,501(75%)	854(25%)
2015-2016	3,042	2,326 (76%)	716 (24%)
2014-2015	3,024	1,975 (65%)	1,049 (35%)
2013-2014	2,399	1,517 (63%)	882 (37%)
2012-2013	2,626	1,856 (71%)	770 (29%)
2011-2012	2,673	1,630 (61%)	1,043 (39%)
2010-2011	3,042	1,922 (63%)	1,121 (37%)
2009-2010	2,551	1,692 (66%)	859 (34%)
2008-2009	2,600	1,828 (70%)	772 (30%)
2007-2008	2,373	1,482 (62%)	891 (38%)
2006-2007	2,498	1,608 (64%)	890 (36%)
2005-2006	2,314	1,314 (57%)	1,000 (43%)
2004-2005	2,012	1,421 (71%)	591 (29%)
2003-2004	1,474	785 (53%)	689 (47%)
2002-2003	1,851	1,242 (67%)	609 (33%)
2001-2002	1,327	757 (57%)	570 (43%)
2000-2001	1,500	941 (63%)	559 (37%)
1999-2000	548	418 (76%)	131 (24%)
1998-1999	389	171 (44%)	218 (56%)
1997-1998	434	210 (48%)	224 (52%)
1996-1997	560	276 (49%)	284 (51%)
1995-1996	141	58 (41%)	83 (59%)

Corp (8), Fuji Electric (8), and Southwest Research Institute (7). New users included CoolCad and STEE-Satellite Systems.

Table I compares the facility usage by commercial and government customers. While commercial hours still dominate, the ratio from this reporting year (75% to 25%) is similar to usage from the 2015-2016 reporting period (see Fig 1). Both commercial and government hours increased by 8% and 19% compared to hours from 2015-2016. 15 MeV/u ions were the most utilized and especially 15 MeV/u Au. No new beams were added to SEELine users list. Much of the testing conducted at the facility continues to be for defense systems by both government and commercial agencies. Almost 21% (528 hours) of the commercial hours were for foreign agencies from Japan, France, and Singapore. It is expected that the facility will continue to be as active in future years.

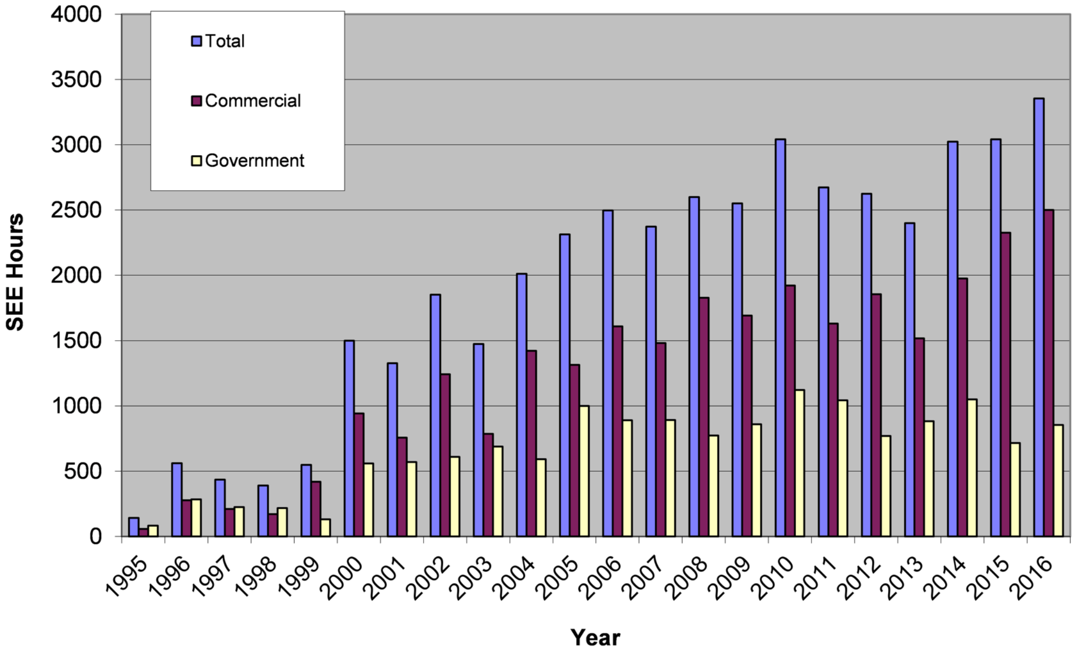

FIG. 1. Radiation Effects Facility usage by commercial and government customers for this and previous reporting years. While commercial hours still dominate, the ratio from this reporting year (75% to 25%) is similar compared to usage from the 2015-2016 reporting period. Almost 21% (528 hours) of the commercial hours were for foreign agencies from Japan, France, and Singapore.

K150 Operations and Development

G.J. Kim, B.T. Roeder, F. Abegglen, H. Clark, L. Gathings, D.P. May, R. Olsen, and H. Peeler

Introduction

We had a very busy year operating the K150 cyclotron. For the reporting period we logged over 3770 hours of beam-on-target and 2900 hours for beam developments. Included in the beam-on-target time was 146 hours for the SEE testing.

As it was in previous years the 15 MeV proton beam was produced regularly throughout the year for the light ion guide (LIG) project. In the fall, the production of the radioactive gallium 64 isotope from a zinc 64 target and subsequent charge breeding using an ECR ion source (CB-ECR) progressed to a point where we sought to test the entire radioisotope production and re-acceleration process by accelerating $^{64}\mathrm{Ga}^{12+}$ to 14 AMeV with the K500 cyclotron. We chose to use ever present and prominent $^{16}\mathrm{O}^{3+}$ ions as a pilot beam to inject and to tune the K500 cyclotron, which in turn selected 12+ for the gallium 64. The oxygen beam was also used in beam transport to the MARS cave, where we sought to identify the radioactive beam. The beam on target was then switched from oxygen to gallium by shifting the K500 RF frequency by +8 kHz while keeping the same cyclotron field. This test is described in detail in a separate section.

Beside the 15 MeV protons, we have produced 40 to 45 MeV protons for the SEE testing for several groups. For the lower end of proton energies, we have developed 6 and 10 MeV proton beams. The 6 MeV beam at 330 amps on the main field marks the lowest operating cyclotron field to date.

The 7.22 AMeV (29 MeV total) alpha beam was accelerated twice during the year for the production test of the astatine 211 on a bismuth target. After the first test, the bismuth target was water-cooled to withstand the higher beam current, and on the second time almost 5 pμA of the beam current was extracted. It was then irradiated for about 8 hours and this resulted in producing about 30 MBq of activity from $^{211}\mathrm{At}$. Of this activity, about 30% could be extracted and separated from the bismuth target using chemical processing. Further testing for the production of $^{211}\mathrm{At}$ is planned for the coming year.

The TIARA experiments have started after the installation of the target and the associated detector assembly at the front the MDM spectrometer. Beginning in the late summer five beams have been transported to the cave for their experiments; beams used were: 10 AMeV $^{19}\mathrm{F}^{7+}$, $^{23}\mathrm{Na}^{8+}$, and $^{25}\mathrm{Mg}^{9+}$, and 7 AMeV $^{22}\mathrm{Ne}^{7+}$ beam.

We have reported in the past of our struggles with 3rd harmonic beams. Last year, our attempt to accelerate 4 AMeV deuteron beam (using 1+ ions from ECR2) failed, the beam current simply died on the way out to the extraction radius. We tried next a slightly higher 4.5 AMeV deuteron beam here we at least were able to guide enough beam to the extraction radius and extract around 20 nA. However the extraction efficiency was poor and the beam proved to be too unstable to be useful. So this year, we tried using D^- ions from the H^- source, taking advantage of its lower emittance to inject more efficiently into the cyclotron. Also, using 50% higher dee voltage than the previous 4 AMeV tuning effort and plus the easier strip extraction, we were able to extract 70 nA out of 10 μA (~1% throughput). The resulting beam was stable enough that it was used in an experiment. So, why did the D^- beam work and not D^+?

Certainly the higher dee voltage helped. It would be interesting to see if the new D^- cyclotron tuning parameters would work with D^+ from ECR2.

Lastly, we tested a compact spiral inflector, see Fig. 1, in place of the mirror inflector for the axial injection into cyclotron. This was a quick test of the design and fabrication process for the inflector (the inflector was machined in-house on our NC machine). We ran a couple of 1st harmonic beams and a 3rd harmonic beam to test that the inflector inflected the beams into the cyclotron, and then we tried to optimize the beam current by varying the inflector rotation angle and the inflector height. For a few days we had for this test (before the inflector had to be removed due to a water leak on the inflector), we were able to achieve about 5% throughput for 6.3 AMeV $^{16}O^{5+}$ beam (as compared with about 10% with the mirror inflector). The inflector height adjustment was rather clumsy and we will need to revisit the spiral inflector. The design and the dimensions of our test spiral inflector are detailed below.

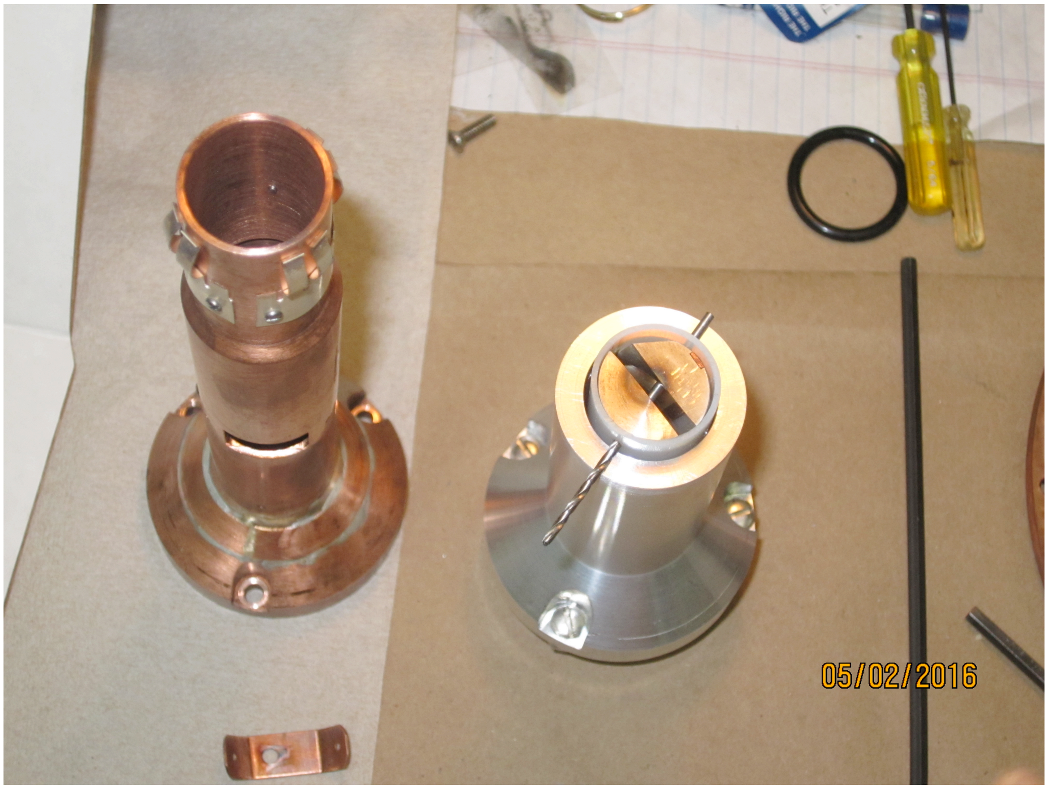

FIG. 1. Compact spiral inflector and its housing.

Compact Spiral Infector

A compact spiral inflector was designed and fabricated with the intent to simply replace the current mirror inflector which is surrounded by the RF dee tips (batwings) at the center of cyclotron. To fit inside the batwings the inflector housing was limited to 1" in diameter and the spiral electrode to ¾" in diameter, see Figs. 2 and 3. The housing was made of a 0.020" thin stainless steel tube and the spiral was machined from an Al rod. The spiral was designed with the well-known equations by Belmont and Pabot (of a particle trajectory in a constant axial magnetic field $-B_0\vec{z}$ with the initial electric field $\mathcal{E}$ alo ng $+\vec{x}$):

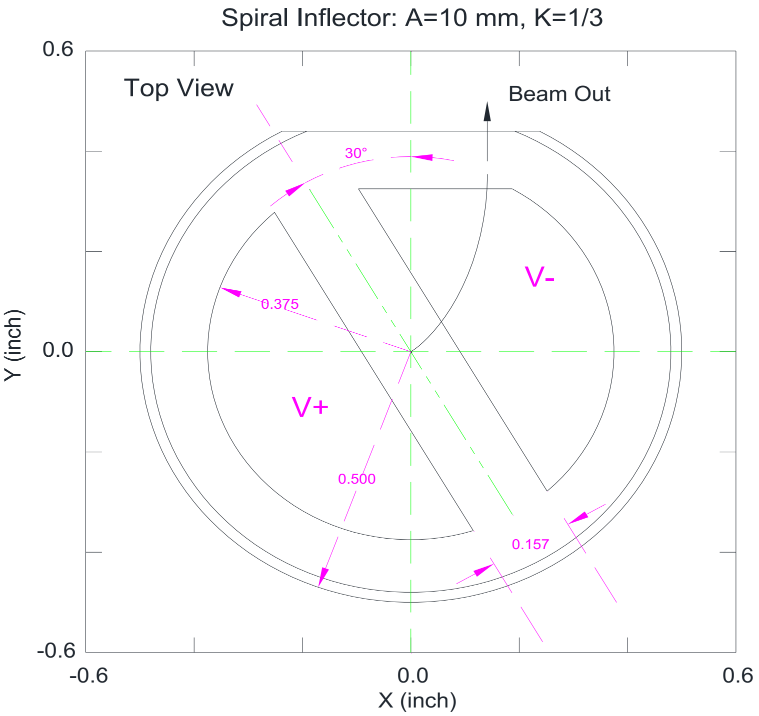

FIG. 2. Top view of our compact spiral inflector.

$$x = \frac{A}{2}\left\{-\frac{2}{(2K+1)(2K-1)} - \frac{\cos(2K+1)b}{2K+1} + \frac{\cos(2K-1)b}{2K-1}\right\},$$

$$y = \frac{A}{2}\left\{-\frac{\sin(2K+1)b}{2K+1} + \frac{\sin(2K-1)b}{2K-1}\right\},$$

$$z = A\{1 - \sin b\},$$

where $A = 2T/(q\mathcal{E})$ is the electric radius of curvature and $K=A/(2\rho)$, $\rho = P/(qB_0)$ is the magnetic radius of curvature, and b is a dimensionless parameter ranging from 0 to $\pi/2$. (T, P, and q are the kinetic energy, the momentum, and the charge of the particle, respectively.) The equations describe the reference beam particle entering the inflector along the central axis (x=0, y=0) at the height of A and then inflected onto the median plane (z=0) and exiting at radius of $(A/|4K^2-1|)\sqrt{1+4K^2-4K\sin K\pi}$. We chose A=10 mm and ρ=15 mm, and so K=1/3 and the exit radius of 0.381" (9.69 mm), slightly larger than 3/8" (9.53 mm) (the radius of Al rod). (The fringe field would extend a little further out to cover this). Also we have squared up the inflector exit by trimming the Al rod and including a matching flat exit window on the inflector housing. The final momentum of the inflected beam is rotated 180K degrees, or 60

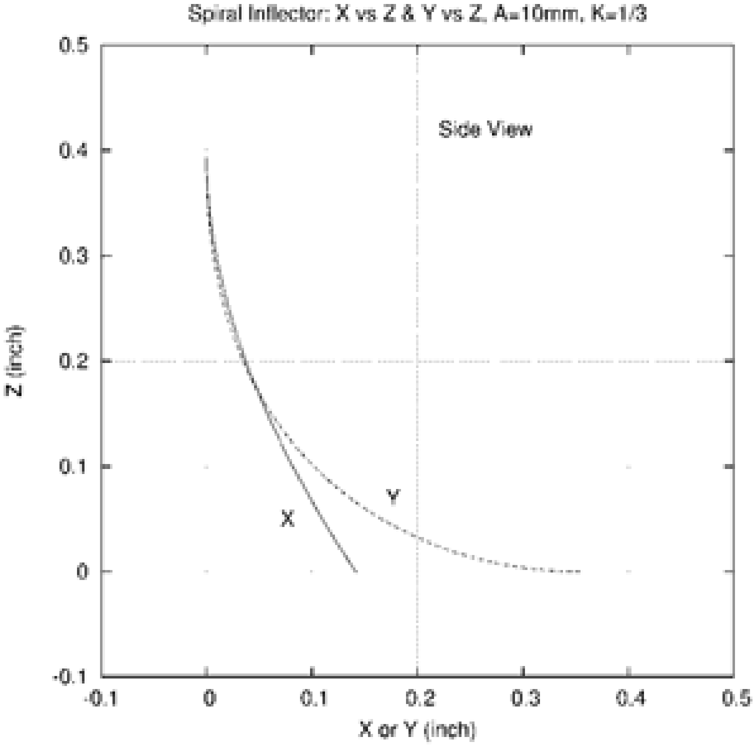

FIG. 3. Side views of X vs Z and Y vs Z of particle trajectory through the spiral inflector.

degrees about the z-axis, from the initial electric field direction (at the entrance of the inflector). So as seen on Fig. 2, by starting the electric field pointing +30 degrees with respect to the + $\vec{x}$ axis, the beam would inflect onto the median plane and exit along the + $\vec{y}$ axis, perpendicular to the notch on the inflector. The required electric field of the inflector is related to the source voltage and the value of A; with a typical value of 10 kV on the ion source, the electric field needed on the inflector is 20 kV/cm, or with a 4 mm gap it would be +4 and -4 kV on the inflector. From the particle trajectory equations, the particle velocity remains constant, and the velocity and the electric field are perpendicular to each other in going through the inflector. One can define the third vector perpendicular to the velocity and the electric field, and interestingly this vector is contained in the horizontal plane (without any z component). This third $\vec{\mathcal{E}} \times \vec{v}$ vector is then parallel with the inflector electrode surface. To machine this curved surface, one can imagine having an Al rod held fixed vertically and a thin, spinning cylindrical cutting tool in the horizontal plane starting at the top of the rod and advancing in small steps along the particle trajectory and at the same time rotating about the instantaneous trajectory point (following the $\vec{\mathcal{E}} \times \vec{v}$ vector), and then finally exiting out of the rod. From Fig. 2, the cutting tool would start at the top of the Al rod tilted -60 degrees with-respect-to the $\vec{x}$ axis and then would emerge 10 mm below the starting point rotated +60 degrees or in align with the $\vec{x}$ axis. In actual machining of the inflector, the spinning cutting tool was held vertically and an Al rod was held horizontally in a rotatable and x-y positioning jaw, and the rod was slowly fed into the cutting tool.

Texas A&M cyclotron K150 radiation effects facility
April 1, 2016 – March 31, 2017

B. Hyman, H.L. Clark, V. Horvat, G.J. Kim, B. Roeder, and S. Russell

Several improvements have been made to the radiation effects facility K150 beamline. A backscatter detection system has been implemented to accommodate high intensity proton dosimetry. The beam shutter control box has been modified to ease the transition between high-intensity and low-intensity set-ups. Also, beamline hardware has been modified and reconfigured to help minimize residual radioactivity.

The backscatter detection system is mounted inside an ISO250 six-way cross (Fig. 1). The system consists of a set of four tantalum foils and four detectors aligned to measure backscattered protons from the foils (Fig. 2). The detectors are mounted on an aluminum ring and are angled to face the foils. The foils are mounted on a separate aluminum ring and are placed perpendicular to the beam path at 90° intervals radially about the beam line center. On average, approximately 10% of the beam is backscattered into the detectors.

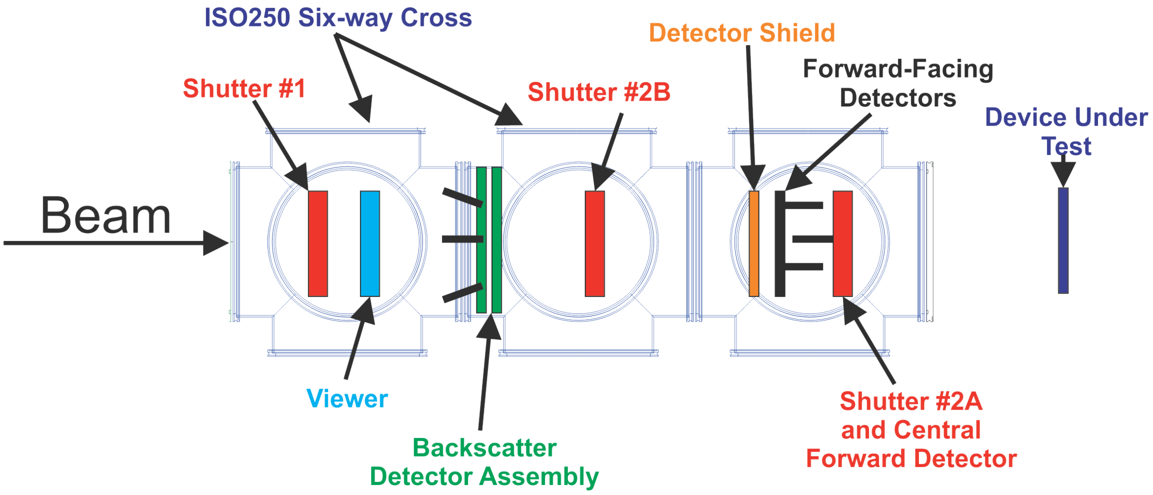

FIG. 1. Radiation effects facility K150 beamline layout.

For high intensity dosimetry (beam flux > 3e7 particles/cm^2/sec), beam uniformity is first confirmed at a lower intensity with the forward-facing detectors (Fig. 1). Then, an aluminum detector shield is positioned in front of the forward-facing detectors to protect them during high intensity irradiations. Next, a calibration measurement is made using the central forward facing detector and the four backscatter detectors. Our custom SEUSS software determines the ratio of the count in the central detector to the average of the counts in the four backscatter detectors. Once this ratio is determined, the central detector is removed from the beam path and disabled. A second beam shutter (Shutter 2B) is then used to block the beam from the device under test (DUT). Finally, the beam intensity is increased and beam flux is determined by multiplying the average of the counts from the backscatter detectors and the calibration ratio.

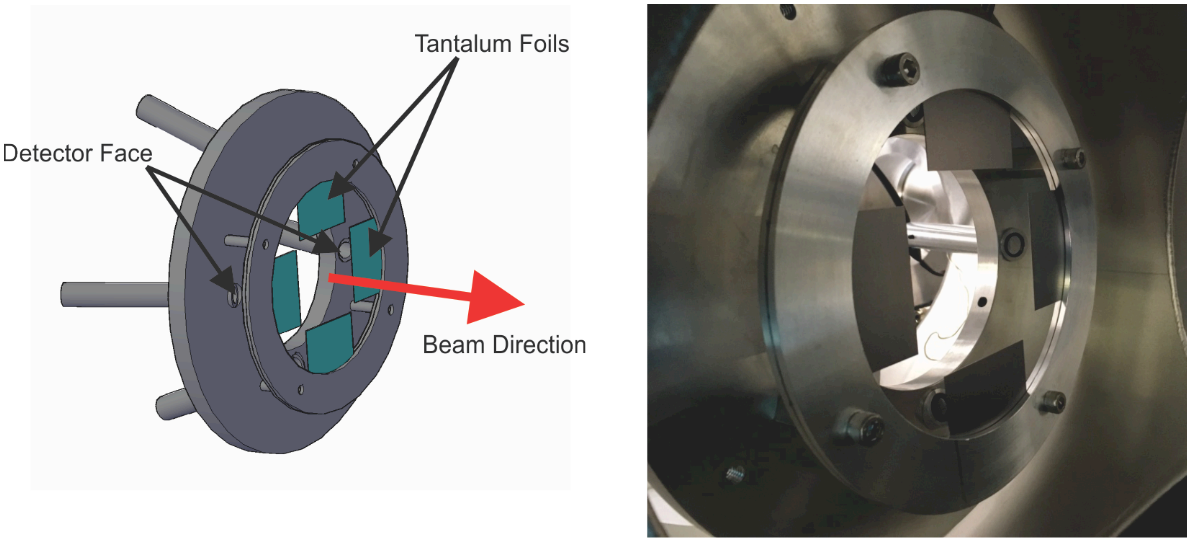

FIG. 2. (Left) CAD 3D model of backscatter detector system. (Right) Backscatter detector system installed in six-way cross.

The transition from low intensity operation and high intensity operation has been made more efficient with modifications to the beamline and the beam shutter control box. A third six-way ISO250 cross was added to the beamline and an additional beam shutter was put in place to block the DUT during high intensity testing (Fig 1). This shutter has been designated as “shutter 2B”, with the original shutter 2 now referred to as “shutter 2A”. Since the thruster with shutter 2A includes the central forward detector, it is removed from the beam path during high intensity beam exposure. A switch, added to the front of the shutter control box, is used to change between the two testing configurations. Control from the SEUSS software is transparent between the 2A/2B switch.

New input and output signals have also been added to the beam shutter control box. The box has now been wired to receive confirmation of detector shield position. Based on detector shield position, signals are provided to veto detector signals. An inhibit signal for non-operational beamline vacuum is now supplied for the high voltage power supplies.

Beamline hardware changes have been made to help reduce residual radioactivity. The standard 4” diameter beam pipe has been replaced with an 8” diameter beam pipe has been installed in front of the six-way crosses. A new 8” diameter beamline valve has also been installed. In order to reduce the stainless-steel valve’s beam exposure, an aluminum collimator has been placed directly in front of the valve. The collimator has a 4” diameter opening and is 2” thick.

These improvements should help increase the ease and safety of operation of the K150 radiation effects facility beamline as we look to increase its use in the future.

Progress on the ECR4 ion source and the ECR1 replacement hexapole

D.P. May, S. Molitor, F.P. Abegglen, H. Peeler, and R. Ohlsen

Construction on the new 6.4 GHz ECR4 ion source is continuing. The axial-field coils have been wound (Fig. 1), and the potting of the coils has started. The twelve permanent-magnet bars for both the ECR4 hexapole and the replacement ECR1 hexapole have been delivered (Fig. 2). Measurements on the bars show that their magnetic fields are much more uniform than the fields of the original ECR1 bars.

FIG. 1. Axial-field before potting.

FIG. 2. One of the twelve assembled NdFeB hexapole bars.

The two new aluminum plasma chambers have been constructed (Fig. 3), and the steel yoke and injection-end plug are now being fabricated. The permanent-magnet bars will be inserted in the plasma chambers either by the magnet vendor or in-house using the mechanism used for the insertion of the bars for ECR2.

Two used 6.4 GHz transmitters have been purchased. Next stands will be fabricated, and pumps will be ordered.

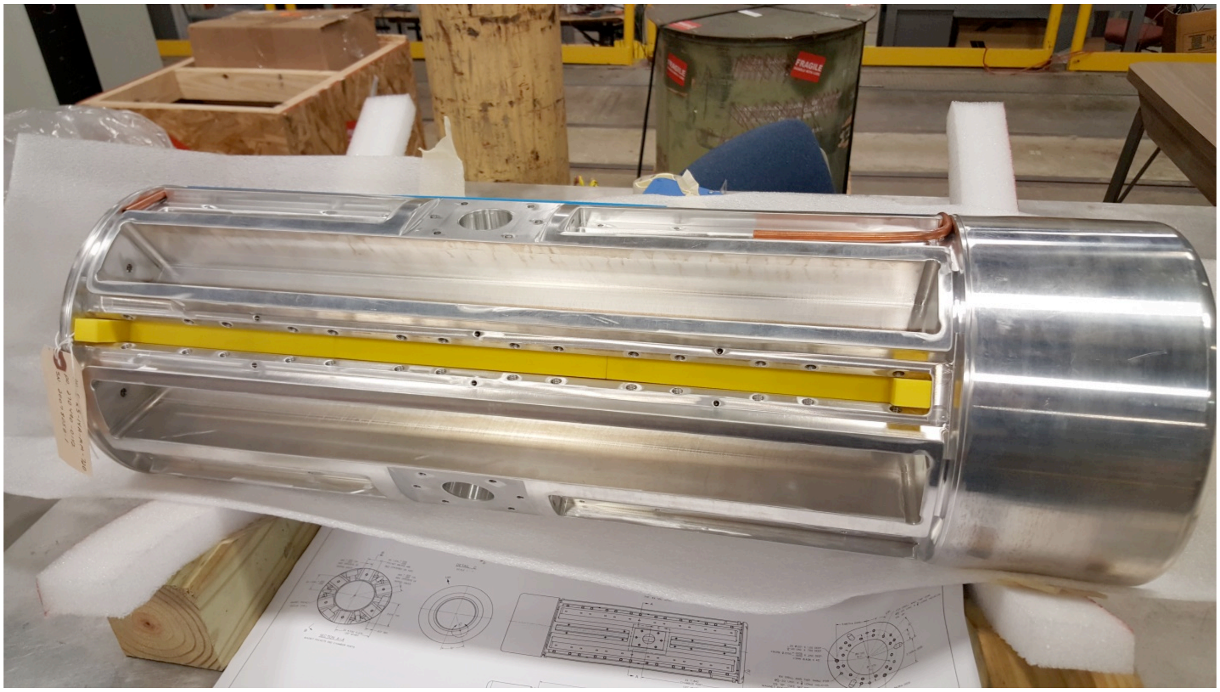

FIG. 3. One of two aluminum plasma chambers.

Progress on the light ion guide

G. Tabacaru, J. Arje, D. May, A. Saastamoinen, F. Abegglen, G. Chubaryan, H. Clark,
G. Kim, S. Molitor, B. Roeder, S.J. Yennello, and R. Wada

The Light Ion Guide project [1,2] continued to advance, one of the main priorities being the increase of the efficiency of the entire system and installing new detection systems for radioactive ion-beam tuning.

Four new detection systems are installed (Fig. 1), all four similar in the design: a thin aluminum foil placed in front of a 300 μm thick silicon detector, coupled to a simple counting and acquisition system – HV detector power supply, preamplifier, amplifier and a multichannel analyzer. The first collection/detection system is mounted on a pneumatic linear actuator, after the extraction tube of the Light Ion Guide. The second collection/detection system consists of a fixed position detector, placed off beam axis, after the Charge Breeding – ECR (CB-ECR) and a collection plate mounted on a pneumatic linear actuator. This system operated as follows: the collection plate is placed in beam for approximately 2 half-lives of the radioactive ion produced, then retracted in front of the detector to measure the decay (positron, beta or alpha particles) of the radioactive product. The third and fourth detection systems are similar, with both the collection thin aluminum foil and the detector in a fixed position on the beam axis: one system is positioned at the first analyzing magnet and the other at the second analyzing magnet.

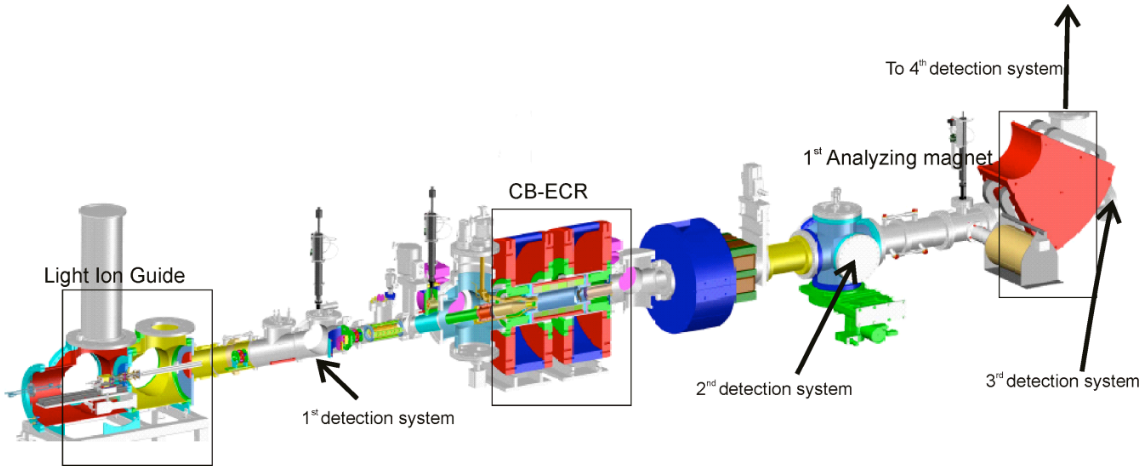

FIG. 1. Schematic of the Light Ion Guide coupled with the CB-ECR. The positions of the detection systems are shown.

Improvements in the pumping speed were made by replacing one 1000 l/s turbo molecular pump with a 2000 l/s water cooled turbo molecular pump at the second chamber of the Light Ion Guide. The replacement helped the extraction and transport of the radioactive ions produced, as well as a more consistent functioning of the entire system. Another improvement made was the purification of the helium gas buffer: a purifier from SAES Pure Gas, model MicroTorr was placed in-line, close to the entrance in the gas cell. The purifier, theoretically, provides impurity removal at part-per-billion levels, the targeted impurities being mainly water, oxygen, hydrocarbons and organic compounds. The tests done with and without the purifier showed a slightly better output of the gas cell in the radioactive products, when the purifier line was not by-passed.

With the new detection systems in place, our ^{228}Th open source has been used in order to check the Light Ion Guide setup, coupled together with the CB-ECR. First the Light Ion Guide was tuned to get maximum output of ^{220}Rn ($T_{1/2}$ = 55.6 s) and ^{216}Po ($T_{1/2}$ = 0.15 s) products, the daughters from ^{228}Th decay chain. The CB-ECR was also retuned for charge breeding, based on previous experimental data and tests. For the first time, the charge breeding of ^{220}Rn and ^{216}Po was observed on the detection system situated after the CB-ECR. The charge state distribution of the ^{220}Rn and ^{216}Po was determined using the last detection system placed at the second analyzing magnet. The maximum of the charge state distribution was found at 21+ (Fig.2). Different charge states of ^{220}Rn and ^{216}Po are mixed and superimposed due to the limited resolution of the analysis system (Fig.3). The extra voltage applied to the Light Ion Guide system in order to overcome the plasma potential and achieve the charge breeding, was in a wide range, varying between 30 V to 80 V.

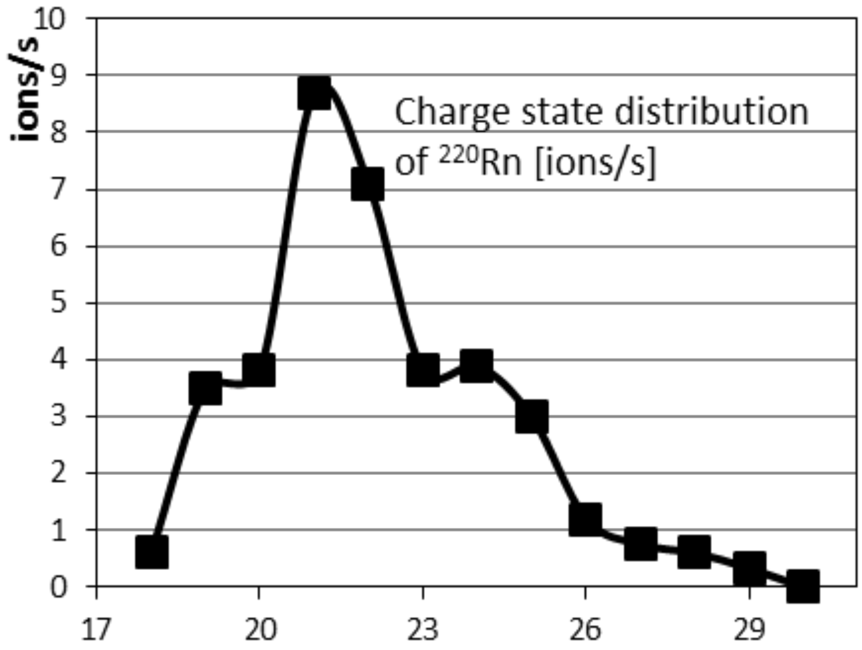

FIG. 2. Charge state distribution for the ^{220}Rn. The distribution is peaked at the charge state 21^{+}.

We continued to use the ^{64}Zn(p,n)^{64}Ga ($T_{1/2}$ =2.6 min) reaction as a test and tuning reaction for the Light Ion Guide. The energy of the proton beam from the cyclotron was 15.7 MeV (15.0 MeV on target). The pressure of the helium in the gas cell, for maximum ^{64}Ga output was 180 mbar. The exit aperture diameter used for the gas cell was 1.5 mm. Other exit apertures were used: 1.2 mm, as well as 2.0 mm, but the 1.5 mm exit aperture proved to be the most efficient. Using the new installed detection systems, the device was carefully tuned: first, find the maximum outputs of ^{64}Ga from the gas cell and the Light Ion Guide extraction system; second, optimize the transport of ^{64}Ga^{1+} radioactive ions through the CB-ECR with the microwave transmitter turned off. Following ^{64}Ga^{1+} transport optimization, the CB-ECR microwave transmitter was turned on, and charge breeding of ^{64}Ga was detected on the second and third detection system. The analyzing magnet was changed for O^{3+} transport, which corresponds to $^{64}Ga^{12+}$ transport and the b^+ decay of ^{64}Ga was detected on the fourth detection system.

The charge breeding efficiency was extremely low, under 0.1%, and our efforts were focused to improve this efficiency. A series of factors have been determined to be crucial in the increasing of the efficiency of the charge breeding: injection of the 1+ ions into the plasma chamber, backward extracted beam from CB-ECR hitting elements in the beam line, creating more electrons that disturb plasma and creating vacuum issues or discharge problems. Solving a few of these complications proved to be problematic and, in spite of our efforts, no major improvement in the charge breeding efficiency has been achieved. However we were able to improve the stability and reproducibility of the entire system, the Light Ion Guide coupled with the CB-ECR, reducing the time for tuning and optimization.

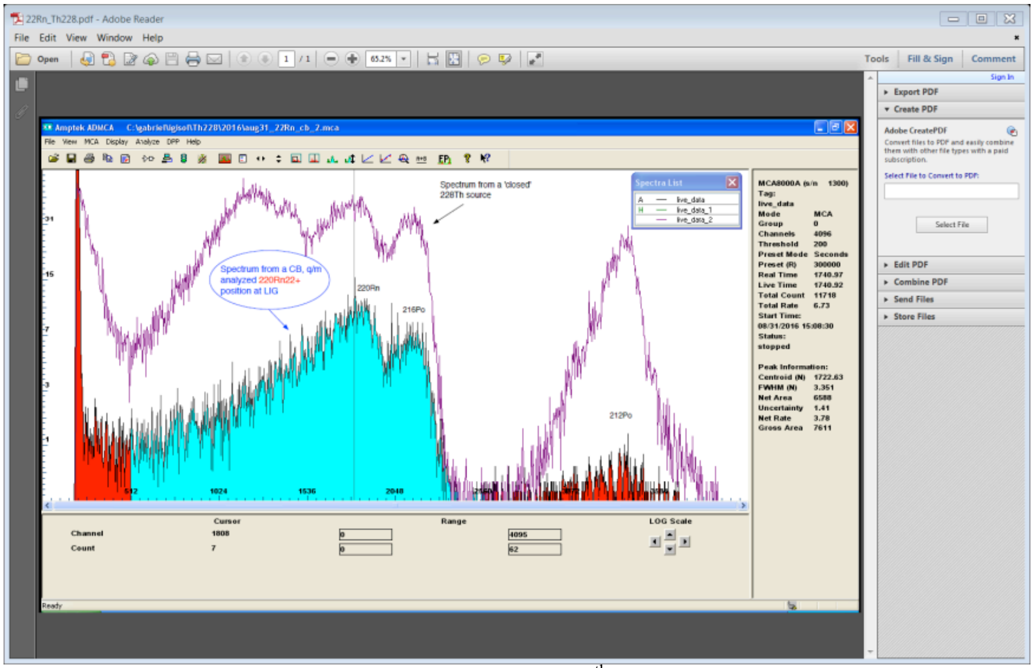

MCA8000A (s/n 1300)
Tag:
live_data
Mode MCA
Group 0
Channels 4096
Threshold 200
Preset Mode Seconds
Preset (R) 300000
Real Time 1740.97
Live Time 1740.92
Total Count 11718
Total Rate 6.73
Start Time:
08/31/2016 15:08:30
Status:
stopped

Peak Information:
Centroid (N) 1722.63
FWHM (N) 3.351
Net Area 6588
Uncertainty 1.41
Net Rate 3.78
Gross Area 7611

	Cursor		Range	
Channel	1808	0	4095	
Count	7	0	62	

LOG Scale

FIG. 3. Screenshot of the acquisition system of the 4th detection system, showing in blue the alpha particle peaks of $^{220}Rn^{22+}$ and ^{216}Po (daughter of ^{220}Rn and $^{216}Po^{21+}$). The purple line/empty area is the detector response from a regular ^{228}Th source in secular equilibrium.

The conclusions after almost a year of working to achieve charge breeding of radioactive ions, are the following: reliable detection systems are needed and their importance for tuning, diagnostic and characterization of the device is being essential; the charge breeding efficiency is critical in obtaining good, reliable re-accelerated radioactive ion beams; any advances in the vacuum systems and helium gas-transfer will improve the stability, reproducibility and overall radioactive ion beam output of the Light Ion Guide and CB-ECR couple. In the near future, our efforts will be intensified towards increasing the charge breeding efficiency, considering major changes in the injection scheme of the 1+ ions.

[1] H.L. Clark *et al.*, *Progress in Research*, Cyclotron Institute, Texas A&M University (2014-2015), p. IV-15.

[2] G. Tabacaru *et al.*, *Progress in Research*, Cyclotron Institute, Texas A&M University (2013-2014), p. IV-9. http://cyclotron.tamu.edu/2014%20Progress%20Report/cyclotron_progress_2014.pdf

Acceleration and identification of charge-bred ions from the light-ion guide with MARS

B.T. Roeder, F. Abegglen, J. Arje, G.J. Kim, A. Saastamoinen, and G. Tabacaru

Last year, charge-bred ^{85}Rb from the charge breeding electron-cyclotron resonance ion source (CB-ECR) was accelerated with the K500 and identified with the MARS spectrometer and associated silicon detectors [1]. This year, a follow-up experiment was designed to search for ^{64}Zn and ^{64}Ga ions that had been produced and transported with the Light-Ion Guide (LIG) to the CB-ECR in an attempt to produce the first re-accelerated radioactive beam at the Cyclotron Institute.

The experiment was carried out in a similar way as the ^{85}Rb experiment. To calibrate the detectors at the focal plane of the Momentum Acromat Recoil Separator (MARS) [2], a beam of ^{63}Cu at 14 MeV/u was accelerated with the K500 cyclotron and was transported to the target chamber of MARS. The ^{63}Cu beam impinged on a thin ^{12}C stripper foil that was 103 μg/cm^2 thick. The stripper foil removed electrons from the beam such that the resulting charge states of the beam could be tuned through MARS at rigidities calculated with the LISE++ model of MARS [3]. Once each charge state was tuned through MARS, it was measured at the focal plane with detectors consisting of a ΔE-E silicon telescope. The ΔE detector was a 64 μm thick, position sensitive strip detector and the E detector was a single pad detector that was 500 μm thick. The type and thicknesses of the detectors were chosen such that the ^{63}Cu, and also the desired ^{64}Zn and ^{64}Ga, could be detected and identified using their energy loss in the silicon detectors and their position at the MARS focal plane. During the calibration, charge states 23+ through 29+ for ^{63}Cu were measured. An average energy of 880.5 ± 2 MeV was observed by calculating the beam energy based on a prior calibration of the MARS D1 dipole field and comparing the energy deposits in the silicon telescope for each charge state. The result of the tune for the ^{63}Cu^{29+} charge state is shown in Fig. 1. It was also noted that the energy resolution (FWHM) of the ΔE and E detectors were 7 MeV and 8 MeV respectively. This resolution was sufficient for the separation of beam species with mass=64, but different

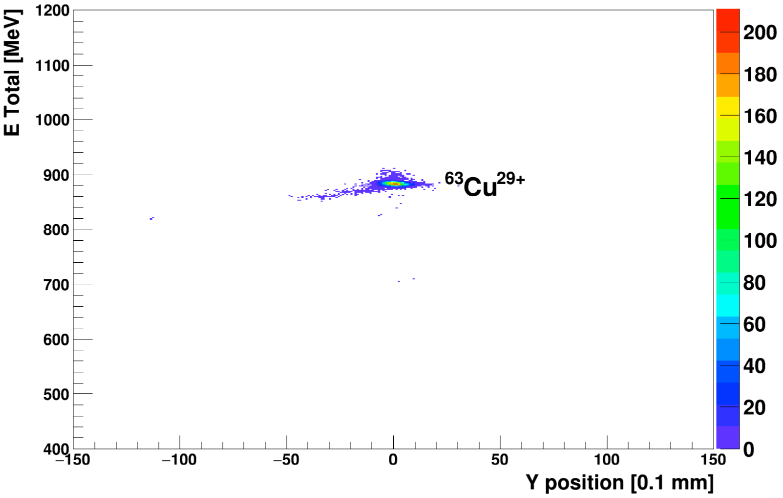

FIG. 1. Total Energy vs. Y-position spectrum obtained for the ^{63}Cu^{29+} calibration beam tune.

charge “Q” as was needed to measure ^{64}Zn and ^{64}Ga simultaneously.

To search for ^{64}Zn and ^{64}Ga ions that had been accelerated by the K500, first a pilot beam of $^{16}O^{3+}$ at 14 MeV/u was tuned through the K500 cyclotron. The charge-to-mass ratios (Q/M) for $^{16}O^{3+}$, $^{64}Zn^{12+}$, $^{64}Ga^{12+}$ are 0.18756, 0.18773 and 018771 respectively. It was calculated for the ^{85}Rb at 14 MeV/u in the previous experiment that a radiofrequency (RF) shift of about 6 kHz corresponded to changing the Q/M ratio accelerated by the K500 by about $\Delta Q/\Delta M \approx 0.0001$. Thus, to shift the frequency for $^{16}O^{3+}$ to $^{64}Ga^{12+}$, corresponding to $\Delta Q/\Delta M \approx 0.00015$, a frequency shift of about +8 kHz to +9 kHz was expected. However, it was also noted in the experiment last year that the $^{16}O^{3+}$ beam could still be observed as much as 12 kHz away from the optimum frequency. As a result, it was expected that all three beams, $^{16}O^{3+}$, $^{64}Zn^{12+}$ and $^{64}Ga^{12+}$ would be transported to the MARS target chamber simultaneously despite the slight change in the frequency of the K500 cyclotron. But, after being stripped with the thin carbon stripper foil, the ^{64}Zn and ^{64}Ga for the charge states where the Q/M were different would be cleanly separated in rigidity from the ^{16}O pilot beam.

The ^{64}Zn and ^{64}Ga ions were produced by bombarding a thin, enriched ^{64}Zn target with about 5 μA of 15 MeV protons from the K150 cyclotron. The ^{64}Zn ions, produced from proton elastic scattering, and the ^{64}Ga ions, produced from the $^{64}Zn(p,n)^{64}Ga$ reaction, were stopped in pure He gas and transported by the Light Ion Guide (LIG) [4] to the CB-ECR. Inside the CB-ECR, the ions were charge-bred in the plasma to $^{64}Zn^{12+}$ and $^{64}Ga^{12+}$ ions. Since $^{16}O^{3+}$ is also extracted from the CB-ECR with the same extraction voltage and magnet settings as the $^{64}Zn^{12+}$ and $^{64}Ga^{12+}$ ions, the $^{16}O^{3+}$ was used as a pilot beam to develop the tune from the CB-ECR through the K500 cyclotron and eventually to MARS. Then, once the $^{16}O^{3+}$ beam was tuned to the entrance of MARS, the frequency of the K500 cyclotron was shifted +8 kHz (to optimize for the $^{64}Ga^{12+}$) to begin the search for the re-accelerated $^{64}Zn^{12+}$ and $^{64}Ga^{12+}$.

Prior to sending the $^{16}O^{3+}$ beam through the K500, a β-decay rate of 20 decays/s was observed with the same magnet settings after the CB-ECR on the silicon detector in the vertical injection line. These β-decays were assumed to arise from the decay of the $^{64}Ga^{12+}$ ions. Assuming a 1% efficiency for the acceleration of these ions, that would imply that about 0.2 ions/sec would be transported to MARS. Following the charge-stripping models available in LISE++, about 35% of these ions were expected to be in the 29+ charge state following the ^{12}C stripper foil. Taking these efficiencies into account, about one $^{64}Ga^{29+}$ ion per 14 seconds was expected on the MARS silicon detectors.

MARS was tuned with magnetic rigidity settings optimized to observe the ^{64}Ga and ^{64}Zn in charge states 29+ and 27+. Settings to observe the $^{64}Ga^{31+}$ were also attempted. The magnetic rigidity of MARS was set with the currents on the magnets as determined by the LISE++ model of MARS [3]. Data were taken separately with the K150 proton beam both on and off.

Since both $^{64}Zn^{29+}$ and $^{64}Ga^{29+}$ have the same mass and charge, then they should have the same total energy, 892 MeV, as measured by the silicon detector telescope. However, the energy loss of the two ions in the ΔE detector was different by 19 MeV; 320.6 MeV for ^{64}Zn and 339.8 MeV for ^{64}Ga as calculated by LISE++ [3,5]. In the measurement, a peak corresponding to ^{64}Zn was observed in the ΔE detector spectrum when the K150 proton beam was both on and off. The peak was asymmetric on the high-energy side, leading to background in the region where the ^{64}Ga could be expected. In one experiment run, a shoulder peak with about 100 counts above the background was observed at the energy loss corresponding to ^{64}Ga. Due to the background in the high-energy tail of the ^{64}Zn peak, cleaner separation of the ^{64}Ga from the ^{64}Zn was not possible in this setup. Assuming a constant background rate, the rate of the ^{64}Ga was about one ion per 30 seconds; about half of what was expected. However, since the background rate in the high-energy tail was about the same as the ^{64}Ga rate with the proton beam on and the shoulder peak was not reproducible, the results were inconclusive. A higher intensity peak with about 680 MeV total energy, consistent with ^{48}Ti^{22+}, was also observed. The origin of the ^{48}Ti background is unknown but may be due to the specific aluminum alloy in the CB-ECR plasma chamber. Perhaps the ^{64}Zn that is observed with the K150 proton beam off arises from the same origin. ΔE detector spectra showing measurements of the ^{64}Zn peak with MARS set for the 29+ charge state with the K150 proton beam on and off are shown in Fig. 2.

With MARS set to measure the ^{64}Zn^{27+} and ^{64}Ga^{27+}, a peak corresponding to ^{64}Zn was observed again, confirming the identification of the ^{64}Zn. No ^{64}Ga was observed at this setting. However, surprisingly, ^{64}Ni^{27+} was also observed, well separated by 40 MeV from the ^{64}Zn^{27+} in the ΔE detector spectrum. Like the ^{48}Ti, the origin of the ^{64}Ni background is unknown but may be due to contamination in the CB-ECR plasma chamber as before.

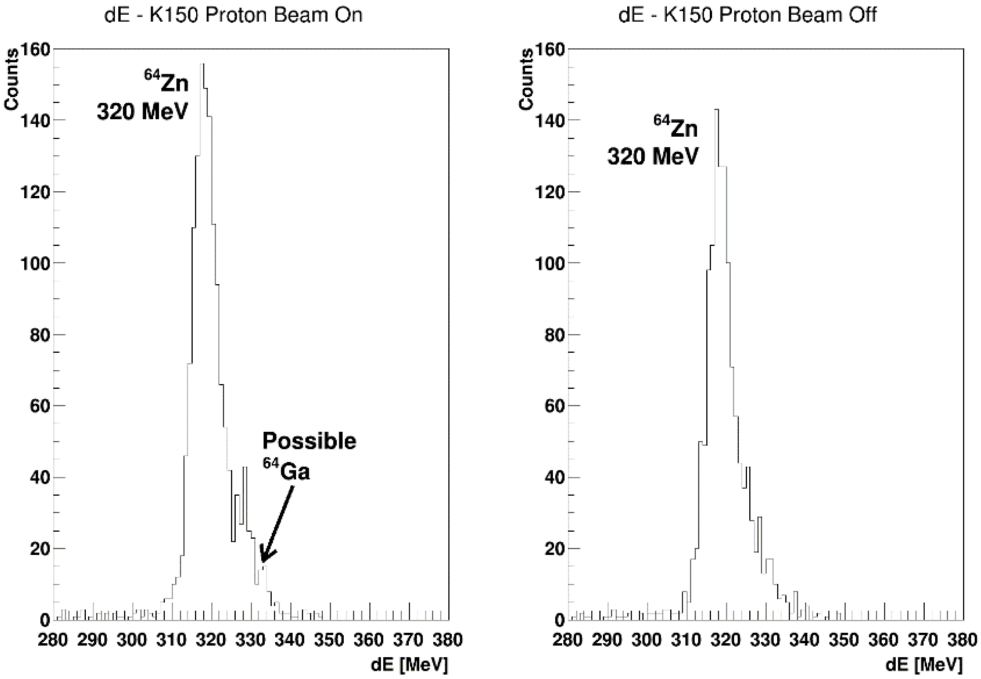

FIG. 2. Spectra showing the ^{64}Zn and possible ^{64}Ga peak for 29+ charge state setting. Clear identification of the ^{64}Ga was not possible. With the K150 proton beam "On", about 100 counts above background were observed in the region where ^{64}Ga was expected.

A large background from the remnants of the pilot beam was expected with the tunes for the ^{64}Ga 28+ and 24+ charge states, since they are charge-to-mass analogs with the ^{16}O^{7+} and ^{16}O^{6+} respectively. Surprisingly, large background rates of greater than 10 kHz were also observed for when MARS was tuned for the ^{64}Ga 30+ and 26+ charge states. This background was later determined to be from ^{32}S^{15+} and

$^{32}S^{13+}$, which are charge-to-mass analogs of the ^{64}Ga 30+ and 26+ charge states and are not easily separated with MARS. The source of the ^{32}S background beam is also unknown.

No $^{64}Ga^{31+}$ was observed even after a measurement of one hour. However, due to the low beam energy, populating the "fully-stripped" charge state of ^{64}Ga was unlikely (~1%) according to the LISE++ charge state models [5].

In future measurements, the following changes are envisioned. First, planned improvements to the LIG and the CBECR will produce a higher rate of ^{64}Ga ions, making them easier to separate from the other background beams. Second, a ΔE detector with better resolution for mass-64 separation will be installed such that ^{64}Ga can be better resolved from the ^{64}Zn that comes with it. Finally, a thick Aluminum degrader/stripper foil about 50.8 microns thick will be used in place of the carbon stripper foil. This thicker foil will separate ^{64}Ga from ^{64}Zn in energy and magnetic rigidity, making it possible to tune them separately to the detector chamber of MARS. The planned measurements will be conducted in the coming year when the improvements to the LIG and CB-ECR have been implemented.

In conclusion, re-acceleration of $^{64}Zn^{12+}$ and $^{64}Ga^{12+}$ ions from the LIG and CB-ECR has been attempted. A peak from $^{64}Zn^{29+}$ ions, obtained after passing the beam through a stripper-foil, was observed confirming that the tune of the K500 cyclotron, the beam-line optics, and MARS was correct. A small shoulder peak, perhaps arising from $^{64}Ga^{29+}$ ions, was also observed in one experiment run. Beam contamination from higher intensities of ^{48}Ti, ^{64}Ni, and ^{32}S were also present in the re-accelerated beam, independent of if the K150 proton beam was on or off. The possible observation of the ^{64}Ga ions represents the first re-accelerated radioactive ions from the LIG and the CB-ECR. However, further experiments with higher injected ^{64}Ga intensities and higher resolution detector systems should be conducted in order to confirm these results.

[1] B.T. Roeder *et al.*, *Progress in Research*, Cyclotron Institute, Texas A&M University (2015-2016), p. IV-16; http://cyclotron.tamu.edu/progress-reports/2015-2016/SECTION IV.html.

[2] R.E. Tribble, R.H. Burch, and C.A. Gagliardi, Nucl. Instrum. Methods Phys. Res. **A285**, 441 (1989).

[3] B.T. Roeder *et al.*, *Progress in Research*, Cyclotron Institute, Texas A&M University (2013-2014), p. IV-40; http://cyclotron.tamu.edu/progress-reports/2013-2014/SECTION IV.html.

[4] H.L. Clark *et al.*, *Progress in Research*, Cyclotron Institute, Texas A&M University (2014-2015), p. IV-15;http://cyclotron.tamu.edu/progress-reports/2014-2015/SECTION IV.html.

[5] O.B. Tarasov and D. Bazin, Nucl. Instrum. Methods Phys. Res. **B266**, 4657 (2008).

Cyclotron computing

R. Burch, S. Wuenschel, and K. Hagel

Cyclotron Institute research programs require stable, fast, and secure computational and network resources. This past year we transitioned our users to the University authentication and dynamic name service systems and added infrastructure to accommodate the lab's growing need for cpu power, storage, and network throughput.

In order to comply with University computer policy with the least possible effort on our part, we migrated our identity management from our local Kerberos authentication system to the University authentication system which uses the TAMU NetID as the username. This allows us a single username/password combination for University services and our local computational services as well as local Window's PC authentication via the TAMU Open Access Continuum Domain systems. Importantly, all University requirements for identity management are satisfied with no intervention or effort from the computer group at the Cyclotron Institute. We are in the process of migrating administrative servers and identifying a methodology to migrate Macintosh users to use NetID authentication as well.

Given the ever increasing level of malicious attacks and software events of interest, we are implementing an ElasticSearch based log monitoring system which allows us to monitor, analyze, and display log data in real-time graphically and to drill down to view the events of interest. We collect log data from all Linux servers, sending them to the central log servers and we are investigating methodologies to send Macintosh and Windows logs to the central log servers. ElasticSearch has been instrumental in demonstrating the extent to which our ssh gateway is under a constant brute force ssh attack having 200 to 300 failed attempts per day. It illuminates the importance of protecting our servers with a hardened ssh gateway and firewall. To further strengthen our security posture, we are configuring and installing an additional firewall that performs deep packet inspection to run in series with our current firewall.

Infrastructure enhancements in the past year included replacing all our old 3COM 100 mega bit network switches in the server room with new 1 giga bit switches. We added 10 giga bit switches to each server rack, linking them with a 10 giga bit backbone and added 10 giga bit network cards to all file servers enhancing data analysis network reliability and throughput. For the lab's general usage, we added a data file server with 12 disk slots, 3 slots populated with 11 terabytes of capacity. For one group with large data volume requirements, we added a similar server for their data as well as another one for their backups. We added a messaging board system based on a Raspberry Pi and a large screen TV to show lab announcements. We replaced our aging Dell PowerEdge web server that had a power consumption of 450 Watts with a more powerful ODROID-XU4 credit card form factor Linux server that has a power consumption of 20 Watts for about $150 and added to it two high speed USB 3 Flash drives for web storage and local backups.

Several more waveform digitizers were added to our data acquisition system. The software for reading the digitizers was enhanced and made more flexible as we have learned to use them. The critical enhancements had to do with learning how to handle the large buffers that result from reading in multiple long waveforms. In order to have the least impact on users with regards to backwards compatibility, we made the effort to implement the large buffers into our existing data analysis infrastructure. This was complicated by the fact that the raw data buffer had been designed long ago to have a maximum size of 64kB which is the maximum allowed for a 16 bit unsigned integer. It was therefore necessary to implement the option of splitting events across buffers. This was done with a very small impact on the users. The system was debugged and used extensively in a major run in the summer of 2016 in which the readout of the entire waveform was imperative. It was also used in a number of different experiments that, while the experiment could have been executed, would have had to severely curtail the information acquired from the important waveforms.

The preceding enhancements allowed us to utilize the capabilities of the waveform digitizers on an event by event basis. While we could handle the buffers from a software point of view, in fact various bandwidths made reading the long waveforms cause the data acquisition to become prohibitively slow. In fact, most of the events that were acquired did not require the information. We therefore developed software that allowed us to change both the triggering configuration as well as the length of the waveform "on the fly" when we detected an interesting event. Once the interesting information had been acquired, the triggering configuration as well as the length of the waveform read out was returned to the normal running status.

In summary, we have made changes in order to more fully comply with TAMU security policies, implemented an event monitoring system and made enhancements to our network bandwidth. We also implemented several changes to the data acquisition system to fully utilize the power to the waveform digitizers that are being deployed in more and more experiments.

MARS status report for 2016-2017: tuning of rare isotope beams of ^{14}O, ^{10}C, ^{42}Ti, and ^{31}Cl

B.T. Roeder and A. Saastamoinen

This year, we continued the program of providing rare isotope beams for the physics program at the Cyclotron Institute at Texas A&M University with the Momentum Achromat Recoil Separator (MARS) [1]. ^{14}O, ^{23}Si and ^{22}Si beams were provided to outside collaborations. The description of the production of ^{23}Si and ^{22}Si was provided in last year's progress report [2]. The ^{10}C and ^{42}Ti beams were provided to Dr. Hardy's research group for their continuing studies of super-allowed β-decay. A low energy ^{10}C beam at 3.3 MeV/u was also prepared for a planned future experiment with Dr. Rogachev's research group. Finally, a ^{31}Cl beam was made for Dr. Tribble's group for their continuing studies of β-delayed proton decay with the Astrobox2 detector.

^{14}O beam production for the WASHU group

The ^{14}O rare isotope beam has been produced many times with MARS with either the p(^{14}N,^{14}O)n or p(^{15}N,^{14}O)2n reactions. In the latest experiment, a group from Washington University in St. Louis (WASHU) was interested in studying the elastic scattering of ^{14}O with protons in inverse kinematics at two beam energies. For the higher energy case, ^{14}N at 30 MeV/u bombarded the MARS gas target filled with 2 atm of H_2 gas at 77K. This produced the ^{14}O beam secondary beam via a direct transfer reaction with a magnetic rigidity of 1.35 T·m and an energy of 28.3 MeV/u. In this reaction, ^{14}O was produced at a rate of 198 eV/nC with the MARS momentum slits at ± 0.4 cm, which corresponds to a momentum spread of the secondary beam of $\Delta P/P \approx 0.5\%$. This setup gave about $2.7\cdot10^4$ particles/sec ^{14}O for the experiment. About 11% of the rate secondary beam came from ^{7}Be, which has the same charge-to-mass ratio as the ^{14}O and thus could not be separated.

For the lower energy case, ^{14}N at 18 MeV/u bombarded the MARS gas target filled with 2 atm of H_2 gas at 77K. This produced a ^{14}O beam secondary beam via a direct transfer reaction with a magnetic rigidity of 0.999 T·m and an energy of 15.6 MeV/u. In this reaction, ^{14}O was produced at a rate of 100 eV/nC with the MARS momentum slits at ± 0.4 cm, which corresponds to a momentum spread of the secondary beam of $\Delta P/P \approx 0.5\%$. This setup gave about $1\cdot10^4$ particles/sec ^{14}O for the experiment. About 25% of the secondary-beam rate came from ^{7}Be, which has the same charge-to-mass ratio as the ^{14}O and thus could not be separated.

It has been observed during the analysis of the above data that it was possible to obtain a good focus in "X" and "Y" at the target position. The beam spot size was about 4mm in diameter. However, the beam needed to be re-focused strongly to obtain this beam spot size, resulting in a X-divergence of about 40 mrad. Calculations with the MARS LISE++ model [3] are being carried out to attempt to make the beam more parallel in future experiments.

Production of ^{10}C and ^{42}Ti for super-allowed β-decay studies

The ^{10}C rare isotope beam has been produced many times with MARS with either the p(^{10}B,^{10}C)n or p(^{11}B,^{10}C)2n reactions. In the latest experiment, Dr. Hardy's research group planned to obtain a high precision measurement of the branching ratio for the super-allowed β-decay of ^{10}C. Thus, they needed to have ^{10}C provided at the highest production rate possible, but also at sufficiently high enough energy to implant the ^{10}C into their tape transport system. With the p(^{10}B,^{10}C)n reaction at 17.2 MeV/u, we obtained 1500 eV/nC of ^{10}C with the MARS momentum slits at ± 1.5 cm, which corresponds to a momentum spread of the secondary beam of $\Delta P/P \approx 1.8\%$. The beam was easily separated from other reaction products and was thus 100% pure. Considering the production rate and the amount of primary beam available, about $2{\cdot}10^5$ p/s of ^{10}C was available for the experiment at this energy.

^{42}Ti was also produced [4] again this year in order to obtain a high precision measurement of its half-life. With the ^{4}He(^{40}Ca,^{42}Ti)2n reaction at 32 MeV/u, we obtained 5 eV/nC of ^{42}Ti with the MARS momentum slits at ± 0.5 cm, which corresponds to a momentum spread of the secondary beam of $\Delta P/P \approx 0.6\%$. The final energy of the ^{42}Ti was 26.6 MeV/u. In the latest experiment, it was found to be extremely important to remove, as much as possible, the ^{41}Sc and ^{39}Ca components of the beam. This was accomplished by adjusting the bottom slit #4 of MARS and the D3 dipole such that the majority of the ^{42}Ti was still passing into the tape, but the ^{39}Ca and ^{41}Sc had been reduced to less than 1% of the total intensity of the ^{42}Ti. The optimized ^{42}Ti tune for the latest experiment is shown in Fig. 1.

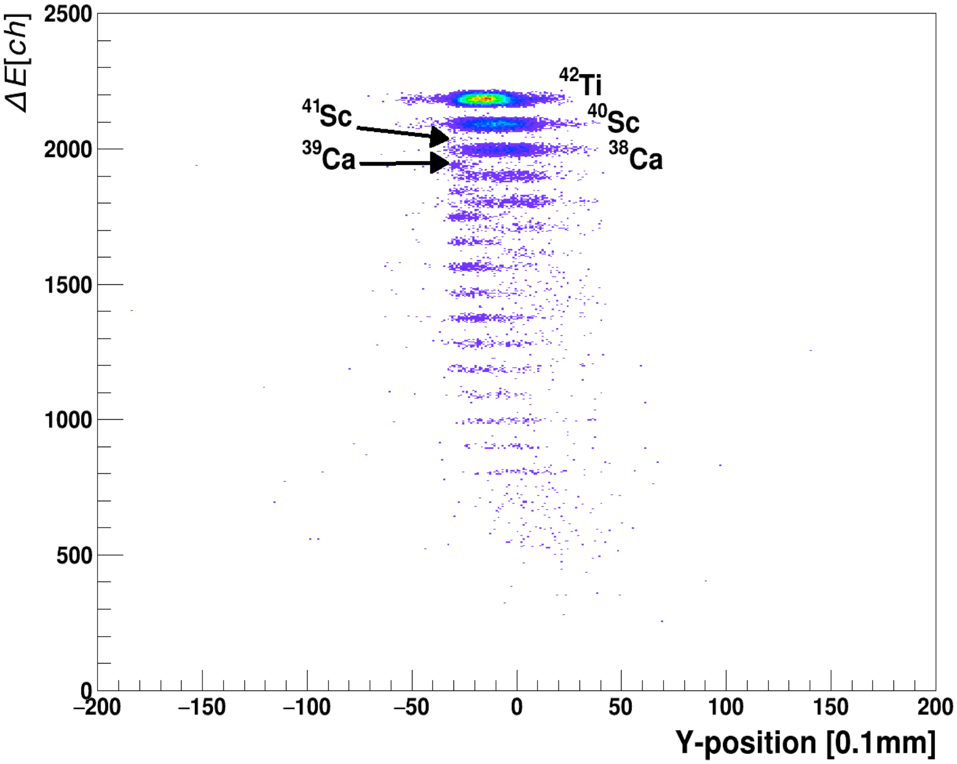

FIG. 1. Result of the ^{42}Ti beam tune. The contributions of the ^{41}Sc and ^{39}Ca contaminants are less than 1% of the total beam.

Production of low energy ^{10}C beam

^{10}C beam at low energy has also been developed for future experiments that are planned with Dr. Rogachev's research group. In this case, the p(^{10}B,^{10}C)n with ^{10}B beam at 7.0 MeV/u from the K150 cyclotron was used. The ^{10}B beam bombarded the MARS gas target filled with 1 atm of H_2 gas at 77K. During the test run, ^{10}C was produced at a rate of 61.5 eV/nC at an energy of 3.3 MeV/u. With this result, a low energy ^{10}C beam with an intensity of 10^4 p/s should be feasible.

Production of ^{31}Cl for the Astrobox2 experiment

The ^{31}Cl rare isotope beam has been produced many times with MARS via the p(^{32}S,^{31}Cl)2n reaction. In the latest experiment, ^{32}S at 40 MeV/u from the K500 cyclotron was used. The ^{32}S beam bombarded the MARS gas target filled with about 2 atm of H_2 gas at 77K. During the experiment, ^{31}Cl was produced at a rate of 3.2 eV/nC with the MARS coffin slits at ± 0.5 cm and at an energy of 35.4 MeV/u. The main contaminant of the beam was ^{28}P, which composed about 17% of the intensity of the secondary beam mixture. Once the beam was implanted into Astrobox2, a nearly pure sample of ^{31}Cl was obtained. A more detailed explanation of the ^{31}Cl experiment can be found in a separate report [5].

[1] R.E. Tribble, R.H. Burch, and C.A. Gagliardi, Nucl. Instrum. and Meth. A **285** (1989) 441.

[2] B.T. Roeder *et al.*, *Progress in Research*, Cyclotron Institute, Texas A&M University (2015-2016), p. IV-21; http://cyclotron.tamu.edu/progress-reports/2015-2016/SECTION IV.html.

[3] B.T. Roeder *et al.*, *Progress in Research*, Cyclotron Institute, Texas A&M University (2013-2014), p. IV-40; http://cyclotron.tamu.edu/progress-reports/2013-2014/SECTION IV.html.

[4] B.T. Roeder *et al.*, *Progress in Research*, Cyclotron Institute, Texas A&M University (2013-2014), p. I-48; http://cyclotron.tamu.edu/progress-reports/2013-2014/SECTION I.html.

[5] A. Saastamoinen *et al.*, *Progress in Research*, Cyclotron Institute, Texas A&M University (2016-2017), p.I-45;http://cyclotron.tamu.edu/progress-reports/2016-2017/SECTION I.html.

^{35}K test run

R. Chyzh, A. Saastamoinen, B. Roeder, and R.E. Tribble

One the most important questions that nuclear physics is trying to address is the origin and abundance of the elements in the universe. Proton-gamma capture reactions, X(p, γ)Y, play an important role in the creation of elements in processes like X-ray bursts or novae explosions [1-3]. The main focus of this work is the reaction ^{34g,m}Cl(p,γ)^{35}Ar. In novae, production of ^{34}S depends on the amount of ^{34}Cl which β-decays into ^{34}S with a half-life $T_{1/2}$=1.5266 s. Sulfur isotopic ratios can be used for classification of presolar grains which can be found in the meteorites. One way to destroy ^{34}Cl is the reaction ^{34g,m}Cl(p,γ)^{35}Ar. The rate of this reaction will eventually determine how much ^{34}Cl will be left for the creation of ^{34}S. To be able to accurately predict the reaction rate of ^{34}Cl(p,γ)^{35}Ar, one needs to know the resonances in ^{35}Ar, including their energy, spin-parity, and proton width. We chose to study this reaction

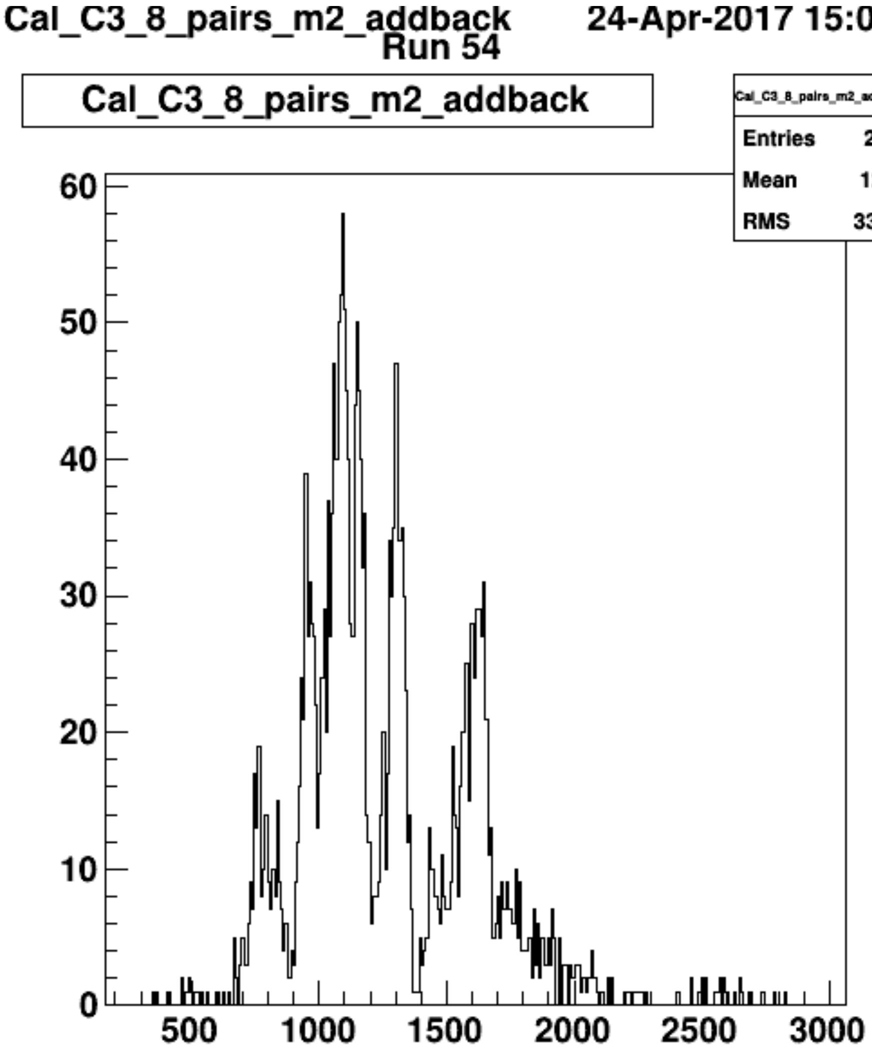

FIG. 1. A proton spectrum obtained in the AstroBoxII following β-decay of ^{35}K.

by means of an indirect method where we populate states in ^{35}Ar just above proton threshold S_p and observe them decaying into the ground level of ^{34}Cl + proton. Therefore detection of low energy protons becomes a challenge. The AstroBoxII was built to address this problem [4] [6]. To test our system, an experiment was conducted in March 2017. A beam of ^{36}Ar at 36 MeV/u was obtained from the K500 cyclotron. In the target chamber of MARS [5] an H_2 gas target was used. Through the reaction ^{1}H(^{36}Ar,^{35}K)2n we created a secondary beam of ^{35}K was made and then implanted into the AstroBoxII. After doing gain matching for the AstroBoxII anode pads, two HPGe detectors were calibrated with ^{137}Cs and ^{152}Eu sources. The estimated production rate for ^{35}K was 2.77 event/nC. An Al degrader (13 mil) on a rotary mechanism was used to control the position for the implantation of ^{35}K in the AstroBoxII. Due to a number of technical issues the beam time was very limited with only about 6 hours of data available. Nonetheless a proton spectrum was obtained (Fig 1.) and it is in good agreement with a similar spectrum that was obtained in 2014, but with the silicon detectors instead of the AstroBoxII.

[1] J. Jose and C. Iliadis Rep. Prog. **74**, 096901 (2011).

[2] J. Jose and M. Hernanz Eur. Phys. J. A **27**, Supplement 1, 107 (2006).

[3] J. Jose, M. Hernanz, and C. Iliadis Nucl. Phys. **A777**, 550 (2006).

[4] A.Saastamoinen *et al.*, Nucl. Instrum. Methods Phys. Res. **A376**, 357 (2016).

[5] R.E. Tribble, R.H. Burch, and C.A. Gagliardi, Nucl. Instrum. Methods Phys. Res. **A285**, 441 (1989).

[6] A.Saastamoinen *et al.*, *Progress in Research*, Cyclotron Institute, Texas A&M Univerisity (2014-2015) p. IV-33; R. Chyzh *et al.*, *Progress in Research*, Cyclotron Institute, Texas A&M Univerisity (2015-2016) p. IV-35.

Beta decay of ^{22,23}Si studied at MARS with the optical time projection chamber

C. Mazzocchi,[1] A.A. Ciemny,[1] W. Dominik,[1] A. Fijałkowska,[2] J. Hooker,[3] K. Hunt,[3]
H. Jayatissa,[3] Ł. Janiak,[1] G. Kamiński,[4] Y. Koshchiy,[3] M. Pfützner,[1] M. Pomorski,[1]
B. Roeder,[3] G. Rogachev,[3] A. Saastamoinen,[3] S. Sharma,[1] and N. Sokołowska[1]
[1]*Faculty of Physics, University of Warsaw, Warsaw, Poland*
[2]*Rutgers University*
[3]*Cyclotron Institute, Texas A&M University, College Station, Texas*
[4]*JINR Dubna, Russia*

A characteristic feature of exotic nuclei at (or very close to) the proton drip-line is the large Q-value window available in beta decay, which opens the possibility to populate highly excited, and (multi) particle unbound, states in the daughter nucleus. As a consequence, beta decay can be followed by emission of (multiple-) protons. Beta-delayed particle spectroscopy becomes therefore a very powerful tool to investigate the structure of such exotic nuclei. It has been demonstrated, e.g. that beta-delayed multi-proton emission of very exotic nuclei can be used to probe the beta-decay strength [1-3] in the high-energy end of the Q-value window, where the excited states are particle unbound.

In this context, the beta-decay of ^{22,23}Si was investigated in an experiment performed in early March 2017 at the focal plane of the MARS spectrometer at the Cyclotron Institute of Texas A&M University, looking for so-far unobserved decay channels of these two very exotic isotopes. They are known to decay via beta-delayed one and two proton emission [4,5], mostly through the IAS in ^{23}Al, but the beta-delayed three proton decay channel, as well as the delayed alpha-proton and the new ^{3}He channels, are opened. Decay through other states than IAS was not observed, nor the beta-delayed three proton branch. Previous measurements of such exotic nuclei with silicon-detector based arrays allowed the measurement only of the higher-energy part of the delayed-proton spectrum, with the consequence that the previously measured branching ratio for (multi-) proton emission in this region very often need to be (re)measured and corrected.

The ^{22,23}Si ions were produced in the reactions of a ^{28}Si beam at 45 A·MeV with a 150 μm-thick Ni target, separated from the unwanted reaction products by using the MARS separator (see Fig. 1) and implanted into the Optical Time Projection Chamber (OTPC) [6], which was installed at the MARS focal plane (see Fig. 2). Incoming ions as well as their charged decay products created ionization electrons along their trajectories in the gas filling the active volume of the chamber. These electrons were transported by the electric field towards a charge-amplification structure. The amplification structure is formed by a set of four gas electron multiplier (GEM) foils with the charge collecting wire–mesh electrode behind. Photons emitted during charge amplification in the last GEM and in the charge collection process were recorded by a sensitive CCD camera (exposition time 150 ms) and two photomultipliers (PMT). The latter were read out by fast oscilloscopes, providing the time distribution of the light emitted in the chamber.

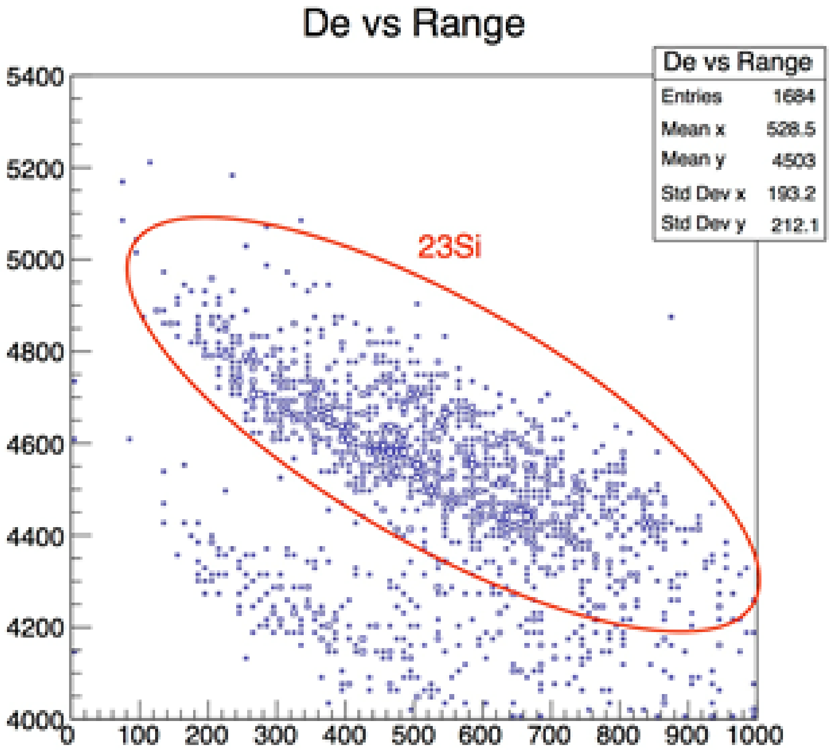

FIG. 1. Identification plot Energy Loss (DE – ordinate, arb. units) versus Range in the OTPC (abscissa, arb. units) for ions reaching the chamber active volume in the setting of the MARS spectrometer optimized for transmission of ^{23}Si.

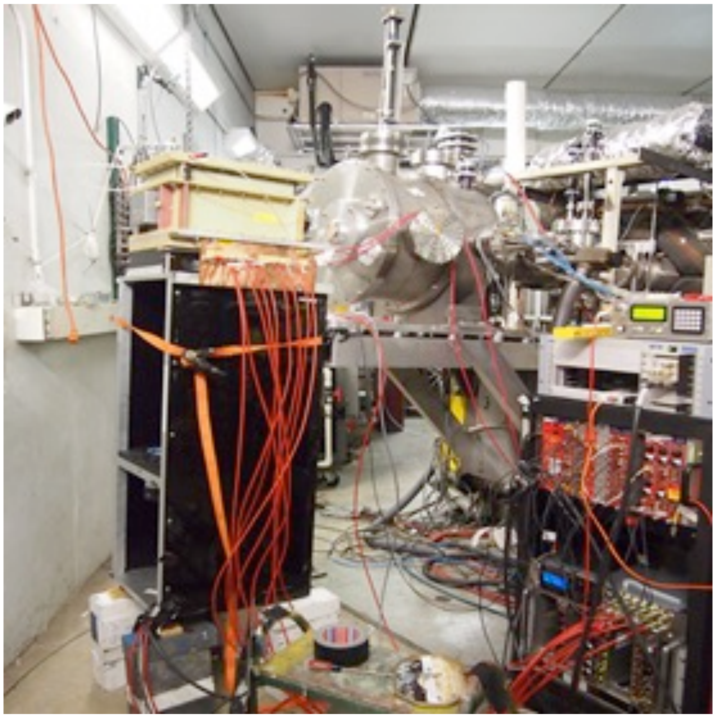

FIG. 2. The OTPC detector installed at the focal plane of MARS.

During one week of beam-on-target, several thousands of ^{23}Si ($T_{1/2}$ = 42 ms) and several hundreds of ^{22}Si ions ($T_{1/2}$ = 29 ms) were implanted into the OTPC and their decay studied. In Fig. 3, an example of the CCD image for the decay of ^{23}Si by beta-delayed two-proton emission is shown. The ion is implanted into the active volume of the chamber and it subsequently decays (about 35 ms after implantation) emitting the two protons. The detector is blind to beta particles. The data are being analyzed to reconstruct the proton spectra and looking for exotic (and hitherto unobserved) decay branches.

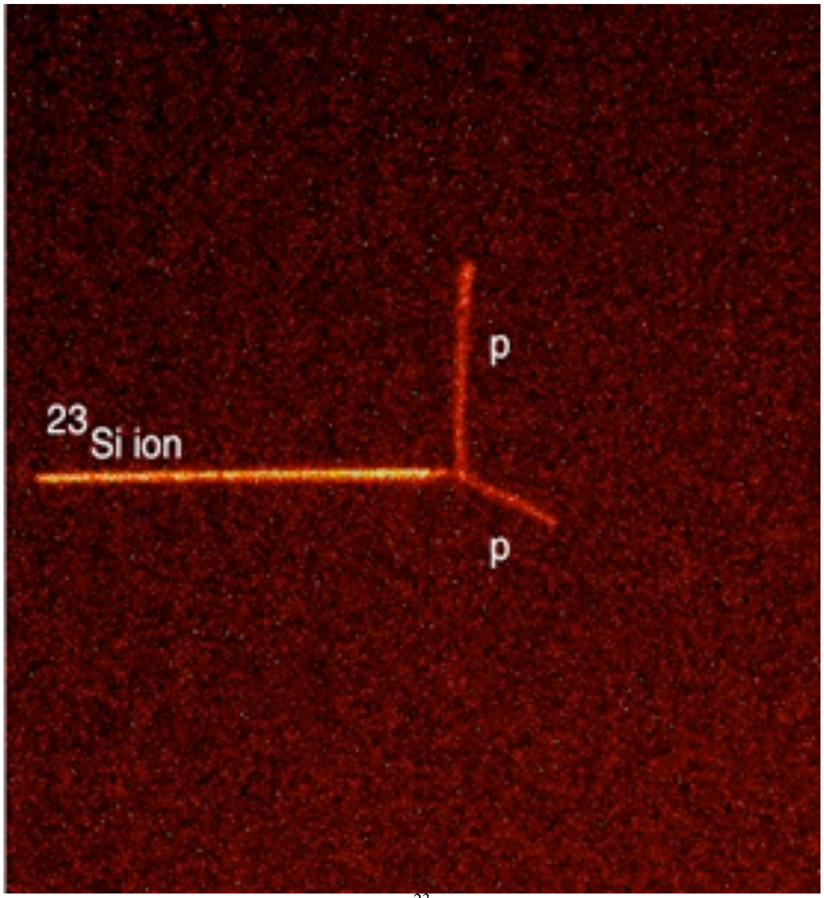

FIG. 3. Example of a decay event of ^{23}Si by beta-delayed two-proton emission as seen by the CCD camera of the OTPC.

[1] G.T. Koldste *et al.*, Phys. lett. B **73**7, 383 (2014).
[2] L. Axelsson *et al.*, Nucl. Phys. **A63**4, 475 (1998).
[3] H.O.U. Fynbo *et al.*, Nucl. Phys. **A677**, 38 (2000).
[4] B. Blank *et al.*, Z. Phys. A **357**, 247 (1997).
[5] X.X. Xu et al., Phys. Lett. B **766**, 312 (2017.
[6 M. Pomorski *et al.*, Phys. Rev. C **90**, 014311 (2014).

Gamma efficiency measurements for the AstroBoxII with two HPGe detectors

R. Chyzh, A. Saastamoinen, and R.E. Tribble

Proton-gamma capture reactions, X(p, γ)Y, play an important role in stellar environments like X-ray bursts or novae [1-3]. Reactions like ^{22}Na(p, γ)^{23}Mg, ^{12}C(p,γ)^{13}N(β^+)^{13}C, and ^{16}O(p, γ)^{17}F(β^+)^{17}O are particularly important in the novae explosions [1-3]. These reactions are characterized by the location and the strength of proton resonances. Many of the important resonances lie just above the proton separation threshold S_p and they can be studied by indirect methods such as proton decay after a β-decay. In this case we populate the important states by means of β-decay. This will necessarily bring a problem of dealing with β-background. The AstroBoxII was specially designed for this purpose and it allows to reduce β-background dramatically and opens up an opportunity to measure proton energies of just a few hundred keV [4] [6]. It is a new detector that is an improvement over the original AstroBox[5]. While measuring low proton energy is the main task for the AstroBoxII, doing gamma spectroscopy helps to answer some important questions about the studied resonances. If we have a state that lies above S_p that can undergo proton decay, it is important to know whether or not this state decays directly to the ground state or to some excited state, which in turn de-excites by emitting gamma rays. By doing proton and gamma measurements in coincidence we can reliably answer that question. The gamma efficiency is needed to determine if the amount of observed coincident protons and gammas agree. Another important problem that can be addressed by doing gamma spectroscopy is answering a question about branching ratios of the resonances that lie just above S_p. A state can decay either by proton emission or gamma emission. To tell how much gamma emission there is relative to proton emission we need to know the efficiency of gamma detection. For this purpose we used two gamma sources: ^{137}Cs with a single gamma line at 661.7 keV,

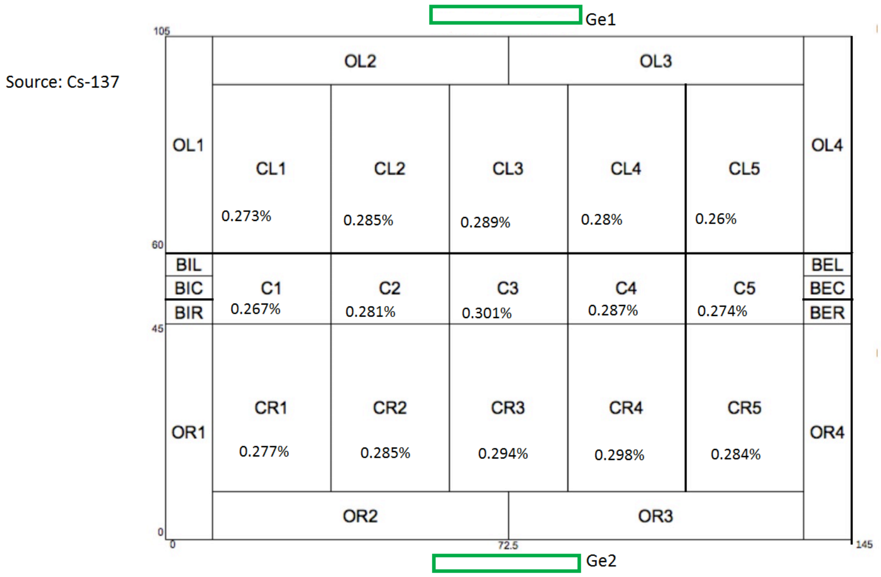

FIG. 1. Gamma efficiency distribution for different pads in the AstroBoxII.

primarily for the efficiency measurements for every pad in the AstroBoxII and ^{152}Eu for efficiency versus energy measurements.

The results for ^{137}Cs are presented in the Fig 1. Two HPGe detectors were placed on the left and on the right side along the beam axis as close to the AstroBoxII as possible. The source (^{137}Cs) was hung on a string that was attached to each individual pad. In each pad we see the combined efficiency from both HPGe detectors. As expected we get the highest efficiency (around 0.3%) in the central pads.

After that we repeated the same measurement with a ^{152}Eu source. Using multiple gamma lines from the source we obtained efficiency curve for the central pad C3.

In Fig 2. it is clear that the efficiency of the gamma detection for the HPGe detectors falls exponentially with energy. Also it is worth mentioning that one the HPGe detectors (Ge2) displayed a little bit better efficiency than the other (Ge1). That can be partially explained by the fact that the positioning of the two detectors relative to the AstroBoxII is not exactly the same.

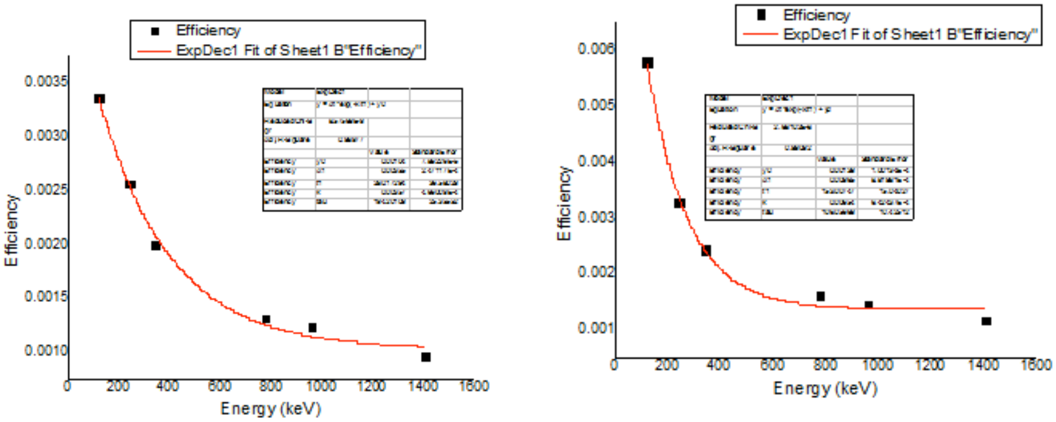

FIG. 2. Efficiency curves for the first (on the left) and the second (on the right) HPGe detectors.

[1] J. Jose and C. Iliadis Rep. Prog. **74**, 096901 (2011).

[2] J. Jose and M. Hernanz Eur. Phys. J. A **27**, Supplement 1, 107 (2006).

[3] J. Jose, M. Hernanz, and C. Iliadis Nucl. Phys. **A777**, 550 (2006).

[4] A.Saastamoinen *et al.*, Nucl. Instrum. Methods Phys. Res. **A376**, 357 (2016).

[5] E. Pollacco *et al.*, Nucl. Instrum. Methods Phys. Res. **A723**, 102 (2013).

[6] A.Saastamoinen *et al.*, *Progress in Research*, Cyclotron Institute, Texas A&M Univeristy (2014-2015) p. IV-33; R. Chyzh *et al.*, *Progress in Research*, Cyclotron Institute, Texas A&M Univeristy (2015-2016) p. IV-35.

Sum-fit method of analysis of nuclear decay spectra affected by extending dead-time

V. Horvat and J.C. Hardy

We have developed a method of analysis of nuclear decay spectra affected by dead-time, in which a non-trivial, but relatively simple correction for dead-time losses is applied to produce an estimate of the spectrum in the absence of dead-time, with negligible bias and negligible deviation from the original Poissonian statistics. The method requires the measurement of arrival times of all observed decay events, but it does not require any knowledge about the dead-time or the nuclear decay. The parameters of nuclear decay can be determined in a subsequent straight-forward analysis of the estimated dead-time-free spectra, individually or in combinations. In a typical realistic situation this approach is expected to contribute 0.001% or less to the systematic error of nuclear half-life or activity. Compared to the exact method of analysis that we developed earlier [1], the present method is much easier to implement and produces the results significantly faster.

The key element in the analysis is the imposition of a known, sufficiently large extending dead-time to the observed sequence of events in order to produce a set of survived events for which the effects of the actual dead-time are completely obliterated by the effects of the imposed dead-time. As a result, the dead-time following each survived event and the live time preceding it are known exactly. The next step involves sorting the survived events into decay spectra, using a chosen channel width Δt.

For an infinitely long sequence of Poissonian events that starts at a known time and under known circumstances, a correction for the effects of an imposed dead-time may depend only on the nature of the dead-time and the product of the ideal rate ρ of the events (*i.e.,* the event rate in the absence of dead-time) and the imposed dead-time per event τ. However, if this sequence of events is limited to time (channel width) Δt, a correction for dead-time losses based exclusively on the information contained within the channel width may also depend on the dimensionless scaling parameter $\tau/\Delta t$.

Since the mathematical complexities associated with the effect of extending dead-time on time-binned Poissonian events are overwhelming [2], we chose to study the effects of dead-time correction using simulated events, with $\rho\tau$ ranging from 10^{-6} to 0.05 and $\tau/\Delta t$ ranging from 10^{-8} to 0.002. We found that a good estimate n_o of the number of original Poissonian events in each channel of a nuclear decay spectrum (that would be observed in the absence of dead-time) can be expressed as

$$n_o = \frac{\Delta t}{\tau} \ln\left(\frac{\Delta t}{t_{\mathrm{live}}}\right) \left[1 + a\,\tau/\Delta t + b \ln\left(\frac{\Delta t}{t_{\mathrm{live}}}\right) + c\,\frac{\tau}{\Delta t} \ln\left(\frac{\Delta t}{t_{\mathrm{live}}}\right)\right]^{-1} . \qquad (1)$$

where t_{live} is the live-time within the channel. The recommended values of parameters *a*, *b*, and *c* were found to be those given in Table 1. Eq.(1) shows that the live-time fractions $t_{\mathrm{live}}/\Delta t$ for each channel are the ultimate channel-specific parameters that define the decay spectra. The actual numbers of survived events in each channel are not needed.

To demonstrate the effectiveness of Eq.(1), we applied it to the most critical of the cases considered: the one with the largest values of $\tau/\Delta t$ (*i.e.*, 0.002) and $\rho\tau$ (*i.e.*, 0.05). Specifically, for an ideal

Table I. Recommended values of the parameters in Eq.(1). The parentheses enclose the umcertainty of the last significant figure.

Parameter	Value
a	0.5004(1)
b	$1.1(1)\cdot 10^{-4}$
c	0.17(1)

rate of 10 s^{-1}, this would imply $\tau = 5$ ms and $\Delta t = 2.5$ s. The resulting distributions of the numbers of events per channel are shown in Fig.1.

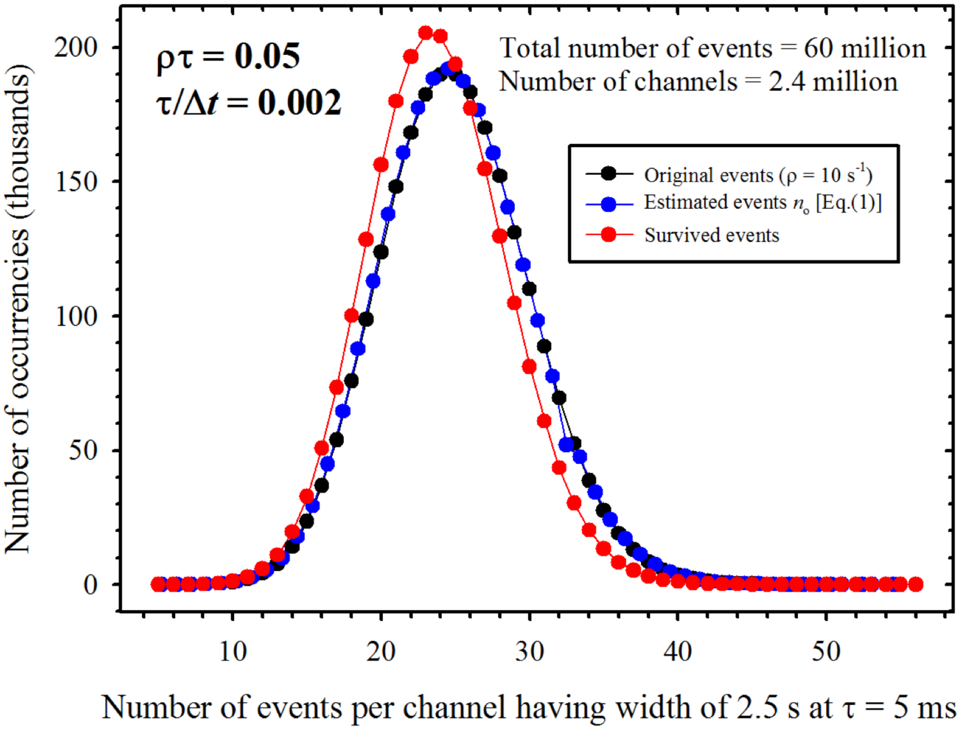

FIG. 1. Distribution of the actual number of events per channel (black); the number of events that survived after the dead-time was imposed (red); and the number of events deduced using Eq.(1) from the known channel live-time fractions (blue). Note that the ordinate of each blue data point corresponds to the number of occurrences of non-integer values that have the same integer part, while its corresponding abscissa is the (non-integer) average of those values. The small dip at an abscissa of about 33 is a consequence of the fact that the corrected numbers of counts are non-integers (shifted up from their integer parts) and are likely to be clustered around a relatively narrow range of typical values. A dip may be expected as this distribution starts to shift and/or broaden enough to extend over the next integer value (or further on). Error bars of the data points cannot be seen because they are smaller than the symbols used. The lines connecting the data points are there only to guide the eye.

Evidently, the distribution of the number of events deduced from the known channel live-time fractions (shown in blue) matches very well the Poissonian distribution of the actual numbers of events per channel (shown in black) before the dead-time was imposed. For the case shown, the former distribution has its mean within 0.02% of the expected value of 25 (which is within the range expected for a 60-million-event statistics), and the ratio of its actual variance to the expected mean value is within only 1.7% of unity, which is not expected to significantly affect the results in the analysis of the dead-time-corrected spectra. Because the number of events lost due to dead-time is larger when the original number of events is larger, the distribution of the actual number of survived events (shown in red) is narrower than the other two distributions and its mean is lower.

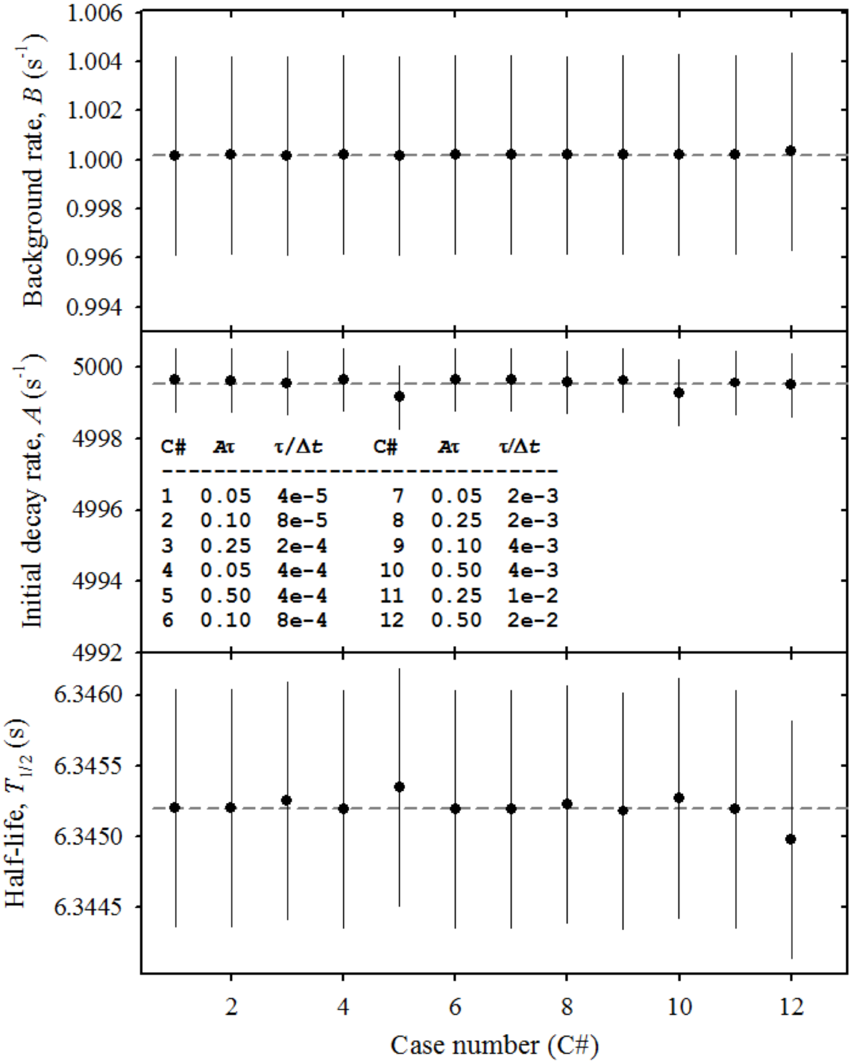

C#	Aτ	τ/Δt	C#	Aτ	τ/Δt
1	0.05	4e-5	7	0.05	2e-3
2	0.10	8e-5	8	0.25	2e-3
3	0.25	2e-4	9	0.10	4e-3
4	0.05	4e-4	10	0.50	4e-3
5	0.50	4e-4	11	0.25	1e-2
6	0.10	8e-4	12	0.50	2e-2

FIG. 2. Effects of using Eq.(1) for dead-time correction of the decay spectra on the results of a measurement of ^{26m}Al half-life. The events used were simulated, using $T_{1/2}$ = 6.3452 s for the half-life of ^{26m}Al, an assumed constant background event-rate of B = 1 s^{-1}, and an initial true decay rate of A = 5000 s^{-1}. The imposed extending dead-time per event τ was 10 µs , 20 µs, 50 µs, and 100 µs, while the channel width Δt was 5 ms, 25 ms, and 250 ms. All combinations of τ and Δt were used and numbered according to the table shown above. There were 1320 samples with duration of 125 s each, containing a total of about 60 million events. The dashed lines are there only to guide the eye.

The final demonstration of the effectiveness of Eq.(1) along with the values of *a*, *b*, and *c* from Table 1 is given in Fig. 2, which shows the effects of using Eq.(1) for dead-time correction of the decay spectra on the results of a typical measurement of nuclear half-life, such as that of ^{26m}Al. The events used were simulated. The same dead-time-free set of events was used in all the cases. Evidently, the use of Eq.(1) for dead-time correction of the decay spectra reproduces the expected results consistently and accurately within the region of its proven validity and somewhat beyond.

[1] V. Horvat and J.C. Hardy, Nuclear Instrum. Methods Phys. Res. **A713,** 19 (2013).
[2] W. Muller, Nucl. Instrum. Methods **117,** 401 (1974).

Increasing effective coverage in FAUST LCP data from recent campaign

L. Heilborn, A. Jedele, C. Lawrence, A.B. McIntosh, A. Rodriguez Manso, A. Zarrella, and S.J. Yennello

Position-sensitive Dual-Axis Dual-Lateral (DADL) detectors in the Forward Array Using Silicon Technology (FAUST) allowed the recovery of data outside of the range of the ADC. These methods will be used in all subsequent data analysis to maximize the quality of data recorded. This analysis focuses on light charged particles (LCP). Cesium Iodide calibrations have also been completed for Z=1 and Z=2.

FAUST is comprised of sixty-eight ΔE-E telescopes arranged to provide coverage of particles emitted from quasiprojectiles (QP, the excited source resulting from heavy ion reactions) [1]. Each telescope consists of a 2x2 cm 300 μm thick DADL silicon diode backed by a CsI(Tl)-photodiode detector [2]. Described here are the new methods for calibration of data from the successful campaign with this position-sensitive upgrade. These CsI calibrations are themselves dependent upon successful particle identification (PID), which has been described previously [3]. The silicon energy signal has been corrected for its dependence upon the position of incident radiation across the face of the detector (Figure 1) and then calibrated to an energy (MeV) scale.

The data was taken with FAUST for reactions of 40 MeV/nucleon ^{40}Ar+^{58}Fe,^{70}Zn and ^{40}Ca+^{58}Ni at the Texas A&M Cyclotron Institute. A representative ΔE-E plot, derived from Si and CsI(Tl) signals

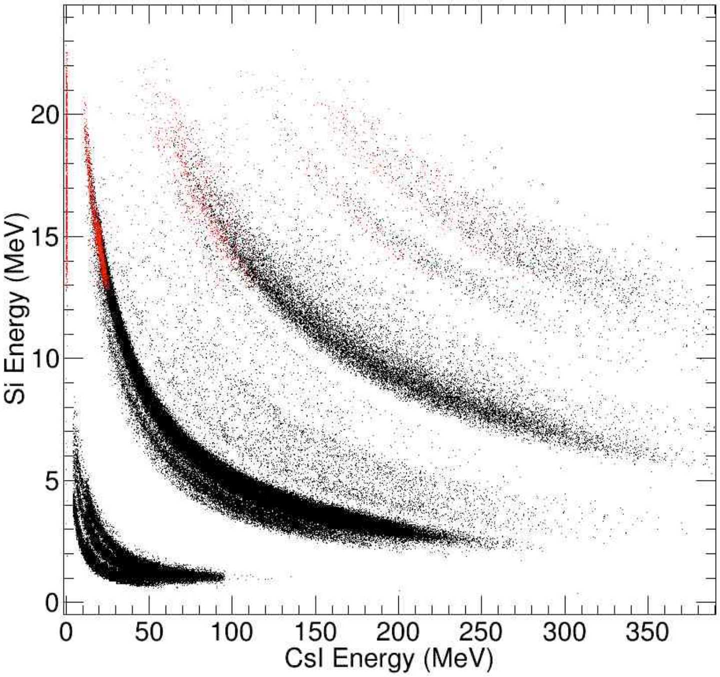

FIG. 1. Two-dimensional plot of dE-E with the calculated 'Missing Fourth' signal in red for detector 9. Low energy alpha particles were the bulk of the additional particles recovered in this experiment.

and demonstrating the excellent p-d-t differentiation for raw signals, is shown in Fig. 1.

The highest energy protons deposit the lowest amount of energy in the silicon detectors. Because the signals get split based upon the position of the incident ionizing radiation, these signals can be above or below the effective range of the ADC, depending upon the energy threshold and offset for at least one side, if it hits near the edge of the detector. Some of the four Si signals may be outside of the range of the ADC. The high-gain preamps ameliorate, but do not entirely eliminate this problem. The equivalence between the energy deposited in the front and back can be used to calculate the lost signal, which is called the "Missing Fourth". This is the method that was used to generate the red points on Fig. 1. It is clear that these calculated energies result in particles on the appropriate PID lines on the dE-E plot.

All LCPs have been identified for this data set. Protons and alphas were used to calibrate the CsI energy spectra in a particle-type dependent manner. Fig. 2 shows that the energy calibration is very different for the Z=1 (red points, pink line) and Z=2 (black points, red line). The point-down triangles are from the 10 MeV/nucleon p-alpha calibration beam. The calibration points fall nicely on top of the calibration fit. This is a typical fit for a representative CsI detector. The data set is particle identified and energy calibrated. (A preliminary position calibration is also complete.)

Proton-proton correlation functions will be extracted from this data set. Simulations are being run to compare correlation functions in momentum space calculated using different forms of the asymmetry energy to the experimental data. The shape and magnitude of the correlation function is predicted to be impacted by this form [4].

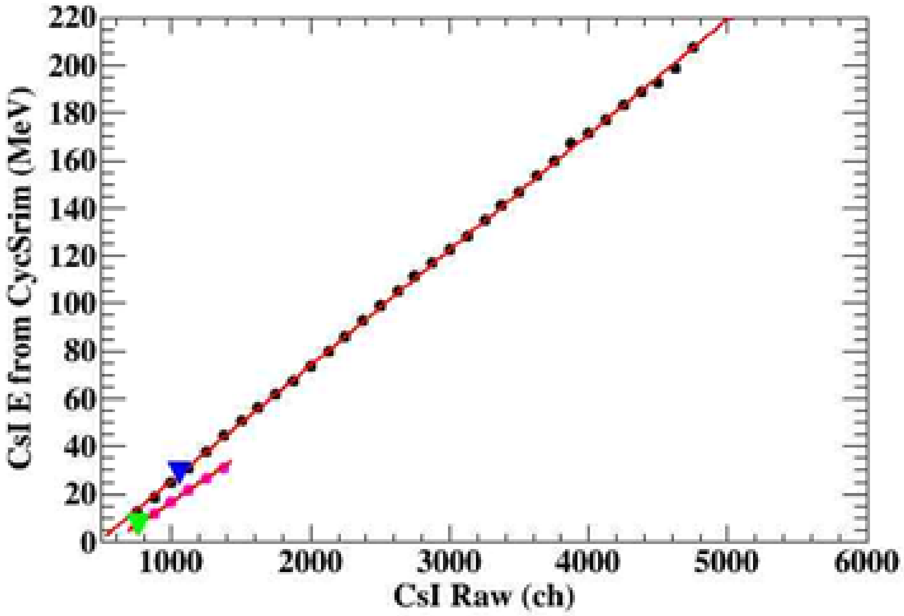

FIG. 2. Linear relationship between the CsI raw and the CsIE pulled from CycSrim for Detector 33. Shown for protons (pink points) and alphas (black points). The point-down triangles are two calibration beams, protons (green) and alphas (blue).

[1] F. Gimeno-Nogues, *et al.* Nucl. Instrum. Methods Phys. Res. **A399**, 94 (1997).
[2] S.N. Soisson, *et al.*, Nucl. Instrum. Methods Phys. Res. **A613**, 240 (2010).
[3] L. Heilborn, *Progress in Research*, Cyclotron Institute, Texas A&M University (2015-2016), p. IV-61.
[4] L.W. Chen, V. Greco, C.M. Ko, and B.A. Li, Phys. Rev. Lett. **90**, 162701 (2003).

Preparations of the TAMU-ORNL BaF2 array

A.B. McIntosh, J. Gauthier, K. Leeper, A. Rodriguez Manso,
L.A. Heilborn, A. Jedele, A. Zarrella, and S.J. Yennello

The TAMU-ORNL BaF_2 Array is comprised of 130 detector modules. Each has a hexagonal prism crystal of BaF_2 20 cm long and 6.5 cm from face to face. The crystal is coupled directly to a UV-sensitive photomultiplier tube (PMT). In preparation for upcoming experiments, the coupling between each crystal and its PMT has been remade. For much of the array, the energy resolution has been checked. The impact of the new coupling on the particle discrimination and the timing has been investigated on a few select detectors.

Previously, the coupling was made with viscous silicone oil ($1x10^5$ centistokes), which is translucent to UV light near 200nm. This transmission is important since the fast component of the scintillation light is primarily at 210nm. Each crystal and PMT is wrapped in polytetraflouroethylene (Teflon) tape to reflect light until it reaches the photocathode. Black electrical tape is then used to completely exclude external light from the detector. Over time, the silicone oil oozes from the coupling and wets the Teflon tape, turning it translucent and thus decreasing the light collection efficiency and therefore the resolution. It was desired to use a coupling that would last longer without sacrificing resolution and without losing the ability to decouple the detectors as needed (e.g. for PMT replacement).

Room-Temperature Vulcanization (RTV) silicone rubber was chosen as the coupling material. It can be made into a very thin layer and has optical transmission near 200nm, though in this region the transmission decreases rapidly with RTV thickness. After cleaning the crystal and PMT faces with anhydrous methanol, a small dab (approximately 0.3mL) of vacuum-degassed RTV (Momentive 615A+B) is applied to the PMT quartz window and allowed to rest a few minutes until flat and smooth. Any stray bubbles are removed, filled in with RTV and again allowed to rest. The PMT is inverted and mated with the crystal face; care is taken not to introduce bubbles. A jig is used to secure the PMT in place while the RTV sets for 5 days, after which time the Teflon tape and electrical tape are applied followed by the mu-metal shield and tension sling to complete assembly. The coupling of the crystal to PMT, which has a surface area of nearly $20cm^2$, can be safely broken by applying a heating tape at 90°C for one hour to the coupling and then twisting carefully. Decoupling is not trivial, but is possible to do without harming the brittle crystal.

Fig. 1 shows data obtained with a BaF_2 detector freshly coupled with RTV. Gamma sources provided peaks at 1173keV and 1332keV (^{60}Co) and 662keV (^{137}Cs). Alpha decay of radium impurities in the detector can also be seen. In the correlation of the fast component of the light output (20ns window around the peak) and the total light output (1.5μs), as seen in Fig. 1, the gamma rays (upper locus) can be distinguished from the charged particles (lower locus). Though the RTV may be attenuating the fast light by some amount [1], the thickness of the RTV layer (which is significantly less than 100μm) does not prevent pulse-shape discrimination. The quality of the neutral and charged band separation is comparable to that achieved with the viscous silicone oil coupling. The projection of the data in Fig. 1 onto the “total” axis is shown in Fig. 2. The lower peak (662keV) has a width (FWHM) of 14.8%.

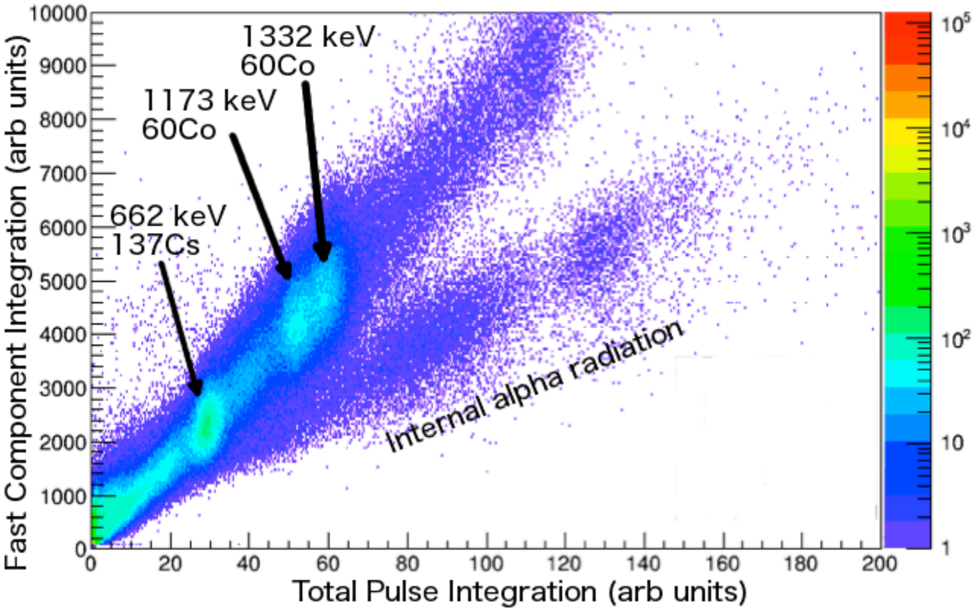

FIG. 1. Fast integral vs total integral for a BaF_2 detector recoupled with RTV. The separation of the gamma line (upper) and alpha line (lower) indicates that the RTV does not significantly attenuate the photons in the fast component.

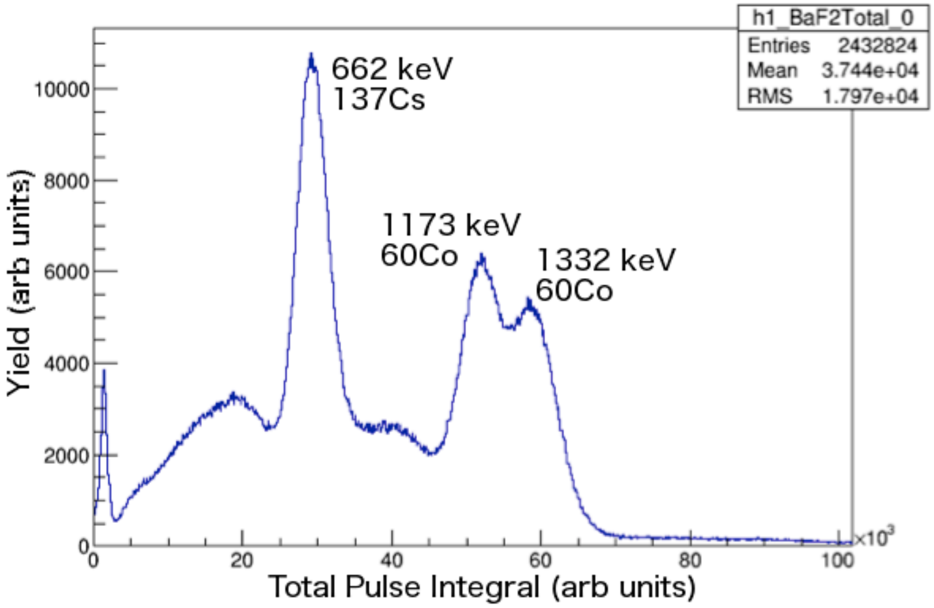

FIG. 2. Total integral after recoupling with RTV. The peaks are obtained using ^{60}Co and ^{137}Cs sources. The 662 keV peak shows resolution of 14.8%.

The resolutions of several detectors before and after recoupling were measured in the same way. Fig. 3 summarizes the results. Certainly, the resolution with the RTV is not worse than with the silicone oil. For a few detectors, the gamma sources were placed very close to the detector to increase the rate of the gammas of interest relative to the background. This improved the resolution slightly, indicating the importance of accurate background subtraction. The detector resolutions are generally between 15% and 20%. This is believed to be limited by the age of the PMTs. Likely with newer PMTs this could be brought down to 10-15%.

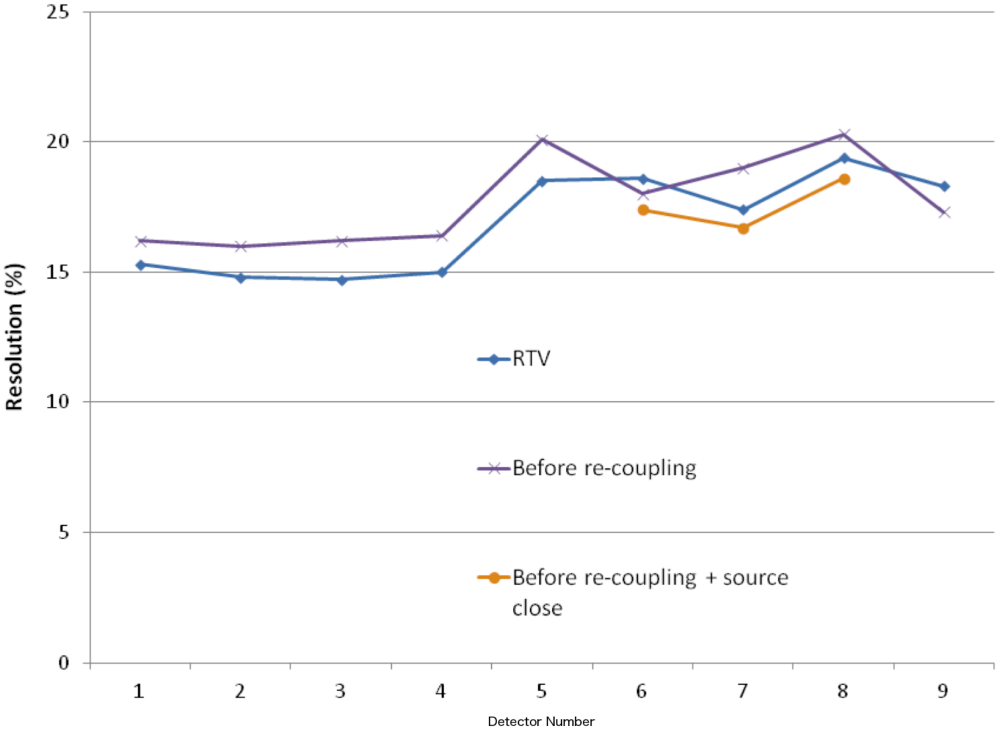

FIG. 3. Resolution of the 662 keV ^{137}Cs peak in nine different detectors before and after recoupling.

Timing resolution is important to discriminate gamma rays from neutrons and from low-energy charged particles. A ^{22}Na source, which produces pairs of photons from positron annihilation, was placed adjacent to two BaF$_2$ detectors. The anode signals were split and sent not only to flash digitizers (SIS3316) as before but also to discriminators (CAEN-V812) followed by time-to-digital converters (CAEN-V775). The time difference is shown in Fig. 4 with arbitrary offset. The width of the timing peak (FWHM) is 0.9ns, which is sufficient to discriminate high-energy neutrons (even beyond 100 MeV) from gamma rays for a flight path of 100cm. Tennelec TC454 CFDs and Philips 708 leading edge discriminators provided poorer resolutions (both 1.6ns FWHM).

The BaF$_2$ array is being prepared to serve in two upcoming experiments. One will measure gamma rays in reactions of ^{59}Fe(d,p)^{60}Fe. The neutron capture cross-section is important as a waiting point in s-process nucleosynthesis [2]. The other experiment will measure hard gamma rays produced in n-p Bremsstrahlung, which are predicted to be sensitive to the symmetry energy in the nuclear equation of state [3].

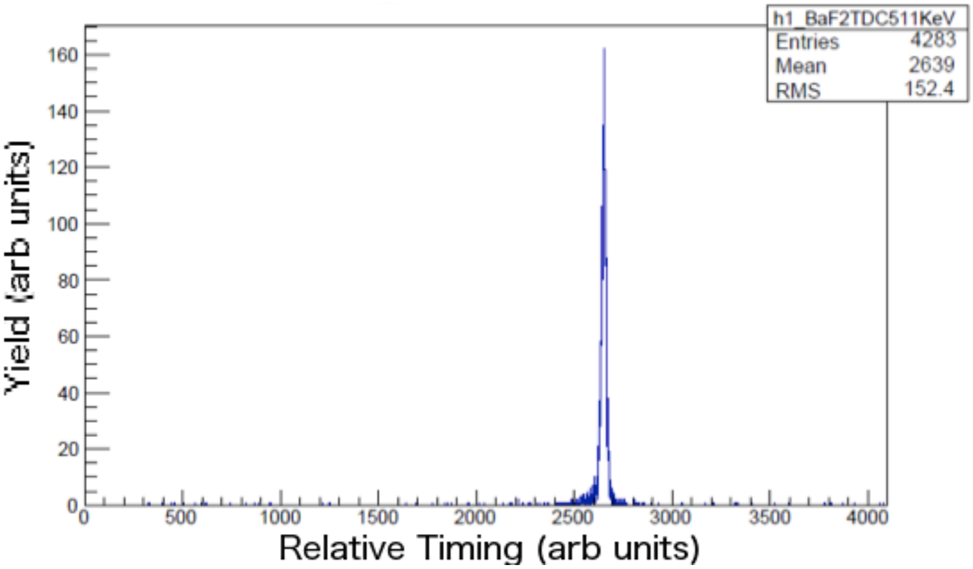

FIG. 4. Time resolution of a pair of positron annihilation photons detected in two BaF_2 modules after recoupling with RTV. The FWHM is 0.9ns. This demonstrates that the RTV does not prevent the fast light from being used for precision timing.

[1] W. Li and G.M. Huber, J. Inst. **9**, P07012 (2014).
[2] Uberseder *et al.*, Phys. Rev. Lett. **102**, 151101 (2009).
[3] Yong *et al.*, Phys. Lett. B **661**, 82 (2008).

Progress in the calibration Kr+C with FAUST-QTS

A.B. McIntosh, A. Keeler, J. Gauthier, L.A. Heilborn, A. Jedele,
A. Rodriguez Manso, A. Zarrella, and S.J. Yennello

Fusion-evaporation residues have for reactions of ^{78,86}Kr+C @ 15,25,35 MeV/nucleon been measured with the Quadrupole Triplet Spectrometer (QTS) in coincidence with the evaporated charged particles in the FAUST array. This report describes progress on the calibration of the data from FAUST. The calibration procedure for this data set is conceptually the same as that of Heilborn [1], and is similar in implementation.

In this experiment, the position-sensitive silicon detectors (DADLs) [2] of FAUST were used. The amplitude of the signals measured by them depends slightly (~5%) on the position of the detector. As a means of observing and correcting for this, data was taken with a ^{228}Th alpha source. Fig. 1 (left panel) shows the sum of the two front signals (F2+F1) from the DADL on detector 21 as a function of their difference (F2-F1). Since the alphas from the ^{228}Th are emitted at discrete and known energies, the data should fall on bands of constant energy (F2+F1). We parameterize the bands with parabolas. Though the curvature and linear coefficients of the parabolas are different for each band, they do vary nearly linearly with the constant coefficient (i.e. F2+F1). Thus the curvature and linear coefficient can be obtained for any arbitrary value of (F2+F1) and subtracted from the sum to obtain the corrected sum, which is shown in Fig. 1 (right panel) as a function of (F2-F1). Though there are exceptions, this is representative of the

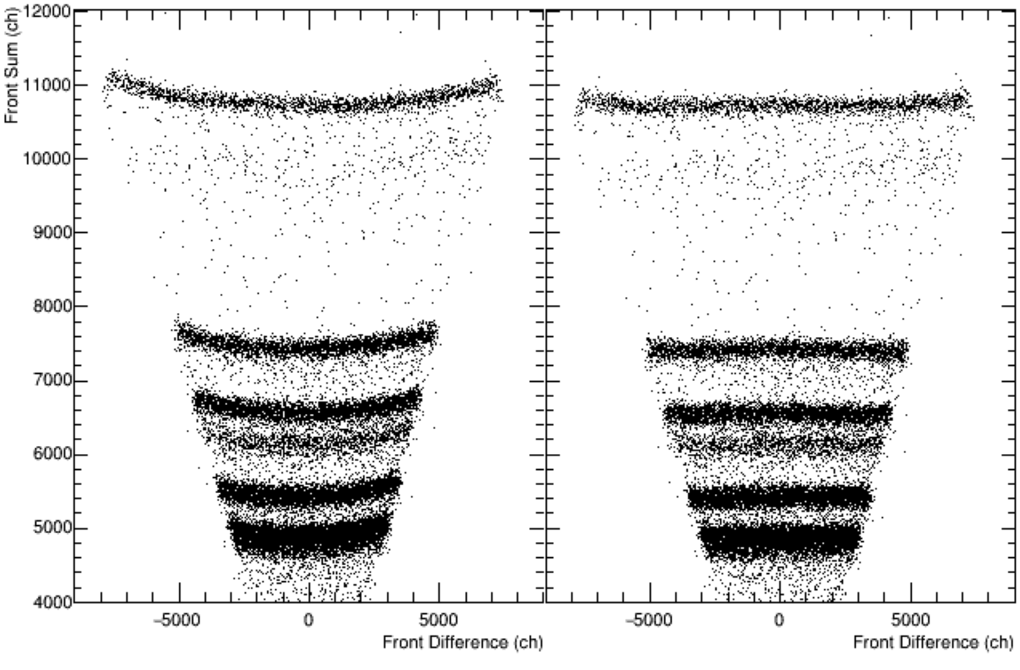

FIG. 1. Measured energy (F2+F1) vs position (F2-F1) before (left) and after (right) the position correction.

correction procedure for the array. The same procedure is applied to the back signals B2 & B1 with similar results.

The next step is to find the correlation from corrected sum to energy deposited in the silicon detector. This is done using the ^{228}Th data as well as beam calibration data. In Fig. 2, the corrected sum is plotted on the x-axis. The corresponding energy calculated, given the known incident energy energy corrected for loss in the target and mylar delta-ray shields as well as punch-through from the silicon detector when appropriate, is plotted on the y-axis. The upper two points correspond to beam calibration; the remainder are thorium peaks. The linear correlation is good to 1.5% for this detector, which is typical of the array. From thorium data and beam calibration data taken at various times throughout the experiment, the calibration appears to be stable in time for all detectors in rings C, D, and E. This remains to be settled for rings A and B.

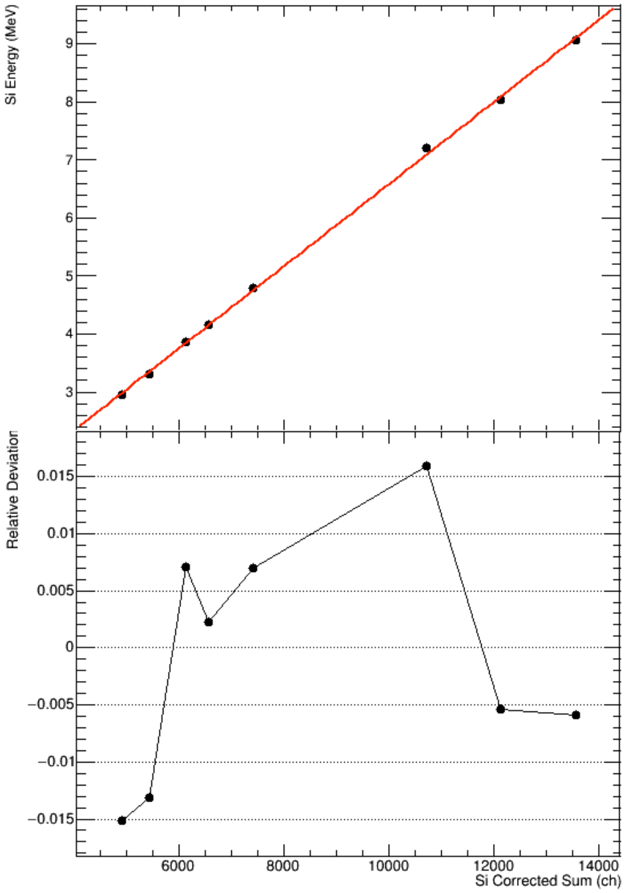

FIG. 2. Top: energy vs measured ADC channel with the linear fit that defines the energy calibration. Bottom: relative deviation of the data points from the linear fit as a function of the ADC channel.

Having corrected the silicon signals, it is also possible to perform the particle identification (PID). The ΔE-E technique is used in FAUST. Since the dynamic range in this experiment is small, covering hydrogen, helium, much of lithium and a sliver of beryllium, it is possible to use a parameterization of the shape of the PID bands (based on the Bethe-Bloch formula) to linearize the PID bands. The formula used is the same as Youngs [3] used, with the addition of independent calibration parameters as Heilborn did [1]. By varying the parameters somewhat, it is possible to obtain the spectrum shown in Fig. 3 where the PID bands for detector 21 have been (nearly) straightened (x-axis) against the raw CsI value. Atomic number and mass number increase from right to left. The data shown corresponds to runs 223-285 (^{86}Kr+C @ 35MeV/nucleon), but the same parameterization works for all other detectors in rings C, D, and E for all five other beam isotope and energy combinations. The PID for the back silicon signals and for rings A and B is underway.

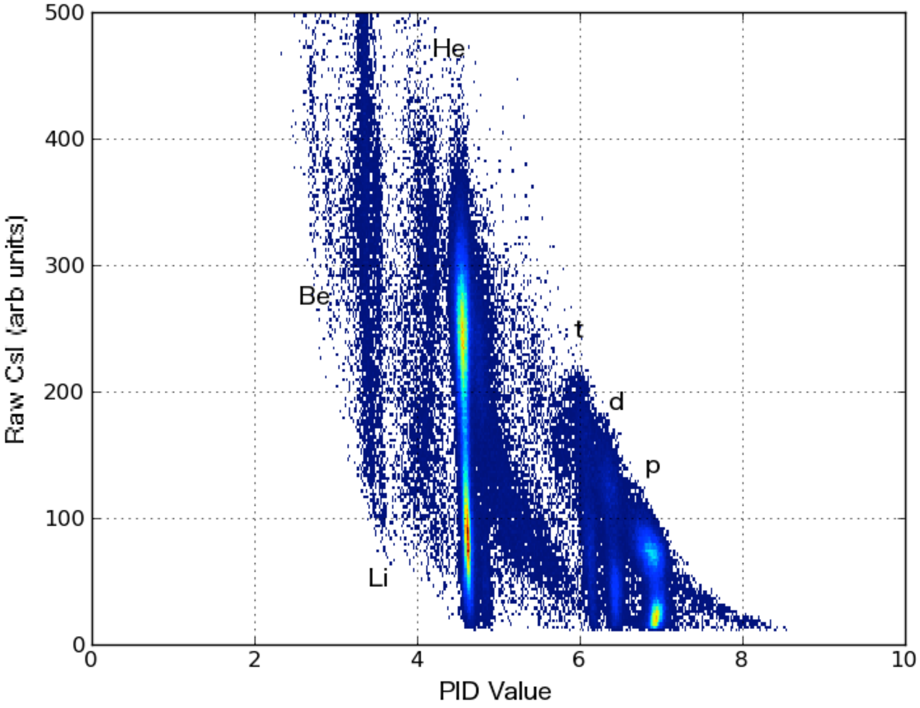

FIG. 3. Particle ID in FAUST.

[1] L.A. Heilborn, Ph.D. Thesis, Texas A&M University,in preparation.

[2] S. Soisson *et al.*, Nucl. Instrum. Methods Phys. Res. **A613**, 240 (2010).

[3] M.D. Youngs, Ph.D. Thesis, University of Michigan, 2013.

Progress with automated particle identification

A.B. McIntosh, S. Wuenschel, K. Hagel, S.J. Yennello, S. He,[1] and J. Huang[1]
[1]*Department of Statistics, Texas A&M University, College Station, Texas*

In the NIMROD multi-detector array [1] particle identification (PID) is achieved by either the ΔE-E technique or by pulse shape discrimination. Though the resolution of the detectors and electronics is excellent, determining the identity of millions of particles in an efficient way is very challenging. A representative E vs ΔE spectrum (CsI-Si) for a well-performing detector is shown in Fig 1. At the lower left, isotopes of hydrogen are seen. Each group of bands corresponds to isotopes for a particular element, reaching up to sodium at the upper right. In the past, a series of points has been manually defined along the dominant isotope for each element in each detector. This procedure, while effective, is labor-intensive. In this report, we present an automated method that acheves PID in far less time and with effective resolution of comparable quality.

The data is put on a square-root scale so that distances between each set of curves are similar; this is already done in Fig. 1. The Curvelet [2] and FISTA [3] methods are used to smooth the data by decomposition into local directionally dependent frequency components. Once this smoothing is done, points along the isotopic ridges are easily automatically found by looking for local maxima in 1D projections of narrow slices of the 2D histogram. These ridge-points are connected by a nearest-neighbor algorithm to form poly-lines along the isotopic ridges. The result is shown in Fig. 2. Here, the blue lines

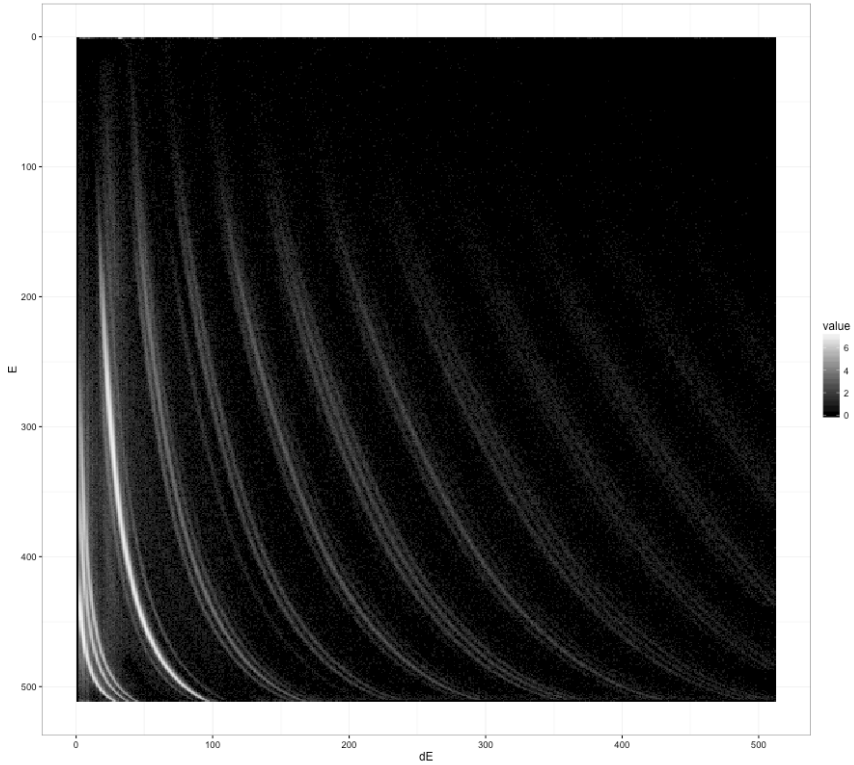

FIG. 1. E vs ΔE spectrum for a NIMROD detector telescope. Square-root axes are used. Units are arbitrary.

show the dominant isotope and the gray lines show other isotopes. While only the poly-line for the dominant isotope is subsequently used, the other poly-lines are important in ensuring that the poly-line for the dominant isotope never jumps from one isotope to another.

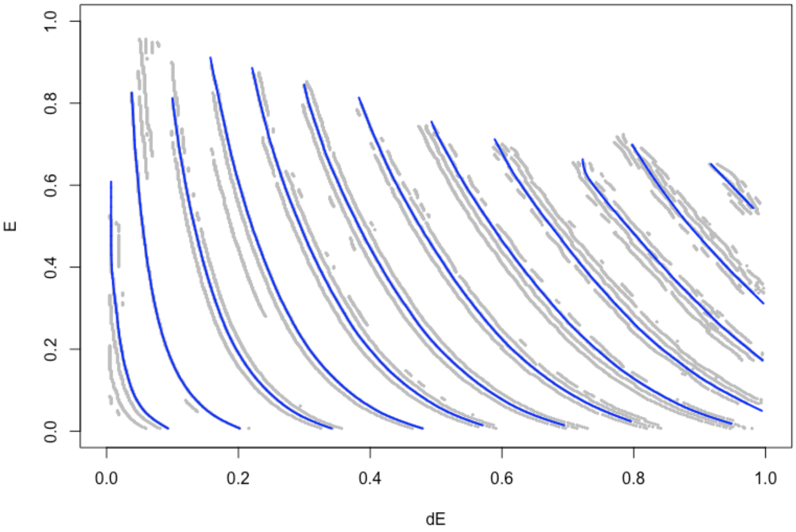

FIG. 2. E vs ΔE showing the dominant-isotope poly-lines (blue) and neighboring-isotope poly-lines.

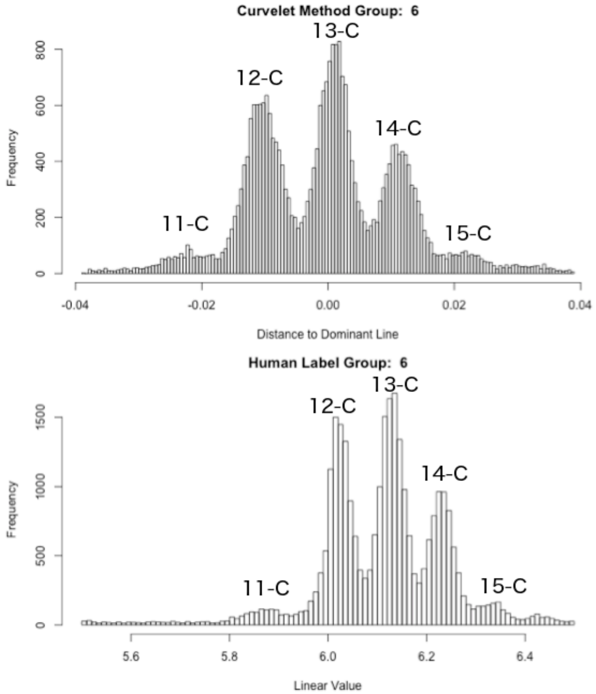

FIG. 3. Linearized PID value for carbon isotopes using the automated method (upper panel) and the manually-defined method (lower panel).

With the dominant-isotope poly-lines automatically generated, the distance of each data point to the nearest two poly-lines is calculated as was done previously for the manually-defined poly-lines. Representative results are shown in Fig. 3 (carbon isotopes) and Fig. 4 (sodium isotopes). The resolution achieved by the automated method is at least as good as by the manual method.

Extension of the method to other detectors will test the versatility and robustness of the application of the Curvelet and FISTS method in extracting PID. If successful, the method may be applied to other ridge-like features in 2D data sets such as the position correction and position calibration of the FAUST DADL detectors.

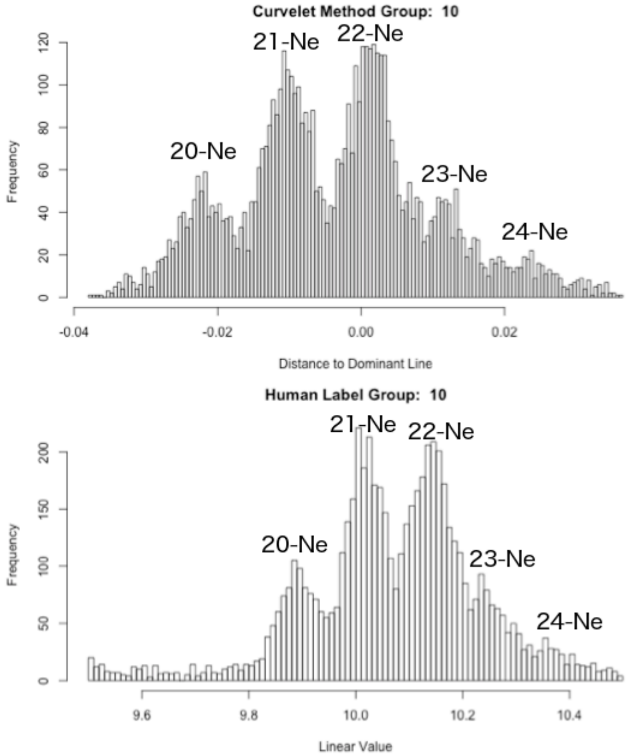

FIG. 4. Linearized PID value for sodium isotopes using the automated method (upper panel) and the manually-defined method (lower panel).

[1] S. Wuenschel *et al.*, Nucl. Instrum. Methods Phys. Res. **A613**, 578 (2009).

[2] Emmanuel Candes *et al.*, Multiscale Modeling & Simulation **5.3**, 861 (2006).

[3] A. Beck and M. Teboulle, SIAM J. Imaging Sciences **2.1**, 183 (2009).

SpiRIT TPC: first experiment and calibrations

A.B. McIntosh and SpiRIT Collaboration

The SpiRIT Time Projection Chamber [1] has been used for physics measurements for the first time. The physics goal is to constrain the density dependence of the asymmetry energy in the nuclear equation of state at supra-saturation density. The SpiRIT TPC is designed to measure pions and light charged particles produced in heavy ion collisions around a few hundred MeV/nucleon. Yield ratios (π-/π+, n/p, t/h) and flow of these particles is predicted to be sensitive to the asymmetry energy [2,3,4].

The SpiRIT TPC was installed in the SAMURAI [5] magnet at RIKEN [6] to measure charged particles produced in reactions of ^{132}Sn+^{124}Sn, ^{108}Sn+^{112}Sn, ^{124}Sn+^{112}Sn and ^{112}Sn+^{124}Sn at 300 MeV/nucleon. The KATANA [7] array and the Kyoto array (both arrays of plastic scintillator paddles) were used to measure charged particle multiplicity to enable effective triggering of the TPC. In addition, neutrons and light charged particles were detected at forward angles with NeuLAND. While only the most neutron-rich reaction would be necessary if all quantities were perfectly understood, the variation of neutron and proton effective masses with the density can be studied in the same data sets by varying the neutron content of the system. Additionally, variation of the neutron content allows rational cancellation of experimental biases prior to comparison to theoretical models.

The charged particles produced in the reactions ionized the P10 gas mixture in the TPC, following curved trajectories due to the 0.5T magnetic field. The liberated electrons drifted to the TPC's pad plane, which imaged the tracks as a function of x-position, z-position (along the beam), and arrival time, producing a 3-dimensional record of the particle tracks. The (z,x) projection of one event is shown in Fig. 1. The color indicates the ionization density. The reaction vertex can be clearly deduced at the left

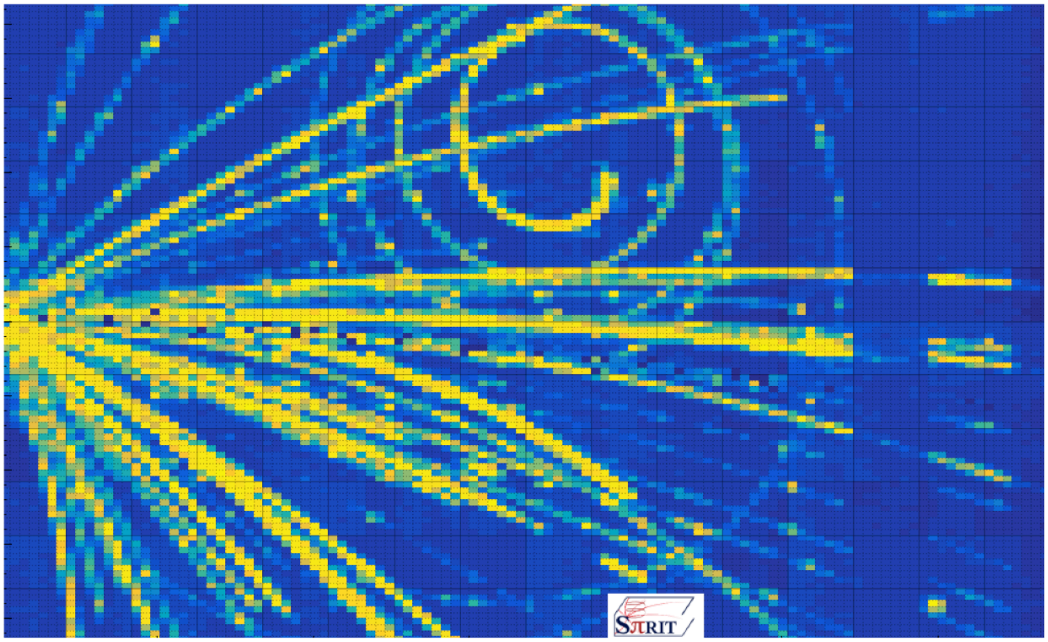

FIG. 1. 2D Projection of tracks from a single event in the SpiRIT TPC. The magnetic field is perpendicular to the plane. The counterclockwise spirals indicate negatively charged particles.

edge of the projection and corresponds to the location of the target. Most tracks (those from positively charged particles) can be seen curving clockwise in this perspective, but two notable exceptions can be seen curving in the opposite direction. Nearly all particles that curve in this way are negative pions. Two regions toward the right (downstream) that seem to show much lower ionization density actually are regions of lower electron amplification; these can allow identification of heavier charged particles. The same event is shown in Fig. 2 in a very different 2D projection to give a 3D perspective of the event.

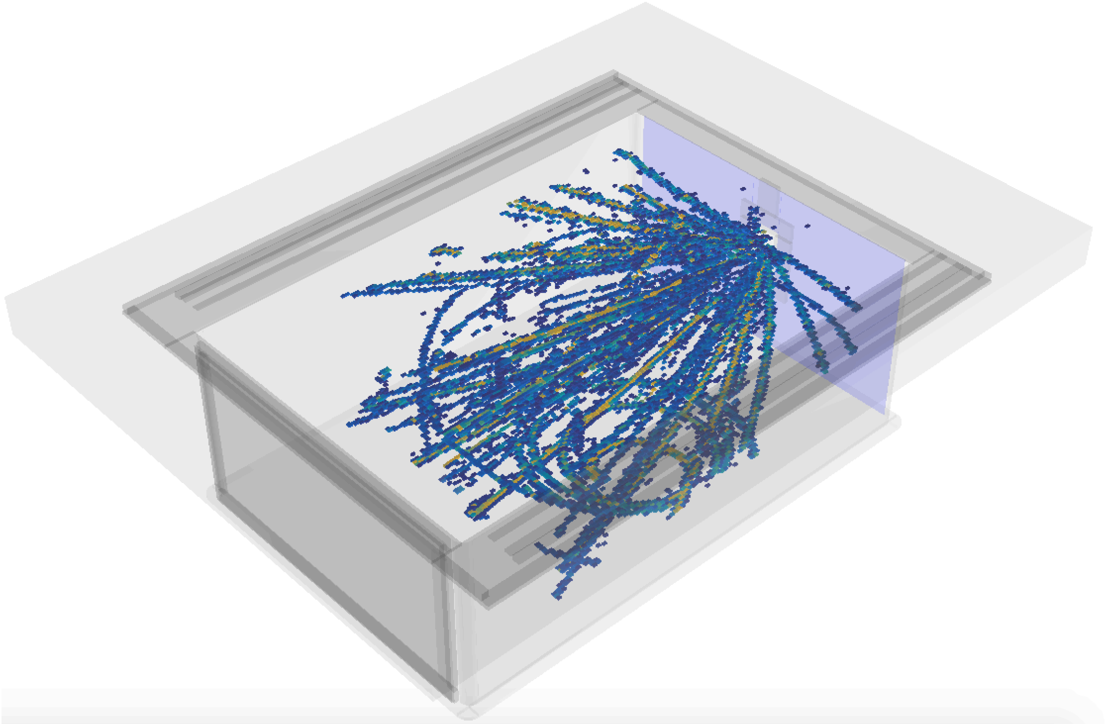

FIG. 2. Tracks in the SpiRIT TPC ("3D" view).

Charged particles are identified by their momentum (track curvature) and energy loss (ionization density). This is shown in Fig. 3. As expected, large numbers of protons, deuterons, and tritons are observed and can be distinguished. At "negative" momentum, the negative pions can be clearly seen. In roughly a mirror image, the positive pions can be seen as a peak just below the proton distribution. Improvements in the tracking algorithm may improve this effective resolution.

Calibration of the data is underway. Constraints are expected on the behavior of the asymmetry energy around twice saturation density.

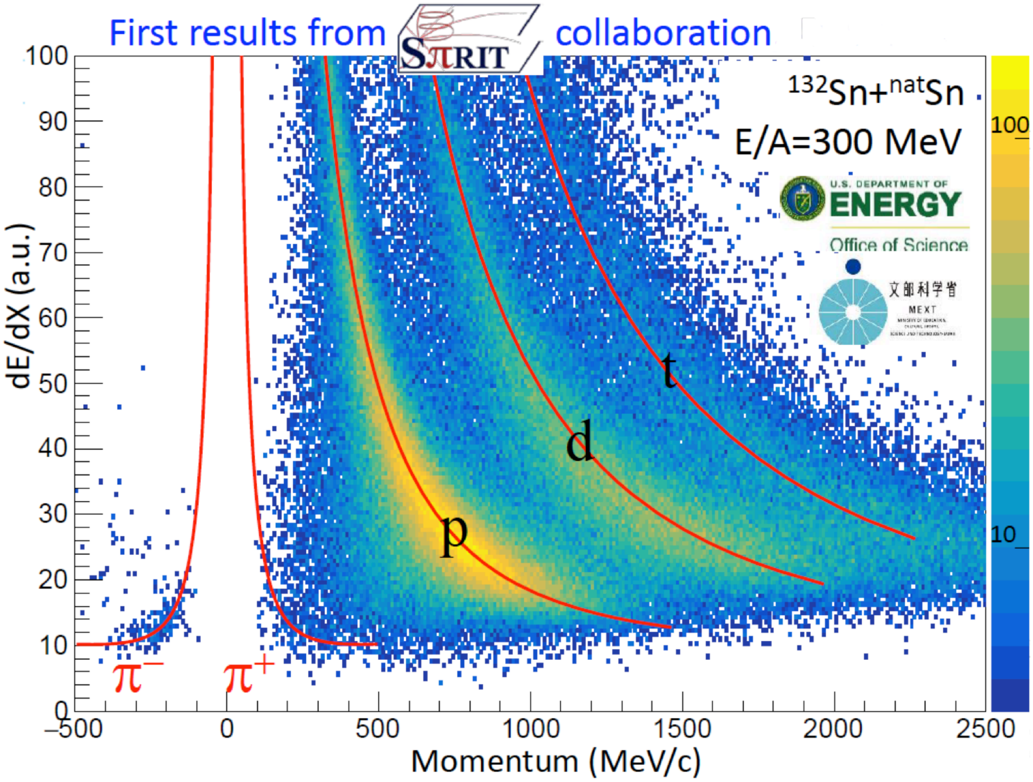

FIG. 3. Particle ID in the SpiRIT TPC.

[1] R. Shane *et al.*, Nucl. Instrum. Methods Phys. Res. **A784**, 513 (2015).
[2] B.A. Li, Phys. Rev. Lett. **88**, 192701 (2002).
[3] J. Hong and P. Danielewicz, Phys. Rev. C **90**, 024605 (2014).
[4] J. Rizzo, M. Colonna, and M. Di Toro, Phys. Rev. C **72**, 064609 (2005).
[5] T. Kobayashi *et al.*, Nucl. Instrum. Methods Phys. Res. **B317**, 294 (2013).
[6] Y. Yano *et al.*, Nucl. Instrum. Methods Phys. Res. **B261**, 1009 (2007).
[7] P. Lasko *et al.*, Nucl. Instrum. Methods Phys. Res. **A856**, 92 (2017).

Active neutron monitors for MINER experiment

J. Hooker, G.V. Rogachev, E. Koshchiy, and the MINER collaboration

The Mitchell Institute Neutrino Experiment at Reactor (MINER) is an international collaboration across 10 institutions over 4 countries that aims at measuring coherent neutrino-nucleus scattering (CNS) – an elusive process that has been predicted long time ago but never observed experimentally. This process is a sensitive probe for physics beyond the Standard Model and has cross section that is two-three orders of magnitude higher than a neutrino-nucleon cross section, making it possible to observe CNS using relatively small quantities of detector material (~10 kg of high purity Germanium or Silicon detectors). The CNS events are identified by the low energy nuclear recoils (Si or Ge) they produce as a result of neutrino elastic scattering. There are many challenges associated with this project. Since energy of the nuclear recoils is in the range from 0 to 2 keV a state-of-the-art detector technology has to be implemented to make these measurements feasible. Another challenge, and the one that we focus on in this report, is accurate characterization and in-situ measurement of neutron background. Elastically scattered neutrons may produce events that have signatures identical to CNS. The MINER experiment uses the TAMU megawatt reactor at the Nuclear Science Center as the neutrino source, therefore neutron flux is a major issue, even after careful shielding is implemented. Development of neutron detectors for neutron background measurements is the main contribution of the Cyclotron Institute to MINER collaboration.

We have built two types of neutron detectors – ^{6}Li glass scintillator detectors for thermal neutrons and P-terphenyl scintillator detectors for fast neutrons. In the ^{6}Li glass detector thermal neutrons (0.025 eV) are measured through the neutron capture reaction,

$$^6\text{Li} + \text{n} \rightarrow {}^4\text{He} + {}^3\text{H} + 4.78\ \text{MeV}$$

Since every thermal neutron capture releases the same amount of energy, 4.78 MeV, there should be a clear signal for those thermal capture events. The ^{6}Li glass scintillator has a diameter of 43 mm and a

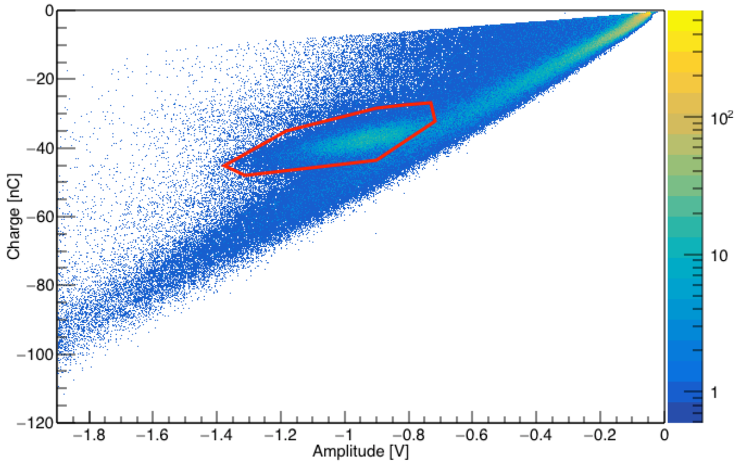

FIG. 1. Plot of the Amplitude vs Total Integrated Charge for the ^{6}Li Glass at 1800V bias. Events in the red outline are the thermal neutron events while those outside are mostly gamma rays.

thickness of 3 mm. It is connected to a Hamamatsu Photonics R7724-100 Photomuplier tube (PMT). Fig. 1 shows the amplitude vs total integrated charge scatter plot that is used to identify thermal neutron peak in the ^{6}Li glass scintillator. The thermal neutron events are circled by the solid red curve.

As we record the waveforms of the signals, we can apply advanced analysis techniques to enhance pulse shape discrimination. Typical neutron and γ-ray waveforms for the P-terphenyl scintillator are shown in Fig. 2. The decay time for the signals associated with neutrons (black) is longer than those for γ rays (red) and that makes the basis for PSD. As shown in [1], continuous wavelet transforms can be applied to vastly improve PSD. By calculating the wavelet coefficients, we can sum the square of these coefficients, or the power spectrum, which can yield different properties for the type of signal that is being transformed. This transformation can be done over different scales to probe different frequencies. Continuous wavelet transform appears to be a very valuable tool as shown in Fig. 3 where the PSD is the ratio of the power spectrum for two different scales vs the amplitude of the signal. Huge PSD improvement was achieved by using continuous wavelet transform analysis as compared to just using the integrated charges as we are able to clearly separate neutron and γ events down to much smaller energies. An initial energy calibration was done using a ^{22}Na and ^{133}Ba sources. By finding the Compton Edge with the P-terphenyl scintillator, we can calibrate the electron equivalent energy. Currently, the lowest separation for the P-terphenyl scintillator is 20 keVee which is also shown in Fig. 3.

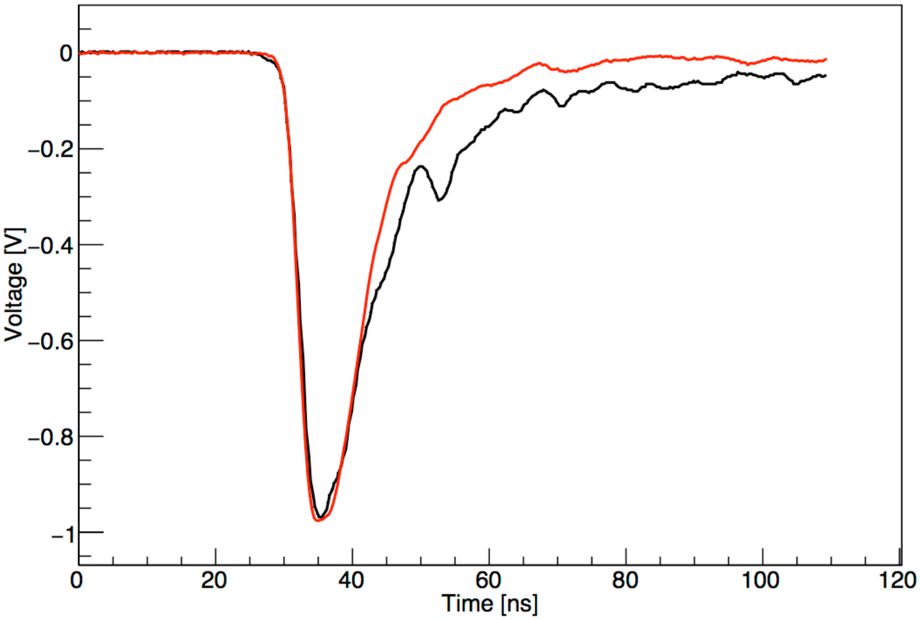

FIG. 2. Example waveforms from the P-terphenyl scintillator. The red signal is from a gamma ray while the black is a neutron signal. The neutron signal has a longer decay time than the gamma ray signal.

The next step for this project is to characterize the efficiency of the neutron detectors as a function of neutron energy with the P-terphenyl scintillator. This is done by measuring the time of flight between the neutron/gamma signal in the P-terphenyl vs the ^{252}Cf fission product measured in another scintillator close to the source.

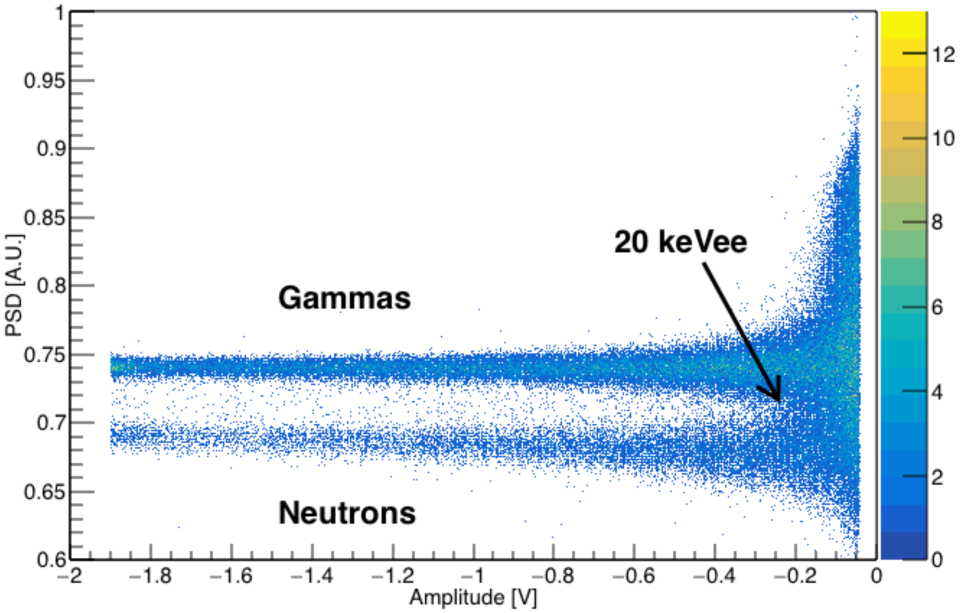

FIG. 3. Plot of the Amplitude vs PSD (using Wavelet Transforms) for the P-terphenyl scintillator at 1800V bias. As shown, there is a clear separation between neutrons and gammas down to 20 keVee.

In summary, two neutron detectors have been developed to characterize neutron background for reactor coherent neutrino scattering experiment (MINER). The ^{6}Li glass scintillator is used for thermal neutron measurements and the P-terphenyl scintillator for the fast neutrons. We now have a complete set of tools that will allow us to characterize neutron background for MINER experiment at all energies except for a small low energy region from about 1 eV to 50 keV, which can be extrapolated from the Monte Carlo simulation coupled to actual measurements at all other energies.

[1] S. Yousefi, L. Lucchese, and M.D. Aspinall, Nucl. Instrum. Methods Phys. Res. **A558**, 551 (2009).

Status of Texas Active Target (TexAT) detector

E. Koshchiy, G.V. Rogachev, E. Uberseder, J. Hooker, S. Upadhiajula, and E. Pollacco[1]
[1]*IRFU, CEA Saclay,Gif-Sur-Ivette, France*

Texas Active Target (TexAT) is being constructed at the Cyclotron Institute (see Ref. [1] for general outline of the detector). It is designed for measurements of the excitation functions for proton, deuteron and alpha particle elastic and inelastic scattering and transfer reactions such as (*d,p*), (*d,t*) and ($d,{}^3He$) in inverse kinematics using radioactive ion beams.

In 2016 all main hardware components of TexAT (the scattering chamber, vacuum and gas handling systems, supporting electronics) were set up and tested. The complete setup is shown in Fig.1. For details of the design see Ref. [1,2].

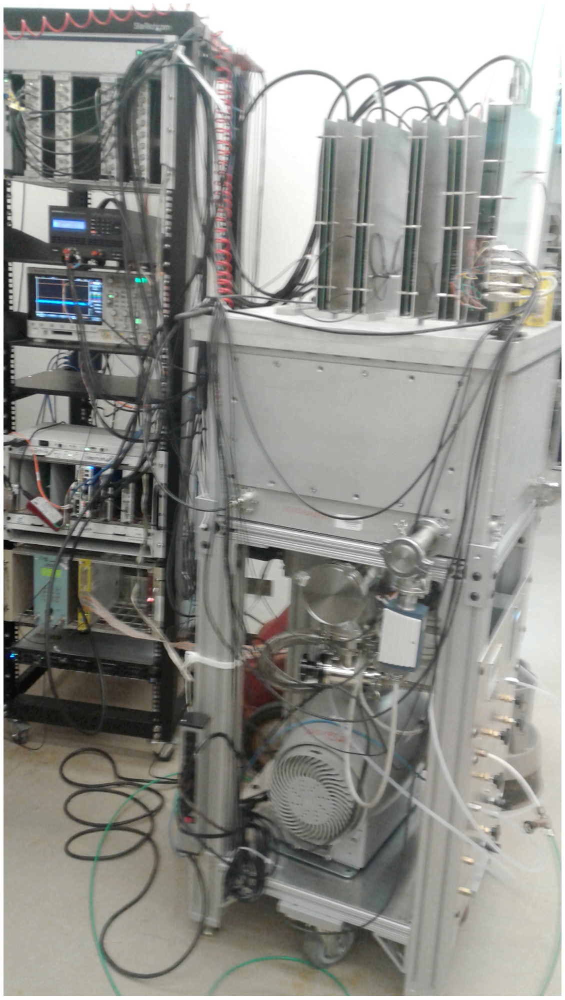

FIG. 1. Photograph showing the outside of the TeXAT.

The key element of TexAT is a Time Projection Chamber (TPC) with highly segmented Micromegas bulk detector [3], that was designed in collaboration with IRFU (Sacle, France). Following our design, two Micromegas detectors (PC-board with the embedded mesh) were fabricated at CERN and delivered to Cyclotron Institute in the Fall of 2016. The active area of PC board is 246mm x 224mm and the total number of readout channels is 1024. The detailed design is described in ref.[2].

One of the Micromegas detectors was set up in custom designed Gas- box and tested with a ^{55}Fe *X*-ray source at argon/methane gas (P-5) mixture at atmosphere pressure. The photo of Gas- box test setup is shown in Fig.2.

FIG. 2. Gas-box (left panel) and test setup (right panel) for Micromegas detector.

The second Micromegas was mounted inside the TexAT scattering chamber and was tested in real TPC-mode with alpha-source in the atmosphere of methane gas (50 torr). To avoid contamination with dust all manipulations with bulk detectors were performed in the clean room.

The transparent field cage, that generate the uniform electric field for the time projection volume was designed for TexAT. The field cage has dimentions of 350mm x 320mm x 135mm. The electric field is created by equipotential set of wires, stretched along the walls. It creates a uniform electric field within the tracking area of Micromegas detector. The pitch between wires is 5 mm, and the electric potential is

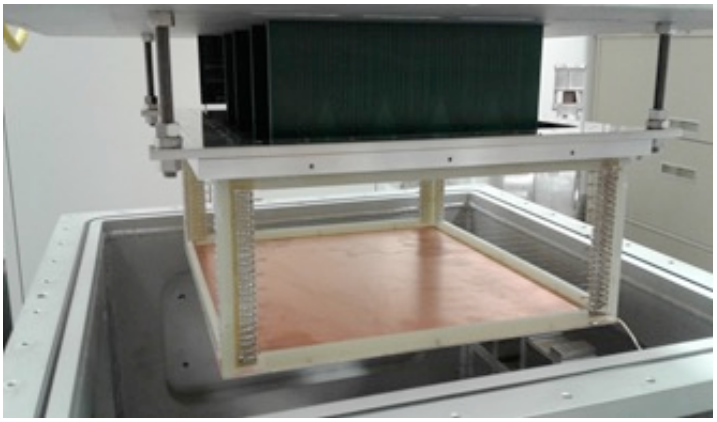

FIG. 3. TPC detector: field cage and Micromegas detector with connected readout ZAP- boards.

distributed between wire planes by the set of serial resistors (1 MOhm, 0.5%). The TPC detector (field cage and Micromegas detector) are shown in Fig.3.

In full configuration the TPC volume is suppose to be surrounded by an array of 50 Si detectors backed with an array of up to 50 CsI detector covering the solid angle of about 3π providing high efficiency for experiments with low intensity exotic beams.

The single sided, square design, 4 quadrants (25mm x 25mm), 1mm thick silicon detectors were chosen for TexAT project. The detectors are based on MSQ25 MicronSemiconductors design. However, to achieve lower price per detector unit, we are developing the process to produce these Si detectors in house. Ten MSQ25-type Si detectors are available for TexAT project at present.

Scintillator array is composed of square face (50mm x 50mm), 40 mm thick CsI(Tl) scintillator from SCIONIX (Holland). They have built-in PiN diode photo-readout and preamplifiers. These detectors are used to identify and measure residual energy of light particles that penetrated through the silicon (i.e. protons with an energy more then 12 MeV). Moreover, in some experiments they can be used to measure γ-rays.

Scintillation detectors (40 total) were tested with alpha- and gamma- sources. The energy resolution at the level of 4 to 5% for alpha- particles and of 6 to 7% for gamma- rays was demonstrated.

A commissioning run with the reduced setup – only 10 Si detectors at forward angles (Fig. 4) is planned for August of 2017.

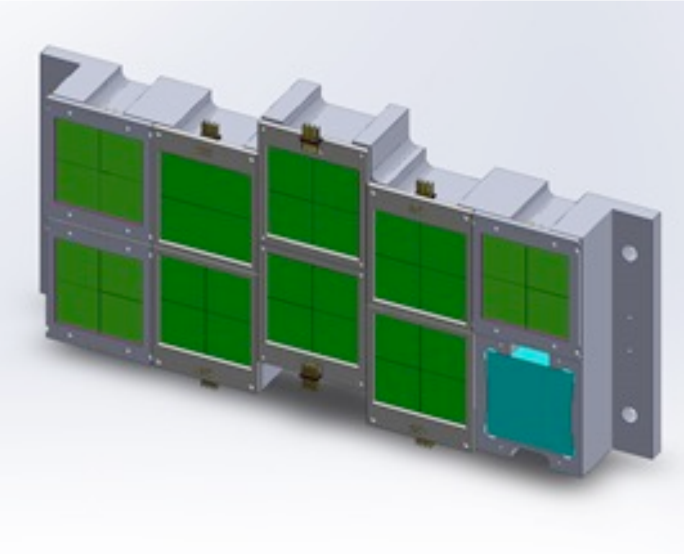

FIG. 4. "Forward"- wall (one Si-detector has been removed in order to show backing CsI(Tl).

[1] G.V. Rogachev, E. Koshchiy, E. Uberseder, and E. Pollacco. *Progress in Research*, Cyclotron Institute, Texas A&M University (2014-2015), p. IV-42.

[2] G.V. Rogachev *et al. Progress in Research*, Cyclotron Institute, Texas A&M University (2015-2016), p. IV-50.

[3] Y. Giomataris *et al.*, Nucl. Instrum. Methods Phys. Res. **A376**, 29 (1996).

SECTION V

PUBLICATIONS

PAPERS PUBLISHED

April 1, 2016 – March 31, 2017

Radiative nucleon capture with quasi-separable potentials, Shubhchintak, C.A. Bertulani, A.M. Mukhamedzhanov, and A.T. Kruppa, J. Phys. **43**, 125203 (2016).

Open heavy flavor in qcd matter and in nuclear collisions, Francesco Prino and Ralf Rapp, J. Phys. **43**, 093002 (2016).

Shape analysis applied in heavy ion reactions near Fermi energy, S. Zhang, M. Huang, R. Wada, X. Liu, W. Lin, and J. Wang, J. Phys. **44**, 035101 (2017).

Symmetry energy and experimentally observed cold fragments in intermediate heavy-ion collisions, Su-Ya-La-Tu Zhang, Mei-Rong Huang, R. Wada, Xing-Quan Liu, Wei-Ping Lin, and Jian-Song Wang, Chinese Phys. C **41**, 044001 (2017).

The study of neutron-rich nuclei production in the region of the closed shell N= 126 in the multi-nucleon transfer reaction ^{136}Xe+^{208}Pb, K. Novikov, I.M. Harca, E.M. Kozulin, S. Dmitriev, J. Itkis, G. Knyazheva, T. Loktev, L. Corradi, J. ValienteDobo´n, E. Fioretto, D. Montanari, A.M. Stefanini, E. Vardaci, D. Quero, G. Montagnoli, F. Scarlassara, E. Strano, G. Pollarolo, J. Piot, T. Mijatovi´c, S. Szilner, D. Ackermann, G. Chubarian, and W.H. Trzaska, in *8th European Summer School on Experimental Nuclear Astrophysics (Santa Tecla School)*, Vol. **703** (2016) p. 012020, 1320 September 2015.

T-matrix approach to strongly coupled QGP, Shuai Y.F. Liu and Ralf Rapp, in *16th International Conference on Strangeness in Quark Matter (SQM2016)*, Vol. **779** (IOP Publishing, 2017) p. 012034.

ψ(2s) production at the LHC, Xiaojian Du and Ralf Rapp, in *16th International Conference on Strangeness in Quark Matter (SQM2016)*, Vol. **779** (IOP Publishing, 2017) p. 012042.

Fast ion emission and parametric instabilities in laser-solid target interaction, A. Curcio, P. Andreoli, M. Barbarino, A. Bonasera, M. Cipriani, F. Consoli, G. Cristofari, R. De Angelis, G. Di Giorgio, M. Galletti, D. Giulietti, and F. Ingenito, in *Plasma Physics by Laser and Applications (PPLA2015)*, Vol. **11** p. C04006 (2016).

Study on a compact and adaptable Thomson Spectrometer for laser-initiated ^{11}B(p, α)^{8}Be reactions and low-medium energy particle detection, F. Consoli, R. De Angelis, A. Bonasera, J. Sura, P. Andreoli, G. Cristofari, M. Cipriani, G. Di Giorgio, F. Ingenito, M. Barbarino, C. Labaune, C. Baccou, S. Depierreux, C. Goyon, and V. Yahia, in *Plasma Physics by Laser and Applications (PPLA2015)*, Vol. **11** p. C05010 (2016).

Jet-like correlations with direct-photon and neutral-pion triggers at $\sqrt{s_{NN}}$ = 200 gev, L. Adamczyk *et al.*, in Phys. Lett. B **760**, p. 689 (2016).

Development of online chemistry for rutherfordium (Element 104): Commissioning of a gas stopper and extraction chromatography of rutherfordium homologs (zirconium And hafnium), M.C. Alfonso, Ph.D. Thesis, Texas AM University, 2016.

Study of ^{12}C excited states decaying into three α particles using the thick target inverse kinematic technique, M. Barbui, K. Hagel, J. Gauthier, S. Wuenschel, R.T. de Souza, S. Hudan, D. Fang, V.Z. Goldberg, H. Zheng, G. Giuliani, G. Rapisarda, E.-J. Kim, X. Liu, and J.B. Natowitz, in *12th International Conference on Nucleus-Nucleus Collisions 2015*, Vol. **117** (2016) p. 07013, June 21-26, 2015.

The cosmological lithium problem revisited, C.A. Bertulani, A.M. Mukhamedzhanov, and Shubhchintak, in *Latin American Symposium on Nuclear Physics and Applications*, Vol. **1753,** p. 040001 (2016).

Giant Resonances in ^{44}Ca, ^{54}Fe, ^{64}Zn, ^{68}Zn, and ^{94}Mo, J. Button, Ph.D. Thesis, Texas A&M University, 2016.

Giuseppe Viesti - an appreciation, Joseph B. Natowitz, in *Latin American Symposium on Nuclear Physics and Application* Vol. **1753** (2016) p. 020001, http://aip.scitation.org/doi/pdf/10.1063/1.4955341.

Partial restoration of chiral symmetry in hot and dense neutron matter, Jeremy W. Holt and Keighley E. Rockcliffe, Int. J. Mod. Phys. E **26,** p. 1740010 (2017), http://www.worldscientific.com/doi/pdf/10.1142/S0218301317400109.

Spinodal instabilities in baryon-rich quark matter, Che Ming Ko and Feng Li, in *Quarks, Nuclei and Stars*, Vol. **26**, 1740012 (2017), http://www.worldscientific.com/doi/pdf/10.1142/S0218301317400122.

Nuclear equation of state and neutron star cooling, Yeunhwan Lim, Chang Ho Hyun, and Chang-Hwan Lee, Int. J. Mod. Phys. E **26,** 1750015 (2017), http://www.worldscientific.com/doi/pdf/10.1142/S021830131750015X.

Precision measurement of the nuclear polarization in laser-cooled, optically pumped ^{37}K, B. Fenker, J.A. Behr, D. Melconian, R.M.A. Anderson, M. Anholm, D. Ashery, R.S. Behling, I. Cohen, I. Craiciu, J. M. Donohue, C. Farfan, D. Friesen, A. Gorelov, J. McNiel, M. Mehlman, H. Norton, K. Olchanski, S. Smale, O. Th´eriault, A.N. Vantyghem, and C.L. Warner, New J. Phys. **18,** p. 073028 (2016).

Precise measurement of the β-asymmetry in the decay of magneto-optically trapped, spin-Polarized ^{37}K, B. Fenker, Ph. D. Thesis, Texas A&M University, 2016.

Jet hadronization via recombination of parton showers in vacuum and in medium, Rainer J. Fries, Kyong Chol Han, and Che Ming Ko, in 7th *International Conference on Hard and Electromagnetic Probes of High Energy Nuclear Collisions*, Vol. **276**, p. 297 (2016).

Jet hadronization via recombination of parton showers in vacuum and in medium, Rainer J. Fries, Kyong Chol Han, and Che Ming Ko, Nucl. Phys. **A956,** 601 (2016).

Thermal dileptons from coarse-grained transport as fireball probes at sis energies, Tetyana Galatyuk, Paul M. Hohler, Ralf Rapp, Florian Seck, and Joachim Stroth, Eur. Phys. J. A **52,** 131 (2016).

Investigation of the energy-averaged double transition density of isoscalar monopole excitations in medium-heavy mass spherical nuclei, M.L. Gorelik, S. Shlomo, B.A. Tulupov, and M.H. Urin, Nucl. Phys. **A955,** 116 (2016).

Jet fragmentation via recombination of parton showers and its medium modification in heavy ion collisions, K.C. Han, Ph.D. Thesis, Texas A&M University, 2016.

Testing CVC and CKM unitarity via superallowed nuclear beta decay, J.C. Hardy and I.S. Towner, in *Proceedings of the 5th International Conference on Proton-emitting Nuclei (PROCON2015)*, Vol. **33**, p. 208 (2016).

Studying correlations in ^{40}Ar + ^{58}Fe with faust, L. Heilborn, C. Lawrence, A.B. McIntosh, M.D. Youngs, and S.J. Yennello, in *International Workshop on Multi facets of Equation of state and Clustering,* Vol. **39 C**, p. 398 (2016).

Dileptons and chiral symmetry restoration, P. M. Hohler and R. Rapp, in 7th *International Conference on Hard and Electromagnetic Probes of High Energy Nuclear Collisions*, Vol. **276,** 253 (2016).

Massive Yang-Mills for vector and axial-vector spectral functions at finite temperature, P.M. Hohler and R. Rapp, Annals of Physics **368,** 70 (2016).

Sum rules and photon emission in hadronic matter, Nathan P.M. Holt, Ph.D. Thesis, Texas AM University, 2016.

Rapidity and centrality dependence of particle production for identified hadrons in Cu plus Cu collisions at $\sqrt{s_{NN}}$ = 200 GeV, I.C. Arsene, I.G. Bearden, D. Beavis, S. Bekele, C. Besliu, B. Budick, H. Boggild, C. Chasman, C.H. Christensen, P. Christiansen, H.H. Dalsgaard, R. Debbe, J.J. Gaardhoje, K. Hagel, H. Ito, A. Jipa, E.B. Johnson, C.E. Jorgensen, R. Karabowicz, N. Katrynska, E.-J. Kim, T.M. Larsen, J.H. Lee, G. Lovhoiden, Z. Majka, M.J. Murray, J. Natowitz, B.S. Nielsen, C. Nygaard, D. Pal, A. Qviller,

F. Rami, C. Ristea, O. Ristea, D. Rohrich, S.J. Sanders, P. Staszel, T.S. Tveter, F. Videbaek, R. Wada, H. Yang, Z. Yin, I.S. Zgura, (BRAHMS Collaboration), Phys. Rev. C **94** (2016); 10.1103/ph~~ysre~~vc.94.014907.

Thermal and log-normal distributions of plasma in laser driven Coulomb explosions of deuterium clusters, M. Barbarino, M. Warrens, A. Bonasera, D. Lattuada, W. Bang, H. J. Quevedo, F. Consoli, R. De Angelis, P. Andreoli, S. Kimura, G. Dyer, A.C. Bernstein, K. Hagel, M. Barbui, K. Schmidt, E. Gaul, M.E. Donovan, J.B. Natowitz, and T. Ditmire, Int. J. Mod. Phys. E **25,** 1650063 (2016).

From femtonova to supernova: Heavy-ion collisions and the supernova equation of state, K. Hagel, M. Hempel, J.B. Natowitz, G. R¨opke, S. Typel, S. Wuenschel, R. Wada, M. Barbui, and K. Schmidt, in *12th International Conference on nucleus-nucleus collisions 2015* , EPJ Web of Conferences, Vol. **117,** edited by V. Greco, M. La Cognata, S. Pirrone, F. Rizzo, and C. Spitaleri, Univ Catania, Dept Phys Astron; INFN Lab Nazionali Sud Sezione Catania; Int Union Pure Appl Phys (EDP SCIENCES, 17 AVE DU HOGGAR PARC D ACTIVITES COUTABOEUF BP 112, F-91944 CEDEX A, FRANCE, 2016) 12th International Conference on Nucleus-Nucleus Collisions, Catania, ITALY, JUN 21-26, 2015-2016.

Density fluctuations in baryon-rich quark matter, Che Ming Ko and Feng Li, Nucl. Sci. Techniques **27**, 140 (2016).

Challenging fission dynamics around the barrier: The case of ^{34}S +^{186} W, E.M. Kozulin, E. Vardaci, I.M. Harca, C. Schmitt, I. Itkis, G. Knyazheva, K. Novikov, A. Bogachev, S. Dmitriev, T. Loktev, F. Azaiez, I. Matea, D. Verney, A. Gottardo, O. Dorvaux, J. Piot, G. Chubarian, W.H. Trzaska, F. Hanappe, C. Borcea, S. Calinescu, and C. Petrone, Euro. Phys. J. A **52,** 293 (2016).

Improvements to titans mass measurement and decay spectroscopy capabilities, D. Lascar, A.A. Kwiatkowski, M. Alanssari, U. Chowdhury, J. Even, A. Finlay, A.T. Gallant, M. Good, R. Klawitter, B. Kootte, T. Li, K.G. Leach, A. Lennarz, E. Leistenschneider, A.J. Mayer, B.E. Schultz, R. Schupp, D.A. Short, C. Andreoiu, J. Dilling, and G. Gwinner, in *Proceedings of the XVIIth International Conference on Electromagnetic Isotope Separators and Related Topics EMIS2* Vol. **376** (2016) p. 292, proceedings of the {XVIIth} International Conference on Electromagnetic Isotope Separators and Related Topics (EMIS2015), Grand Rapids, MI, U.S.A., 11-15 May 2015.

Indications of Bose-Einstein condensation and Fermi quenching in the decay of hot nuclei, P. Marini, H. Zheng, A. Bonasera, G. Verde, and A. Chbihi, in *International Workshop on Multifacets of EOS and Clustering 2016* , Vol. **39**, 389 (2016).

Signals of Bose Einstein condensation and Fermi quenching in the decay of hot nuclear systems, P. Marini, H. Zheng, M. Boisjoli, G. Verde, A. Chbihi, P. Napolitani, G. Ademard, L. Augey, C. Bhattacharya, B. Borderie, R. Bougault, J.D. Frankland, Q. Fable, E. Galichet, D. Gruyer, S. Kundu, M. La Commara, I. Lombardo, O. Lopez, G. Mukherjee, M. Parlog, M.F. Rivet, E. Rosato, R. Roy, G. Spadaccini, Vigilante, P.C. Wigg, and A. Bonasera, Phys. Lett. B **756,** 194 (2016).

Mutual solubility of water and hydrophobic ionic liquids in the presence of hydrochloric acid, Val´erie Mazan, Maria Yu. Boltoeva, Evgeny E. Tereshatov, and Charles M. Folden, III, RSC Advances **6**, 56260 (2016).

Equilibration chronometry, Alan B. McIntosh, Andrea Jedele, and Sherry J. Yennello, in *International Workshop on Multi facets of Equation of state and Clustering* , Vol. **39 C**, p. 405 (2017)

Progress in constraining the asymmetry dependence of the nuclear caloric curve, Alan B. McIntosh and Sherry J. Yennello, in *12th International Conference on Nucleus-Nucleus Collisions 2015* , Vol. **117** (2016) p. 07019, June 21-26, 2015.

Fission product decontamination factors for plutonium separated by {PUREX} from low-burnup, fast-neutron irradiated depleted uo2, Paul M. Mendoza, Sunil S. Chirayath, and Charles M. Folden, III, Applied Rad. Isotopes **118**, 38 (2016).

Implementation of {TTIK} method and time of flight for resonance reaction studies at heavy ion accelerator dc-60, A. K. Nurmukhanbetova, V.Z. Goldberg, D.K. Nauruzbayev, G.V. Rogachev, M.S. Golovkov, A. Mynbayev, S. Artemov, A. Karakhodjaev, K. Kuterbekov, A. Rakhymzhanov, Zh. Berdibek, I. Ivanov, A. Tikhonov, V.I. Zherebchevsky, S. Yu. Torilov, and R.E. Tribble, Nucl. Instrum. Methods Phys. Res. A

Independent isotopic yields in 25 MeV and 50 MeV proton-induced fission of natU, H. Penttil¨a, D. Gorelov, V.-V. Elomaa, T. Eronen, U. Hager, J. Hakala, A. Jokinen, A. Kankainen, P. Karvonen, I.D. Moore, J. Parkkonen, K. Pera¨j¨arvi, I. Pohjalainen, S. Rahaman, S. Rinta-Antila, J. Rissanen, V.A. Rubchenya, A. Saastamoinen, V. Simutkin, T. Sonoda, C. Weber, A. Voss, and J. Aysto Euro. Phys. J. A **52,** 1 (2016).

γ-ray decay from neutron-bound and unbound states in ^{95}Mo and a novel technique for spin determination, M. Wiedeking, M. Krtiˇcka, L.A. Bernstein, J.M. Allmond, M.S. Basunia, D.L. Bleuel, J.T. Burke, B H. Daub, P. Fallon, R.B. Firestone, B.L. Goldblum, R. Hatarik, P.T. Lake, A.C. Larsen, I.-Y. Lee, S.R. Lesher, S. Paschalis, M. Petri, L. Phair, N.D. Scielzo, and A. Volya, Phys. Rev. C **93**, 024303 (2016).

Understanding transport simulations of heavy-ion collisions at 100A and 400A MeV: Comparison of heavy-ion transport codes under controlled conditions, J. Xu, L.-W. Chen, M.-Y.B. Tsang, H. Wolter, Y.-X. Zhang, J. Aichelin, M. Colonna, D. Cozma, P. Danielewicz, Z.-Q. Feng, A. Le F`evre, T. Gaitanos, C. Hartnack, K. Kim, Y. Kim, C.-M. Ko, B.-A. Li, Q.-F. Li, Z.-X. Li, P. Napolitani, A. Ono, M. Papa, T. Song, J. Su, J.-L. Tian, N. Wang, Y.-J. Wang, J. Weil, W.-J. Xie, F.-S. Zhang, and G.-Q. Zhang, Phys. Rev. C **93,** 044609 (2016).

Jet fragmentation via recombination of parton showers, K.C. Han, R J. Fries, and C.-M. Ko**,** Phys. Rev. C **93**, 045207 (2016).

Primordial $\alpha + d \rightarrow {}^{6}\mathrm{Li} + \gamma$ reaction second lithium puzzle, A.M. Mukhamedzhanov, Shubhchintak, and C.A. Bertulani, Phys. Rev. C **93**, 045805 (2016).

Mass measurements of neutron-rich Rb and Sr isotopes, R. Klawitter, A. Bader, M. Brodeur, U. Chowdhury, A. Chaudhuri, J. Fallis, A.T. Gallant, A. Grossheim, A.A. Kwiatkowski, D. Lascar, K.G. Leach, A. Lennarz, T.D. Macdonald, J. Pearkes, S. Seeraji, M.C. Simon, V.V. Simon, B.E. Schultz, and J. Dilling, Phys. Rev. C **93**, 045807 (2016).

Model-independent determination of the astrophysical S factor in laser-induced fusion plasmas, D. Lattuada, M. Barbarino, A. Bonasera, W. Bang, H.J. Quevedo, M. Warren, F. Consoli, R. De Angelis, P. Andreoli, S. Kimura, G. Dyer, A.C. Bernstein, K. Hagel, M. Barbui, K. Schmidt, E. Gaul, M.E. Donovan, J. B. Natowitz, and T. Ditmire, Phys. Rev. C **93,** 045808 (2016).

Divergence of the isospin-asymmetry expansion of the nuclear equation of state in many-body perturbation theory, Corbinian Wellenhofer, Jeremy W. Holt, and Norbert Kaiser, Phys. Rev. C **93**, 055802 (2016).

Microscopic optical potential for exotic isotopes from chiral effective field theory, J.W. Holt, N. Kaiser, and G.A. Miller, Phys. Rev. C **93**, 064603 (2016).

J/ψ production at low ~~tra~~nsverse momentum in p + p and d + au collisions at $\sqrt{s_{N N}}$ = 200 gev, L. Adamczyk *et al.* (STAR Collaboration), Phys. Rev. C **93**, 064904 (2016).

Microscopically constrained mean-field models from chiral nuclear thermodynamics, Ermal Rrapaj, Alessandro Roggero, and Jeremy W. Holt, Phys. Rev. C **93**, 065801 (2016).

Rapidity and centrality dependence of particle production for identified hadrons in cu + cu collisions at $\sqrt{s_{NN}}$ = 200 gev, I.C. Arsene, I.G. Bearden, ~~D.~~ Beavis, S. Bekele, C. Besliu, B. Budick, H. Boggild, C. Chasman, C.H. Christensen, P. Christiansen, H.H. Dalsgaard, R. Debbe, J.J. Gaardhoje, K. Hagel, H. Ito, A. Jipa, E.B. Johnson, C E. Jorgensen, R. Karabowicz, N. Katrynska, E.-J. Kim, T.M. Larsen, J.H. Lee, G. Lovhoiden Z. Majka, M J. Murray, J. Natowitz, B.S. Nielsen, C. Nygaard, D. Pal, A. Qviller, F. Rami, C. Ristea, O. Ristea, D. Rohrich, S.J. Sanders, P. Staszel, T.S. Tveter, F. Videbaek, R. Wada, H. Yang, Z. Yin, and I.S. Zgura (BRAHMS Collaboration), Phys. Rev. C **94**, 014907 (2016).

Near-side azimuthal and pseudorapidity correlations using neutral strange baryons and mesons in d + Au, Ccu + Cu, and Au + Au collisions at $\sqrt{s_{N N}}$ = 200 gev, B. Abelev *et al.* (STAR Collaboration), Phys. Rev. C **94**, 014910 (2016).

Beam-energy dependence of charge balance functions from au + au collisions at energies available at the BNL relativistic heavy ion collider, L. Adamczyk *et al.* (STAR Collaboration), Phys. Rev. C **94**, 024909 (2016).

Isoscalar E0, E1, E2, and E3 strength in ^{94}Mo, J. Button, Y.-W. Lui, D.H. Youngblood, X. Chen, G. Bonasera, and S. Shlomo, Phys. Rev. C **94**, 034315 (2016).

Low-energy enhancement in the γ-ray strength functions of ^{73,74}Ge, T. Renstrøm, H.-T. Nyhus, H. Utsunomiya, R. Schwengner, S. Goriely, A. C. Larsen, D. M. Filipescu, I. Gheorghe, L. A. Bernstein, D. L. Bleuel, T. Glodariu, A. Görgen, M. Guttormsen, T. W. Hagen, B. V. Kheswa, Y.-W. Lui, D. Negi, I. E. Ruud, T. Shima, S. Siem, K. Takahisa, O. Tesileanu, T. G. Tornyi, G. M. Tveten, and M. Wiedeking Phys. Rev. C **93**, 064302 (2016).

Results of the ASY-EOS experiment at GSI: The symmetry energy at suprasaturation density, P. Russotto, S. Gannon, S. Kupny, P. Lasko, L. Acosta, M. Adamczyk, A. Al-Ajlan, M. Al-Garawi, S. Al-Homaidhi, F. Amorini, L. Auditore, T. Aumann, Y. Ayyad, Z. Basrak, J. Benlliure, M. Boisjoli, K. Boretzky, J. Brzychczyk, A. Budzanowski, C. Caesar, G. Cardella, P. Cammarata, Z. Chajecki, M. Chartier, A. Chbihi, M. Colonna, M.D. Cozma, B. Czech, E. De Filippo, M. Di Toro, M. Famiano, I. Gaˇspari´c, L. Grassi, C. Guazzoni, P. Guazzoni, M. Heil, L. Heilborn, R. Introzzi, T. Isobe, K. Kezzar, M. Kiš, A. Krasznahorkay, N. Kurz, E. La Guidara, G. Lanzalone, A. Le F`evre, Y. Leifels, R.C. Lemmon, Q.-F. Li, I. Lombardo, J. Lukasik, W.G. Lynch, P. Marini, Z. Matthews, L. May, T. Minniti, M. Mostazo, A. Pagano, E.V. Pagano, M. Papa, P. Paw-lowski, S. Pirrone, G. Politi, F. Porto, W. Reviol, F. Riccio, F. Rizzo, E. Rosato, D. Rossi, S. Santoro, D.G. Sarantites, H. Simon, I. Skwirczynska, Z. Sosin, L. Stuhl, W. Trautmann, A. Trifiro, M. Trimarchi, M.B. Tsang, G. Verde, M. Veselsky, M. Vigilante, Yongjia Wang, A. Wieloch, P. Wigg, J. Winkelbauer, H.H. Wolter, P. Wu, S.J. Yennello, P. Zambon, L. Zetta, and M. Zoric, Phys. Rev. C **94**, 034608 (2016).

Measurement of elliptic flow of light nuclei at $\sqrt{s_{NN}}$ = 200, 62.4, 39, 27, 19.6, 11.5, and 7.7 GeV at the BNL Relativistic Heavy Ion Collider, L. Adamczyk *et al.* (STAR Collaboration), Phys. Rev. C **94**, 034908 (2016).

Collision energy dependence of elliptic flow splitting between particles and their antiparticles from an extended multiphase transport model, Jun Xu and Che Ming Ko, Phys. Rev. C **94**, 054909 (2016).

Investigation of discrete states and quasidiscrete structures observed in ^{150}Sm and ^{152}Sm using the (*p*, *tγ*) reaction, P. Humby, A. Simon, C.W. Beausang, J.M. Allmond, J.T. Burke, R.J. Casperson, R. Chyzh, M. Dag, K. Gell, R.O. Hughes, J. Koglin, E. McCleskey, M. McCleskey, S. Ota, T.J. Ross, A. Saastamoinen, T. Tarlow, and G. Vyas, Phys. Rev. C **94**, 064314 (2016).

High-energy proton emission and Fermi motion in intermediate-energy heavy-ion collisions, W. Lin,. Liu, R. Wada, M. Huang, P. Ren, G. Tian, F. Luo, Q. Sun, Z. Chen, G.Q. Xiao, R. Han, F. Shi, J. Liu, and B. Gou, Phys. Rev. C **94**, 064609 (2016).

Neutron-rich rare-isotope production from projectile fission of heavy nuclei near 20 mev/nucleon beam energy, N. Vonta, G.A. Souliotis, W. Loveland, Y.K. Kwon, K. Tshoo, S.C. Jeong, M. Veselsky, A. Bonasera, and A. Botvina, Phys. Rev. C **94,** 064611 (2016).

Competition between fermions and bosons in nuclear matter at low densities and finite temperatures, J. Mabiala, H. Zheng, A. Bonasera, Z. Kohley, and S.J. Yennello, Phys. Rev. C **94**, 064617 (2016).

υ production in u + u collisions at $\sqrt{s_{NN}}$ = 193 Gev measured with the star experiment, L. Adamczyk *et al.* (STAR Collaboration), Phys. Rev. C **94**, 064904 (2016).

Measurement of radiative proton capture on ^{18}F and implications for oxygen-neon novae reexamined, C. Akers, A.M. Laird, B.R. Fulton, C. Ruiz, D.W. Bardayan, L. Buchmann, G. Christian, B. Davids, L. Erikson, J. Fallis, U. Hager, D. Hutcheon, L. Martin, A. St. J. Murphy, K. Nelson, D. Ottewell, A. Rojas, and A. Spyrou, Phys. Rev. C **94**, 065803 (2016).

Decay branching ratios of excited ^{24}Mg, J.M. Munson, E.B. Norman, J.T. Burke, R.J. Casperson, L.W. Phair, E. McCleskey, M. McCleskey, D. Lee, R.O. Hughes, S. Ota, A. Czeszumska, P.A. Chodash, A.J. Saastamoinen, R.A.E. Austin, A.E. Spiridon, M. Dag, R. Chyzh, M.S. Basunia, J.J. Ressler, and T.J. Ross, Phys. Rev. C **95**, 015805 (2017).

Charge-changing cross-section measurements of $^{12\text{-}16}$C at around 45 AMev and development of a glauber model for incident energies 10A−2100A Mev, D.T. Tran, H.J. Ong, T.T. Nguyen, I. Tanihata, N. Aoi, Y. Ayyad, P.Y. Chan, M. Fukuda, T. Hashimoto, T.H. Hoang, E. Ideguchi, A. Inoue, T. Kawabata, L.H. Khiem, W.P. Lin, K. Matsuta, M. Mihara, S. Momota, D. Nagae, N.D. Nguyen, D. Nishimura, A. Ozawa, P.P. Ren, H. Sakaguchi, J. Tanaka, M. Takechi, S. Terashima, R. Wada, and T. Yamamoto (RCNP-E372 Collaboration), Phys. Rev. C **94**, 064604 (2016).

Internal and external radiative widths in the combined r-matrix and potential-model formalism, A.M. Mukhamedzhanov, Shubhchintak, C.A. Bertulani, and T.V. Nhan Hao, Phys. Rev. C **95**, 024616 (2017).

Q_{EC} value of the superallowed β emitter ^{42}Sc, T. Eronen, J.C. Hardy, L. Canete, A. Jokinen, J. Hakala, A. Kankainen, V.S. Kolhinen, J. Koponen, I.D. Moore, I.M. Murray, H. Penttil¨a, I. Pohjalainen, O. Poleshchuk, J. Reinikainen, S. Rinta-Antila, N. Soukouti, A. Voss, and J.A¨ ysto¨, Phys. Rev. C **95**, 025501 (2017).

Assessing the near threshold cross section of the ^{17}O(n, α)^{14}C reaction by means of the Trojan Horse method, G.L. Guardo, C. Spitaleri, L. Lamia, M. Gulino, M. La Cognata, X. Tang, R. deBoer, X. Fang, V. Goldberg, J. Mrazek, A. Mukhamedzhanov, M. Notani, R.G. Pizzone, G.G. Rapisarda, M.L. Sergi, and M. Wiescher, Phys. Rev. C **95**, 025807 (2017).

Nuclear energy density functional and the nuclear α decay, Yeunhwan Lim and Yongseok Oh, Phys. Rev. C **95**, 034311 (2017).

Precise measurement of αK for the 88.2-kev M4 transition in ^{127}Te: Test of internal-conversion theory, N. Nica, J.C. Hardy, V.E. Iacob, H.I. Park, K. Brandenburg, and M.B. Trzhaskovskaya, Phys. Rev. C **95**, 034325 (2017).

Equation of state of nuclear and neutron matter at third-order in perturbation theory from chiral effective field theory, J.W. Holt and N. Kaiser, Phys. Rev. C **95**, 034326 (2017).

Elliptic flow of electrons from heavy-flavor hadron decays in Au +Au collisions at $\sqrt{s_{NN}}$ = 200, 62.4, and 39 Gev, L. Adamczyk ~~*et al*~~. (STAR Collaboration), Phys. Rev. C **95**, 034907 (2017).

Chiral vortical and magnetic effects in the anomalous transport model, Yifeng Sun and Che Ming Ko, Phys. Rev. C **95**, 034909 (2017).

Measurement of the ^{10}B(p, α_0)^{7}Be cross section from 5 kev to 1.5 Mev in a single experiment using the Trojan Horse method, C. Spitaleri, S.M.R. Puglia, M. La Cognata, L. Lamia, S. Cherubini, A. Cvetinovi´c, G. D'Agata, M. Gulino, G.L. Guardo, I. Indelicato, R.G. Pizzone, G.G. Rapisarda, S. Romano, M.L. Sergi, R. Spart´a, S. Tudisco, A. Tumino, M. Gimenez Del Santo, N. Carlin, M.G. Munhoz, F.A. Souza, A. Szanto de Toledo, A. Mukhamedzhanov, C. Broggini, A. Caciolli, R. Depalo, R. Menegazzo, V. Rigato, I. Lombardo, and D. Dell'Aquila, Phys. Rev. C **95**, 035801 (2017).

Erratum: Novel determination of density, temperature, and symmetry energy for nuclear multifragmentation through primary fragment-yield reconstruction [phys. rev. c 89, 021601(r) (2014)], W. Lin, X. Liu, M.R.D. Rodrigues, S. Kowalski, R. Wada, M. Huang, S. Zhang, Z. Chen, J. Wang, G.Q. Xiao, R. Han, Z. Jin, J. Liu, F. Shi, T. Keutgen, K. Hagel, M. Barbui, C. Bottosso, A. Bonasera, J.B. Natowitz, E.-J. Kim, T. Materna, L. Qin, P.K. Sahu, K.J. Schmidt, S. Wuenschel, and H. Zheng, Phys. Rev. C **95**, 039907 (2017).

Detailed characterization of neutron-proton equilibration in dynamically deformed nuclear systems, A. Rodriguez Manso, A.B. McIntosh, A. Jedele, K. Hagel, L. Heilborn, Z. Kohley, L.W. May, A. Zarrella, and S.J. Yennello, Phys. Rev. C **95**, 044604 (2017).

Measurement of the transverse single-spin asymmetry in p↑ + p → W ±/Z0 at RHIC, L. Adamczyk *et al.* (STAR Collaboration), Phys. Rev. Lett. **116**, 132301 (2016)**.**

Direct measurement of the astro-physical ^{38}K(p, γ)^{39}Ca reaction and its influence on the production of nuclides toward the end point of nova nucleosynthesis, G. Lotay, G. Christian, C. Ruiz, C. Akers, D.S. Burke, W.N. Catford, A.A. Chen, D. Connolly, B. Davids, J. Fallis, U. Hager, D.A. Hutcheon, A. Mahl, A. Rojas, and X. Sun, Phys. Rev. Lett. **116**, 132701 (2016).

Charge-dependent directed flow in Cu + Au collisions at $\sqrt{s_{NN}}$ = 200 Gev, L. Adamczyk *et al.* (STAR Collaboration), Phys. Rev. Lett. **118**, 012301 (2017).

Characterizing neutron-proton equilibration in nuclear reactions with subzeptosecond resolution, A. Jedele, A.B. McIntosh, K. Hagel, M. Huang, L. Heilborn, Z. Kohley, L.W. May, E. McCleskey, M. Youngs, A. Zarrella, and S.J. Yennello, Phys. Rev. Lett. **118**, 062501 (2017).

Thermal electromagnetic radiation in heavy-ion collisions, R. Rapp and H. van Hees, Eur. Phys. J. A **52**, 257 (2016).

Elastic and inelastic scattering of 15N ions by 7Li at 81 Mev versus that of 14N ions by 7Li at 80 and 110 Mev, A.T. Rudchik, A.A. Rudchik, L.M. Muravynets, K.W. Kemper, K. Rusek, E. Piasecki, A. Trzcin´ska, E.I. Koshchy, Val. M. Pirnak, O.A. Ponkratenko, I. Strojek, A. Stolarz, O.V. Herashchenko, Yu. M. Stepanenko, V.A. Plujko, S.B. Sakuta, R. Siudak, and A. Szczurek, Nucl. Phys. A **958**, 234 (2017).

The ASY-EOS experiment at GSI, P. Russotto, M. Chartier, M.D. Cozma, E. De Filippo, A. Le F`evre, S. Gannon, I. Gaˇspari´c, M. Kiˇs S. Kupny, Y. Leifels, R.C. Lemmon, Q. Li, J.Lukasik, P. Marini, P. Pawl-owski, W. Trautmann, L. Acosta, M. Adamczyk, A. Al-Ajlan, M. Al Garawi, S. Al-Homaidhi, F. Amorini, L. Auditore, T. Aumann, Y. Ayyad, V. Baran, Z. Basrak, R. Bassini, J. Benlliure, C. Boiano, M. Boisjoli, K. Boretzky, J. Brzychczyk, A. Budzanowski, G. Cardella, P. Cammarata, Z. Chajecki, A. Chbihi, M. Colonna, B. Czech, M. Di Toro, M. Famiano, V. Greco, L. Grassi, C. Guazzoni, P. Guazzoni, M. Heil, L. Heilborn, R. Introzzi, T. Isobe, K. Kezzar, A. Krasznahorkay, N. Kurz, E. La Guidara, G. Lanzalone, P. Lasko, I. Lombardo, W.G. Lynch, Z. Matthews, L. May, T. Minniti, M. Mostazo, A. Pagano, M. Papa, S. Pirrone, R. Pleskac, G. Politi, F. Porto, R. Reifarth, W. Reisdorf, F. Riccio, F. Rizzo, E. Rosato, D. Rossi, S. Santoro, H. Simon, I. Skwirczynska, Z. Sosin, L. Stuhl, A. Trifiro, M. Trimarchi, M.B. Tsang, G. Verde, M. Veselsky, M. Vigilante, A. Wieloch, P. Wigg, H.H. Wolter, P. Wu, S. Yennello, P. Zambon, L. Zetta, and M. Zoric, in *12th International Conference on Nucleus-Nucleus Collisions 2015* , 12th International Conference on Nucleus-Nucleus Collisions 2015, Vol. **117** (2016) p. 07010, June 21-26, 2015.

Beta-decay of ^{31}Cl: an Indirect probe of the ^{30}P(p, γ)^{31}S reaction: Present status and future perspectives, Antti Saastamoinen, Anu Kankainen, and Livius Trache, Eur. Phys. J. Plus **131**, 272 (2016).

AstroBox2 – detector for low-energy β-delayed particle detection, A. Saastamoinen, E. Pollacco, B.T. Roeder, A. Spiridon, M. Dag, L. Trache, G. Pascovici, R. De Oliveira, M.R.D. Rodrigues, and R.E. Tribble, Nuc. Instrum. . Methods Phys. Res. B**376**, 35 (2016).

Direct-photon+hadron correlations to study parton energy loss with the STAR experiment, Nihar Ranjan Sahoo, in *25th International Conference on Ultra-Relativistic Nucleus-Nucleus Collisions (Quark Matter 2015)*, Vol. **956,** p. 621 (2016).

Investigation of the role of ^{10}Li resonances in the halo structure of ^{1}1Li through the transfer reaction, A. Sanetullaev, R. Kanungo, J. Tanaka, M. Alcorta, C. Andreoiu, P. Bender, A.A. Chen, G. Christian, B. Davids, J. Fallis, J.P. Fortin, N. Galinski, A.T. Gallant, P.E. Garrett, G. Hackman, B. Hadinia, Ishimoto, M. Keefe, R. Kru¨cken, J. Lighthall, E. McNeice, D. Miller, J. Purcell, J.S. Randhawa, Roger, A. Rojas, H. Savajols, A. Shotter, I. Tanihata, I.J. Thompson, C. Unsworth, P. Voss, and Z. Wang, Phys. Lett. B **755**, 481 (2016).

Properties of excited A = 40 nuclear systems with varying matter composition, K. Schmidt, J.B. Natowitz, M. Barbui, K. Hagel, A. Bonasera, G. Giuliani, H. Zheng, M. Rodrigues, R. Wada, M. Huang, C. Bottosso, and S. Kowalski, EPJ Web of Conferences **117**, 07021 (2016).

Collision dynamics of alpha-conjugate nuclei, K.J. Schmidt, X. Cao, E.-J. Kim, K. Hagel, M. Barbui, J. Gauthier, S. Wuenschel, G. Giuliani, M.R.D. Rodrigues, H. Zheng, M. Huang, A. Bonasera, R. Wada, G. Zhang, and J.B. Natowitz, in *International Workshop on Multifacets of EOS and Clustering 2016* , Vol. **39**, p. 394 (2016).

Upgrade of the TAMU MDM-focal plane detector with micromegas technology, A.Spiridon, E.Pollacco, B.T. Roeder, A. Saastamoinen, R. Chyzh, M. Dag, R.E. Tribble, L. Trache, G. Pascovici, and R. De Oliveira, in *The XVIIth International Conference on Electromagnetic Isotope Separators and Related Topics (EMIS2015)*, Vol. **376**, p. 364 (2016).

Nuclear astrophysics and the Trojan Horse method, C. Spitaleri, M. La Cognata, L. Lamia, A.M. Mukhamedzhanov, and R.G. Pizzone, Eur. Phys. J. A **52**, 1 (2016).

Three-particle correlations in a multiphase transport model, Yifeng Sun and Che Ming Ko, Phys. Lett. B **769**, 219 (2017).

Experimental and computational forensics characterization of weapons-grade plutonium produced in a fast reactor neutron environment, Mathew W. Swinney, Charles M. Folden, III, Ronald J. Ellis, and Sunil S. Chirayath, Nucl. Tech. **197**, 1 (2017).

First evidence of metal transfer into hydrophobic deep eutectic and low-transition-temperature mixtures: indium extraction from hydrochloric and oxalic acids, E.E. Tereshatov, M. Yu. Boltoeva, and C.M. Folden III, Green Chem. **18**, 4616 (2016).

Decay of quasimolecular states in ^{26}Mg, S.Yu. Torilov, N.A. Maltsev, V.Z. Goldberg, K.A. Gridnev, V.I. Zherebchevsky, T. L¨onnroth, M. Mutterer, B. G. Novatsky, R.B. Panin, J.M.K. Slotte, Yu. G. Sobolev, W.H. Trzaska, G.P. Tyurin, and S.V. Khlebnikov, in *LXV International Meeting on Nuclear Spectroscopy and Nuclear Structure*, Vol. **80**, p. 871 (2016).

Using heavy-ion collisions to elucidate the asymmetric equation-of- state, Sherry Yennello and Alan McIntosh, in *XXI International School on Nuclear Physics and Applications International Symposium on Exotic Nuclei* Vol. **724** (2016) p. 012054, 612 September 2015.

Evaporation residue cross sections measured near the N = 126 spherical cClosed sShell in ^{45}Sc- and ^{44}Ca-induced reactions, T.A. Werke, Ph.D. thesis, Texas A&M University (2016).

A novel approach to the island of stability of super-heavy elements search, A. Wieloch, M. Adamczyk, M. Barbui, N. Blando, G. Giuliani, K. Hagel, E.-J. Kim, S. Kowalski, Z. Majka, J. Natowitz, K. Pelczar, R. Pl-aneta, K. Schmidt, Z. Sosin, S. Wuenschel, K. Zelga, and H. Zheng, EPJ Web of Conferences **117**, 01003 (2016).

Constraints on the asymmetric equation of state from heavy-ion collisions, Sherry Yennello, Alan McIntosh, and Lauren Heilborn, in *12th International Conference on Nucleus-Nucleus Collisions 2015*, Vol. **117** (2016) p. 07004, June 21-26, 2015.

Nuclear equation of state and the structure of neutron stars, Yeunhwan Lim, Taehyun Kim, and Yongseok Oh, New Physics: Sae Mulli **66**, 1571 (2016).

Observation of different isoscaling behavior between emitted fragments and residues, M. Youngs, A. B. McIntosh, K. Hagel, L. Heilborn, M. Huang, A. Jedele, Z. Kohley, L.W. May, E. McCleskey, A. Zarrella, and S.J. Yennello, Nucl. Phys. **A962**, 61 (2017).

SECTION VI

APPENDIX

TALKS PRESENTED
April 1, 2016 – March 31, 2017

Testing CVC and CKM unitarity via superallowed nuclear β decay, **J.C. Hardy**, **Invited Talk**, XIIth Rencontres du Vietnam, on High Sensitivity Experiments Beyond the Standard Model, Quy Nhon, Vietnam (July 2016).

Testing the standard model via superallowed nuclear beta decay, **J.C. Hardy**, **Invited Talk**, 24th International Conference on the Application of Accelerators in Research and Industry, CAARI 2016, Fort Worth, Texas (October 2016).

$|V_{ud}|$ *from nuclear beta decays,* **J.C. Hardy**, **Invited Talk**, 9th International Workshop on the CKM Unitarity Triangle, CKM2016, Mumbai, India (November 2016).

Current status of superallowed 0^+*-to-* 0^+ *nuclear β decay and the value of* V_{ud}*,* **J.C. Hardy**, **Requested Talk**, 2016 APS Division of Nuclear Physics Meeting, Vancouver, British Columbia, Canada (October 2016).

Precise test of the unitarity of the CKM matrix via superallowed nuclear beta decay, **H.I. Park**, **Invited Talk**, APS Meeting, Salt Lake City, Utah (April 2016).

Superallowed nuclear beta decay for V_{ud} *and CKM unitarity,* **H.I. Park**, **Invited Talk**, International Workshop on Future Potential of High Intensity Accelerators for Particle and Nuclear Physics, J-PARC, Tokai-village, Ibaraki, Japan (December 2016).

Precise test of the unitarity of the CKM matrix via superallowed nuclear beta decay, **H.I. Park**, **Invited Talk**, APCTP2016 Workshop on Frontiers of Physics: Dense Matter from Chiral Effective Theories, Pohang, Korea (December 2016).

Test of internal-conversion theory with a measurement in ^{111}*Cd,* **N. Nica**, **Invited Talk**, International Conference on Nuclear Data for Science and Technology, Bruges, Belgium (September 2016).

Test of internal-conversion theory with a measurement in ^{111}*Cd,* **N. Nica**, **Seminar**, Horia Hulubei National Institute of Physics and Nuclear Engineering, Bucharest, Romania (September 2016).

Test of internal-conversion theory with a measurement in ^{111}*Cd,* **H.I. Park**, U.S. Nuclear Data Week Annual Meeting, Brookhaven National Laboratory, Upton, New York (November 2016).

Branching ratio for the superallowed beta decay of ^{10}*C,* **T. Eronen**, M. Bencomo, L. Chen, J.C. Hardy, V. Horvat, V. Iacob, N. Nica, H.I. Park, B. Roeder and A. Saastamoinen, APS Meeting, Salt Lake City, Utah (April 2016).

Improving the precision of the half-life of ^{34}*Ar,* **V.E. Iacob**, J.C. Hardy, M. Bencomo, L. Chen, V. Horvat, N. Nica and H.I. Park, APS Meeting, Salt Lake City, Utah (April 2016).

What makes the proton spin?, **C.A. Gagliardi**, **Colloquium**, Rice University, Houston, Texas (March 2017).

Optimizing the Drell-Yan trigger for the STAR forward meson spectrometer, **J.R. Pybus**, Z. Chang, and C.A. Gagliardi (for the STAR Collaboration), 2016 APS Division of Nuclear Physics Meeting, Vancouver, British Columbia, Canada (October 2016).

Probing the Origin of the Proton Spin with Jets at STAR, **C.A. Gagliardi** (for the STAR Collaboration), Int. Nucl. Phys. Conf. 2016, refereed, Adelaide, Australia (September, 2016).

What do we learn from the giant monopole resonance measurement at Texas A&M University? **Y.-W. Lui**, **Seminar**, Henan Normal University, Xinxiang, Henan, China (April 2016).

Resonance Reactions Resulting in Neutron Decay as a New Field at Low Energy Heavy Ion Accelerators, **V.Z. Goldberg**, **Seminar**, Nazarbayev University, Astana, Kazahstan, (July 2016).

Precision measurement of the positron asymmetry of laser-cooled, spin-polarized ^{37}K, **D. Melconian**, APS Meeting, Washington D.C. (January 2017).

Precise measurement of the positron asymmetry in the decay of spin-polarized ^{37}K, **B. Fenker**, 2016 APS Division of Nuclear Physics Meeting, Vancouver, British Columbia, Canada (October 2016).

Status of the TAMUTRAP facility at Texas A&M University, **D. Melconian**, 2016 APS Division of Nuclear Physics Meeting, Vancouver, British Columbia, Canada (October 2016).

Status of the Cyclotron Institute Upgrade (and current research), **D. Melconian**, **Invited Talk**, 2016 APS Division of Nuclear Physics Meeting, Vancouver, British Columbia, Canada (October 2016).

Single event effect microchip testing at the Texas A&M University Cyclotron Institute, **D. Melconian**, **Invited Talk**, Radiation Technologies Event – New Developments and Current Challenges with Radiation Technologies, NASA Johnson Space Center, Houston, Texas (September 2016).

Probing fundamental symmetries via precision correlation measurements of β *decay*, **D. Melconian**, **Invited Talk**, High Sensitivity Experiments Beyond the Standard Model, Quy Nhon, Vietnam (August 2016).

Study of resonances in $^{23}Mg(p,\gamma)^{24}Al$ *via neutron transfer to analog states in* ^{24}Na, **G. Christian**, 2016 APS Division of Nuclear Physics Meeting, Vancouver, British Columbia, Canada (October 2016).

Toward a gamma-jet measurement at the STAR experiment, **S. Mioduszewski**, **Invited Talk**, (for the STAR Collaboration), 11th International Workshop on High p_T Physics in the RHIC-LHC Era, Brookhaven National Laboratory, Upton, New York (April 2016).

Gamma-jet studies at RHIC, **Nihar R. Sahoo**, **Invited Talk**, Jets Workshop of the 2016 RHIC/AGS Users' Meeting, Brookhaven National Laboratory, Upton, New York (May 2016).

Jets and high-p_T *probes measured in the STAR experiment*, **Nihar R. Sahoo**, (for the STAR Collaboration), 38th International Conference on High Energy Physics, Chicago, Illinois (August 2016).

Direct photon-hadron correlation measurement at RHIC, **Nihar R. Sahoo**, **Plenary Talk**, (for the STAR Collaboration), 7th Workshop for young scientists on the physics of ultrarelativistic nucleus-nucleus collisions (Hot Quarks), South Padre Island, Texas (September 2016).

Photon-triggered jet reconstruction at the STAR experiment, **D. Anderson**, (for the STAR Collaboration), 2016 APS Division of Nuclear Physics Meeting, Vancouver, British Columbia, Canada (October 2016).

Jet measurements with neutral and di-jet triggers in central Au+Au collisions at $\sqrt{s_{NN}} = 200$ *GeV with STAR*, **Nihar R. Sahoo**, XXVI international conference on ultrarelativistic heavy-ion collisions (Quark Matter), Chicago, Illinois (February 2017).

Recent advances in understanding of shell evolution in N=7 isotones and nitrogen isotopes, **G. Rogachev**, **Invited Talk**, Workshop on Predictive Theories of Nuclear Reactions Across the Isotopic Chart, Institute for Nuclear Theory, Seattle, Washington (March 2017).

Stable and radioactive ion beams at Texas A&M University, **G. Rogachev**, **Invited Talk**, Low Energy Nuclear Physics community workshop, August 2016, Notre Dame, Indiana (August 2016).

Quantifying clustering near alpha-threshold, **G. Rogachev**, **Invited Talk**, 11th International Conference on Clustering Aspects of Nuclear Structure and Dynamics, Naples, Italy (May 2016).

Structure of light exotic nuclei and nuclear astrophysics through the lens of nuclear reactions, **G. Rogachev**, **Seminar**, Ohio University, Athens, Ohio (November 2016).

Structure of light exotic nuclei and nuclear astrophysics through the lens of nuclear reactions, **G. Rogachev**, **Seminar**, University of Notre Dame, South Bend, Indiana (October 2016).

Structure of light exotic nuclei and nuclear astrophysics through the lens of nuclear reactions, **G. Rogachev**, **Seminar**, Argonne National Laboratory, Argonne, Illinois (September 2016).

Texas Active Target (TexAT), **G. Rogachev**, Low Energy Nuclear Physics community workshop, South Bend, Indiana (August 2016).

Recent experience with ReA3 beam time structure, **G. Rogachev**, Low Energy Nuclear Physics community workshop, South Bend, Indiana.

Nuclear structure beyond the drip-line: ^{9}*He and* ^{10}*N*, **G. Rogachev**, Workshop on Direct Reactions with Exotic Beams 2016, Halifax, Canada (July 2016).

Alpha-capture reaction rates via sub-Coulomb alpha-transfer, **H. Jayatissa**, Nuclei in the Cosmos XIV (NIC XIV), Toki Messe, Niigata, Japan (June 2016).

Alpha-capture reaction rates for ^{22}*Ne(alpha,n) via sub-Coulomb alpha-transfer*, **H. Jayatissa**, 2016 APS Division of Nuclear Physics Meeting, Vancouver, British Columbia, Canada (October 2016).

Probing the cluster structure in ^{10}*Be using resonant* ^{6}*He +* α *scattering*, **S. Upadhyayula**, 2016 APS Division of Nuclear Physics Meeting, Vancouver, British Columbia, Canada (October 2016).

Probing the role of alpha clustering in collisions of alpha-conjugate nuclei, **J.B. Natowitz**, **Invited Talk**, International Workshop on Multi facets of EoS and Clustering 2016, Caen, France (May 2016).

Low density nuclear matter, **J.B. Natowitz**, **Invited Talk**, France-U.S. Theory Institute for Physics with Exotic Nuclei Workshop-2016, Caen, France (May 2016).

Deep inelastic multinucleon transfer for creation of super-heavy and hyper-heavy elements, **J.B. Natowitz**, **Invited Talk**, Shanghai Institute for Nuclear and Applied Physics, Shanghai, China (December 2016).

Alpha conjugate neck structures in the collisions of 35 MeV/nucleon ^{40}Ca *with* ^{40}Ca, **J.B. Natowitz**, **Invited Talk**, France-U.S. Theory Institute for Physics with Exotic Nuclei Woprkshop-2016, Huizhou, China (December, 2016).

In and Tl extraction from HCl media into ionic liquids and deep eutectic solvents for a future investigation of Nh (E113) chemistry, **M.F. Voia**, 3rd International Conference on Ionic Liquids in Separation and Purification Technology, Kuala Lumpur, Malaysia (January 2017).

Experimental and computational assessment of fission product residue in plutonium from low-burn-up thermal reactor fuel and inverse analysis for nuclear forensics, **C.M. Folden III**, **Invited Talk**, (with Sunil S. Chirayath), DNDO ARI Grantees Program Review, Atlanta, Georgia (July 2016).

Metal extraction by green solvents: ionic liquids and hydrophobic deep eutectic mixtures, **E.E. Tereshatov**, 18th International Conference on Green Chemistry, San Francisco, California (June 2016).

Studying the stars here on earth: How the equation of state of nuclear matter impacts the formation of the elements, **S.J. Yennello**, **Invited Talk**, San Jose State University, San Jose, California (July 2016).

Supporting undergraduate researchers, **S.J. Yennello**, **Invited Talk**, REU site director's workshop, Houston, Texas (October 2016).

Accelerated learning: undergraduate research experiences at the Texas A&M Cyclotron Institute, **S.J. Yennello**, **Invited Talk**, International Conference on the Application of Accelerators in Research and Industry (CAARI – 2016), Fort Worth, Texas (November 2016).

ARUNA facilities overview, **S.J. Yennello**, **Invited Talk**, Low energy community meeting, South Bend Indiana (August 2016).

LCP correlations with improved resolution, **L. Heilborn**, 2016 APS Division of Nuclear Physics Meeting, Vancouver, British Columbia, Canada (October 2016).

Studying correlations in $^{40}Ca+^{58}Fe$ *with FAUST*, **L. Heilborn**, International Workshop on Multifragmentation, Equation of State, and Clusterization, Caen, France (May 2016).

Equilibration chronometry, **A.B. McIntosh**, **Invited Talk**, Transport 2017, East Lansing, Michigan (March 2017).

Equilibration chronometry: characterizing neutron-proton equilibration with sub-zeptosecond resolution, **A.B. McIntosh**, 6th International Symposium on the Nuclear Symmetry Energy (NuSym16), Beijing, China (June 2016).

Equilibration chronometry: characterizing neutron-proton equilibration with sub-zeptosecond resolution, **A.B. McIntosh**, International Workshop on the Multi-facets of the Equation-of-state and Clustering, Caen, France (May 2016).

The partial trucated icosahedron (ParTI) phoswich detector array: a light charged particle array for pionic fusion measurements, **A. Zarrella**, Conference on Application of Accelerators in Research and Industry (CAARI), Forth Worth, Texas (November 2016).

Pionic fusion at TAMU, **A. Zarrella**, Mini Workshop on Nuclear Reactions (CUSTIPEN) Commerce, Texas (November 2016).

Equilibration chronometry, **A. Jedele**, Int. Nucl. Phys. Conf. 2016, Adelaide, Australia (September, 2016).

Equilibration chronometry, **A. Jedele**, 2016 APS Division of Nuclear Physics Meeting, Vancouver, British Columbia, Canada (October 2016).

Equilibration chronometry, **A. Jedele**, CUSTIPEN Mini-Workshop, Commerce, Texas (November 2016).

Characterizing NZ equilibration in nuclear reactions with subzeptosecond resolution, **A. Rodriguez Manso**, CUSTIPEN Mini-Workshop, Commerce, Texas (November 2016).

Neutron-proton equilibration in dynamically-deformed nuclear systems (at 35 MeV/nucleon), **A. Rodriguez Manso**, APS Meeting, Washington D.C. (January 2017).

Status of the Texas A&M University Cyclotron Institute, **D.P. May**, J.E. Ärje, L.N. Gathings, B.T. Roeder, F.P. Abegglen, G. Chubaryan, H.L. Clark, G.J. Kim, G. Tabacaru, andA. Saastamoinen, the 21st International Cyclotron Conference, Zurich, Switzerland (September 2016).

Properties of nuclei and nuclear matter within the mean-field approximation, **S. Shlomo**, **Seminar**, Department of Physics, Costa Rica, National University, Heredia, Costa Rica (June 2016).

A novel method for determining the mean-field directly from the single particle matter density: Application to the measured charge density difference between the Isotones ^{206}Pb – ^{205}Tl, **S. Shlomo**, **Invited Talk**, Carpathian Summer School of Physics-2016 (CSSP16), Sinaia, Romania, (June 2016).

The charge density difference between the isotones ^{206}Pb – ^{205}Tl and the effect of short-range correlations, **S. Shlomo**, **Invited Talk**, The Israel Physical Society, Tel-Aviv, Israel (December 2016).

On the unitarity of the particle-hole dispersive optical model, **M.L. Gorelik**, S. Shlomo, B.A. Tulupov, and M.H. Urin, MEPHI Conference, Moscow, Russia (January 2017).

Generalized R-matrix and Trojan horse method, **A.M. Mukhamedzhanov**, **Invited Talk**, R-matrix methods workshop, Santa Fe, New Mexico (June 2016).

Heavy-flavor transport in QCD matter, **R. Rapp**, **Invited Talk**, 11th International workshop on "High-p_T Physics in the RHIC and LHC Era", Brookhaven National Laboratory, Upton, New York (April 2016).

Heavy-Flavor Probes of QCD Phase Structure, **R. Rapp**, **Invited Talk**, Int. Workshop on QCD Phase Structure III, Wuhan, China (June 2016).

Theory of heavy flavor in matter, **R. Rapp**, **Invited Plenary Talk**, 2016 RHIC & AGS Users' Meeting on "RHIC Upgrades in the Era of 1/fb Precision", Brookhaven National Laboratory, Upton, New York (June 2016).

An in-medium potential and its applications to heavy-quark diffusion and QCD equation of state, **S.Y.F. Liu**, Int. Conference on Strangeness in Quark Matter (SQM2016), Berkeley California (June 2016).

Sequential regeneration of charmonia in heavy-ion collisions, **X. Du,** Int. Conference on Strangeness in Quark Matter (SQM2016), Berkeley, California (June 2016).

Calculation of the electric conductivity of hot hadronic matter, **J. Atchison**, Hot Quarks 2016 conference, South Padre Island, Texas (September 2016).

What can we extract from thermal electromagnetic radiation in heavy-ion collisions? **R. Rapp**, **Invited Lecture,** 38th Int. School on Nuclear Physics on "Nuclear Matter under Extreme Conditions – Relativistic Heavy-Ion Collisions", Erice, Italy (September 2016).

What can we learn from heavy-flavor observables in heavy-ion collisions? **R. Rapp**, **Invited Talk**, Workshop on "Recent RHIC and LHC Results and their Implications for Heavy-ion Physics in the 2020's", MIT, Boston, Massachusetts (October 2016).

Brownian motion in the quark-gluon plasma and in heavy-ion collisions, **R. Rapp**, **Invited Talk**, STAR analysis meeting pre-workshop on "Beam Energy Dependence of Strangeness and Heavy-Quark Production", LBNL, Berkeley, California (November 2016).

Perspectives on heavy flavor and EM probes with heavy ions at LHCb, **R. Rapp**, **Invited Talk**, Int. Workshop LHCb Heavy-Ion and Fixed-Target Physics, CERN, Geneva, Switzerland (January 2017).

Theoretical perspective on quarkonia from SPS via RHIC to LHC, **R. Rapp**, **Invited Plenary Talk**, XXVI Int. Conf. on Ultra-Relativistic Heavy-Ion Collisions (Quark Matter 2017), Chicago, Illinois (February 2017).

In-medium bottomonium production in heavy-ion collisions, **X. Du**, **Plenary Flash Talk**, XXVI Int. Conf. on Ultra-Relativistic Heavy-Ion Collisions (Quark Matter 2017), Chicago, Illinois (February 2017).

Thermal dileptons from high to low energies, **R. Rapp,** **Invited Talk**, ISF research workshop on "Study of High-Density Matter with Hadron Beams", Weizmann Institute, Rehovot, Israel (March 2017).

Many-body T-matrix approach to strongly coupled quark-gluon plasma, Matter, **S.Y.F. Liu**, **Nuclear/Particle Theory Seminar,** Tsinghua University, Beijing, China (December 2016).

Many-body T-matrix approach to strongly coupled quark-gluon plasma, Matter, **S.Y.F Liu**, **Nuclear Theory Seminar**, Inst. for Modern Physics, Chinese Academy of Sciences, Lanzhou, China (December 2016).

Density fluctuations in baryon-rich quark matter, **C.M. Ko**, **Invited Talk**, International Workshop on Nuclear Dynamics in Heavy-Ion Reactions", Xinxiang, Henan, China (May 2016).

Effects of Medium Modification of Pion Production Threshold in Heavy Ion Collisions and the Nuclear Symmetry Energy, **C.M. Ko**, **Invited Talk**, The 6th International Symposium on Nuclear Symmetry, Beijing, China (June 2016).

Theoretical Challenges at RHIC, **C.M. Ko**, **Invited Talk**, QCD Workshop, Shanghai, China (August 2016).

Chiral magnetic effect in the anomalous transport model, **Y. Sun,** Workshop for Young Scientists on the Physics of Ultrarelativistic Nucleus-Nucleus Collisions, Padre Island, Texas (September 2016).

Spinodal instability of baryon-rich quark matter, **F. Li,** Workshop for Young Scientists on the Physics of Ultrarelativistic Nucleus-Nucleus Collisions, Padre Island, Texas (September 2016).

Anomalous Transport Model Study of Chiral Magnetic Effects in Heav Ion Collisions, **C.M. Ko**, **Invited Talk**, 5th International Symposium on Non-equilibrium Dynamics, Phuket, Thailand (October 2016).

Medium Effects on Pion Production in Heavy Ion Collisions, **Z. Zhang**, **Invited Talk**, CUSTIPEN Mini-Workshop on Nuclear Reactions, Commerce, Texas (November 2016).

Pion Production in Heavy Ion Collisions, **C.M. Ko**, **Invited Talk**, CUSTIPEN Mini-Workshop on Nuclear Reactions, Commerce, Texas (November 16, 2016).

RVUU description, **Z. Zhang**, **Invited Talk**, International Workshop on Transport Simulations for Heavy Ion Collisions under Controlled Conditions", FRIB-MSU, East Lansing, Michigan (March 2017).

Medium Effects on Pion Production in Heavy Ion Collisions, **C.M. Ko**, **Invited Talk**, International Workshop on Transport Simulations for Heavy Ion Collisions under Controlled Conditions", FRIB-MSU, East Lansing, Michigan (March 2017).

Anomalous transport model study of chiral magnetic effects in heavy ion collisions, **C.M. Ko**, **Seminar**, Shanghai Jiao Tong University, Shanghai, China (May 2016).

Anomalous transport model study of chiral magnetic effects in heavy ion collisions, **C.M. Ko**, **Seminar**, Shanghai Institute for Applied Physics, Shanghai, China (May 2016).

Overview on coalescence model: theoretical developments and applications, **C.M. Ko**, **Seminar**, Shanghai Institute for Applied Physics, Shanghai, China (May 2016).

Microscopic optical potentials in neutron-rich matter from chiral EFT, **J. Holt**, **Invited Talk**, ECT* Workshop: Towards consistent approaches for nuclear structure and reactions, Trento, Italy (June 2016).

Nuclear equation of state from chiral effective field theory, **J. Holt**, **Invited Talk**, INT workshop: The phases of dense matter, Institute for Nuclear Theory, University of Washington, Seattle, Washington (July 2016).

Structure and dynamics of neutron-rich matter on earth and in the stars, **J. Holt**, **Invited Physics Colloquium**, Texas A&M University-Commerce, Commerce, Texas (October 2016).

Single-particle potential for transport model simulations from two- and three-body chiral nuclear forces, **J. Holt**, **Invited Talk**, CUSTIPEN Mini workshop on nuclear reactions, Texas A&M Commerce, Commerce, Texas (November 2016).

Structure and dynamics of neutron-rich matter on earth and in the stars, **J. Holt**, **Invited Physics Colloquium**, Washington State University, Pullman, Washington (March 2017).

Microscopic optical potentials in neutron-rich matter from chiral EFT, **J. Holt**, **Invited Talk**, INT workshop: Toward predictive theories of nuclear reactions across the isotopic chart, Institute for Nuclear Theory, University of Washington, Seattle, Washington (March 2017).

A hadronization model for jets based on quark recombination, **R.J. Fries**, **Invited Talk**,, 11th Int. High-PT Workshop 2016, Upton, New York (April 2016).

Early time dynamics: Pressure and 3+1D flow from classical gluon fields, **R.J. Fries**, **Invited Plenary Talk**, 3rd International Conference on the Initial Stages in High-Energy Nuclear Collisions (Initial Stages 2016), Lisbon, Portugal (May 2016).

Early time dynamics in nuclear collisions: A semi-analytic approach, **R.J. Fries**, **Invited Talk**, Ultrarelativistic Heavy Ion Workshop, CERN, Geneva, Switzerland (July 2016).

A novel approach for event-by-event early gluon fields, **R.J. Fries**, 8th International Conference on Hard and Electromagnetic Probes of High-energy Nuclear Collisions (Hard Probes 2016), Wuhan, China (September, 2016).

The initial phase in high energy nuclear collisions: How far can we go with analytic solutions?, **R.J. Fries**, **Seminar,** McGill University, Montreal Quebec, Canada (November 2016).

Analytic results for CGC in space-time coordinates, **R.J. Fries**, **Seminar**, Brookhaven National Laboratory, Upton, New York (December 2016).

Deciphering high energy nuclear collisions, **R.J. Fries**, **Colloquium**, Bose Institute, Kolkata, India (January 2017).

Nuclear physics using lasers, **A. Bonasera**, **Invited Talk**, Carpathian Summer School of Physics 2016 (CSSP16), Sinaia, Romania, (June 2016).

Measuring fusion cross sections in deuterium plasmas created by few energetic nanosecond laser beams: The effect of ternary fusion reactions, **A. Bonasera**, **Invited Talk**, Shanghai Institute of Optics and Fine Mechanics Chinese Academy of Science (SIOM), Shanghai, China (2016).

RESEARCH PERSONNEL AND ENGINEERING STAFF

April 1, 2016 - March 31, 2017

Faculty and Research Group Leaders

Aldo Bonasera, Senior Scientist
Charles M. Folden III, Assist. Prof. of Nuclear Chemistry
Gregory Christian, Assist. Prof. of Physics
Rainer Fries, Assoc. Professor of Physics
Carl A. Gagliardi, Professor of Physics
John C. Hardy, Professor of Physics, Ralph and Marsha Schilling Chair in Physics
Jeremy Holt, Assist. Professor of Physics
Che Ming Ko, Professor of Physics
Dan Melconian, Assoc. Professor of Physics
Ania Kwiatkowski, Assist. Professor of Physics
Saskia Mioduszewski, Assoc. Prof. of Physics
J. B. Natowitz, Professor of Chemistry – Retired 12/31/2016
Ralf Rapp, Professor of Physics
Grigory Rogachev, Professor of Physics
Shalom Shlomo, Senior Scientist
Robert E. Tribble, Professor of Physics (20%)
Sherry J. Yennello, Professor of Chemistry, Bright Chair, Director
Dave H. Youngblood, Professor of Physics - Retired 1/13/2017
Akram M. Zhanov, Senior Scientist

Research Staff

Juha Arje
Marina Barbui, Assist. Research Scientist
Henry Clark, Accelerator Physicist (50%)
Grigor Chubaryan, Research Scientist
Vladilen Goldberg, Research Scientist
John C. Hagel, Research Scientist (50%)
Vladimir Horvat, Research Scientist (50%)
Victor Iacob, Research Scientist
Yevgen Koshchiy, Assist. Research Scientist
Yiu-Wing Lui, Research Scientist
Ninel Nica, Associate Research Scientist
Alan McIntosh, Assist. Res. Scientist
Antti Saastamoinen (50%)
Praveen Shidling
Sara Wuenschel
Roichi Wada (40%)

Visiting Scientists

Tommi Eronen – To 8/31/16
Guoqiang Zhang – To 3/15/17

Accelerator Physics and Radiation Line Staff

Joseph Brinkley, Research Associate
Lixin Chen, Research Associate
Henry Clark, Accelerator Physicist (50%)
Vladimir Horvat, Research Scientist (50%)
Bruce Hyman, Research Associate
George Kim, Accelerator Physicist
Don May, Accelerator Physicist
Brian Roeder, Accelerator Physicist
Antti Saastamoinen (50%)
Gabriel Tabacaru, Accelerator Physicist

Computer Systems Staff

Robert Burch, Jr., Lead Microcomputer/LAN Administrator
John C. Hagel, Research Scientist (50%)

Engineering Staff

Robert Olsen, Senior Mechanical Engineer

Postdoctoral Research Associates

Shadi Bedoor – To 9/12/16
Xiguang Cao – To 11/1/16
Jerome Gauthier
Yeunhwan Lim – From 7/6/16
Shuya Ota
Hyo-In Park
Alis Rodriguez Manos – From 5/2/16
Nihar Sahoo
Renee Steinbruegge – To 9/1/16
Tyler Werke – From 8/15/16
Michael Youngs – To 8/22/16
Zhen Zhang

STUDENTS

April 1, 2016 - March 31, 2017

Graduate Students

Joseph Atchison
Miguel Bencomo
Eames Bennett
Giacomo Bonasera
Jonathan Button – To 8/31/16
Zilong Chang – To 12/31/16
Roman Chyzh
Murat Dag – To 12/31/16
Xiaojian Du
Benjamin Fenker – To 8/12/16
Alex Fleming
Kevin Glennon
Kyong Choi Han – To 5/15/16
Lauren Heilborn
Lawrence Henderson
Nathan Holt – To 12/31/16
Josh Hooker
Curtis Hunt
Heshani Jayatissa
Andrea Jedele
Feng Li – To 9/22/16
Shuai Liu
Yanfang Liu
Cordero Magana
Matthew Morrison – To 5/31/16
John Patti – To 7/12/16
Steven Rose
Issac Sarver
Alexandra Spiridon – To 1/15/17
Sidharth Somanathan – To 12/31/16
Sriteja Upadhyayula
Merinda Volia
Tyler Werke – To 8/14/16
David Wright – To 12/31/16
Zidong Yang
Andrew Zarrella
Zhaojie Xu – From 5/31/16

Undergraduates and Student Technicians

Lindsay Bryce – To 5/31/16
Andrew Bellesio – From10/16/16
Haley Forbe – From 9/5/16
Stephen Gerlt
Srivivas P. Harshal – To 5/15/16
Christine Lawrence
Magaret Moetteli – To 8/15/16
Mateo Muzak – From 10/28/16
Jackson Pybus – From 5/4/16
Victoria Tepe – From 6/6/16

ORGANIZATIONAL CHART - CYCLOTRON INSTITUTE

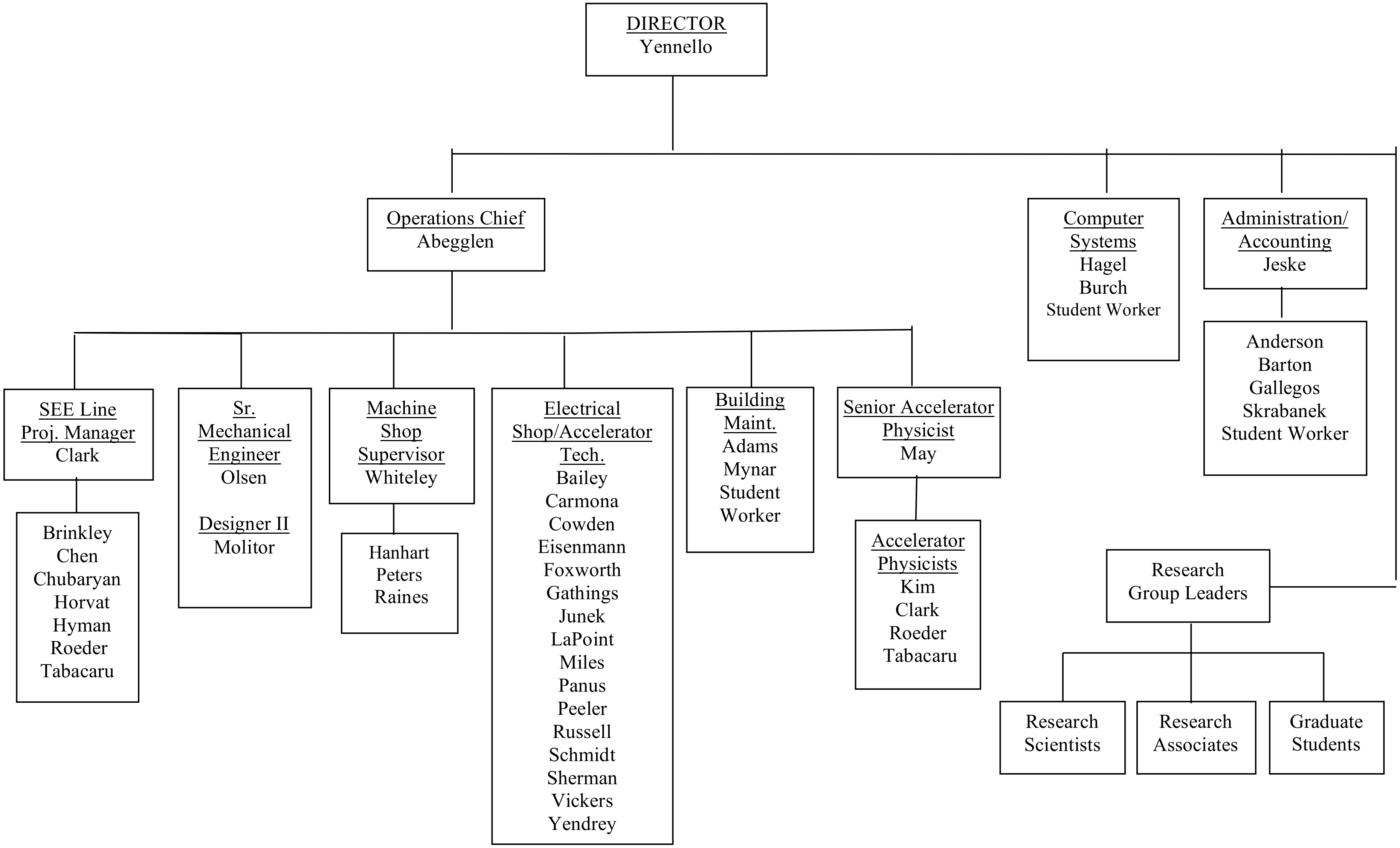

STUDENTS WHO RECEIVED GRADUATE DEGREES FROM THESIS WORK CONDUCTED AT THE CYCLOTRON INSTITUTE

April 1, 2016 – March 31, 2017

Name	Year	Thesis Title	Advisor	Present Position
Matteo Barbarino	2016	*Fusion reactions in laser produced plasma*	Aldo Bonasera	National Institute for Laser, Plasma and Radiation Physics (INFLPR), Bucharest, Romania
Zilong Chang	2016	*Inclusive jet longitudinally double spin asymmetry* A_{LL} *measurements in 510 GeV Polarized pp Collisions at STAR*	C.A. Gagliardi	Post Doc. RHIC, Brookhaven National Laboratory, Upton, New York
Marisa C. Alfonso	2016	*Development of online chemistry for rutherfordium (element 104): commissioning of a gas stopper and extraction chromatography of ruthfordium homologs (zirconium and hafnium)*	C.M. Folden III	Radiochemist, Eckert & Ziegler Analytics, Atlanta, Georgia
Kyong Chol Han	2016	*Jet fragmentation via recombination of parton showers and its medium modification at RHIC and LHC*	Che-Ming Ko	Post. Doc. Department of Physics and Astronomy, Texas A&M University, College Station, Texas
Jonathan Thomas Button	2016	*Giant monopole resonance in* ^{44}*Ca,* ^{54}*Fe,* ^{64}*Zn,* ^{68}*Zn, and* ^{94}*Mo*	D.H. Youngblood	ORISE Fellow at Center for Disease Control, an CDC Chamblee Facility, Atlanta, Georgia
Feng Li	2016	*Spinodal instabilities in NJL and PNJL model*	Chi-Ming Ko	Post-doc, Frankfurt institute for advanced studies, Frankfurt, Germany
Nathan Prescott Montgomery Holt	2016	*Sum rules and photon emission in hardonic matter*	Ralf Rapp	Assistant Professor, Piedmont College, Demorest, Georgia
Benjamin B. Fenker	2016	*Sum rules and photon emission in hardonic matter*	D. Melconian	Programmer Analyst Tessella, Houston, Texas

INSTITUTE COLLOQUIA AND SEMINARS
April 1, 2016- March 31, 2017

2016

April 5	Prof. W. Udo Schroeder, Department of Chemistry and Physics, University of Rochester, Rochester, New York	*”Fission Chips” – Unusual Flavors (Dynamic Nuclear Instabilities in Fission-Like Reactions)*
April 12	Professor D. Lee, Department of Physics, North Carolina State University, Raleigh, North Carolina	*Recent Results in Nuclear Lattice Effective Field Theory*
May 17	Professor Aurel Bolgac, Department of Physics, University of Washington, Seattle, Washington	*Induced Fission in Real-Time*
May 24	Professor Dr. Klaus Blaum, Max-Planck-Institut für Kernphysik, Heidelberg, Germany	*Fundamental Tests of Nature with Cooled and Stored Exotic Ions*
May 31	Dr. Kyle W. Brown, Washington University in St. Louis, St. Louis, Missouri	*Continuum Nuclear Structure Accessed via the Invariant-Mass Method*
June 15	Dr. Brent Barker, Physical Science, Roosevelt University, Chicago, Illinois	*Predicting Post-Impact Dynamics in Intermediate Energy Nuclear Collisions.* *Using Competency-Based Assessment to Develop Collaborative Classrooms.*
July 21	Prof. Umesh Garg, Department of Physics, University of Notre Dame, South Bend, Indiana	*Nuclear Incompressibility, the Asymmetry Term, and Fluffiness of Open-Shell Space*
August 17	Dr. Justin Mabiala, Cyclotron Institute, Texas A&M University, College Station, Texas	*Pre-equilibrium Emission and Its Possible Relation to Alpha-Clustering in Nuclei*
September 9	Dr. Andre Mischke, Department of Physics and Astronomy, University of Utrecht, Utrechht, The Netherlands	*Hot QCD Matter*
September 14	Dr. Tommi Eronen, Cyclotron Institute, Texas A&M University, College Station, Texas	*Probing Fundamental Physics: The Fruitful IGISOL/JYFLTRAP (ion Guide/Penning Trap) Combination*

November1	Dr. Gavin Lotay, Department of Physics, University of Surrey, England, United Kingdom	*Frontiers in Explosive Nuclear Astrophysics*
November 15	Professor Tetyana Galatyuk, Institute of Nuclear Physics, Technische Universität Darmstadt, Darmstadt, Germany	*Shine a Light! When Matter Shatters*

2017

January 10	Assistant Prof. Kyujin Kwak, Ulsan National Institute of Science and Technology,Ulsan, South Korea	*Nuclear Astrophysics in Korea: Experience with RAON (Korean Rare Isotope Accelerator) and Related Astrophysical Research*
January 24	Dr. Volker Koch, Nuclear Science, Lawrence Berkeley National Laboratory, Berkeley, California	*Fluctuations, Correlations and the QCD Phased Diagram*
February 14	Associate Professor Vincenzo Greco, Nuclear and Theoretical Physics, University of Catania, Catania, Sicily, Italy	*Open Heavy Flavor Dynamics in the Hot QCD Created in URHICs*
February 21	Associate Professor Chiho Nonaka, Particle and Astrophysical Science, University of Nagoya, Nagoya, Japan	*Radiative Recombination at the Quark-Hardon Phase Transition*
March 8	Dr. Lee Bernstein, Lawrence Berkeley National Laboratory, University of California, Berkeley, Calfornia	*Inelastic Neutron Scattering – From Baghdad to Berkeley*
March 10	Assistant Prof. Kohshin Washiyama, Institute of Medical, Pharmaceutical and Health Sciences, Kanazawa University, Kanazawa, Japan	*Current Status of Medical Alpha Emitter Production in Japan*
March 24	Dr. Oscar Trippella, Instituto Nazionale di Fisica Nucleare, University of Perugia, Perugia, Italy	*The* ^{13}*C Neutron Source for the S-Process in AGB Low-Mass Stars*